



High Resolution Spectroscopy of Classical Cepheids and multiwavelength calibration of PLZ and PWZ relations

Erasmus Trentin

Universitätsdissertation
zur Erlangung des akademischen Grades

doctor rerum naturalium
(*Dr. rer. nat.*)

in der Wissenschaftsdisziplin
Astrophysik

Eingereicht an der
Mathematisch-Naturwissenschaftlichen Fakultät
Institut für Physik und Astronomie
der Universität Potsdam
und
das Leibniz-Institut für Astrophysik Potsdam (AIP)

Datum der Disputation: 20/03/2025

Betreuer

Prof. Dr. Maria-Rosa Cioni

Leibniz Institute für Astrophysik Potsdam (AIP)

Gutachter

Prof. Dr. Katja Poppenhäger

Leibniz Institute für Astrophysik Potsdam (AIP)

Prof. Dr. Hans Van Winckel

Instituut voor Sterrenkunde

Dr. Jesper Storm

Leibniz Institute für Astrophysik Potsdam (AIP)

Abstract

Classical Cepheids are a type of variable stars critical for establishing distances in the Local Group. These stars are young, intermediate-mass stars evolving through a specific phase of the star evolution in which radial pulsation is excited, resulting in a change of brightness. What makes them one of the primary tools in estimating distances is the correlation between their intrinsic luminosities and pulsational periods. For this reason, they are usually referred to as "standard candles". This property, known as the Period-Luminosity (PL) relation, enables Cepheids to serve as fundamental anchors on the cosmic distance ladder, which allows us to determine the scale of the Universe. On the other hand, they represent powerful tools as tracers of the young population in the Milky Way disc, with the possibility to study variations in their chemical abundances as a function of their location in the Galaxy. The first part of this dissertation revolves around the description of the astrophysical characteristics of Cepheids, their progenitors, evolution and ultimate fate. The origin of stellar pulsation is explored, starting from the basics of stellar structure to the development of a pulsational theory. The main objective is to discover which mechanisms ignite pulsation, which are the constraints that define the region in the Hertzsprung-Russell diagram, called the instability strip, where these mechanisms become relevant and what are the main implications and uses of the PL relation. Furthermore, we will navigate through the basics of spectroscopic analysis, the elements necessary to build an atmospheric model and which physical quantities play a relevant role in influencing the photosphere and need to be determined in order to characterise a star.

The remaining chapters are based on three peer-reviewed published papers and part of the C-MetaLL project survey: In Chapter 2 we have collected high-resolution spectroscopy with UVES@VLT for a sample of 65 DCEPs. The majority of them are the faintest DCEPs ever observed in the Milky Way. For each target, we derived accurate atmospheric parameters, radial velocities, and abundances for 24 different species. The resulting iron abundances range between +0.3 and -1.1 dex with the bulk of stars at $[\text{Fe}/\text{H}] = -0.5$ dex. Our sample includes the most metal-poor DCEPs observed so far with high-resolution spectroscopy. Exploiting the role of Cepheids as tracers of young population stars, the radial metallicity gradient is studied together with the distribution of the sample in the disc.

In Chapter 3 we quantify the metallicity dependence of the PL and PW relations

of the Galactic DCEPs for a variety of photometric bands, ranging from optical to near-infrared. We gathered a sample of 910 DCEPs with available $[\text{Fe}/\text{H}]$ values from high-resolution spectroscopy or metallicities from the Gaia Radial Velocity Spectrometer. For all these stars, we collected photometry in the GBP, GRP, G, I, V, J, H, and KS bands and astrometry from Gaia Data Release 3 (DR3). We used these data to investigate the metal dependence of both the intercepts and slopes of a variety of PL and PW relations at multiple wavelengths.

In Chapter 4, a follow-up of Chapter 2, we enlarge the sample of DCEPs with accurate abundances from high-resolution spectroscopy. We present the results of the analysis of 331 spectra obtained for 180 individual DCEPs with a variety of high-resolution spectrographs. As already done in Chapter 2 we derived accurate atmospheric parameters, radial velocities, and abundances for up to 29 different species. A robust sample is obtained, distributed almost homogeneously in both distance and metallicity ranges. The radial metallicity gradient is studied for all the chemical species, highlighting the role of Cepheids as a powerful means to trace spiral arms not yet well constrained.

Zusammenfassung

Klassische Cepheiden sind eine Art von veränderlichen Sternen, die für die Bestimmung von Entfernungen in der Lokalen Gruppe entscheidend sind. Bei diesen Sternen handelt es sich um junge, mittelschwere Sterne, die eine bestimmte Phase der Sternentwicklung durchlaufen, in der radiale Pulsationen angeregt werden, was zu einer Helligkeitsänderung führt. Die Korrelation zwischen ihrer Eigenleuchtkraft und den Pulsationsperioden macht sie zu einem der wichtigsten Hilfsmittel bei der Abschätzung von Entfernungen. Aus diesem Grund werden sie gewöhnlich als „Standardkerzen“ bezeichnet. Dank dieser Eigenschaft, die als Perioden-Leuchtkraft-Beziehung (PL) bekannt ist, dienen uns Cepheiden als fundamentale Ankerpunkte auf der kosmischen Entfernungsleiter, was uns ermöglicht, die Größe des Universums zu bestimmen. Andererseits sind sie ein leistungsfähiges Instrument, um die junge Population in der Milchstraßenscheibe aufzuspüren, und bieten die Möglichkeit, Variationen ihrer chemischen Häufigkeiten in Abhängigkeit von ihrer Position in der Galaxie zu untersuchen. Der erste Teil dieser Dissertation befasst sich mit der Beschreibung der astrophysikalischen Eigenschaften von Cepheiden, ihren Vorläufern, ihrer Entwicklung und ihrem endgültigen Schicksal.

Der Ursprung stellarer Pulsation wird erforscht, ausgehend von den Grundlagen der stellaren Struktur bis hin zur Entwicklung einer Pulsationstheorie. Das Hauptziel besteht darin, herauszufinden, welche Mechanismen die Pulsation auslösen, welche Einschränkungen den Bereich im Hertzsprung-Russell-Diagramm, den so genannten Instabilitätsstreifen, definieren, in dem diese Mechanismen relevant werden, und was die wichtigsten Auswirkungen und Anwendungen der PL-Beziehung sind. Darüber hinaus werden wir die Grundlagen der spektroskopischen Analyse, die Elemente, die für den Aufbau eines Atmosphärenmodells erforderlich sind, und die physikalischen Größen, die eine wichtige Rolle bei der Beeinflussung der Photosphäre spielen und für die Charakterisierung eines Sterns bestimmt werden müssen, durchgehen. Die übrigen Kapitel basieren auf drei von Fachleuten begutachteten Veröffentlichungen und sind Teil der C-MetaLL-Projektstudie: In Kapitel 2 haben wir hochauflösende Spektroskopie mit UVES@VLT für eine Probe von 65 DCEPs gesammelt. Die meisten von ihnen sind die schwächsten DCEPs, die jemals in der Milchstraße beobachtet wurden. Für jedes Ziel haben wir genaue atmosphärische Parameter, Radialgeschwindigkeiten und Häufigkeiten für 24 verschiedene Elemente abgeleitet. Die resultierenden Eisenhäufigkeiten liegen zwischen +0,3

und -1,1 dex, wobei der Großteil der Sterne $[\text{Fe}/\text{H}] \approx -0,5$ dex aufweist. Unsere Probe umfasst die metallärmsten DCEPs, die bisher mit hochauflösender Spektroskopie beobachtet wurden. Unter Ausnutzung der Rolle von Cepheiden als Indikatoren für junge Sternpopulationen wird der radiale Metallizitätsgradient zusammen mit der Verteilung der Probe in der Scheibe untersucht.

In Kapitel 3 quantifizieren wir die Metallizitätsabhängigkeit der PL- und PW-Relationen der galaktischen DCEPs für eine Vielzahl photometrischer Filter, die vom optischen bis zum nahen Infrarot reichen. Wir haben eine Stichprobe von 910 DCEPs mit verfügbaren $[\text{Fe}/\text{H}]$ -Werten aus hochauflösender Spektroskopie oder Metallizitäten aus dem Gaia Radialgeschwindigkeitsspektrometer gesammelt. Für alle diese Sterne haben wir Photometrie in den Bändern GBP, GRP, G, I, V, J, H und KS sowie Astrometrie aus Gaia Data Release 3 (DR3) gesammelt. Anhand dieser Daten untersuchten wir die Metallabhängigkeit sowohl der Schnittpunkte als auch der Steigungen einer Reihe von PL- und PW-Beziehungen bei verschiedenen Wellenlängen.

In Kapitel 4, einer Fortsetzung von Kapitel 2, erweitern wir die Stichprobe von DCEPs mit genauen Elementhäufigkeiten aus hochauflösender Spektroskopie. Wir stellen die Ergebnisse der Analyse von 331 Spektren vor, die für 180 einzelne DCEPs mit einer Vielzahl von hochauflösenden Spektrographen gewonnen wurden. Wie bereits in Kapitel 2 haben wir genaue atmosphärische Parameter, Radialgeschwindigkeiten und Häufigkeiten für bis zu 29 verschiedene Elemente abgeleitet. Wir haben eine robuste Stichprobe erhalten, die sowohl in den Entfernungs- als auch in den Metallizitätsbereichen nahezu homogen verteilt ist. Der radiale Metallizitätsgradient wurde für alle chemischen Spezies untersucht, was die Rolle der Cepheiden als leistungsfähiges Mittel zum Aufspüren von Spiralarmen unterstreicht, die noch nicht gut erforscht sind.

Statement of own contribution

This doctoral dissertation is based on 3 peer-reviewed articles (from Chapters 2 to 4) published in Monthly Notices of the Royal Astronomical Society (MNRAS) and Astronomy and Astrophysics (A&A). The formatting of these articles was adopted to give the doctoral dissertation a uniform layout. In the following I (Erasmus Trentin) outline my contribution:

- **Cepheid Metallicity in the Leavitt Law (C- MetaLL) survey - II. High-resolution spectroscopy of the most metal poor Galactic Cepheids**
 - **Trentin, E.**; Ripepi, V.; Catanzaro, G.; Storm, J.; Marconi, M.; De Somma, G.; Testa, V.; Musella, I.
 - Pub Date: February 2023, Monthly Notices of the Royal Astronomical Society, Volume 519, Issue 2, pp.2331-2348
 - DOI: 10.1093/mnras/stac2459 , 10.48550/arXiv.2209.03792
 - In this article, I spectroscopically analysed the stars, estimated the atmospheric parameters, abundances, and took care of the fit to estimate the radial galactic gradient. I wrote the manuscript under the guidance of my collaborators.
- **Cepheid Metallicity in the Leavitt Law (C- MetaLL) survey. IV. The metallicity dependence of Cepheid period-luminosity relations**
 - **Trentin, E.**; Ripepi, V.; Molinaro, R.; Catanzaro, G.; Storm, J.; De Somma, G.; Marconi, M.; Bhardwaj, A.; Gatto, M.; Testa, V.; Musella, I.; Clementini, G.; Leccia, S.
 - Pub Date: January 2024, Astronomy & Astrophysics, Volume 681, id.A65,
 - DOI: 10.1051/0004-6361/202347195 , 10.48550/arXiv.2310.03603
 - In this article, I collected the literature information, the sample and estimated the parameters to calibrate the PLZ and PWZ. I wrote the manuscript under the guidance of my collaborators.

- **Cepheid Metallicity in the Leavitt Law (C- MetaLL) survey: VI: Radial abundance gradients of 29 chemical species in the Milky Way Disk**

- **Trentin, E.**; Catanzaro, G.; Ripepi, V.; Alonso-Santiago, J.; Molinaro, R.; Storm, J.; De Somma, G.; Marconi, M.; Bhardwaj, A.; Gatto, M.; Musella, I.; Testa, V.
- Pub Date: October 2024, *Astronomy & Astrophysics*, Volume 690, id. A246
- DOI: 10.1051/0004-6361/202450376
- In this article, I spectroscopically analysed the stars, estimated the atmospheric parameters, abundances, and took care of the fit to estimate the radial galactic gradient. I wrote the manuscript under the guidance of my collaborators.

Contents

Abstract	iii
Zusammenfassung	v
Statement of own contribution	vii
Contents	ix
1 Introduction	1
1.1 Variable stars	1
1.2 Evolution of intermediate-mass stars	4
1.3 Introduction to pulsation theory	7
1.3.1 Basic equations of Stellar Structure and Evolution	7
1.3.2 Timescales and Ritter’s Relation	9
1.3.3 Equations of (Radial) Stellar Pulsation Theory	10
1.3.4 The ϵ, κ, γ mechanisms	13
1.4 The Period-Luminosity relation and the role of the metallicity	16
1.5 Determination of chemical abundances through spectroscopic techniques	18
1.5.1 The radial transfer equation	19
1.5.2 How to compute a photosphere model	22
1.5.3 Sneak peek about the role of convection	26
1.5.4 Equivalent widths	26
1.5.5 The Effective Temperature, T_{eff}	27
1.5.6 The surface gravity, $\log g$	29
1.5.7 Rotation and turbulence	29
2 C-MetaLL Survey II	33
2.1 Introduction	33
2.2 Data	35
2.2.1 Selection of the targets	35
2.2.2 Observations and data reduction	35
2.3 Abundance analysis	36
2.3.1 Stellar parameters	36

2.3.2	Abundances	39
2.4	Comparison with the literature	43
2.4.1	Literature sample	43
2.4.2	Element by element comparison	44
2.5	The Galactic radial gradient	47
2.5.1	Distance estimate	47
2.5.2	Metal radial gradient of the MW disc	48
2.6	Discussion	53
2.6.1	Iron abundance disc gradient	53
2.6.2	Disc gradient for elements other than iron	57
2.7	Summary	58
2.A	Abundances for target stars	60
3	C-MetaLL Survey IV	65
3.1	Introduction	65
3.2	Description of the data used in this work	69
3.2.1	Photometry	69
3.2.2	Metallicity	71
3.2.3	Astrometry	73
3.3	Derivation of the PLZ/PWZ relations	73
3.4	Results	75
3.4.1	Literature and <i>Gaia</i> DR3 sample	75
3.4.2	Literature sample only	80
3.4.3	Comparison between Lit.+ <i>Gaia</i> and Lit. samples	83
3.5	Discussion	84
3.5.1	Parallax correction	84
3.5.2	Distance to the LMC	86
3.5.3	Metallicity sampling	87
3.5.4	Comparison with the literature	87
3.6	Conclusion	90
3.A	PLZ/PWZ coefficients for the F pulsators only sample	92
3.B	Parallax correction for the Lit. sample	92
4	C-MetaLL Survey VI	97
4.1	Introduction	97
4.2	Observations	101
4.2.1	Sample	101
4.2.2	Instruments used for the observations and data reduction	103

4.3	Spectroscopy	104
4.3.1	Stellar parameters	104
4.3.2	Abundances	106
4.4	Results	107
4.4.1	Abundances results	107
4.4.2	Radial gradients and spatial distribution	112
4.5	Comparison with recent literature results	117
4.6	Summary	120
4.A	Stars with uncertain classification	122
4.B	Phases for seven DCEPs devoid of Gaia periods and epochs of maximum light.	125
5	Conclusions	127
	Bibliography	131
	Publications and Workshops	151

1.1 Variable stars

When talking about variability, one of the first questions that astronomers should ask themselves is: when should a star be defined as a variable? Indeed, if we consider several mechanisms such as mass loss, pulsation, accretion or stripping events from the surrounding environment (caused for example by the presence of a companion in the case of a binary system), granulation in the photosphere, magnetism cycles, stellar winds and many others, the distinction between star and variable star becomes inexistent.

On the other side, it is ironic that historically these spots that appeared in the night sky have been believed to be fixed and unchanging in both position and brightness. When we take into account the great distances at which stars are and the fact that only a few of the mechanisms mentioned above can induce a change in brightness big enough to be seen by the naked eye, then it is easier to understand how astronomers used to treat these events as unique. In those rare documented cases where a star was observed as it disappeared (and surprisingly appeared again months later) rotation and eclipses were the only explanations that seemed to be reasonable.

It was only by the start of the twentieth century that, when comparing the light curves of different stars, the differences were so evident that astronomers were forced to explore new theories. At that period, several kinds of variable stars had already been observed (among these, those that nowadays are classified as Mira, RR Lyrae and Cepheids) and the advent of photographic plates would have soon allowed their number to increase even more, which would furthermore increase exponentially with the introduction, in the last decade of the twentieth century, of CCDs. To put in crisis the binary hypothesis as a justification for the variability in the luminosity of all the stars was δ Cepheid, the prototype of those variable stars that constitute the main protagonists of this thesis. By the start of the twentieth century, binary stars had already been discovered and for one of them, Algol, its nature was confirmed by Vogel [Vog90] analysing the Doppler shifts in its spectroscopic lines. On the other hand, although *delta* Cepheid's radial velocity was confirmed to change as well, its light curve was deeply different from Algol's (a comparison is shown in Fig. 1.1).

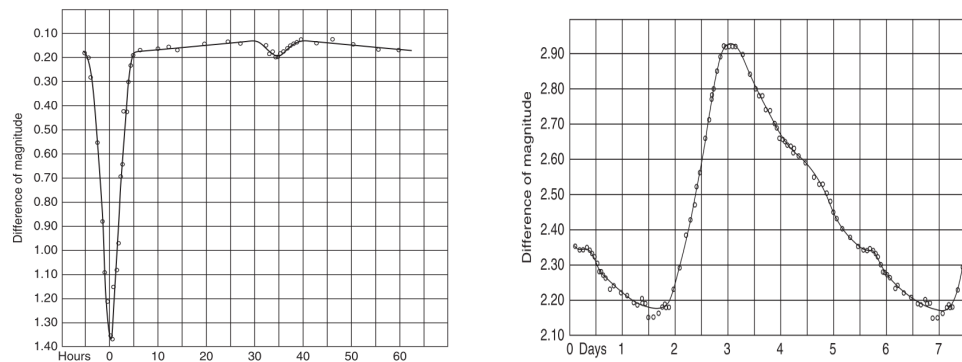


Figure 1.1: Comparison of light curves between Algol (on the left, Stebbins [Ste10]) and δ Cepheid (on the right, Stebbins [Ste08]).

Even after the strong arguments by Shapley [Sha14] against the binary nature of δ Cepheid, in favour of a radial pulsation, more than three decades had to elapse before Zhevakin [Zhe53] and Cox and Whitney [CW58] began to put some lights on the driving mechanisms that caused the pulsations of Cepheid variable stars.

Nowadays, when it comes to classification, the starting point is to look at the nature of the process. Stars may owe their variability to processes inherent to the star, in which case astronomers would refer to it as an intrinsic variable (such as cataclysmic variables or pulsating variables), otherwise the label assigned would be extrinsic variables (eclipsing variables being the prototypical example of this category). Figure 1.2 shows a recently updated version of the variability tree (from Eyer and Mowlavi [EM08]).

As can be seen, this classification contains both stellar and non-stellar objects, such as active galactic nuclei (AGN) for the intrinsic variables and asteroids for the extrinsic ones. Further subdivisions involve several kinds of parameters and characteristics: the nature of a companion (if present), the shape of the light curve and/or the presence of certain spectral lines. The list of different cases and strategies adopted to classify variability can continue for pages. As someone might expect, each subdivision is not driven by a single feature and are not uncommon cases where researchers still debate either on which characteristics must be taken into account to divide unambiguously a certain kind of variable object or, vice-versa, in which category an astronomical object falls (and we must not exclude the cases where, for example, a star is both a pulsating variable but also part of a binary system).

As already mentioned, this thesis will explore one particular kind of variable stars called Classical Cepheids, sometimes also termed as δ Cepheids or type I

offers the precious opportunity to calculate the luminosity, and hence the distance (once the apparent magnitude is known) of stars and galaxies that host these stars and build the first rung of the so-called cosmic distance ladder. We will see more in detail in Sect. 1.4 the theoretical framework that leads to the formulation of this relation and what kind of approximations are hidden behind it. In the next section, instead, we first have an insight into the origin and the fate of these stars. Then, in Sec. 1.3 we explore how it is possible to build a pulsation theory starting from the basic equations that describe the stellar structure and evolution and the mechanisms that allow some stars, in particular those who in their lives cross the so-called instability strip (Cepheids included), to ignite pulsations.

1.2 Evolution of intermediate-mass stars

When looking at the mass of stars, it is generally common to divide them into three categories: low-mass ($\lesssim 3M_{\odot}$), intermediate-mass (between 3 and $40 M_{\odot}$) and high-mass ($>40 M_{\odot}$) stars. As already mentioned, Classical Cepheids are pulsators with typical masses between 3 and $13 M_{\odot}$, which makes them intermediate-mass stars. In order to understand the origins of these stars and their fate, we will follow the evolutionary path model by Ekström et al. [Eks+12] for a star of mass $5 M_{\odot}$ and shown in Figure 1.3. Both cloud-collapsing and pre-MS phases are omitted for clarity and discussed in detail by Iben Jr [Ibe65]. The instability strip, this still "magic" region of the HR diagram where a star starts pulsating, is also shown. Both low- and intermediate-mass share the main evolution processes that are described in this section and the main differences are highlighted for each stage. More details of each evolutionary phase are discussed in Catelan [Cat07], Salaris and Cassisi [SC05] and references therein.

1. When the core of the proto-star starts to ignite efficiently the hydrogen in the core, the newly born star settles in the so-called Zero Age Main Sequence (ZAMS) in the HR diagram, where it will slowly evolve in terms of nuclear timescales transforming the hydrogen in the core into helium.
2. At a certain point, the almost depleted hydrogen in the core is not capable of supporting the structure of the star through nuclear reactions and will contract. It is worth noting that due to the higher temperatures of the core, for intermediate-mass stars the H-burning mechanism is dominated by the CNO cycle instead of the proton-proton chain in low-mass stars. This leads in the former case to develop a convective core.

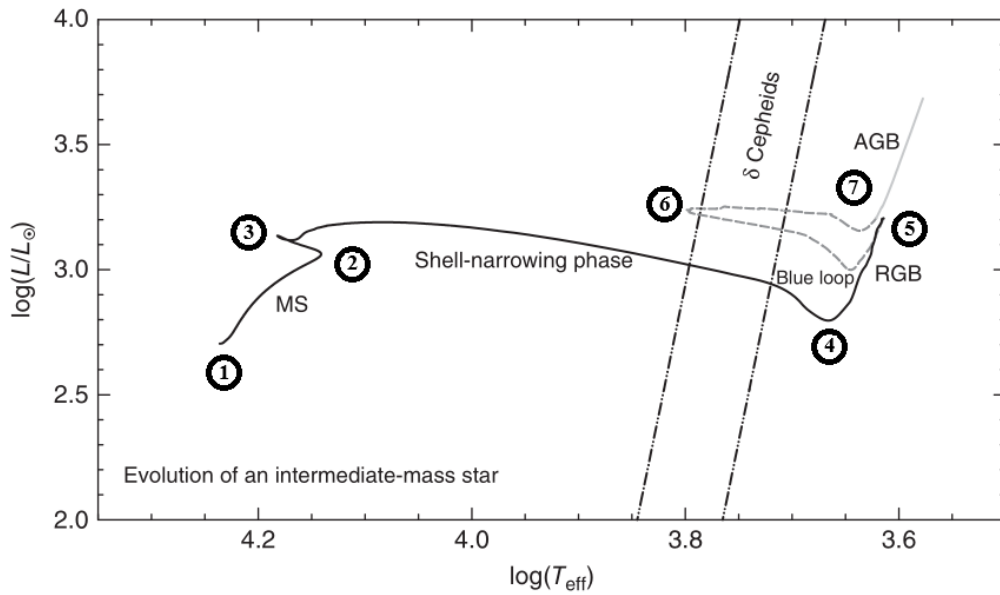


Figure 1.3: Evolution of an intermediate-mass star, based on a $5 M_{\odot}$, rotating stellar model from Ekström et al. [Eks+12] with metallicity $Z = 0.014$. The different stages highlighted by the numbers are explained in the text. Boundaries of the instability strip based on Tammann et al. [TSR03b] are shown in dotted lines.

3. This point corresponds to the total depletion of H in the core, completely transformed into He. Because of the convective core discussed in the previous point, the region devoid of hydrogen in intermediate-mass stars is significantly larger and the contraction process is more marked and fast, creating "gaps" at the top of the MS in photometric studies of open clusters (e.g. the case of M67 in Sandquist [San04]). Similarly to what happens for lower-mass stars, the H-burning region shifts from the core to a surrounding shell, continuing the enrichment process of the He core.
4. The contraction of the core heats the surrounding H-burning shell, which becomes progressively thinner. Since part of the energy released by the H-burning shell is being used in the expansion of the star, the outer layers cool down, leading to the development of a convective envelope and the star reaches the base of the Red Giant Branch (RGB). If the convective envelope extends further into deeper layers, the first dredge-up event takes place and the inner material is dragged up to more external layers.
5. When the right conditions for the ignition of He accumulated in the core are

reached, the star stops ascending along the RGB, reaches what inevitably becomes the tip of the RGB and starts its descent. Here lies one of the most important differences between low- and intermediate-mass stars. Indeed, in the former case, the growing process is slower and the core reaches a level of electron degeneracy. Part of the energy at the very centre of the core is freed through the creation of neutrinos, which means that the hottest region of the core where He starts to ignite is not the centre but a shell surrounding it. Because of the degeneracy, the energy generated by the new nuclear reactions does not increase the local pressure and the region where the burning has started does not expand (and subsequently cool down). This means that a counter-balance effect does not take place, the thermonuclear reaction rate dramatically increases until a thermonuclear runaway, also called "He flash", sets off and most of the energy is used to lift up the degeneracy. For more massive stars, the ignition of the helium commences before the core reaches a degenerate state and the whole process is less abrupt. Also in this case the timescales are reduced respect with to the low-mass case. After this event, the star descends the RGB and lays down to the horizontal branch (HB), the name derived from the fact that at this phase the luminosity is essentially independent of the temperature, which in turn depends on the amount of mass lost during the previous phases.

6. Since the instability strip crosses the HB at intermediate temperatures, some stars might fall within it after the ignition of the He core, resulting in RR Lyrae for the low-mass case. Moreover, even in the case of a blue HB star, it can cross the instability strip after it departs from the HB, on its way to becoming an Asymptotic Giant Branch (AGB) star. On the other side, depending on the relative efficiency of the H-burning shell compared with the He-burning core, a star can develop blueward loops. This means that, similarly to what happens with blue HB stars, also red HB stars can cross the instability strip depending on the maximum extension of the blue loop and give rise to our protagonists, the Classical Cepheids.
7. Eventually, also the He in the core will be depleted and the story seems to repeat itself, with the star further evolving toward the aforementioned AGB, reaching a state where the core is inert and both H and He burn in progressively thinner shells. In these stars, He- and H-burning shells will compete and take turns as the most efficient energy sources. While many other events can take place, like a second and third dredge up and/or a thermal pulse phase, AGB stars will eventually lose their envelope leaving

exposed the core, which is now named White Dwarf (WD). Depending on the mass loss rate and the efficiency of nuclear reactions, WDs can differentiate themselves in size and chemical composition: for low-mass stars, the He core might never ignite, leaving a He WD, while in more massive ones the carbon generated by the He reactions could reach the condition to burn itself resulting in a O-Ne-Mg WD. In general, the expected final product is a C-O WD. Further details on the final stages of AGB stars can be found in the review by Herwig [Her05].

At this point, we know the origin and destiny of classical Cepheids, what remains obscure is the reason why they pulsate, why the instability strip exists and which physical properties define its boundaries. In the next section, the mystery will be finally unveiled, while in Sect. 1.4 we will interrogate ourselves about the origin of the PL relation and its relation with the metallicity.

1.3 Introduction to pulsation theory

1.3.1 Basic equations of Stellar Structure and Evolution

This section will be dedicated to developing and showing how we can theoretically build a pulsating model suitable for our stars. Luckily for us, we will not focus on the specific mathematical passages, our attention will move towards the assumptions and approximations that allow us to obtain a formula and highlight the physical limits of these equations. Let's start with the evergreen stellar structure equations:

$$\frac{\partial r}{\partial m} = \frac{1}{4\pi r^2 \rho}, \quad (1.1)$$

$$\frac{\partial P}{\partial m} = -\frac{Gm}{4\pi r^4}, \quad (1.2)$$

$$\frac{\partial L}{\partial m} = \epsilon - \epsilon_\nu - \epsilon_g, \quad (1.3)$$

$$\frac{\partial T}{\partial m} = -\frac{GmT}{4\pi r^4 P} \nabla. \quad (1.4)$$

These correspond to the *continuity of mass*, the *hydrostatic equilibrium*, the *conservation of energy* and *energy transport* equations, respectively. In these relations, r is the radius, m the mass, ρ the density, P the pressure, G the gravitational constant, L the luminosity, ϵ energy generated per unit time and unit mass (those with subscripts ν and g corresponds to the energy loss due to neutrinos and work performed

on the gas), T the temperature and ∇ is commonly called "temperature gradient" and takes different forms depending of which mean of transport, either radiative, conductive or convective. While the latter case is a well-known complicated and debated problem in astrophysics, the former can be easily treated, obtaining:

$$\nabla = \frac{3}{16\pi acG} \frac{\kappa_R L P}{m T^4} \quad \text{and} \quad L = -\frac{64\pi^2 ac}{3} r^4 \frac{T^4}{\kappa_R} \frac{\partial T}{\partial m}, \quad (1.5)$$

where a is the radiation constant, c is the speed of light and κ_R the *Rosseland mean opacity*. Is it possible to include in this formula also the conductive case through an equivalent *conductive opacity* κ_c which leads to a generalised opacity:

$$\frac{1}{\kappa} = \frac{1}{\kappa_R} + \frac{1}{\kappa_c} \quad (1.6)$$

One first step towards the formulation of a pulsation theory is to modify the hydrostatic equilibrium equation, which is necessary when the balance between pressure and gravity is broken. During pulsations, the mass element will undergo an acceleration, and equation 1.2 becomes the *conservation of momentum*:

$$\frac{\partial^2 r}{\partial t^2} = -4\pi r^2 \frac{\partial P}{\partial m} - \frac{Gm}{r^2}. \quad (1.7)$$

In order to have all the information needed to solve this set of equations, a further set of the so-called *constitutive equations* is needed, composed by the *equation of state*:

$$\rho = \rho(P, T, \mu), \quad (1.8)$$

the dependence of the specific heat at constant pressure as a function of pressure, temperature and mean molecular weight (necessary for describing the convective energy transport):

$$c_P = c_P(P, T, \mu), \quad (1.9)$$

the opacity relation (both in the radiative and conductive cases), required to compute ∇ :

$$\kappa = \kappa(P, T, \mu), \quad (1.10)$$

the thermonuclear rate of transformation of nuclei j to nuclei k :

$$r_{jk} = r_{jk}(P, T, \mu), \quad (1.11)$$

and, finally, the rate of energy generation:

$$\epsilon = \epsilon(P, T, \mu). \quad (1.12)$$

Last but not least, we report the definition of the *mean molecular weight*:

$$\mu = \left[\sum_i [1 + \nu_e(i)] \frac{X_i}{A_i} \right]^{-1}, \quad (1.13)$$

where X_i is the chemical abundance by mass fraction with atomic mass and number A_i and Z_i , respectively, and $\nu_e(i)$ is the average number contribution of free electrons for the element i , and the time evolution of the abundance:

$$\frac{\partial X_i}{\partial t} = \frac{m_i}{\rho} \left(\sum_j r_{ji} - \sum_k r_{ik} \right) \quad (1.14)$$

The evolutionary track discussed in the previous section could indeed be computed by solving these equations. The next step is to modify (where necessary) these formulae and create a new recipe that allows us not only to describe pulsation but to predict under which condition a star will pulsate.

1.3.2 Timescales and Ritter's Relation

By the end of the nineteenth century, it became clear that the observed oscillatory phenomenon could not be purely electromagnetic (i.e. what happens, for instance, to an electric bulb connected to a varying source of power), but involved macroscopic movements that involved at least the surface of the star. Mechanical oscillations interpreted as sound waves which propagate through the several layers of the star are one of the possible explanations of pulsation. If we consider the definition of the speed of sound:

$$v_s = \sqrt{\frac{\Gamma_1 P}{\rho}} = \sqrt{\frac{\Gamma_1 k_B T}{\mu m_H}} \quad (1.15)$$

where Γ_1 is the first adiabatic index, k_B is the Boltzmann constant, m_H is the hydrogen mass, μ the mean molecular weight, P is the pressure and T the temperature, then it is easy to have a rough first estimation of the typical timescale for the

propagation of these waves in a star:

$$\mathcal{P} \sim \frac{2R}{v_s} \quad (1.16)$$

With R being the radius of the star. In the case of δ Cep, we would obtain 22 days, which is surprisingly close to the period of δ Cep (5.3 days) considering the approximation we applied. Furthermore, if we assume a homogeneous state, both Γ_1 and ρ in Eq 1.15 are constants, and integrating the hydrostatic equation (1.2) in its Eulerian formalism (that is, using r as independent parameters using the transformation $dm = 4\pi\rho r^2 dr$) we obtain:

$$\frac{dP}{dr} = -\frac{Gm\rho}{r^2} = -\frac{4\pi G\rho^2 r}{3} \Rightarrow P(r) = \frac{2\pi\rho^2 G}{3}(R^2 - r^2) \quad (1.17)$$

This way, we can compute the time needed for the sound wave to travel back and forth across the diameter of the star:

$$\mathcal{P} = 2 \int_0^R \frac{dr}{\sqrt{\Gamma_1 2\pi\rho G(R^2 - r^2)/3}} \Rightarrow \mathcal{P} = \sqrt{\frac{3\pi}{2\Gamma_1 G\rho}}, \quad (1.18)$$

which can be written as:

$$\mathcal{P}\sqrt{\rho} = Q \quad (1.19)$$

This is the first version of the so-called *period-mean density relation*, obtained by Ritter [Rit79]. A more rigorous derivation still leads to a very similar relation, which suggests that less dense stars will have longer radial pulsation periods and vice versa. Moreover, this expression can also be interpreted as the dynamical timescale, many orders of magnitude shorter than other typical timescales of stars (i.e. thermal or nuclear timescales). In other words, crucial phenomena for the description of the star structure and evolution (e.g. change of chemical composition described in Eq. 1.14) can be ignored.

1.3.3 Equations of (Radial) Stellar Pulsation Theory

Among the several physical parameters present in the Stellar Structure equations, ϵ_g (often misinterpreted as "gravity term") stands out as essential to describe pulsation as a mechanical movement. Without this term, all the energy released by nuclear reaction would be either lost through neutrinos or affect the luminosity of the star, excluding a process of absorption and successive release of energy during a pulsation cycle (Eddington [Edd88]). Since ϵ_g represents the rate dQ/dt at which

energy is absorbed or released (per unit mass and time for a given layer) and using the First Law of Thermodynamics, we obtain:

$$\epsilon_g = \frac{dQ}{dt} = \frac{\partial E}{\partial t} + P \frac{\partial}{\partial t} \left(\frac{1}{\rho} \right) = \left(\frac{\partial E}{\partial T} \right)_\rho \frac{\partial T}{\partial t} + \left(\frac{\partial E}{\partial \rho} \right)_T \frac{\partial \rho}{\partial t} + P \frac{\partial}{\partial t} \left(\frac{1}{\rho} \right) \quad (1.20)$$

where we take advantage of being able to express E in terms of two of the variables ρ , P or T while the dependence on the mean molecular weight is neglected (this can be done thanks to the discussion on the timescales in the previous section). After some mathematical passages and remembering the definition of the specific heat at constant volume and the adiabatic exponents, we obtain :

$$\frac{\partial \ln T}{\partial t} = (\Gamma_3 - 1) \frac{\partial \ln \rho}{\partial t} + (c_V T)^{-1} \left(\epsilon - \epsilon_v - \frac{\partial L}{\partial m} \right). \quad (1.21)$$

At this point, our objective is to find a way to linearise our nonlinear system of partial differential equations. An effective method is to apply a very famous approximation used in several branches of physics, where we consider a time-dependent phenomenon (in our case, a pulsation) as a small perturbation around a time-independent equilibrium state. This way, for any physical quantity f we can then write:

$$f(m, t) = f_0 + \delta f(m, t), \quad (1.22)$$

where we use the subscript 0 to define the unperturbed solution and δ for the small variation around it. In the case of our distance from the centre $r = r(m, t)$ we thus obtain:

$$r(m, t) = r_0 \left(1 + \frac{\delta r(m, t)}{r_0} \right) = r_0 (1 + \xi) \quad (1.23)$$

The linearisation of our equations is then possible under the following conditions:

$$\xi \ll 1 \quad \text{and} \quad \frac{\delta f}{f} \approx \frac{\delta f}{f_0} \ll 1 \quad (1.24)$$

After some tedious mathematical passage, our basic equations transform into:

$$\frac{\delta \rho}{\rho_0} = -3\xi - 4\pi r_0^3 \rho_0 \frac{\partial \xi}{\partial m}, \quad (1.25)$$

$$r_0 \frac{\partial^2 \xi}{\partial t^2} = -4\pi r_0^2 \left(4\xi + \frac{\delta P}{P_0} \right) \frac{dP_0}{dm} - 4\pi r_0^2 P_0 \frac{\partial}{\partial m} \left(\frac{\delta P}{P_0} \right), \quad (1.26)$$

$$\frac{\partial}{\partial t} \left(\frac{\delta T}{T_0} \right) = (\Gamma_{3,0} - 1) \frac{\partial}{\partial t} \left(\frac{\delta \rho_0}{\rho_0} \right) + (c_{V,0} T)^{-1} \delta \left(\epsilon - \epsilon_v - \frac{\partial L}{\partial m} \right), \quad (1.27)$$

and (for the radiative plus conductive case):

$$\frac{\delta L}{L} = 4\xi + 4 \frac{\delta T}{T} - \frac{\delta \kappa}{\kappa} + \left(\frac{\partial \ln T}{\partial m} \right)^{-1} \delta \left(\frac{\partial \ln T}{\partial m} \right). \quad (1.28)$$

It is worth noting that the second of our new set of Stellar equations can be interpreted in the following way: since dP_0/dm is always negative, in the hypothesis of an expansion, the first term on the right side indicates that as a layer moves further away from the centre ($\xi > 0$) it will feel a drop in the gravitational potential, favouring further expansion. In response to this effect, the second and third terms, associated with the pressure drop, express the tendency to reverse the movement. At this point, further discussions confronting the pulsation timescale (P) with the thermal one (also known as Kelvin-Helmholtz timescale, t_{KH}) would allow us to treat these equations in the adiabatic case (with $P \ll t_{KH}$) and simplify the conservation of energy equation (1.27). After combining our equations, we would obtain the *Linear Adiabatic Wave Equation*, or LAWE, which resembles the *Sturm-Liouville* equation. Although this approximation would greatly simplify the equations, the research of solutions and the calculation of pulsation periods, it does not allow us to achieve any information about the mechanisms that make a star pulsate. Indeed, the adiabatic condition is global and does not involve individual layers undergoing pulsation, leaving us with the question of why and how a star may pulsate. Back on the mathematical side, it can be demonstrated (Catelan and Smith [CS15]) that it is not possible to reproduce phase lags between physical quantities (e.g. between pressure and density). For these reasons, a non-adiabatic treatment is necessary. A simple condition can be shown starting from Eq. 1.7 multiplying both sides by $\partial r / \partial t$ and integrating over the whole star, obtaining:

$$\begin{aligned} \int_M \frac{1}{2} \frac{\partial}{\partial t} (v^2) dm &= -\frac{d}{dt} \left(\int_M -\frac{Gm}{r} dm \right) - \int_M 4\pi r^2 \frac{\partial P}{\partial m} \frac{\partial r}{\partial t} dm = \\ &= -\frac{d\Omega}{dt} - \left(4\pi r^2 P \frac{\partial r}{\partial t} \right)_0^M + \int_M P \frac{\partial}{\partial m} \left(4\pi r^2 \frac{\partial r}{\partial t} \right) dm, \end{aligned} \quad (1.29)$$

with Ω being the gravitational potential. The second term on the right side can be neglected, since at the centre of the star $r = 0$ and at the surface the pressure is many orders of magnitude lower than it is in the stellar interior. Integrating over a complete pulsation cycle (with the first term on the right side becoming zero thanks to the conservative nature of Ω) we obtain the average total mechanical work that

is transformed into kinetic energy of the stellar layers. Taking into consideration that the partial derivative in the last integral can be written as $\frac{\partial}{\partial m}(1/\rho)$ (Eq. 1.1.), and averaging into a pulsation cycle, we obtain:

$$W = \int_{\mathcal{P}} dt \int_M P \frac{\partial}{\partial t} \frac{1}{\rho} dm \Rightarrow \left\langle \frac{dW}{dt} \right\rangle \equiv \frac{W}{\mathcal{P}} = \frac{1}{\mathcal{P}} \int_{\mathcal{P}} dt \int_M \frac{dQ}{dt} dm \quad (1.30)$$

If this quantity is positive, the star will pulsate. Similar to what can be done with LAWE, we combine our equations without the adiabatic condition, but now the solution will contain a phase factor, which induces phase lags between the physical quantities. Last but not least, W can be linked to the so-called stability coefficient (Cox [Cox67]). This coefficient contains two terms, associated with energy generation and energy transfer, respectively. When the conditions for pulsation are met, we can then distinguish different driver mechanisms, the most famous being the ϵ *mechanism* (induced by the thermonuclear reactions) and the κ and γ *mechanisms* (where the energy transfer term is predominant). The last part of this section will be dedicated to briefly discussing these 3 mechanisms and finally discovering which one can explain Classical Cepheids' pulsations, as well as the origin of the instability strip.

1.3.4 The ϵ , κ , γ mechanisms

The main idea behind the ϵ mechanism is that thermonuclear reactions have generally a strong dependence on the temperature. The temperature fluctuations in the regions where these reactions take place may induce a fluctuation in the supply of energy and support the pulsations. Early conclusions by Cowling [Cow34; Cow35] and confirmed some years later by Cox [Cox55], Ledoux et al. [LSB55] and Rabinowitz [Rab57] showed that for stars like RR Lyrae and Cepheids, the size of fluctuations in both the H-burning shell and He-burning core (shown in Fig. 1.4 for a RR Lyrae model) is many orders of magnitude smaller than would be required for an efficient ϵ mechanisms.

The other two mechanisms sometimes referred to collectively as the *heat mechanism* are instead connected to the different behaviours that some layers may have in response to compression (or expansion). In more detail, the κ mechanism refers to the ability of a layer to increase its opacity (whose symbol is used to name the mechanism) in response to compression (i.e. an increase in temperature) instead of decreasing. As shown in Fig. 1.5, at high temperatures "normal" layers tend to decrease their opacity due to the temperature rise, following the so-called Kramers-Eddington opacity law (Kramers [Kra23], Eddington [Edd88]). On the other side,

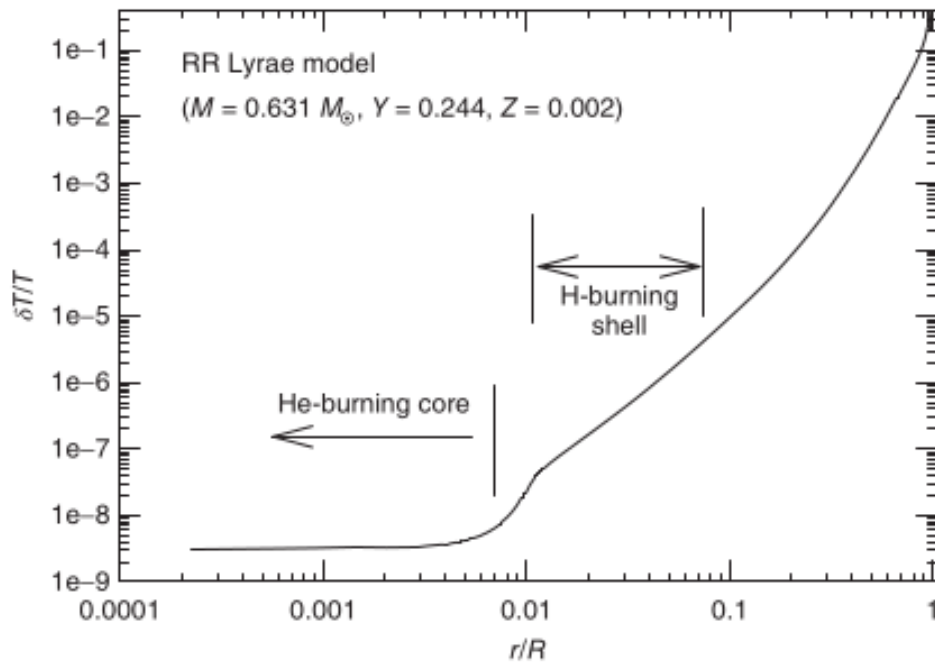


Figure 1.4: Relative temperature variation $\delta T/T$ plotted as a function of the stellar radius fraction r/R for an RR Lyrae model (Sweigart [Swe71; Swe87; Swe97]). Regions of the H-burning shell and the He-burning core are schematically indicated.

a few "bumps" are present in which this behaviour is reversed. At these temperatures, ionization of hydrogen and/or partial ionization of helium occur and the corresponding region of the star will "store" energy during compression, releasing it in a subsequent expansion. Similarly, the ability of these same layers to gain heat during compression is called the γ mechanism (a simple way to distinguish these two similar but different mechanisms is to remember that γ is a clear reference to the adiabatic index for an ideal gas, while κ refers to the symbol used for the opacity). These regions where ionization takes place will heat up less during compression (and cool less during expansion) respect with to their surroundings since the energy that would heat the layer is indeed stored in the form of ions. These two mechanisms suffice to explain the event of pulsation instabilities for those stars falling along the instability strip. Other mechanisms which become relevant in other types of stars (e.g. hot stars) and non-radial pulsation modes can be found in Catelan and Smith [CS15] and reference therein.

Before closing this section, we can qualitatively understand also what are the physical limits in the onset of pulsations for Classical Cepheids, that is what defines

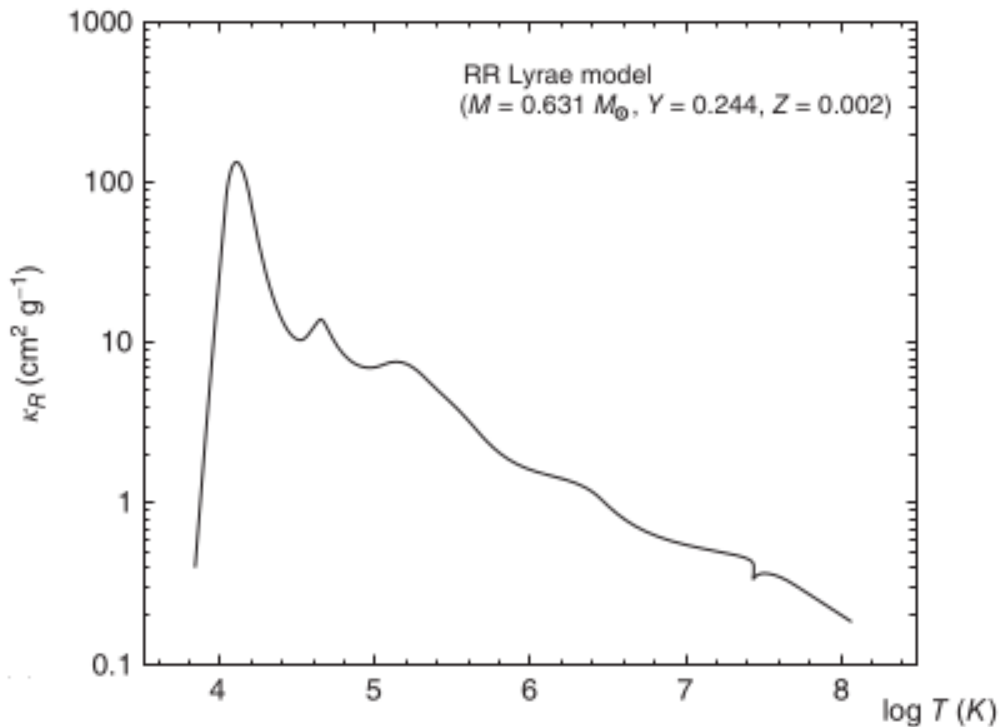


Figure 1.5: The temperature dependence of the Rosseland mean opacity for the same RR Lyrae model shown in Fig. 1.4.

the boundaries of this so many times mentioned instability strip. If the star is sufficiently hot, the ionization layers, fundamental in exciting pulsation in Classical Cepheids and other kinds of stars, will either be located too far out or not be present at all. That means that it is possible to define a blue edge. On the other hand, convection works in the opposite sense, storing energy in specific layers, quenching pulsation and leading to the definition of the red edge for the onset of pulsation instabilities. Further discussions of the non-verticality of these edges (evident in Fig. 1.3) are outside the main scope of this thesis, but it is important to highlight the fundamental role that the location of these ionization layers plays and the complicated interplay between pulsation and convection (see e.g. Bono et al. [BMS99a] and King and Cox [KC68]).

1.4 The Period-Luminosity relation and the role of the metallicity

Luckily for us, a rough derivation of the Period-Luminosity (PL) relation does not require particularly complicated equations or long and tedious mathematical steps. It is indeed quite easy/straightforward to understand why a relation between luminosity and period subsists for pulsating stars. We start with the Stefan-Boltzmann law:

$$L = 4\pi R^2 \sigma T_{eff}^4, \quad (1.31)$$

and we express it in terms of bolometric magnitude, obtaining:

$$M_{bol} = a \log R + b \log T + c. \quad (1.32)$$

Using Ritter's equation 1.19 and remembering that the mean density ρ is equal to $M/[(4\pi/3)R^3]$, we can then substitute R obtaining a relation that links absolute magnitude, mass, period and temperature. Since Cepheids obey a mass-luminosity relation, we can further substitute M , obtaining something similar to:

$$M_{bol} = a' \log \mathcal{P} + b \log T + c'. \quad (1.33)$$

One first argument that can be raised is that the instability strip has a finite non-infinitesimal width in temperature, which means that we should expect luminosity and period to also be connected through the temperature. If we express the latter in terms of a color index, we find out that what we have called so far PL relation is actually a Period-Luminosity-Color (PLC) relation, the former being a projection made by averaging over the temperature. From the observational point of view, we find another evident problem in the calibration of this relation: the interstellar extinction. Anything along the path between our object and the telescope can absorb part of the light emitted by the star and have repercussions on the observed magnitude. One way to minimise this effect would be by observing at longer wavelengths. An alternative is the use of a reddening-free Wesenheit magnitude introduced by Madore [Mad82]. To construct a Wesenheit magnitude we start by explicating the difference between observed and intrinsic magnitude (and colour). If we consider as an example the V and B optical filters we have:

$$V_{obs} = V_0 + A_v \quad \text{and} \quad (B - V)_{obs} = (B - V)_0 + E(B - V), \quad (1.34)$$

where the subscripts *obs* and *0* indicate the observed and intrinsic magnitude (colour), while A_v and $E(B_V)$ are the reddening and the colour excess, respectively.

We then define the total-to-selective absorption as:

$$R_V = A_V/E(B - V) \quad (1.35)$$

At this point it is easy to demonstrate that:

$$W_{obs} = V_{obs} - R_V(B - V)_{obs} = V_0 - R_V(B - V)_0 = W_0. \quad (1.36)$$

This quantity W , a magnitude subtracted by a colour index scaled by the term R , is independent of the reddening. Once a reddening law is assumed, the Wesenheit magnitude can be used in substitution of the normal magnitude in order to calibrate a Period-Wesenheit (PW) relation. At this point, we must ask ourselves whether this relation is universal, that is, if cepheids in different galaxies and different metallicities obey the same relation. It is important to raise this issue because, as already briefly mentioned, we can obtain distances of galaxies thanks to classical Cepheids. If these galaxies host a particular type of Supernova called SN Type Ia, we can push our distance calibration even further. Eventually, we reach unperturbed galaxies in the Hubble flow, whose velocity is dictated by the expansion of the Universe. This way, we can build the so-called cosmic distance ladder (Freedman et al. [Fre+01]; Riess et al. [Rie+22a]), which leads us to the estimation of the Hubble constant H_0 (connected with the expansion of the Universe) of the late evolutionary universe. This method is independent of the theoretical estimation by the Planck Cosmic Microwave Background project (Planck Collaboration et al. [Pla+20]) which, adopting the flat Λ Cold Dark Matter model, leads to an estimation of the expansion in the early universe. The problems arise because these two values are currently discrepant for more than 4σ . Suppose this tension indeed exists between the Hubble constant measurements from the two extreme ends of the Universe. In that case, it may be a hint at new or missing physics in the standard cosmological model (see e.g. Di Valentino et al. [Di+21], Abdalla et al. [Abd+22]). On the other side, it becomes of vital importance to calibrate with great accuracy and precision the Cepheid-based distance measurements in the traditional cosmic distance ladder, which nowadays are now only limited by the systematic uncertainties in the calibration of their PL relation and its metallicity dependence. Before the advent of the Gaia astrometric satellite (Gaia Collaboration et al. [Gai+16]), the absolute calibration of Cepheid PL relations was mostly based on a limited sample of Cepheids with Hubble Space Telescope parallaxes (Benedict et al. [Ben+07], Riess et al. [Rie+14]) or using distances determined from independent methods, such as the Baade-Wesselink or infrared surface brightness methods (the theoretical background some application can be found in Baade [Baa26], Wesselink [Wes46], Storm et

al. [Sto+11], Gieren et al. [Gie+12]). This is now changing thanks to increasingly more accurate and precise geometric parallaxes of thousands of Cepheids in the Milky Way from the Gaia mission (Gaia Collaboration et al. [Gai+16], Ripepi et al. [Rip+23]). The increasing precision of Gaia parallaxes also enabled some of the above-mentioned studies to investigate the metallicity dependence of Cepheid PL relations at multiple wavelengths. We will see in Chapter 3 an application of Gaia parallaxes in combination with high-resolution spectroscopic metallicities to calibrate both the Period-Luminosity-Metallicity (PLZ) and Period-Wesenheit-Metallicity (PWZ) relations.

1.5 Determination of chemical abundances through spectroscopic techniques

This section is dedicated to introducing the basics of spectroscopy, atmosphere modelling and determination of atmosphere parameters. These techniques are extensively used in Chapter 2 and 4 for the High-Resolution spectral analysis of Classical Cepheids. The main objective is the determination of the metallicity (that is, $[Fe/H]$) which is necessary to calibrate Period-Luminosity-Metallicity and Period-Wesenheit-Metallicity relations, but we can exploit the high resolution, good signal-to-noise and wavelength coverage of the data to estimate other chemical species and for example study the chemical distribution in the MW disc. Our first step into spectroscopy requires us to understand what kind of information a spectrum carries and what we can achieve from it. Indeed, the light we observe from the star comes from a region of the atmosphere called the photosphere. All the light generated in more internal regions does not penetrate to the surface because of absorption and scattering processes. This means that when the radius and the temperature of a star are mentioned, for example, it is the size of the apparent stellar disc defined by the photosphere and its characteristic temperature to which it is referred, respectively. Outer layers, the chromosphere and the corona, emit most of their light in the ultraviolet (UV) and x-ray regions. The starlight that reaches our instruments originates from a very small region of our object: in the case of the Sun, the photosphere is 700 km thick, while its radius is 696 100 km. Depending on several factors (such as temperature, surface gravity and chemical composition), the thickness of the photosphere varies from star to star, and for a single object how deep we observe depends on whether the light comes from the centre or the edges of the stellar disc (the so-called limb-darkening). But this does not mean that the level of information we can achieve from a star is small (although of course limited). Since physical quantities like the already mentioned temperature,

surface gravity and composition affect the spectra, it is possible to estimate them by studying their effect on the total flux. Spectral lines bear the signatures of the velocity fields pervading stellar atmospheres. Their presence, intensity and shape allow us to differentiate between different stars and classify them into several classes and subclasses. Convective movements and nuclear processes leave their mark on the chemical composition. Once we collect all the information we can gather, we can build models of the atmosphere and create synthetic spectra. A confrontation between synthetic and observed spectra gives us hints of the physics that is missing and how acceptable are our approximations. In the following, we will take a journey into the basics of atmosphere modelling, building a base into which it will be possible to extract the procedures that make it possible to estimate the main atmospheric parameters: effective temperature, surface gravity, metallicity, radial velocity and velocity fields information (generally divided into micro- and macro-velocity). More details can be found in Gray [Gra21] and references therein.

1.5.1 The radial transfer equation

The starting point can not be anything but the definition of the specific intensity. If we consider the infinitesimal energy dE_ν that passes through the surface dA in a spectral interval $d\nu$ and time dt and reaches the observer under the solid angle $d\omega$ in the direction θ respect with to the normal to the surface dA (Fig. 1.6 for a representation at macroscopic scales), the specific intensity I_ν is defined as:

$$I_\nu = \frac{dE_\nu}{dt dA d\omega d\nu \cos \theta}. \quad (1.37)$$

It is possible to replace the frequency interval with a wavelength one, since $I_\nu d\nu = I_\lambda d\lambda$. The flux, what we actually observe, is the total net energy from our source. In formulae:

$$\mathcal{F}_\nu = \oint I_\nu \cos \theta d\omega \quad (1.38)$$

Next, we introduce the quantities that either reduce or increase the intensity. Consider radiation passing through a layer of a material with density ρ . Because of photon absorption (transformed into thermal energy) and/or scattering (photons deviated and removed from the solid angle), we find that the intensity, after passing through a length dx , is diminished by an amount:

$$dI_\nu = -\kappa_\nu \rho I_\nu dx, \quad (1.39)$$

where κ_ν is the absorption coefficient (the opacity we saw in Eq. 1.10) and depends

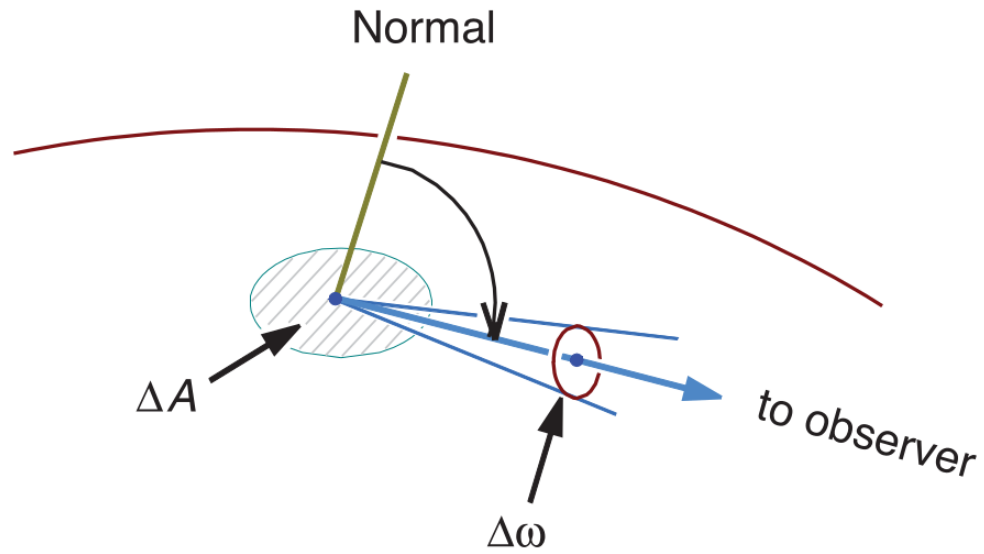


Figure 1.6: Geometrical representation of the specific intensity from Gray [Gra21].

on the state of the material and frequency. If we had pure absorption, the integration over a path length L we would obtain a typical exponential law where the quantity $\tau_\nu = \int_0^L \kappa_\nu \rho dx$ (called optical depth) establishes the reduction rate of the intensity. Following the same treatment, an increment of radiation (because of emission and/or scattering) can happen:

$$dI_\nu = j_\nu \rho dx, \quad (1.40)$$

with j_ν called emission coefficient. The ratio j_ν/κ_ν gives the source function S_ν . Two easy examples of source functions are Planck's radiation law of a blackbody when we are in thermodynamic equilibrium, and the mean intensity $1/4\pi \oint I_\nu d\omega$, for pure isotropic scattering. In the general case where we have both absorption and emission, we obtain the equation of radiative transfer:

$$\frac{dI_\nu}{d\tau_\nu} = -I_\nu + S_\nu, \quad (1.41)$$

whose general solution is:

$$I_\nu(\tau_\nu) = \int_0^{\tau_\nu} S_\nu(t_\nu) e^{-(\tau_\nu - t_\nu)} dt_\nu + I_\nu(0) e^{-\tau_\nu}. \quad (1.42)$$

This can be interpreted as follows: at a point τ_ν , the initial intensity $I_\nu(0)$ is reduced by the exponential extinction $e^{-\tau_\nu}$; on the other side, the source function contributes at each point t_ν between 0 and τ_ν , each contribution reduced by the absorption process by a term $e^{-(\tau_\nu - t_\nu)}$. Now, if we consider a star and approximate it as a spherical object (which is fairly true for slow rotators) we can write Eq. 1.41 in spherical coordinates (with the z-axis chosen toward the observer). If we assume that the intensity has no azimuthal dependence and the plane-parallel approximation is valid (that is, no dependence of θ on z, which is true since the photosphere is very small compared to the stellar radius) we obtain:

$$\cos \theta \frac{dI_\nu}{d\tau_\nu} = I_\nu - S_\nu \quad \text{where} \quad d\tau_\nu = -\kappa_\nu \rho dr \quad (1.43)$$

The sign inversion in both the equation and the new definition of the optical depth is easy to justify when we consider that the observer is looking from the outside toward the inner regions of the stars, in the opposite direction of dx in Eq. 1.41. Moreover, because now we are considering a spherical object, the optical depth is not always oriented along the radius, with the latter forming an angle θ with the line of sight of the observer. This corresponds to a length path ds equals dx scaled by a factor $1/\cos \theta = \sec \theta$ (see Fig. 1.7).

In this new formulation, we can differentiate the case of radiation going inward (coming from more external layers, and $\theta > 90^\circ$) from the radiation going outward (generated in the inner layers, $\theta < 90^\circ$). For this reason, we replace the initial intensity $I_\nu(0)$ with a general integration limit c and the solution of Eq. 1.43 becomes:

$$I_\nu(\tau_\nu) = - \int_c^{\tau_\nu} S_\nu(t_\nu) e^{-(t_\nu - \tau_\nu) \sec \theta} \sec \theta dt_\nu. \quad (1.44)$$

When we start from the outer boundary, $c = 0$ and we integrate the radiation generated from the surface till the "depth" τ_ν , going inward. On the other side, the radiation working outward comes from the inner regions of the star (until we reach the point that no more radiation can be seen coming out) which corresponds to the integration limit $c = \infty$. At the stellar surface ($\tau_\nu = 0$) there is no radiation going inward and:

$$I_\nu(0) = \int_0^\infty S_\nu(t_\nu) e^{-t_\nu \sec \theta} \sec \theta dt_\nu. \quad (1.45)$$

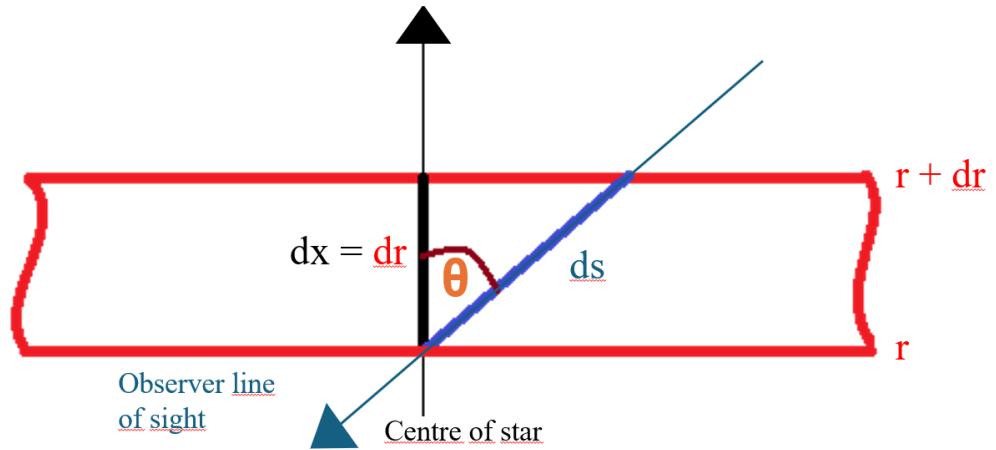


Figure 1.7: Geometrical representation of the plane parallel approximation. The dx term in Eq. 1.41 is now dr , while ds (in the opposite verse and inclined of an angle θ) is oriented as the observer's line of sight.

With some mathematical steps, we obtain a similar equation for the flux at the surface, i.e. the stellar spectrum:

$$\mathcal{F}_v(0) = 2\pi \int_0^\infty S_v(t_v) E_2(t_v) dt_v \quad \text{where} \quad E_n(x) = \int_1^\infty \frac{e^{-xw}}{w^n} dw. \quad (1.46)$$

One way to deal from a theoretical framework with this integral is to specify the quantities inside it as functions of optical depth at a reference wavelength (usually 5000 \AA and denoted with the symbol τ_0), use the definition of optical depth to "rescale" for the other wavelengths ($\rho dx = d\tau_v/d\kappa_v = d\tau_0/d\kappa_0$) and shift to a logarithmic scale (which also helps in the numerical computation), obtaining:

$$\mathcal{F}_v(0) = 2\pi \int_0^\infty S_v(\tau_0) E_2(\tau_v(\tau_0)) \frac{\kappa_v(\tau_0) \tau_0}{\kappa_0(\tau_0) \log e} d \log \tau_0. \quad (1.47)$$

1.5.2 How to compute a photosphere model

In the following, we are going to summarise the basic assumptions useful to the computation of the photosphere's model:

- The plane-parallel geometry was already mentioned and used in the previous calculations.

- Hydrostatic equilibrium, that is, there are no significant accelerations comparable to the surface gravity and no sensible mass loss.
- Granulation, starspots and magnetic fields are secondary and can be neglected.
- Local thermodynamic equilibrium (LTE): excitation and ionization follow the Boltzmann and Saha (Saha [Sah21]) distributions, respectively, and the source function corresponds to Planck's law.

While the hydrostatic equation links the pressure with gravity and particle densities, the LTE shows the importance of the temperature, directly connected to the source function. To these points, we can further assume the radiative equilibrium and the charge conservation. While the latter simply expresses the global neutrality of the medium, the former is an expression of the conservation of energy under the condition that there are no sources or sinks of energy within the photosphere (see Milne [Mil30] and Gray [Gra21] for a derivation of the so-called Milne equations that explicit the conservation of the total integrated flux at each layer of the photosphere).

If we shift our attention to the absorption coefficient, Eq. 1.10 already highlighted that it depends on both temperature, (electron) pressure and chemical composition. For its determination, we can separate the contributions that directly affect and shape the continuum from those that create spectral lines:

- For the continuum, we can categorise all the processes into two main groups: ionization events (bound-free transitions) and excitation events (free-free transitions). In some of these, we can include the stimulated emission, which can be considered as a negative absorption. As can be seen in Fig. 1.8 for cool stars the main contribution comes from the hydrogen negative ion, at higher temperatures neutral hydrogen starts to be the dominant process.
- Regarding the spectral lines, the main processes are natural atomic absorption, pressure broadening (collisional interaction between the atoms that are absorbing the light and other particles) and thermal Doppler broadening. Each process results in a particular shape of the spectral line, and the effect of all of them is the convolution of the singular shapes. Luckily, the natural absorption and most of the pressure-broadening events assume the shape of a dispersion profile (one exception is for example Hydrogen, which needs a different treatment (see e.g. Holtmark and Trumphy [HT25] and Struve [Str29])). Thermal motions, on the other side, reflect the Maxwellian

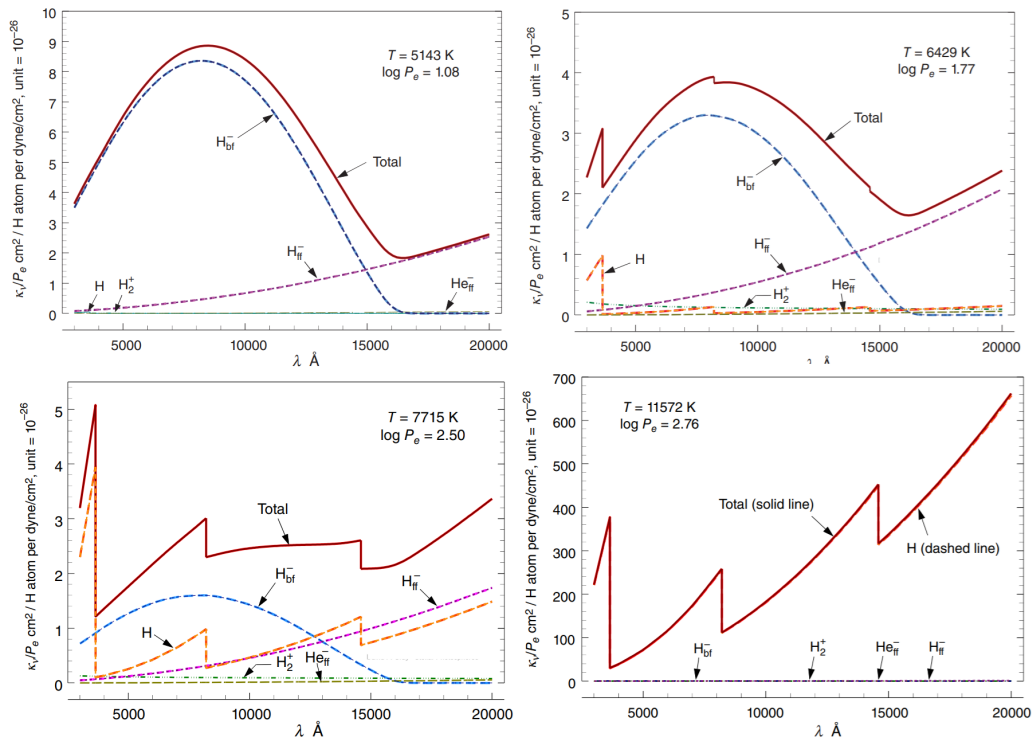


Figure 1.8: Hydrogen contribution to the continuum absorption coefficients (per unit electron pressure) shown for four different models. Temperature and pressure values are shown in each panel.

velocity distribution and the resulting wavelength shape is a Gaussian. Since the convolution of dispersion profiles is still a dispersion profile and the convolution of Gaussian profiles is still a Gaussian, the total line shape is a convolution of a dispersion profile with a Gaussian. The spectral line will have a core similar in shape to a Gaussian, with wings that reflect the shape of a dispersion profile. Additionally, we have to take into account those effects, initially considered secondary in our previous assumptions, such as stellar rotation and velocity fields that can form in the photosphere (called initially turbulence by Rosseland [Ros28]). These can be divided into two groups: when the size of the turbulent element is large compared to the unit optical depth we can talk of macroturbulent velocities, in the opposite case we name them as microturbulent. These two components will be discussed more in Sect. 1.5.7

Now all the information to compute our model has been finally gathered. By

the term "model atmosphere" we indicate a specification of all the atmospheric state parameters. The effective temperature sets the scale of the temperature as a function of the optical depth ($T(\tau_0)$). Likewise, surface gravity sets the scale for the pressure generated by the gas ($P_g(\tau_0)$) and by the electrons ($P_e(\tau_0)$). The metallicity is the collective abundance of those elements, other than hydrogen and helium, that can be ionized and contribute electrons to the photospheric plasma. Since realistic analytical solutions are impossible to construct, the depth coordinate is discretised and a finite number of depth points are considered (typically of the order of several tens to a few hundreds). A model atmosphere is then a table of values of the state parameters in these discrete depth points. The computational process starts by assuming $T(\tau_0)$. This can be done by studying the Sun thanks to the already mentioned limb darkening effect. Its explanation can be found in Eq. 1.45, where we see the dependence of the surface intensity on the angle θ , that is, which region of the star we are observing. We can help ourselves by looking again at Fig. 1.7. When we move from the centre to the edges of the stellar disc (increasing θ), the optical depth along the line of sight (represented by the element ds) corresponds to smaller optical depths along the radius of the star (represented by the element dr), hence we are collecting light from higher (and colder) photospheric layers. The key role at this point is played by the Eddington-Barbier relation (whose origin is discussed in Paletou [Pal18]) since we can correlate the specific intensity at the position θ with the source functions at the depth τ_0 . An example is the (unrealistic but useful) case of the so-called "grey atmosphere", where the absorption coefficient is independent of the frequency. In this case, we found out that $S_\nu = a + b\tau$ and $I_\nu(0) = a + b \cos \theta$. When $\cos \theta = \tau$, we obtain the Eddington-Barbier relation. We can set up a purely numerical grid of the source function (as a function of the optical depth) to match the observed intensity (as a function of the angle) until the model matches the observations. Under the LTE assumption, that means the temperature has been successfully modelled. Since the temperature distribution for the Sun and those of other stars have nearly the same shape, we can just rescale our grid and we are finished. The next step is the pressure. From the hydrostatic equilibrium, $dP = \rho g dx$, or, since the gas accounts for the bulk of the total pressure in cool stars, $dP_g = g/\kappa_0 d\tau_0$. To compute the gas pressure we need to compute first κ_0 , which in turn depends on the temperature and electron pressure. For the latter, we start from Saha's equation:

$$\frac{N_{1j}}{N_{0j}} = \frac{\Phi_j(T)}{P_e}, \quad (1.48)$$

where N_{ij} is the number per unit volume of the element j in the ionization state

i (0 for a neutral element, 1 for ions and so on), and Φ is a function that groups all the constants and temperature factors. With good approximation, we can neglect double ionizations so that the number of free electrons per unit volume N_{ej} contributed by the element j is equal to N_{1j} . If we denote by N_j the total number of the element j ($= N_{1j} + N_{0j}$), we can write then the following equations:

$$N_{ej} = N_j \frac{\Phi_j(T)/P_e}{\Phi_j(T)/P_e + 1} \quad P_e = \sum_j N_{ej} kT \quad \text{and} \quad P_g = \sum_j (N_{ej} + N_j) kT. \quad (1.49)$$

If we normalise all the N_j by the number of hydrogen particles N_H we obtain the relative abundances A_j and we can finally write the equation to obtain the electron pressure:

$$P_e = \left\{ P_g \frac{\sum_j A_j \frac{\Phi_j(T)}{\Phi_j(T)/P_e + 1}}{\sum_j A_j \left[1 + \frac{\Phi_j(T)/P_e}{\Phi_j(T)/P_e + 1} \right]} \right\}^{1/2}, \quad (1.50)$$

that can be resolved by iteration if we have P_g . We have to take a first guess at $P_g(\tau_0)$ and compute iteratively $P_e(\tau_0)$, which leads to the determination of $\kappa_0(\tau_0)$. Iterating again, we solve for the gas pressure. Our models are ready.

1.5.3 Sneak peek about the role of convection

As the title of Sect. 1.5.1 suggests, we only treated the radiative transport, neglecting the tricky and thorny aspect of the convection. In cool stars (Classical Cepheids included), the convective envelopes extend up to the bottom of the photosphere. For these stars, convection carries just enough energy to slightly lower the temperature gradient in the deepest photospheric layers. At the same time, there are several other aspects where convection plays a relevant role: it shapes line profiles through the Doppler shifts, generates sound waves (P-mode oscillations) that are internally reflected at the internal boundaries of the convective zone and possibly resonate, wiggles the magnetic field lines, directly induces mixing mechanisms and so on. In summary, convection has a profound influence on stars even though it is a trivial player in the conveyance of energy through the photosphere.

1.5.4 Equivalent widths

In the present and following sections, we present some of the possible techniques to estimate the atmospheric parameters. Once we obtain them, we can feed our models and compute synthetic spectra, useful for example in the determination of chemical

abundances. We have already mentioned that in Eq. 1.47 we can distinguish an absorption coefficient that contributes to the formation of the continuum (we will continue to use the symbol κ_v) from the one that shapes the spectral lines (we will denote it with the symbol ℓ_v). In this context, one can expect that the number of absorbers is of primary interest and can be led to think that the strength of a spectral line depends on how much the photosphere is populated by the element producing that line. But the number of absorbers also accumulates along the path length through the photosphere. If the continuous absorption is strong, the path length will be short and vice versa. In effect, the depth of the photosphere changes with the amount of continuous absorption. Because of this, it is the ratio of the line absorption to the continuous absorption, ℓ_v/κ_v , that determines line strength. A useful way to express the strength of a line is a quantity called equivalent width:

$$W = \int \frac{\mathcal{F}_c - \mathcal{F}_v}{\mathcal{F}_c} d\lambda, \quad (1.51)$$

where \mathcal{F}_c and \mathcal{F}_v denote the flux of the continuum and the line, respectively and the integral covers the spectral line over the range where the profile can be distinguished from the continuum. The dependence of the strength of a line on the abundance is called the curve of growth. In the presence of weak lines (with a Gaussian core dominating over the dispersion-shaped wings), without saturation causing distortion, we can associate the strength of a line with the ratio of the line to continuous absorption, so that $W \propto \ell_v/\kappa_v \propto A_j$. In good approximation, W grows linearly with the abundance. Increasing this quantity, the core of the line gets saturated and the only way to increase the equivalent width is by growing wider, through the wings of the line and the linearity of the curve of growth is broken. We will see soon how weak lines can be crucial in the estimation of atmospheric parameters.

1.5.5 The Effective Temperature, T_{eff}

The temperature is the variable that most controls the line strength. The reason behind this is the deep dependence on the temperature of both processes of excitation and ionization. What is different is how each element and/or spectral line behaves by changing the temperature. If two spectral lines behave differently in response to different values of this parameter, it is possible to build a temperature scale, a thermometer. The more couples are available, the better the estimation. An example of suitable pairs is shown in Fig. 1.9 Since in cool stars blending and overlap of weak lines becomes common, it can be difficult to estimate equivalent

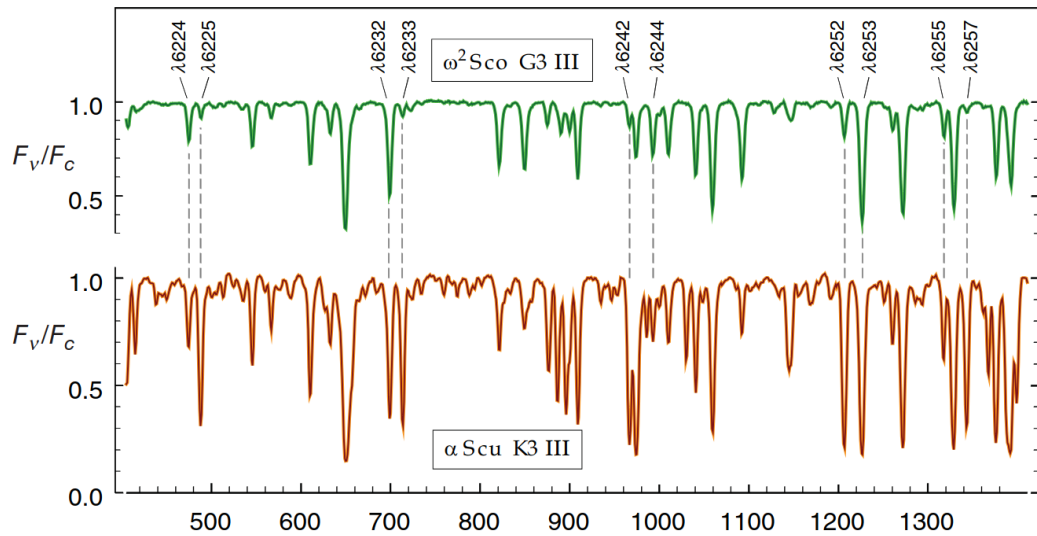


Figure 1.9: Pairs of suitable lines for the line-depth-ratio method are shown for two different stars. The change of strength and the line overlap discussed in the text results are evident, especially for the cooler star at the bottom.

widths, substituted by the core depths of spectral lines and the method takes the name of line-depth-ratio (Kovtyukh and Gorlova [KG00]). Since broadening effects (discussed in Sect. 1.5.7) are essentially the same for lines with similar wavelength and strength, their influence cancels out.

When it is not possible to find enough pairs, another method involves excitation potentials. The main idea is that abundances from the same element must agree for all excitation potentials. In a similar way as explained later in Sect. 1.5.7 for the microturbulence velocity, you can impose that there is no residual correlation between the iron abundance and the excitation potential of the neutral iron lines. This method requires the computation of photosphere models, so initial values of gravity and microturbulence are needed. As explained in the next section, Fe I lines are independent on $\log g$ so any reasonable value can be inserted in our model, while it is needed to iterate this method and the one used to compute the microturbulence till convergence is reached for both parameters.

1.5.6 The surface gravity, $\log g$

A useful and effective method for estimating the surface gravity is to use weak lines (i.e. shape not saturated and fairly approximated with Gaussian profiles), for which we can distinguish three cases:

1. An element is mostly in a certain ionization stage and a weak line is formed by that element in the previous ionization stage;
2. An element is mostly in a certain ionization stage and a weak line is formed by that element in the same ionization stage;
3. An element is mostly in a certain ionization stage and a weak line is formed by that element in the next ionization stage;

In the first case $N_{(i+1)j} \sim N_j = \text{constant}$. From Eq. 1.48 $\ell_\nu \propto N_{ij} \propto P_e$. In cool stars, we have seen that the main contribution to the continuum comes from the negative hydrogen ion, which implies $\kappa_\nu \propto P_e$. This means that the equivalent widths for these lines are independent of P_e , or, these lines are insensitive to gravity. With similar arguments, we find that lines that fall in either the second or third case are sensitive to gravity. For cool stars like Classical Cepheids, most of the iron is ionised, which means that Fe I lines are insensitive to $\log g$, while Fe II can be used as a discriminant to estimate it. Indeed, through the curve of growth, we can associate the equivalent width of a line with the abundance of that element. The value of surface gravity requested is the one for which Fe I and Fe II abundances match.

1.5.7 Rotation and turbulence

Similarly to what happened with convection, which role for the transportation of energy through the photosphere can be safely neglected but is relevant for other aspects of the structure of the star, rotation and velocity fields were ignored during the building process of the photosphere model but their effect on the spectral lines is sensible. The rotation profile caused by the Doppler shifts can be easily modelled (see Gray [Gra21]), including both the effects of limb darkening and the inclination of the rotational axis. This function must be convoluted with the intensity I_ν and then follow a similar procedure done in the previous sections to obtain the theoretical spectrum. Our main interest here is to study its effect on the spectral lines. As can be seen in Fig. 1.10, spectral lines widen up while getting shallower with increasing the rotational velocity (projected along the line of sight, called

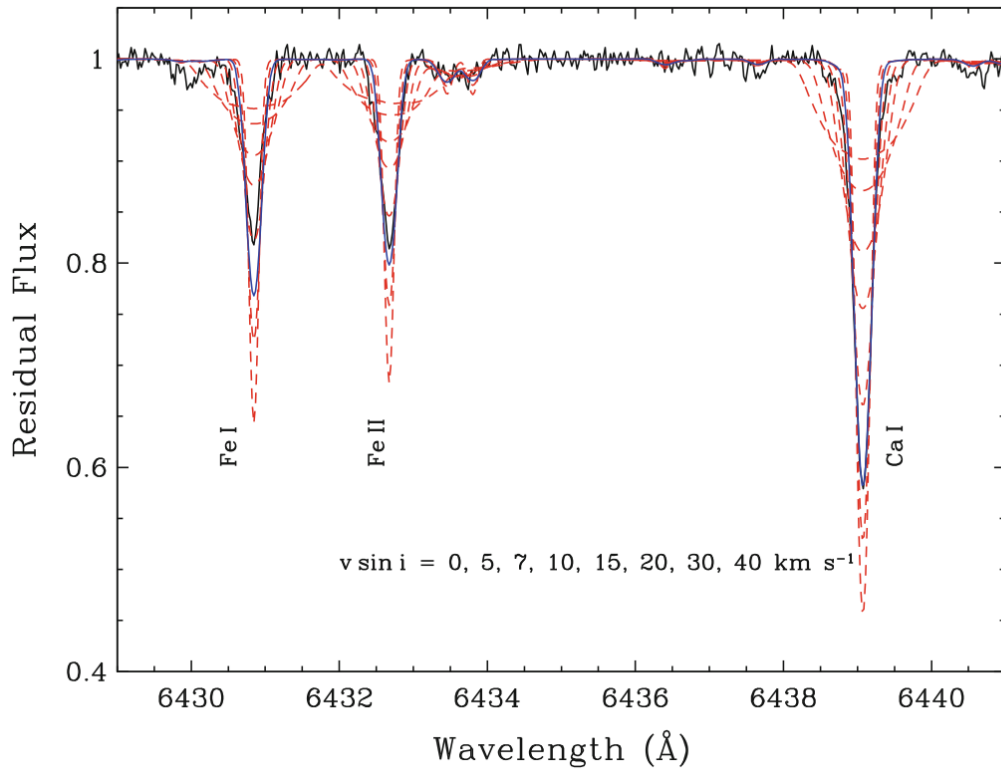


Figure 1.10: Theoretical spectra for different rotational velocities are shown in red and compared with the observed spectrum in black. The best fit achieved in this case is 7 km s^{-1} .

$v \sin i$). It is important to highlight that the total strength of the line, or analogously the equivalent width, remains invariant: rotation only affects the shape of the line.

The next quantity we investigate is the effect of macroturbulence velocity (whose effect is evident in the form of granulation on the solar surface). When these "turbulent cells" are large enough for photons to remain trapped until they escape from the star, lines subdue a Doppler shift. Although Gaussian profile models were sufficient to cover this quantity in the past decades, a more accurate theoretical treatment is needed. Cells of gas indeed rise and fall, but they also have horizontal motion. In the "radial-tangential" model introduced by Gray [Gra75], we divide the stellar surface area into regions with either radial or tangential motions. Although the velocity distributions are Gaussian, the net profile takes the form of a cuspid with a sharp peak and wide wings. As happened for the rotational velocity, macroturbulence profiles must be convoluted with the intensity profile before, and

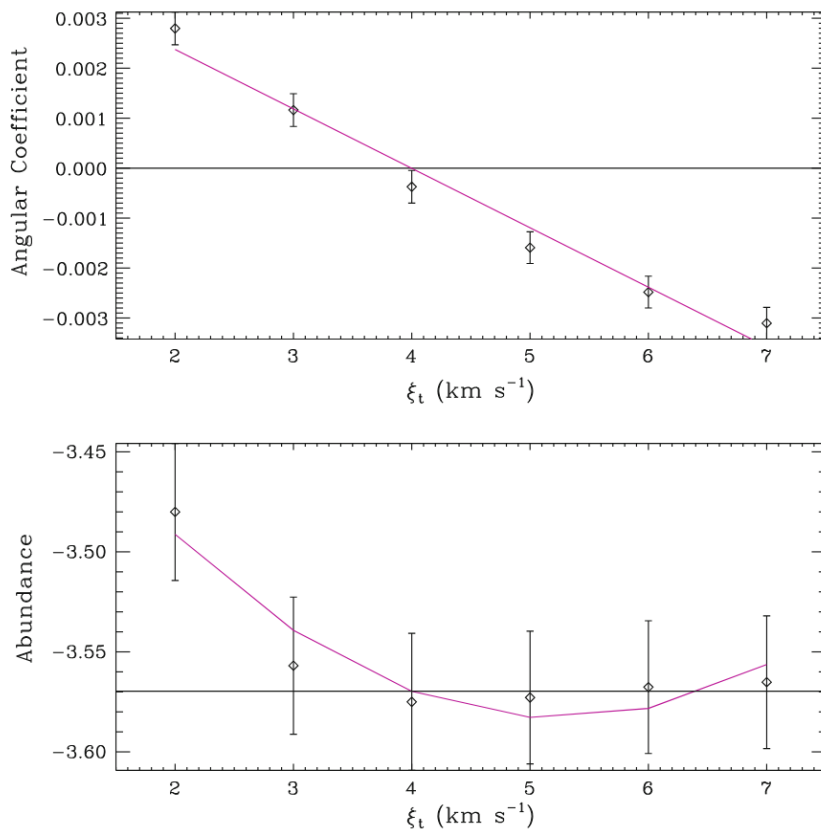


Figure 1.11: In the upper panel, the dependence of the angular coefficient on ξ . The required value is 4 km s^{-1} , for which the angular coefficient is zero. In the bottom panel, the intercept dependence on ξ gives an estimation of the abundance.

then integrated to obtain the stellar flux. The curious yet important effect on the spectral line is equivalent to that of star rotation, that is, it is possible to compensate in our analysis for a decrease in one quantity increasing the other. For this reason, both effects are usually referred to as "broadening velocity".

Last but not least is the microturbulence velocity (denoted with ξ). Since in this case, the size of the cells is small compared with the mean free path of the photon, the line-of-sight penetrates through many cells of motion, which velocity distribution behaves like the particle velocity distribution. Since typical values for ξ are small enough compared to other components of line broadening (see Landstreet et al. [Lan+09]), it has become standard practice to assume a Gaussian profile for the microturbulence, similar to what is done for thermal broadening. On the practical side, its effect in shaping line profiles is difficult to detect. One way to estimate

this velocity comes from the idea that broadening due to microturbulence should not affect the abundance of an element, which can be estimated independently of the spectral line used. Given a set of spectral lines for a specific chemical species, we can plot the calculated equivalent widths and the estimated abundances thanks to the curve of growth. The required microturbulence is that value for which the angular coefficient is nil. At the same time, we can estimate the abundance of the element through the intercept of the fit "abundances vs equivalent widths", as shown in Fig. 1.11. For Classical Cepheids, we can use the gravity-independent Fe I lines (once we know the temperature) to create atmospheric models varying only ξ to estimate the iron abundance. Then, as explained in the previous section, we can use Fe II lines to estimate the gravity.

We are now ready to see some of the various possible studies that can be done using these stars.

2

Cepheid Metallicity in the Leavitt Law (C- MetaLL) survey: II. High-resolution spectroscopy of the most metal-poor Galactic Cepheids

E. Trentin, V. Ripepi, G. Catanzaro, J. Storm, M. Marconi, G. De Somma, V. Testa, I. Musella

This paper was published in MNRAS, Volume 519, Issue 2 pp. 2331-2348¹

2.1 Introduction

Classical Cepheids (DCEPs) are fundamental astrophysical objects. Since their discovery, the period-luminosity (PL) and period-Wesenheit² (PW) relations that hold for these pulsators, represent the base for the cosmic distance scale (e.g. Caputo et al. [Cap+00], Leavitt and Pickering [LP12], Madore [Mad82], and Riess et al. [Rie+16]). Once calibrated by means of geometric methods such as trigonometric parallaxes, eclipsing binaries and water masers, these relations can be used to calibrate secondary distance indicators like Type Ia Supernovae (SNe), which are sufficiently powerful to reach the unperturbed Hubble flow, allowing us to measure the Hubble constant (H_0 , see eg. Freedman et al. [Fre+12], Riess et al. [Rie+16; Rie+19; Rie+21a], and Sandage and Tammann [ST06] and references therein).

In recent years this topic has been at the centre of a heated debate as the values of H_0 based on the cosmic distance scale (e.g. Riess et al. [Rie+21b] and Verde et al. [VTR19] and references therein) are in significant disagreement with those estimated from the Planck Cosmic Microwave Background (CMB) measurements under the flat Λ Cold Dark Matter (Λ CDM) model. The latest estimate of H_0 from the cosmic distance scale is $H_0=73.04\pm 1.04$ km s⁻¹ Mpc⁻¹ Riess et al. [Rie+21a], which is 5σ different from the value estimated by Planck+ Λ CMB, namely $H_0=67.4\pm 0.5$ km s⁻¹ Mpc⁻¹ Planck Collaboration et al. [Pla+20]. This discrepancy, known as the H_0 tension, has still unknown origins, in spite of many observational and theoretical efforts to study the possible causes as well as residual systematics (see e.g. Dainotti et al. [Dai+21], Freedman [Fre21], and Riess et al. [Rie+21b] and reference therein).

In this context, it is crucial to identify any residual systematic effect which could in principle affect the cosmic distance scale path to the measure of H_0 . One of the

¹ Based on observations European Southern Observatory programs P105.20MX.001/P106.2129.001

² The Wesenheit magnitudes are quantities that are reddening free by construction, once the reddening law is known (see Madore [Mad82])

most controversial candidates is the metallicity dependence of the DCEP PL and PW relations. Several recent results based on *Gaia* mission Data Release 2 (DR2 Gaia Collaboration et al. [Gai+16; Gai+18]) and Early Data Release 3 (EDR3 Gaia Collaboration et al. [Gai+21]) parallaxes are indeed in disagreement one each other (see e.g. Breuval et al. [Bre+21], Groenewegen [Gro18], Riess et al. [Rie+21a], and Ripepi et al. [Rip+19; Rip+20; Rip+21a; Rip+22]). To overcome these difficulties and to establish accurately the metallicity dependence of the DCEPs PL and PW relations and its impact on the measure of H_0 , we undertook a project dubbed C-MetaLL (Cepheid - Metallicity in the Leavitt Law) which is fully described in Ripepi et al. [Rip+21a]. One of the immediate objectives of the project is to measure the chemical abundance of a sample of 250-300 Galactic DCEPs through high-resolution spectroscopy, specifically aiming at enlarging as much as possible the metallicity range of the targets towards the metal-poor regime ($[Fe/H] < -0.4$ dex), where only a few objects are present in the literature.

Here we present the spectroscopic observations of a considerable sample (i.e. 65 objects) of recently discovered faint DCEPs whose Galactocentric distance, $R_{GC} > 15$ kpc, makes them excellent metal-poor candidates (see Section 2.2.1 for details).

The DCEP sample discussed in this work has not only relevance for the cosmic distance scale, but also for Galactic studies. Indeed, the accurate distances which can be measured for DCEPs allow one to carry out the chemical tagging of the disc and in particular to study how the abundance of the different chemical elements varies with R_{GC} , from the central regions of the MW towards the outer regions of the disc. Many studies exist already in the literature facing this problem with a variety of tracers other than DCEPs, such as OCs (e.g. Casamiquela et al. [Cas+19], Cunha et al. [Cun+16], Donor et al. [Don+20], Netopil et al. [Net+16], and Spina et al. [Spi+21] just to mention the most recent ones). Focusing on the most recent works using DCEPs, we notice that their majority (Genovali et al. [Gen+14], Lemasle et al. [Lem+18], Luck and Lambert [LL11], Luck [Luc18], Ripepi et al. [Rip+22], and Silva et al. [Sil+22]) agree on measured iron gradients in the interval 0.05-0.06 dex kpc^{-1} . However, all these investigations followed the radial gradient of the MW disc only up to about $R_{GC} \sim 13-14$ kpc, not exploring the outer and possibly most metal-poor regions of the disc, with the exception of Minniti et al. [Min+20], who obtained a metallicity estimate for three DCEPs with $15 < R_{GC} < 22$ kpc, beyond the Galactic bulge. Our sample will allow us increase significantly the number of DCEPs with $R_{GC} > 15$ kpc and get new insights on the metallicity gradient of the MW disc. The application of our sample to the determination of the metallicity dependence of the DCEPs PL/PW relations will be the subject of a separate paper.

2.2 Data

2.2.1 Selection of the targets

Our targets have different characteristics due to the displacement of the MW disc during the different seasons. During the southern winter we can observe in the direction of the Galactic centre, while the opposite is true for the summer season. Given the Galactic gradient, the southern winter and summer seasons allow us to observe DCEPs with solar or super-solar and sub-solar metallicity, respectively. The targets towards the Galactic centre were selected among the list published by Skowron et al. [Sko+19], requiring that the relative error on the parallax published in the *Gaia* DR2 were better than 20% and that $G < 13$ mag (note that EDR3 was not available at the time of proposal submission). This limit ensures that the target were observable in less than 1 h (the maximum allowed duration of an "Observing Block" at ESO) in any weather condition (so called ESO "filler program"). To choose the winter sample, we used again the Skowron et al. [Sko+19] catalog, and by relying on the distances therein, we selected the targets with Galactocentric distance larger than 15 kpc. In this way, thanks to the metallicity gradient of the Galactic disc (see e.g. Kovtyukh and Gorlova [KG00], Luck and Lambert [LL11], and Ripepi et al. [Rip+22] and references therein), we could reasonably expect that the large majority of these DCEPs had [Fe/H] values lower than -0.4 dex, which is one of our main aims.

2.2.2 Observations and data reduction

The spectra analysed in this work have been obtained in the context of two ESO (European Southern Observatory) proposals, namely P105.20MX.001 and P106.2129.001. The observations foreseen for P105 were postponed due to pandemic issues and were collected in service mode between January, 2nd and September, 13th 2021. For P106 the observations were carried out in virtual visitor mode in the period December 12–19, 2020 under very good sky conditions. We used the UVES (Ultraviolet and Visual Echelle Spectrograph³) instrument, attached at the UT2 (Unit Telescope 2) of VLT (Very Large Telescope), placed at Paranal (Chile). We used the red arm equipped with the grism CD#3, covering the wavelength interval 4760–6840 Å, and the central wavelength at 5800 Å. We adopted the 1 arcsec slit, which provides a dispersion of $R \sim 47,000$. The exposure times and the signal to noise (S/N) for each target are listed in Table 2.1, together with the identification of the targets, coordinates, period, G magnitude and mode of pulsation.

³ <https://www.eso.org/sci/facilities/paranal/instruments/uves.html>

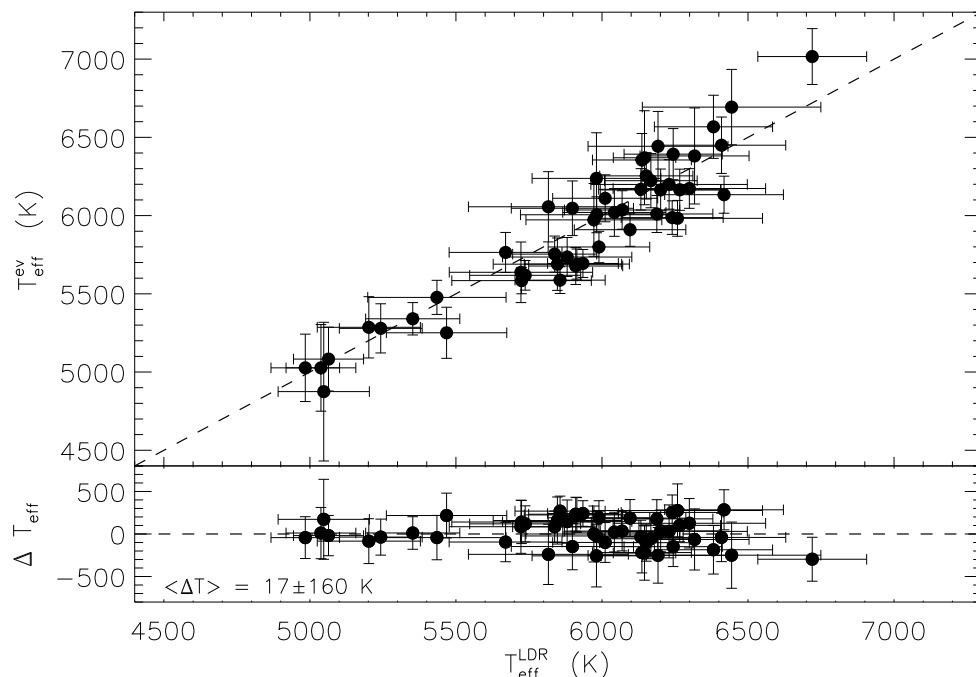


Figure 2.1: Effective temperatures derived by excitation potential of neutral iron lines versus those derived by LDR. The upper panel shows the direct comparison between the two estimates, while the lower panel displays their differences.

The data reduction was carried out using the standard UVES pipeline version 6.1.6. which provides fully calibrated spectra. The spectra were normalized using the *IRAF* task *continuum* after dividing each spectrum into intervals (usually 3/4) in order to have a better continuum detection in each interval.

2.3 Abundance analysis

2.3.1 Stellar parameters

The first step when measuring chemical abundances is the estimation of the main atmospheric parameters, namely the effective temperature (T_{eff}), surface gravity ($\log g$), microturbulent velocity (ξ) and line broadening parameter (v_{br}), i.e. the combined effects of macroturbulence and rotational velocity (in the case of DCEPs, macroturbulence often represents the dominating factor).

Table 2.1: Properties of the observed stars. From left to right, the columns report: Identification of the star; source ID from Gaia; right ascension and declination at J2000; period in days; pulsation mode (fundamental F, first overtone 1O, mixed-mode (both first and second overtone 1O/2O)); G magnitude; distance (in kpc); both exposure time (in seconds) and period of observation (P105 or P106); signal to noise ration at the wavelengths: 5050 and 6300 Å.

Star	GaiaID	Ra (J2000)	Dec (J2000)	P (days)	Mode	G_{mag} (mag)	distance (kpc)	T_{exp} (s)	S/N
ASAS J060450+1021.9	3329807983320140160	91.20833	10.36348	3.075512	1O	12.403	8.44 ± 0.58	900 P106	69/90
ASAS J062939-1840.5	2940212053953709312	97.41343	-18.67407	16.942502	F	12.803	19.82 ± 1.23	1200 P106	48/83
ASAS J064001-0754.8	3099655288815382912	100.00495	-7.91417	1.604003	1O	13.194	8.37 ± 0.50	1800 P106	63/83
ASAS J065758-1521.4	2947876298535964416	104.49359	-15.35740	2.415850	1O	13.219	10.16 ± 0.60	1500 P106	58/71
ASAS J074401-3008.4	5598852026287511424	116.00046	-30.14147	3.390517	F	13.248	9.80 ± 0.62	1800 P106	89/112
ASAS J074925-3814.4	5538569613358406144	117.35519	-38.23936	10.503835	F	12.675	11.93 ± 0.69	1200 P106	58/85
ASAS J084127-4353.6	5522522863932402432	130.36186	-43.89295	25.364784	F	12.027	5.82 ± 0.38	1500 P105	42/87
ASAS J164120-4739.6	5942521668514052608	250.33354	-47.66079	13.018153	F	11.653	4.02 ± 0.23	1200 P105	10/62
ASAS SN-J061713.86+022837.1	3124796657276655488	94.30773	2.47701	2.019309	F	14.447	9.41 ± 0.64	3000 P106	49/70
ASAS SN-J063841.36-034927.7	3104095494729372032	99.67234	-3.82435	3.860779	F	14.003	10.45 ± 0.65	2400 P106	42/64
ASAS SN-J072739.70-252241.1	5613685331497869312	111.91542	-25.37809	2.760085	1O	13.879	10.30 ± 0.67	1800 P106	40/57
ASAS SN-J074354.86-323013.7	5594991812757424768	115.97856	-32.50378	3.149330	F	14.855	11.00 ± 0.76	3000 P106	20/43
ASAS SN-J091822.17-542444.5	5310669788148987520	139.59224	-54.41227	13.120770	F	13.671	16.84 ± 1.05	1800 P106	45/81
ATLAS J102.7978-10.2541	3050117174686674560	102.79785	-10.25419	4.908117	1O	13.758	10.43 ± 0.68	1800 P106	42/72
ATLAS J106.7120-14.0234	304446557737521792	106.71207	-14.02341	1.394987	1O	14.707	9.30 ± 0.61	3000 P106	33/54
ATLAS J113.8534-31.0749	5599120204043561600	113.85342	-31.07500	1.748419	1O	13.583	10.50 ± 0.65	1800 P106	54/64
BQ Vel	5516452460238707968	125.52707	-47.30396	3.372479	F	14.251	13.85 ± 0.92	2400 P106	43/63
GDS J133950.2-634049	5864243376958232576	204.95960	-63.68047	3.791978	1O	12.354	3.36 ± 0.21	3000 P105	40/70
OGLE GD-CEP-0029	3344577418076306944	93.72745	13.87880	5.992352	F	14.975	6.71 ± 0.43	3000 P106	11/31
OGLE GD-CEP-0089	2936063665309240576	107.55532	-15.19940	1.975315	1O	13.548	9.16 ± 0.61	1800 P106	49/67
OGLE GD-CEP-0120	5614916921960857088	114.04436	-25.36404	7.959546	F	14.498	14.31 ± 0.87	3000 P106	20/46
OGLE GD-CEP-0123	5615958881027868544	115.24714	-22.49207	1.399290	F	15.521	12.83 ± 0.78	4800 P106	29/49
OGLE GD-CEP-0127	5586922973654572416	116.29912	-36.97476	13.766689	F	12.217	10.92 ± 0.65	1800 P106	103/154
OGLE GD-CEP-0134	5594793935021492992	117.62511	-32.77881	1.978211	1O	15.703	10.75 ± 0.71	4800 P106	17/34
OGLE GD-CEP-0156	5546003793739552896	119.74496	-34.07070	2.488076	1O	14.639	11.85 ± 0.70	3000 P106	31/53
OGLE GD-CEP-0159	5534744416711687424	119.86020	-40.02831	2.368497	F	14.827	12.39 ± 0.76	3000 P106	32/54
OGLE GD-CEP-0162	5534048803808721664	120.14347	-41.68488	3.516367	F	14.569	11.91 ± 0.69	3000 P106	39/61
OGLE GD-CEP-0168	5543972789600867328	121.20575	-38.05453	2.116514	1O	15.065	12.01 ± 0.71	3000 P106	26/42
OGLE GD-CEP-0176	5533237604747205120	122.05544	-43.25774	1.502544	1O	13.934	12.01 ± 0.78	2400 P106	54/73
OGLE GD-CEP-0179	5540666145820286848	122.38303	-39.20109	2.236739	1O	15.040	12.48 ± 0.90	3000 P106	24/41
OGLE GD-CEP-0181	5521137101325930624	122.45845	-42.97273	2.342181	F	14.327	12.71 ± 0.79	3000 P106	53/67
OGLE GD-CEP-0185	5520935444020919296	122.93821	-44.17211	2.540510	F	15.004	13.05 ± 0.88	3600 P106	29/57
OGLE GD-CEP-0186	5533407170051636608	122.95172	-42.05165	4.764552	F	14.786	13.17 ± 0.82	3000 P106	22/45
OGLE GD-CEP-0196	5520993099661921536	123.96589	-44.01581	2.808806	F	15.302	12.51 ± 0.79	3600 P106	31/48
OGLE GD-CEP-0206	5519997491885313280	125.34584	-44.51655	1.681608	1O	15.388	12.14 ± 0.84	3600 P106	16/31
OGLE GD-CEP-0213	5516789701069413504	125.61290	-46.21620	1.466897	1O	14.776	12.99 ± 0.84	3000 P106	36/50
OGLE GD-CEP-0214	5543722994310379136	125.64924	-34.40032	2.039692	1O	14.330	14.30 ± 0.93	3000 P106	54/74
OGLE GD-CEP-0224	5515778734493663232	127.31511	-46.74925	2.716676	F	14.837	12.79 ± 0.83	3000 P106	45/64
OGLE GD-CEP-0228	5515442352654094976	127.55723	-47.29202	2.596410	F	15.176	15.45 ± 1.00	3600 P106	33/48
OGLE GD-CEP-0247	5329302696287713152	129.39239	-47.57711	1.649005	F	15.682	14.36 ± 0.91	4800 P106	23/38
OGLE GD-CEP-0252	5322878146768508800	129.73195	-49.77017	3.184702	F	14.617	13.92 ± 0.85	3000 P106	48/71
OGLE GD-CEP-0271	5318708901756763520	131.02836	-51.91946	2.984789	F	15.076	16.25 ± 1.03	3600 P106	31/46
OGLE GD-CEP-0316	5310969267622303872	136.56212	-54.93719	2.927582	F	14.586	16.84 ± 1.01	3000 P106	40/58
OGLE GD-CEP-0342	5310717135870439424	139.24329	-53.96897	2.920501	1O	14.904	14.48 ± 0.85	3000 P106	29/44
OGLE GD-CEP-0348	5310642025484526208	139.98489	-54.44281	2.404135	F	15.225	14.67 ± 0.88	3600 P106	36/49
OGLE GD-CEP-0353	5306782361701536128	140.15438	-56.85402	4.862639	F	13.944	14.89 ± 0.91	1800 P106	41/54
OGLE GD-CEP-0516	5255256669866274816	156.87433	-59.35961	0.394959	1O/2O	12.462	2.72 ± 0.18	3000 P105	81/105
OGLE GD-CEP-0568	5350409780509559040	160.82905	-59.19156	45.449567	F	12.227	5.20 ± 0.34	1500 P105	14/53
OGLE GD-CEP-0575	5350281236399037696	161.68646	-60.26828	6.611049	F	12.048	2.80 ± 0.18	1500 P105	22/54
OGLE GD-CEP-0889	5859114571927308672	198.46073	-64.44122	45.179934	F	13.232	10.65 ± 0.70	3000 P105	18/46
OGLE GD-CEP-0974	5854021702729341952	213.76026	-62.73593	12.540476	F	12.675	3.23 ± 0.20	2400 P105	16/63
OGLE GD-CEP-0996	5878506555352293888	219.96841	-60.56111	6.750565	F	12.727	2.17 ± 0.15	453 P105	10/21
OGLE GD-CEP-1012	5877982466278766208	223.59745	-60.45781	15.967508	F	12.268	3.53 ± 0.23	1800 P105	36/52
OGLE GD-CEP-1111	5932882731154933888	240.67672	-53.54162	4.594834	F	13.219	2.25 ± 0.16	3000 P105	24/57
OGLE GD-CEP-1210	4256467552765653376	279.99422	-5.83193	35.823278	F	12.380	3.40 ± 0.24	2100 P105	19/37
OGLE GD-CEP-1285	3329873163744496000	92.63155	9.90423	1.523069	1O	13.362	7.09 ± 0.51	1800 P106	59/80
OGLE GD-CEP-1311	2949613084534085760	103.66101	-13.45176	3.868596	F	13.447	9.17 ± 0.53	1800 P106	42/62
OGLE GD-CEP-1337	5613275454180075264	112.04712	-26.49072	1.307503	1O	15.423	13.22 ± 0.84	4500 P106	33/53
V1253 Cen	6153387928308811264	189.51591	-38.52351	4.320929	F	12.069	10.95 ± 0.62	1500 P105	55/57
V1819 Ori	3343252261748847104	88.61981	-12.53213	3.149580	F	12.527	7.61 ± 0.46	1200 P106	91/114
V418 CMa	2936165984303583360	105.87696	-15.54335	3.522430	F	13.495	9.48 ± 0.58	1800 P106	68/90
V459 Set	4153177128348076032	276.46232	-12.33285	5.762921	F	11.467	2.32 ± 0.15	1500 P105	43/93
V480 Aql	4285878256152184832	282.64531	7.12600	18.998974	F	10.999	2.67 ± 0.18	2100 P105	25/92
V881 Cen	5865214662485305216	201.84005	-63.01964	15.217374	F	12.013	5.33 ± 0.31	1500 P105	18/52
VX CMa	2928096226097916160	109.16267	-22.18043	2.043935	F	14.789	9.61 ± 0.58	3000 P106	27/44

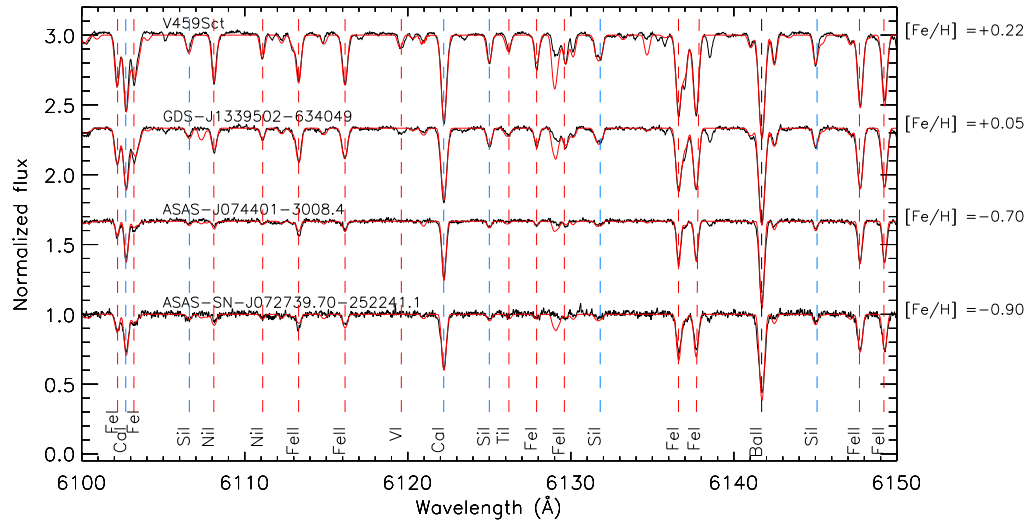


Figure 2.2: Example of high-resolution spectra in the range $\lambda\lambda$ 6100-6150 Å. Stars are ordered from top to bottom with decreasing metallicity (see Sec. 2.3.2 for its estimation). The vertical dashed lines identify the position of atomic lines, the meaning of the colours are: red for lines of vanadium, iron, and nickel, blue for lines of silicon and calcium, and black for the line of barium.

A useful tool extensively adopted in the literature to evaluate the effective temperature, is the line depth ratios (LDR) method (Kovtyukh and Gorlova [KG00]). This method has the advantage of being sensitive to temperature variations, but not to abundances and interstellar reddening. Typically in our targets we measured about 32 LDRs for each spectrum.

For some targets, because of their low metallicity, the number of couples of spectral lines useful for the LDR method is not enough to guarantee accurate results. For these stars the effective temperature can be determined by imposing excitation equilibrium, that is, by imposing that there is no residual correlation between the iron abundance and the excitation potential of the neutral iron lines (see e.g. Mucciarelli and Bonifacio [MB20]). To check the consistency of both methods, we computed the effective temperatures by using excitation potentials

for all the targets for which LDRs gave accurate results. In total we selected 55 targets for which we calculated T_{eff} with both methods. The average difference among all these values is $\Delta T = 17 \pm 160$ K, thus we can conclude that both methods are consistent, The results of this comparison are shown in Fig. 2.1.

For the other parameters (ξ and $\log g$) an iterative approach was adopted: micro-turbulences were estimated by demanding the iron abundances do not depend on the equivalent widths (EWs), that is, the slope of the $[\text{Fe}/\text{H}]$ as a function of EWs is null. For this purpose, we first measured the equivalent widths of a sample of 145 Fe I lines using a python3 semi-automatic custom routine. The lines sample was extracted from the line list published by Romaniello et al. [Rom+08] and the routine minimizes errors in the continuum estimation on the wings of the spectral lines. The conversion of the EWs in abundances has been performed through the WIDTH9 code (Kurucz and Avrett [KA81]) applied to the corresponding atmospheric model calculated by using ATLAS9 (Kurucz [Kur93]). In this calculation we did not consider the influence of $\log g$ since neutral iron lines are insensitive to it. Then, the surface gravities were estimated with a similar iterative procedure imposing the ionization equilibrium between Fe I and Fe II. The adopted list of 24 Fe II lines was extracted from Romaniello et al. [Rom+08].

The atmospheric parameters estimated, and summarized in Table 2.2, were used as input values for the abundance analysis presented in the next section.

2.3.2 Abundances

In order to avoid problems from spectral line blending caused by line broadening, a spectral synthesis technique was applied to our spectra. Synthetic spectra were generated in three steps: i) plane parallel local thermodynamic equilibrium (LTE) atmosphere models were computed using the ATLAS9 code Kurucz [Kur93], using the stellar parameters in Table 2.2; ii) stellar spectra were synthesized by using SYNTH3 Kurucz and Avrett [KA81]; iii) the synthetic spectra were convoluted for instrumental and line broadening. This was evaluated by matching the synthetic line profiles to a selected set of the observed metal lines.

For a total of 24 different chemical elements it was possible to detect spectral lines used for the estimation of the abundances. For all elements we performed the following analysis: we divided the observed spectra into intervals, 25 Å or 50 Å wide, and derived the abundances in each interval by performing a χ^2 minimization of the differences between the observed and synthetic spectra. The minimization algorithm was written in IDL⁴ language, using the *amoeba* routine.

⁴ IDL (Interactive Data Language) is a registered trademark of L3HARRIS Geospatial

Table 2.2: Atmospheric parameters estimated for each star. The various columns provide: identification, Julian date at the middle of the observation, effective temperature, gravity, microturbulent velocity, broadening parameter and radial velocities.

Star	HJD (days)	Teff (K)	log g (dex)	ξ (km s ⁻¹)	v_{br} (km s ⁻¹)	v_{rad} (km s ⁻¹)
ASAS J060450+1021.9	59202.5964	6409 ± 220	2.2 ± 0.1	3.0 ± 0.4	15 ± 1	36.1 ± 0.3
ASAS J062939-1840.5	59196.5666	5100 ± 83	1.0 ± 0.1	4.2 ± 0.3	22 ± 1	145.4 ± 0.3
ASAS J064001-0754.8	59202.7323	6137 ± 169	1.8 ± 0.1	2.3 ± 0.4	12 ± 1	98.3 ± 0.2
ASAS J065758-1521.4	59201.6212	6266 ± 140	2.0 ± 0.1	3.0 ± 0.4	12 ± 1	113.2 ± 0.1
ASAS J074401-3008.4	59197.8179	6444 ± 306	1.5 ± 0.1	2.9 ± 0.4	8 ± 1	101.1 ± 0.1
ASAS J074925-3814.4	59196.6319	5838 ± 144	1.4 ± 0.1	4.4 ± 0.5	21 ± 2	127.7 ± 0.3
ASAS J084127-4353.6	59270.6998	6167 ± 159	0.5 ± 0.1	3.5 ± 0.4	15 ± 1	48.7 ± 0.2
ASAS J164120-4739.6	59424.6099	4890 ± 120	0.8 ± 0.1	2.9 ± 0.5	11 ± 1	-29.9 ± 0.1
ASAS SN-J061713.86+022837.1	59198.5960	6629 ± 328	1.6 ± 0.1	3.2 ± 0.4	13 ± 1	30.7 ± 0.2
ASAS SN-J063841.36-034927.7	59199.5975	6259 ± 291	1.9 ± 0.1	3.1 ± 0.4	11 ± 1	96.7 ± 0.1
ASAS SN-J072739.70-252241.1	59202.6672	6382 ± 202	2.0 ± 0.1	2.8 ± 0.4	10 ± 1	113.8 ± 0.1
ASAS SN-J074354.86-323013.7	59198.6348	5981 ± 220	2.0 ± 0.1	3.7 ± 0.4	15 ± 1	171.0 ± 0.3
ASAS SN-J091822.17-542444.5	59196.7584	5243 ± 142	0.2 ± 0.1	2.8 ± 0.2	10 ± 1	135.3 ± 0.1
ATLAS J102.7978-10.2541	59196.5892	6042 ± 177	1.7 ± 0.1	3.4 ± 0.4	13 ± 1	79.3 ± 0.1
ATLAS J106.7120-14.0234	59202.6341	6304 ± 159	1.5 ± 0.1	3.2 ± 0.2	13 ± 1	72.6 ± 0.1
ATLAS J113.8534-31.0749	59201.6430	6244 ± 168	2.1 ± 0.1	3.3 ± 0.4	21 ± 1	116.9 ± 0.4
BQ Vel	59198.8353	5847 ± 220	1.6 ± 0.1	3.1 ± 0.4	12 ± 1	139.9 ± 0.2
GDS J133950.2-634049	59294.7621	6146 ± 107	1.1 ± 0.1	3.0 ± 0.4	12 ± 2	-68.4 ± 0.1
OGLE GD-CEP-0029	59197.6209	5817 ± 274	0.9 ± 0.1	2.7 ± 0.4	11 ± 1	8.3 ± 0.2
OGLE GD-CEP-0089	59201.5986	6240 ± 175	1.8 ± 0.1	3.1 ± 0.4	11 ± 1	100.4 ± 0.1
OGLE GD-CEP-0120	59197.6572	5435 ± 237	0.9 ± 0.1	3.2 ± 0.4	15 ± 2	150.9 ± 0.1
OGLE GD-CEP-0123	59198.7220	5990 ± 174	1.8 ± 0.1	3.3 ± 0.4	12 ± 1	148.7 ± 0.2
OGLE GD-CEP-0127	59196.6970	5202 ± 176	0.7 ± 0.1	3.2 ± 0.4	15 ± 1	130.1 ± 0.1
OGLE GD-CEP-0134	59201.7136	5732 ± 285	1.6 ± 0.1	3.2 ± 0.4	17 ± 1	127.5 ± 0.2
OGLE GD-CEP-0156	59202.6981	6230 ± 268	1.6 ± 0.1	2.3 ± 0.4	6 ± 1	131.2 ± 0.1
OGLE GD-CEP-0159	59197.7810	5910 ± 161	2.2 ± 0.1	3.8 ± 0.4	13 ± 1	145.8 ± 0.2
OGLE GD-CEP-0162	59197.6942	6133 ± 145	1.6 ± 0.1	3.1 ± 0.4	11 ± 1	90.1 ± 0.1
OGLE GD-CEP-0168	59202.7614	6069 ± 197	1.6 ± 0.1	2.9 ± 0.4	13 ± 1	132.6 ± 0.1
OGLE GD-CEP-0176	59201.8437	6201 ± 207	1.4 ± 0.1	2.2 ± 0.4	7 ± 2	154.8 ± 0.1
OGLE GD-CEP-0179	59201.8097	6188 ± 192	1.7 ± 0.1	2.9 ± 0.4	10 ± 1	125.6 ± 0.1
OGLE GD-CEP-0181	59198.6715	5982 ± 261	1.3 ± 0.1	2.4 ± 0.4	13 ± 1	124.8 ± 0.2
OGLE GD-CEP-0185	59196.7954	5737 ± 190	1.5 ± 0.1	3.3 ± 0.4	11 ± 1	154.1 ± 0.1
OGLE GD-CEP-0186	59196.6597	5723 ± 246	1.7 ± 0.1	2.9 ± 0.4	12 ± 1	128.1 ± 0.1
OGLE GD-CEP-0196	59197.7388	6011 ± 180	1.3 ± 0.1	3.3 ± 0.4	11 ± 1	107.5 ± 0.1
OGLE GD-CEP-0206	59201.7645	6192 ± 240	1.9 ± 0.1	2.7 ± 0.4	9 ± 1	119.7 ± 0.1
OGLE GD-CEP-0213	59202.7983	6342 ± 162	1.4 ± 0.1	3.0 ± 0.2	10 ± 1	146.8 ± 0.2
OGLE GD-CEP-0214	59202.8390	6720 ± 186	1.6 ± 0.1	2.9 ± 0.3	8 ± 1	150.1 ± 0.2
OGLE GD-CEP-0224	59196.7282	6815 ± 211	1.8 ± 0.1	3.4 ± 0.2	14 ± 1	122.5 ± 0.3
OGLE GD-CEP-0228	59198.7974	5935 ± 121	1.9 ± 0.1	3.1 ± 0.4	10 ± 1	142.2 ± 0.1
OGLE GD-CEP-0247	59199.6770	5899 ± 209	1.7 ± 0.1	2.5 ± 0.3	7 ± 1	145.8 ± 0.2
OGLE GD-CEP-0252	59196.8361	6418 ± 203	2.1 ± 0.1	3.8 ± 0.5	12 ± 1	99.5 ± 0.2
OGLE GD-CEP-0271	59199.7473	5914 ± 180	1.5 ± 0.1	3.2 ± 0.5	14 ± 1	158.0 ± 0.2
OGLE GD-CEP-0316	59199.7894	5881 ± 221	2.0 ± 0.1	3.7 ± 0.4	15 ± 1	159.7 ± 0.2
OGLE GD-CEP-0342	59203.8370	6096 ± 191	1.0 ± 0.1	2.5 ± 0.4	13 ± 1	120.4 ± 0.1
OGLE GD-CEP-0348	59199.8311	6152 ± 160	1.3 ± 0.1	2.3 ± 0.4	12 ± 1	112.2 ± 0.1
OGLE GD-CEP-0353	59197.8401	5725 ± 239	1.4 ± 0.1	3.3 ± 0.4	11 ± 1	118.2 ± 0.1
OGLE GD-CEP-0516	59217.6507	6367 ± 151	1.5 ± 0.1	2.4 ± 0.2	13 ± 1	-9.0 ± 0.2
OGLE GD-CEP-0568	59271.6099	5086 ± 118	0.2 ± 0.1	3.8 ± 0.5	15 ± 1	-37.4 ± 0.2
OGLE GD-CEP-0575	59271.6462	5352 ± 161	0.9 ± 0.1	4.4 ± 0.5	18 ± 1	12.7 ± 0.1
OGLE GD-CEP-0889	59294.7240	5670 ± 116	0.4 ± 0.1	5.3 ± 0.2	29 ± 1	48.1 ± 0.8
OGLE GD-CEP-0974	59458.5146	4984 ± 117	0.5 ± 0.1	3.0 ± 0.4	11 ± 1	-44.3 ± 0.3
OGLE GD-CEP-0996	59294.7855	5506 ± 175	1.0 ± 0.1	3.0 ± 0.5	11 ± 1	-40.1 ± 2.8
OGLE GD-CEP-1012	59471.5399	5038 ± 119	0.5 ± 0.1	3.0 ± 0.4	13 ± 1	-55.8 ± 0.3
OGLE GD-CEP-1111	59471.5722	6239 ± 386	1.4 ± 0.1	3.5 ± 0.3	11 ± 1	-92.4 ± 0.3
OGLE GD-CEP-1210	59464.5956	5047 ± 156	0.9 ± 0.1	4.4 ± 0.3	13 ± 1	70.7 ± 0.6
OGLE GD-CEP-1285	59201.6706	6038 ± 105	0.9 ± 0.1	3.4 ± 0.2	26 ± 3	46.2 ± 0.4
OGLE GD-CEP-1311	59196.6139	5856 ± 154	1.5 ± 0.1	3.8 ± 0.4	18 ± 1	121.9 ± 0.2
OGLE GD-CEP-1337	59203.7932	5977 ± 151	0.6 ± 0.1	1.9 ± 0.2	9 ± 1	145.2 ± 0.1
V1253 Cen	59294.6819	5670 ± 193	1.5 ± 0.1	3.8 ± 0.4	16 ± 1	119.1 ± 0.3
V1819 Ori	59199.7206	6342 ± 95	1.2 ± 0.1	3.7 ± 0.1	19 ± 1	27.2 ± 0.3
V418 CMa	59198.7652	6299 ± 261	1.8 ± 0.1	3.8 ± 0.5	13 ± 1	105.5 ± 0.2
V459 Sct	59370.9059	5972 ± 233	1.1 ± 0.1	3.4 ± 0.2	11 ± 1	-4.1 ± 0.1
V480 Aql	59464.6236	5019 ± 122	1.0 ± 0.1	3.6 ± 0.8	12 ± 1	29.1 ± 0.1
V881 Cen	59294.6322	5064 ± 120	0.3 ± 0.1	3.2 ± 0.4	11 ± 1	-34.5 ± 0.1
VX CMa	59199.6303	5820 ± 106	1.2 ± 0.1	3.7 ± 0.2	14 ± 1	128.4 ± 0.2

We considered several sources of uncertainties in our abundances. First, we evaluated the expected errors caused by variations in the fundamental stellar parameters of $\delta T_{\text{eff}} = \pm 150$, $\delta \log g = \pm 0.2$ dex, and $\delta \xi \pm 0.3 \text{ km s}^{-1}$. According to our simulations, those errors contribute $\approx \pm 0.1$ dex to the total error budget. Total errors were evaluated by summing in quadrature this value to the standard deviations obtained from the average abundances.

The adopted lists of spectral lines and atomic parameters are from Castelli and Hubrig [CH04], who have updated the original parameters of Kurucz [Kur95]. When necessary we also checked the NIST database (Ralchenko and Reader [RR19]).

An example of four spectra in the range $\lambda\lambda$ 6100-6150 Å is displayed in Fig. 2.2. With the aim of comparing the differences in the spectral line depth, each spectrum reports, as a side label, with the metallicity derived in our analysis (see Sec. 2.3.2).

In Fig. 2.3 we show the distribution of the elements derived in this analysis in the form of histograms, where bins have been fixed to 0.15 dex, in order to be representative of the errors. The literature sample is also shown for comparison (see Sect. 2.4). For each element, The Gaussian fit has been over-imposed with the respective mean value and its FWHM is reported in the upper right corner of each box.

- Carbon, Oxygen: the following spectral lines were used for carbon: $\lambda\lambda$ 4932.049, 5052.144 and 5380.0325 Å. The Gaussian fit reports a mean abundance of 0.80 dex below the solar one, with an asymmetrical tail towards higher values. For oxygen, the forbidden line O I at 6300.304 Å and the O I triplet at 6155-8 Å, obtaining a broader distribution centered at -0.37 dex. No Nitrogen lines could be detected in our observed spectral range.
- Sodium: six neutral lines have been found for this element: $\lambda\lambda$ 5682.647, 5688.217, 5889.930, 5895.910, 6154.230 and 6160.753 Å. The mean value is slightly under abundant, at -0.15 dex.
- Aluminum: Two aluminum neutral lines have been detected for our spectra, $\lambda\lambda$ 6696.018 and 6698.667 Å, obtaining a distribution slightly under abundant.
- α -elements: Magnesium (four Mg I spectral lines: $\lambda\lambda$ 5167.320, 5172.680, 5183.600 and 5528.405 Å), Silicon (four Si II lines at $\lambda\lambda$ 5041.024, 5055.984, 6347.11 and 6371.370 Å) and Calcium (via Ca I lines, $\lambda\lambda$ 5598.480, 6162.170, 6166.433, 6169.042, 6169.583, 6462.567, 6471.662, 6493.781, 6499.65 Å) result under-abundant, while Sulfur (three S II at $\lambda\lambda$ 6743.585, 6748.153, 6757.153 Å) and Titanium (several Ti I and Ti II all over the spectrum) are consistent

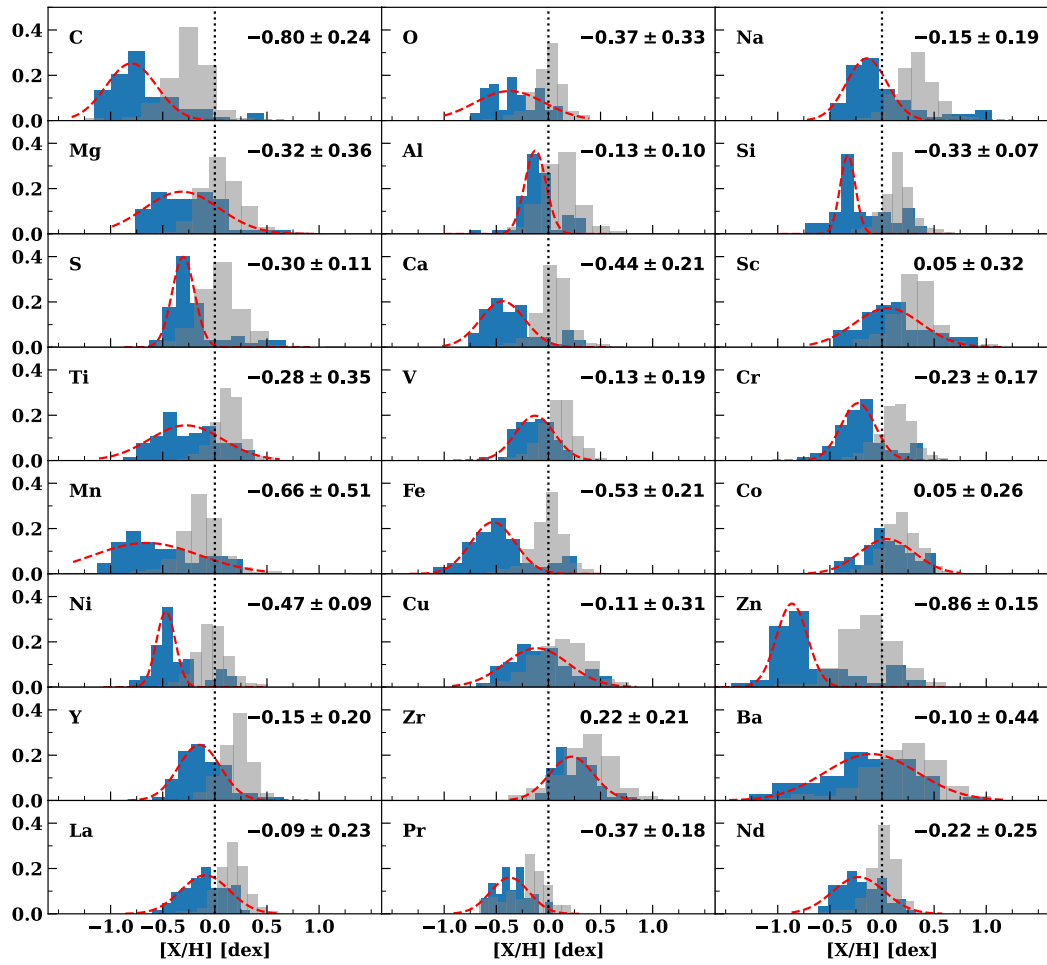


Figure 2.3: Histograms of the distribution of the chemical abundances derived in this study (blue histograms) compared with literature data as defined in Sect. 2.4.1 (grey histograms). Gaussian fits have been overlaid in our data (red dashed curves) and the respective mean value and FWHM reported in each box.

with about -0.30 dex under solar abundances although the latter has a wider distribution.

- Scandium: Five Sc II lines were measured at $\lambda\lambda$ 5031.021, 5237.813, 5526.818, 5684.000 and 6245.621 Å. The resulting distribution is centered on about solar value.
- Iron peak elements: V, Cr, Mn, Fe, Co, Ni, Co and Zn: four neutral vanadium

lines ($\lambda\lambda$ 5698.482, 5703.569, 6090.194 and 6243.088 Å) distributed around -0.13 dex. Whilst Cobalt is consistent with solar abundances (measured using three Co I lines at $\lambda\lambda$ 5266.490, 5352.000 and 6450.067 Å), manganese has a spread distribution around -0.66 dex (five Mn I lines at $\lambda\lambda$ 4823.515, 5341.057, 6013.458, 6016.638 and 6021.790 Å) and Chromium is slightly under abundant (with five Cr II spectral lines: $\lambda\lambda$ 4824.131, 4876.339, 5204.506, 5206.037, 5208.419 Å), Iron and Nickel (Ni I: $\lambda\lambda$ 5080.533, 5081.110, 5084.011, 5094.411, 5099.931 Å) are significantly under abundant, with distributions centered at -0.53 and -0.47 dex respectively. We used two Cu I neutral lines at $\lambda\lambda$ 5105.500 and 5218.201 Å, with abundances consistent with the solar ones. For zinc only one neutral line could be measured at λ 6362.338 Å. The mean value of the distribution is centered on -0.86 dex.

- Yttrium and Zirconium: with four Y II lines ($\lambda\lambda$ 4883.682, 4900.120, 5087.418, 5402.774 Å) and one Zr II line (λ 6114.853 Å) we obtained two distributions centered at -0.15 and 0.22 dex respectively.
- Barium: as expected, using four Ba II spectral lines at $\lambda\lambda$ 4934.100, 5853.625, 6141.713, 6496.897 Å, we estimated abundances centered on -0.10 dex but distributed over a wide range, from ≈ -1.5 to ≈ 1.0 dex.
- Rare earth elements: we obtained distributions centered at -0.09 , -0.37 and -0.22 dex, respectively for Lanthanum (La II lines at $\lambda\lambda$ 4921.776, 5114.559 and 5290.818 Å), Praseodymium (one Pr II line at λ 5219.045 Å) and Neodymium (five Nd II lines at $\lambda\lambda$ 4959.119, 4989.950, 5092.794, 5293.163, 5688.518 Å).

A comprehensive list of all estimated abundances is shown in Table 2.5.

The differences between our results and the literature values are largely due to the location of a significant fraction of our targets in the galactic anti-center region, characterized by significantly lower abundances than in regions closer to the galactic center (see discussion in Sect. 2.4).

2.4 Comparison with the literature

2.4.1 Literature sample

For the following analysis, we complemented the sample studied in this work with stars from the literature. More in detail, we considered the large compilation of homogenised literature iron abundances for 436 DCEPs presented by Groenewegen [Gro18] (G18 hereinafter), complemented with literature results for a few

additional stars by Gaia Collaboration et al. [Gai+17] (GC17 hereinafter). To these data we added the sample of 49 stars presented in our previous works Catanzaro et al. [Cat+20] and Ripepi et al. [Rip+21a; Rip+21b] (collectively called R21 hereinafter) and the recently published large sample of 104 stars by Kovtyukh et al. [Kov+22] (K22 hereinafter). There is almost no overlap between the G18/GC17 and the R21 sample, apart from the stars V5567 Sgr and X Sct (see Ripepi et al. [Rip+21a]). On the contrary, there is some overlap between K22 and the other samples, including the dataset presented in this paper. More precisely, K22 has 13, 2, 14 and 2 stars in common with G18, GC17, R21 and this paper, respectively.

In order to use all the data together, we seek for any systematic difference between the K22 and the other datasets. Albeit there is a large scatter, it can be seen that K22 on average tends to overestimate the $[\text{Fe}/\text{H}]$ value by 0.06 ± 0.02 dex (the error is the standard deviation of the mean). In order to obtain a literature homogenised sample, we decided to remove from the K22 sample the stars in common with the other datasets and to add -0.06 dex to the $[\text{Fe}/\text{H}]$ of the remaining 73 stars. Therefore, the total sample of DCEPs with $[\text{Fe}/\text{H}]$ from high-resolution spectroscopy is therefore composed of 637 objects.

Concerning the elements other than iron that are not present in G18 or GC17, we adopted the homogeneous and extensive list published by Luck [Luc18] (L18 hereinafter) for 435 Galactic DCEPs and merged it with that of K22, as performed above for iron. There were 9 stars in common between L18 and K22 which were removed from the merged list.

2.4.2 Element by element comparison

In Fig. 2.4 we plot both our abundances and those from the literature, expressed in the form $[\text{X}/\text{Fe}]$, as a function of metallicity, expressed as $[\text{Fe}/\text{H}]$. It is worth mentioning that, as can be seen also in Fig. 2.3, most of our stars cover the metallicity region between $-0.8/-0.4$ dex, previously less populated.

In the following, we describe the behaviour of each element with respect to the iron content, dividing each group of elements in a similar way as listed in Sect.2.3.2.

- Carbon results from the first dredge-up Iben Jr [Ibe67], where the incomplete CN-process outcomes mix to the surface. As for Oxygen, it is mostly released by type II supernovae (SNe II), whose progenitors are young massive stars. Due to their short lifetime, they pollute the interstellar medium essentially instantaneously with respect to the timescale of Galactic evolution, so we expect higher abundances for lower metallicities, with decreasing values as the metallicity increases and other slower mechanisms start to have a major

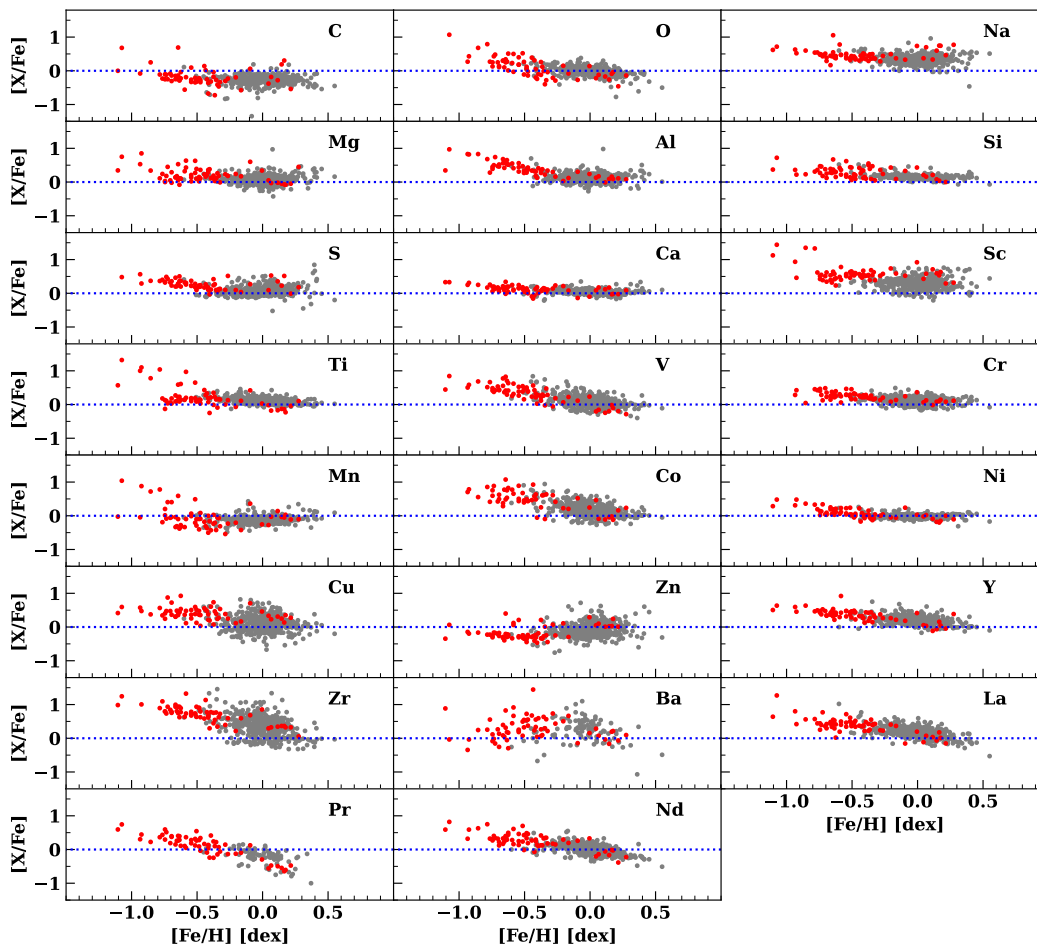


Figure 2.4: Chemical element abundances (expressed as $[X/Fe]$) as a function of the iron content for both literature and our sample of stars. Red and gray points are the observed and literature abundances, respectively. The blue dotted horizontal lines point out the solar reference. The corresponding element of each plot is written on the top right.

impact. What we find is a negative trend for oxygen, with metal-poor stars having over solar abundances, and an almost flat distribution for carbon.

- Both Sodium and Aluminum are odd- z elements that should be produced by core-collapse SNe. Nevertheless, we find a relatively flat trend for sodium and an average overabundance, interpreted by Sasselov [Sas86] as the result of the Na-Ne cycle for luminous stars. On the other hand, we find for Al an

almost flat trend down to $[\text{Fe}/\text{H}] \approx -0.5$ and a rise of abundance toward lower metallicities.

- α -elements (Mg, Si, S, Ca, Ti): as for Oxygen, the α -elements production is due to core-collapse supernovae, so we should expect a similar trend as Oxygen. However, in Fig. 2.5 we plotted α -elements vs. metallicity and we observe a general increase of their abundance toward lower metallicities.
- Scandium can be seen as an intermediate element between the α elements and the iron peak group. Similar to α elements, Scandium is produced in the innermost ejected layers of core-collapse SNe (type II) as reviewed by Romano et al. [Rom+10], while the contribution from type Ia SNe seems to be negligible Clayton [Cla03]. For this element we find a quite flat distribution over the metallicities, with the exception of the most metal poor of our sample, that seem to have an overabundance of scandium.
- Iron peak elements (V, Cr, Mn, Co, Ni, Cu, Zn) are those elements close to Iron, produced especially by Type Ia supernovae (SN Ia), the final stage of white dwarfs that undergo a binary merging. In general we observe an increase of abundances toward lower metallicities for elements like vanadium, chromium, cobalt and nickel, an almost flat trend for elements such as manganese and copper, while only zinc seems to increase with metallicities.
- For heavier elements, starting from Y, there are two main processes both based on neutron-capture. The so-called rapid neutron-process (r-process) whose possible channels refer to neutron star mergers, supernova explosions and electron capture SN (see Argast et al. [Arg+04], Cowan et al. [Cowan+21], Korobkin et al. [Kor+12], and Surman et al. [Sur+08] and are responsible for the production of Y, Zr, La, Pr and Nd, for which we have found negative trend with metallicities. The slow neutron-process (or s-process) which occurs in low and intermediate mass stars during the AGB phase (Karakas and Lugaro [KL16]), is the primary source for barium formation. The trend of barium with respect to iron seems to have a maximum close to $[\text{Fe}/\text{H}] \approx -0.2$ dex and decrease both toward higher and lower metallicities, but given the high scatter of the measurements no conclusions can be drawn. The cause of this high scatter of the measurements has been noticed in previous papers (see e.g. Andrievsky et al. [And+13] and Simmerer et al. [Sim+04]) and ascribed to the variation of microturbulent velocities from star to star.

The behaviour of each element with respect to the iron abundance is in general agreement with recent results based on high-resolution spectroscopy of static

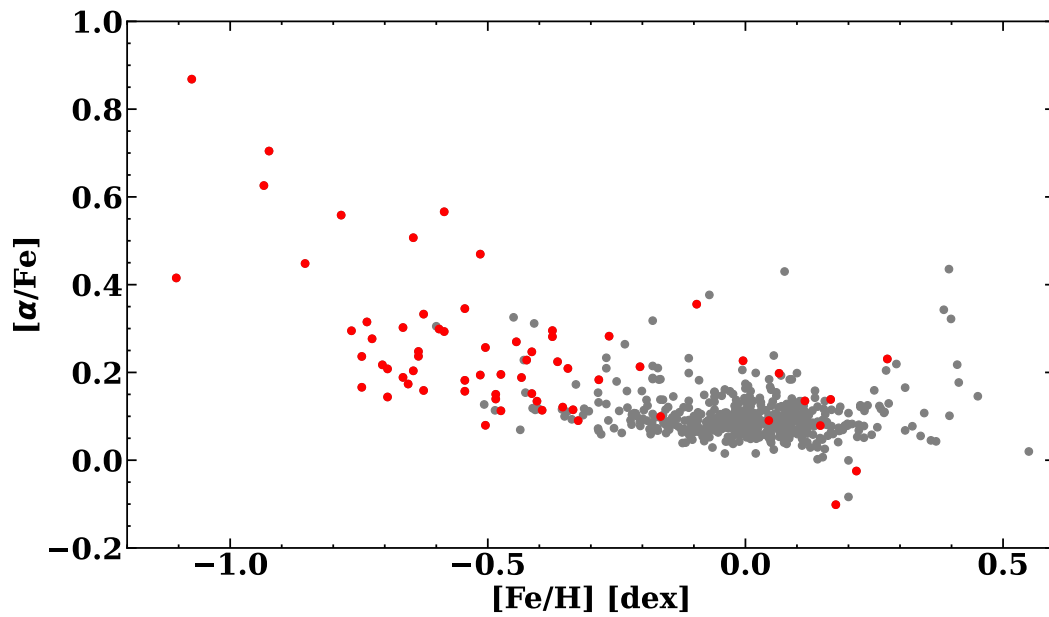


Figure 2.5: As in Fig. 2.4 but for α -elements abundance.

stars belonging to the Galactic disc (see for example Hayden et al. [Hay+17], Silva Aguirre et al. [Sil+18], and Spitoni et al. [Spi+19] and references therein). A detailed discussion of the evolution of the chemical elements is beyond the scope of this paper. Here we only mention that, in general, the time-delay model (see Matteucci [Mat21] for a review) represents a robust interpretation of the observed abundance ratio versus metallicity ($[\text{Fe}/\text{H}]$) diagrams.

2.5 The Galactic radial gradient

2.5.1 Distance estimate

To estimate the distances D to each DCEP in our sample, we used the distance modulus definition $w - W = -5 + 5 \log_{10} D$, where w and W represent the apparent and absolute Wesenheit magnitudes, respectively. These magnitudes are reddening-free by construction (see Madore [Mad82]), assuming that we know the extinction law. We adopted the Wesenheit magnitude in the *Gaia* bands which was empirically defined by Ripepi et al. [Rip+19] as $w = G - 1.90 \times (G_{BP} - G_{RP})$, where G , G_{BP} and G_{RP} are the magnitudes in the *Gaia* bands. The Wesenheit coefficient was estimated on the basis of the synthetic *Gaia* photometry by Jordi et al. [Jor+10] and then

fine-tuned to minimize the spread in the PW relation in the LMC. However, the same coefficient can be safely used in the MW (see Gordon et al. [Gor+03]). The absolute Wesenheit magnitude W was calculated according to the period-Wesenheit-metallicity (PWZ) relation published by Ripepi et al. [Rip+22]:

$$W = (-5.988 \pm 0.018) - (3.176 \pm 0.044)(\log P - 1.0) - (0.520 \pm 0.090)[Fe/H] \quad (2.1)$$

where P and $[Fe/H]$ are the period and the iron abundance of each DCEP, listed in Table 2.1 and Table 2.5. To calculate the w values, we retrieved the *Gaia* magnitudes for our DCEP sample from the EDR3 catalog (Gaia Collaboration et al. [Gai+21]). In principle, we should adopt intensity-averaged magnitudes, that is, calculated over the light curves after transforming the magnitudes into intensities and then converting the resulting mean intensity into magnitude (e.g. Bono et al. [BMS99b] and Clementini et al. [Cle+16]). However, these magnitudes will be available for all our targets only after the publication of *Gaia* data release 3. Luckily enough, we can safely use the mean magnitudes in the *Gaia*EDR3 catalogue because it has been demonstrated that the difference between the Wesenheit magnitudes calculated in the two different fashions is very small (see a detailed discussion on this point in Poggio et al. [Pog+21] and Ripepi et al. [Rip+22]). The distances can thus be derived from the values of w and W . To estimate the uncertainty on the distance, we adopted the equation $\sigma_D = 0.4605\sigma_\mu D$, where σ_μ is the error on the distance modulus, estimated by adding in quadrature the errors on w and W . The former was estimated by propagating the errors on the *Gaia* magnitudes taking also into account the uncertainty of ± 0.05 in the Wesenheit coefficient (Ripepi et al. [Rip+19]), while for the latter we propagated the errors in the coefficients of Eq. 2.1, as well as that on the iron abundance⁵. Distances and relative errors are listed in Table 2.1. Having estimated the distances, we transformed the equatorial coordinates listed in Table 2.1 into the Galactic coordinate system and adopted standard transformations to calculate Galactocentric Cartesian coordinates (see e.g. eq. 4 in Ripepi et al. [Rip+19]), using a distance of 8.277 kpc for the Galactic centre (Gravity Collaboration et al. [Gra+22]). From the Cartesian coordinates it was straightforward to calculate the Galactocentric radius R_{GC} for each target.

2.5.2 Metal radial gradient of the MW disc

The relation between the iron abundance ($[Fe/H]$) and the Galactocentric radius (R_{GC}), is displayed in Fig. 2.6, for both our and literature samples. Our data extends

⁵ The error on the periods is negligible.

Table 2.3: Results of the Galactic metallicity gradient derived in this work. Literature estimates are also shown for comparison. The radial gradient has the form: $[Fe/H] = \alpha \times R_{GC} + \beta$. Columns 1 and 2 list the values of the slope (α) and zero point (β) of the radial gradient; column 3 (when possible) the rms; column 4 reports the number of objects used; column 5 and 6 includes the literature source and the notes, respectively.

α (dex kpc ⁻¹)	β (dex)	rms (dex)	n.obj.	Source	Notes
This work					
-0.060 ± 0.002	0.573 ± 0.017	0.12	637	This Work	$R_{GC} > 4$ kpc
-0.064 ± 0.007	0.588 ± 0.053	0.11	333	This Work	$4 \text{ kpc} \leq R_{GC} \leq 9.25$ kpc
-0.080 ± 0.003	0.829 ± 0.038	0.13	304	This Work	$R_{GC} > 9.25$ kpc
-0.066 ± 0.009	0.64 ± 0.11	0.07	12	This Work	Bin sample, $R_{GC} > 4$ kpc
-0.068 ± 0.004	0.62 ± 0.27	0.04	4	This Work	Bin sample, $4 \text{ kpc} \leq R_{GC} \leq 9.25$ kpc
-0.078 ± 0.002	0.81 ± 0.26	0.08	8	This Work	Bin sample, $R_{GC} > 9.25$ kpc
Literature (using Cepheids)					
-0.062 ± 0.002	0.605 ± 0.021		313	Luck and Lambert [LL11] (L11)	
-0.051 ± 0.003	0.49 ± 0.03		128	Genovali et al. [Gen+14] (G14)	UVES and FEROS only
-0.060 ± 0.002	0.57 ± 0.02		450	Genovali et al. [Gen+14] (G14)	Whole sample
-0.051 ± 0.002			411	Luck [Luc18] (L18)	
-0.045 ± 0.007			25	Lemasle et al. [Lem+18] (Lem18)	Mixed F/10 Cepheids
-0.054 ± 0.008	0.52 ± 0.08		30	Minniti et al. [Min+20] (M20)	Far side of the MW
-0.062 ± 0.013	0.59 ± 0.13		28	Minniti et al. [Min+20] (M20)	$R_{GC} \leq 17$ kpc
-0.0527 ± 0.0022	0.511 ± 0.022	0.11	489	Ripepi et al. [Rip+22] (R22)	
-0.055 ± 0.003	0.43 ± 0.03			Silva et al. [Sil+22] (Da22)	
Literature (using Open Clusters)					
-0.035 ± 0.007			29	Cunha et al. [Cun+16] (C16)	
-0.068 ± 0.017			29	Cunha et al. [Cun+16] (C16)	Two-fit line $R_{GC} < 12$ kpc
-0.030 ± 0.009				Cunha et al. [Cun+16] (C16)	$R_{GC} > 12$ kpc
-0.025 ± 0.017			7	Cunha et al. [Cun+16] (C16)	age < 0.5 Gyr
-0.086 ± 0.008	0.72 ± 0.08		88	Netopil et al. [Net+16] (N16)	$R_{GC} < 12$ kpc
-0.066 ± 0.007	0.54 ± 0.07		82	Netopil et al. [Net+16] (N16)	Excluding outliers
-0.016 ± 0.007	-0.04 ± 0.12		12	Netopil et al. [Net+16] (N16)	$R_{GC} > 12$ kpc
-0.079 ± 0.015	0.62 ± 0.12		35	Netopil et al. [Net+16] (N16)	Age ≤ 0.5 Gyr
-0.06 ± 0.01			11	Casamiquela et al. [Cas+19] (C19)	Age < 1.5 Gyr
-0.068 ± 0.004			128	Donor et al. [Don+20] (D20)	Whole sample
-0.068 ± 0.004			71	Donor et al. [Don+20] (D20)	Two-fit line, $R_{GC} < 13.9$ kpc
-0.009 ± 0.011				Donor et al. [Don+20] (D20)	and $R_{GC} > 13.9$ kpc
-0.050 ± 0.003			13	Donor et al. [Don+20] (D20)	Age ≤ 0.4 Gyr
-0.073 ± 0.003			16	Donor et al. [Don+20] (D20)	$0.4 < \text{Age} \leq 0.8$ Gyr
-0.076 ± 0.009	0.60 ± 0.08		134	Spina et al. [Spi+21] (S21)	
-0.054 ± 0.008	0.32 ± 0.07	0.116	503	Gaia Collaboration et al. [Gai+22] (G22)	

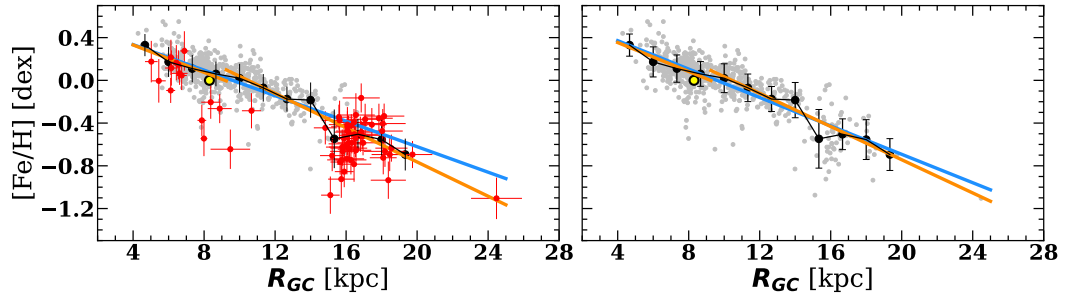


Figure 2.6: Galactic iron abundance radial gradient. Left: Grey and red dots show the data from the literature and this work, respectively. The big black dots with relative error-bars represent a binning of the data with bins of 1.33 kpc each. The light blue line shows a linear fitting to the data over the entire range of Galactocentric distances, while the two orange lines represent the fit to the data carried out by dividing the sample into two pieces with a break at $R_{GC}=9.25$ kpc. The sun is shown with a yellow-black symbol. Right: Same as left, where all the data are in grey dots, and the lines represent the fit on the binning points.

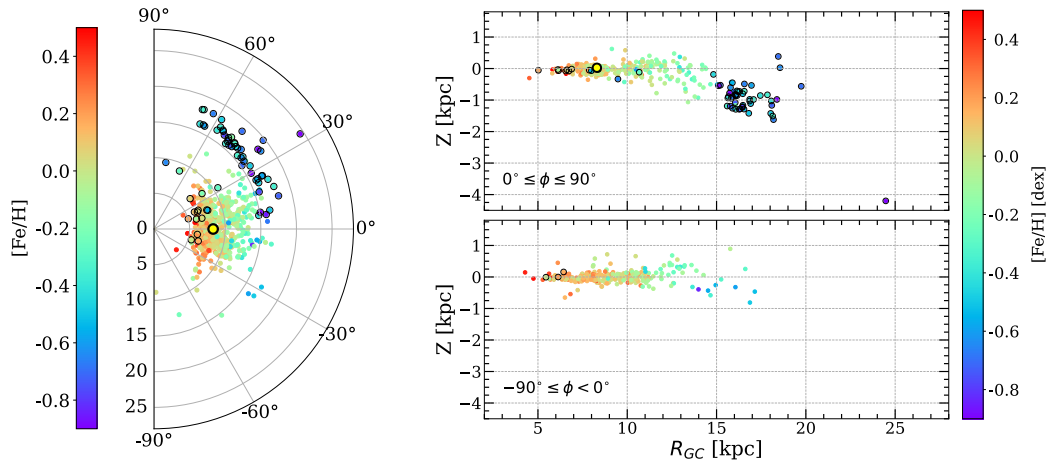


Figure 2.7: Left panel: polar representation (the radial coordinate is R_{GC}) of the 637 Galactic DCEPs with metallicity from high-resolution spectroscopy (see Sect. 2.4). The colour is coded according to the measured iron abundance. The stars presented in this work are identified by additional black circles. The position of the sun is shown with a yellow-black symbol. Right panel: Cartesian representation of the height above or below the galactic plane as a function of R_{GC} in two opposite directions with respect to the Galactic centre-Sun line (top and bottom panels, respectively). The colour coding and the symbols are as in the left panel.

significantly the range in R_{GC} over which it is now possible to investigate the metallicity disc gradient, reaching up to 18-20 kpc. It is noticeable the presence of the star ASAS J062939-1840.5 with $[Fe/H]=-1.10\pm 0.19$ dex, which is perfectly placed at the ideal extension of the metallicity disc gradient at 25 kpc.

We carried out a linear regression adopting the *python LtsFit* package (Cappellari et al. [Cap+13]). This software allows one to use weights on both axes and implement a robust outlier removal. We adopted a conservative 3σ clipping procedure, obtaining the $[Fe/H]-R_{GC}$ relation. At a first glance, it appears that the fitting line does not represent well the data at low values of $[Fe/H]$. This could be due to the non-uniform sampling of the data. For this reason we operated a binning division of the entire sample in 12 intervals of around 1.33 kpc and subsequently estimated the coefficients of the $[Fe/H]-R_{GC}$ relation. In the right panel of Fig. 2.6 we highlight the binned points and the relative fitting line. Furthermore, different regimes might be identified in this diagram. Following the suggestion made by Genovali et al. [Gen+14], it could be possible to distinguish an inner and an outer sample, with a break at about 9.25 kpc. The extension at

lower metallicities presented in this work allows us to better verify this early proposal. Therefore, we decided to quantitatively estimate the metallicity radial gradient in an alternative way, that is dividing the sample into two sub-samples separated at $R_{GC}=9.25$ kpc. We applied this division to both the data and the binning points. All the coefficients are listed at the beginning of Table 2.3. For each relation we estimated the root means square (rms) as a test of the goodness of the fit. The first three relations are over-imposed on the data on the left panel in Fig. 2.6, the last three, corresponding to the fitted relation on the binned points, are plotted on the right panel of the same figure. We point out that in both cases the inner and

Table 2.4: Coefficients of the linear fit of the form $[X/H] = \alpha_{rgc} \times R_{gc} + \beta_{rgc}$ with relative dispersion relative to Fig 2.8.

Element	α_{rgc} (dex kpc ⁻¹)	β_{rgc} (dex)	rms (dex)
C	-0.068±0.002	0.371±0.023	0.14
O	-0.046±0.002	0.414±0.022	0.12
Na	-0.060±0.002	0.901±0.022	0.15
Mg	-0.056±0.002	0.588±0.024	0.17
Al	-0.045±0.002	0.538±0.022	0.14
Si	-0.053±0.002	0.640±0.022	0.10
S	-0.060±0.002	0.618±0.023	0.15
Ca	-0.057±0.002	0.564±0.022	0.13
Sc	-0.045±0.003	0.731±0.028	0.20
Ti	-0.046±0.002	0.543±0.022	0.14
V	-0.028±0.002	0.341±0.023	0.16
Cr	-0.049±0.002	0.577±0.022	0.14
Mn	-0.061±0.002	0.436±0.025	0.17
Co	-0.020±0.003	0.363±0.027	0.18
Ni	-0.055±0.002	0.479±0.022	0.11
Cu	-0.041±0.003	0.497±0.034	0.23
Zn	-0.084±0.003	0.669±0.031	0.21
Y	-0.040±0.002	0.562±0.021	0.14
Zr	-0.012±0.003	0.474±0.036	0.25
Ba	-0.051±0.007	0.636±0.087	0.38
La	-0.029±0.002	0.421±0.021	0.15
Pr	-0.010±0.004	-0.157±0.046	0.19
Nd	-0.026±0.002	0.247±0.021	0.14

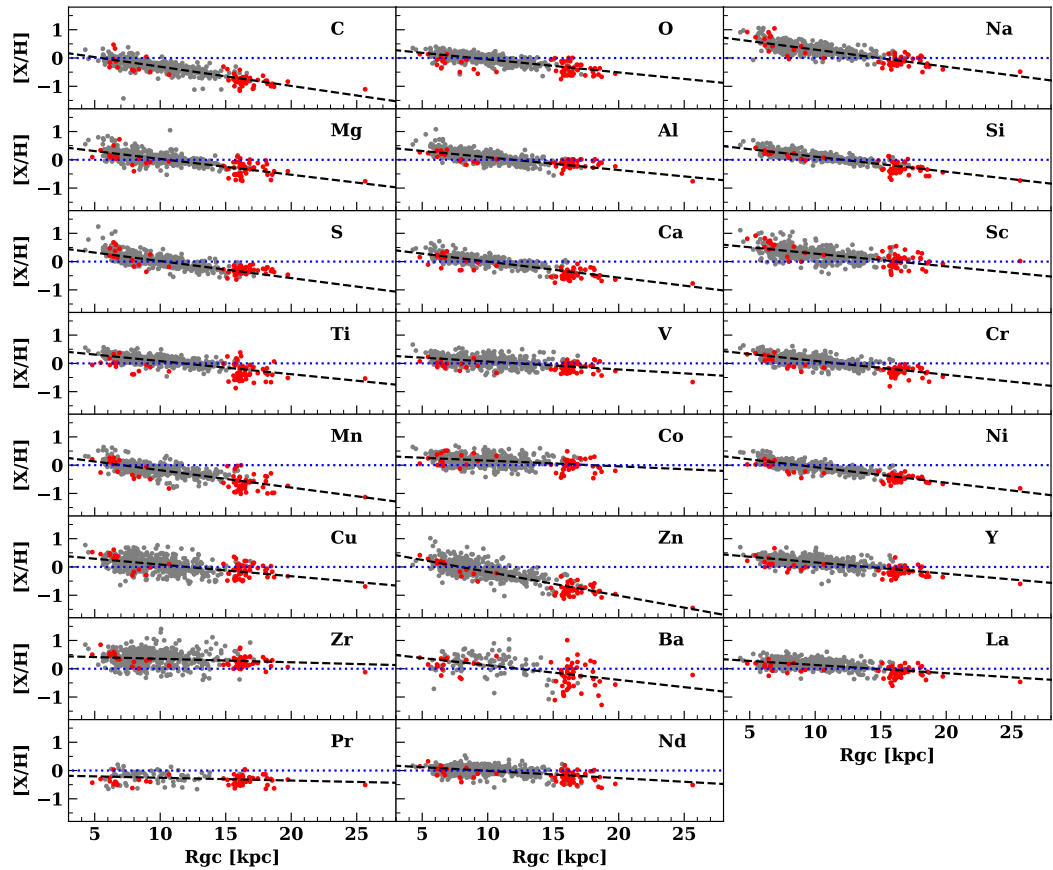


Figure 2.8: Galactic gradient for all the estimated abundances for our sample of stars (in red) and the literature stars (in gray, see section 2.4). The black dashed line represents the linear fit computed using both literature and our stars, while the dotted blue horizontal line highlights the solar abundance. The coefficients of the fits are listed in Table 2.4.

outer slopes differ at more than 1σ . The two-samples fits appear to reproduce well both the data and the binned point distributions. This occurrence suggests that the break in the Galactic disc metallicity gradient is plausible, but since the rms are comparable with that of the single line fit, for both the data and the binned points, we can conclude that a single line fit can certainly reproduce the data, but the hypothesis of the break cannot be ruled out on the basis of the present data sample.

It is instructive to inspect the location on the Galactic disc of the sample adopted for the analysis of the metallicity gradient. This is shown in the left panel of Fig. 2.7, where we show the location of both literature and our samples in polar

coordinates. The metal gradient is qualitatively visible also in this representation, and it is noticeable how our outer sample nicely traces a spiral arm of the MW disc, which we identify as the Outer arm (see e.g. Minniti et al. [Min+21]). The scatter of iron abundance at this location is of the order of 0.4 dex which is not surprising, as we sampled the Outer arm for more than 15 kpc. The right panel of Fig. 2.7 shows the height above/below the Galactic disc (Z coordinate of the Galactocentric Cartesian representation) as a function of R_{GC} . The sample was divided according to the positive (top panel) or negative (bottom panel) values of the polar angle ϕ . The presence of the disc warp (see e.g. Skowron et al. [Sko+19]) can be clearly seen, especially in the top panel, where our outer sample is present. Indeed, in the panel many objects have $Z < -0.5$ kpc for $R_{GC} > 15$ kpc, while in the bottom panel, in the same region there are very few stars. The lower visibility of the warp for negative values of ϕ could be due to the fact that this direction is closer to the line of nodes of the warped disc structure (see fig. 2 in Skowron et al. [Sko+19]). Also noticeable is the extreme negative height below the Galactic plane of ASAS J062939-1840.5, which appears however in line with the bending of the disc. The same figure exhibits a small but noticeable difference in the metallicity distribution between the upper and lower panels, that is at positive and negative azimuthal angles, respectively. Indeed, for $\phi > 0$ it seems that the iron abundance decreases more steeply than for $\phi < 0$, especially at $R_{GC} > 8-10$ kpc which could tentatively be associated with the previously mentioned break in the radial gradient visible in Fig. 2.6.

The relation between DCEPs metal abundance and Galactocentric radius can be investigated for elements other than iron. We noted hints of the same break at $R_{GC}=9.25$ kpc that was suggested for the iron in several elements of his group, especially in V, Cr, Mn and Ni. However, the two-lines fits for these elements were not convincing, so that we only report single line fits for these and all elements other than iron. The result of this procedure is shown in Fig. 2.8 and Table 2.4.

2.6 Discussion

2.6.1 Iron abundance disc gradient

Several works focused their attention on the radial gradient of the MW disc, using as tracers either DCEPs or other objects such as OCs, groups of stars that formed at the same time from the same material and therefore have similar distances from the sun as well as the same chemical composition and kinematics. They have been used to study Galactic chemical trends since Janes [Jan79] where it has been shown how

they could be treated as tracers of the Galactic iron gradient. Furthermore, OCs span a wide range of ages, from Myr to Gyr, making them optimal tools for Galactic evolution studies as well. Since DCEPs are young stars (spanning approximately the age range between 20 and 500 Myr) we compared, when possible, results from OCs studies that split their sample into different age intervals.

Some estimates for the metal gradient of the Galactic disc, based on both DCEPs and OCs studies are listed in Table 2.3, and compared graphically with our work in Fig. 2.9, showing the results only relative to the data and not to the binned points, since they are comparable within the errors.

We point out that most of the previous gradient estimations come from objects with distances up to $\approx 10\text{-}15$ kpc, so for the following discussion we took in consideration, except when specified, the gradients from the whole sample and the "inner" slope ($R_{GC} < 9.25\text{kpc}$) from the two-fit case. In more detail:

- Genovali et al. [Gen+14] estimated two slopes, first considering UVES, NARVAL and FEROS spectra only and then including also the literature data. The slope obtained in the second case is steeper than the first and in good agreement with our results for both single and two-fit lines (when considering our "inner" slope). Although the same agreement was found with Luck and Lambert [LL11] and Silva et al. [Sil+22], other recent studies (Lemasle et al. [Lem+18], Luck [Luc18], and Ripepi et al. [Rip+22]) estimated flatter slopes, but comparable within 2σ . It is interesting the method used by Lemasle et al. [Lem+18], where the metallicity of Galactic F/10⁶ DCEPs was estimated from the P_1/P_0 ratio. The low number of stars used should increase in future Gaia releases.
- Cunha et al. [Cun+16], studying APOGEE OCs, found a generally flatter slope than those provided by our and other literature DCEPs studies. It is worth mentioning the presence in Cunha et al. [Cun+16]'s work of an object distant 25 kpc. Following the possible break at about 10-12 kpc hypothesized for OCs as well (see e.g. Frinchaboy et al. [Fri+13], Magrini et al. [Mag+10], and Yong et al. [YCF12]), the sample was divided into an inner region, where the slope of the gradient is as steep as ours, and a flatter outer slope (not shown in Fig. 2.9), in contrast with the results obtained using the DCEPs as tracers. Moreover, fitting only young clusters (age < 500 Myr) resulted in a very low slope, which is in complete disagreement with all DCEPs results. But, since this result is based on only 7 OCs, it has a very limited statistical value.

6 F/10 indicates DCEPs pulsating simultaneously in the fundamental and first overtone mode.

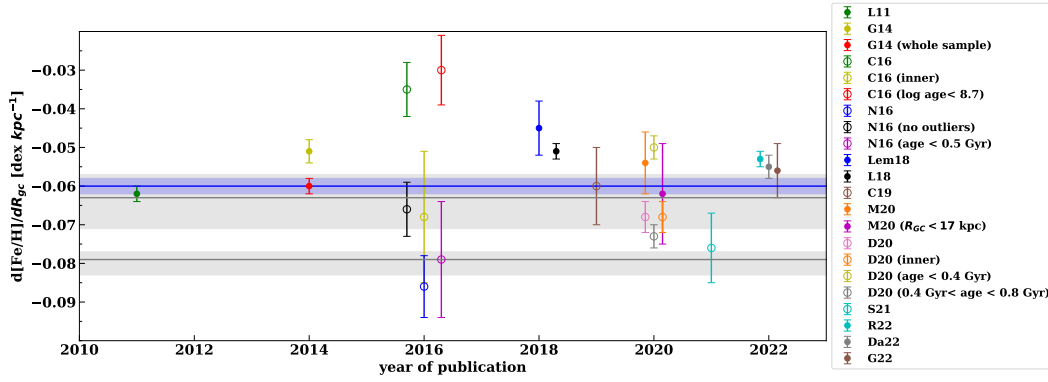


Figure 2.9: Radial gradient comparison between our work and previous ones listed in Table 2.3. Open circles symbols represent results from OCs works, filled circles symbols from DCEPs ones. Colors for different works (or same work but different sample configuration) are described in detail in the legend on the right, with reference acronyms the same as Table 2.3. Results are plotted in order of year publication on the x-axis. In order to avoid overlapping, results from the same work have been slightly shifted on the x-axis. Blue and gray horizontal lines represent the results in our work in the case of one and two-line fitting on the data, while shaded regions correspond to the 1σ dispersion around the respective results.

- Netopil et al. [Net+16] studied the iron gradient using about 100 OCs in the MW disc. They estimated the gradient in different ways, subdividing their sample according to the R_{GC} or age (see Table 2.3). Using all the OCs within 12 kpc they found a slope significantly steeper than ours both using the whole sample and for $R_{GC} < 9.25$ kpc. The same is true for the comparison with the other literature DCEPs results. The agreement with all DCEPs results improves when Netopil et al. [Net+16] exclude outliers from the calculation. Similarly to Cunha et al. [Cun+16], and at odds with DCEPs results, also Netopil et al. [Net+16] found that the iron gradient flattens for $R_{GC} > 12$ kpc. However, this result is based on only 12 objects and it should be verified with a more consistent sample. Finally, Netopil et al. [Net+16] divided their sample into three different age bins. Considering the sample with age < 0.5 Myr, that is the age range spanned by DCEPs, they find a steep slope, similar to what we find for $R_{GC} > 9.25$ kpc, but in complete disagreement with Cunha et al. [Cun+16] in the same OCs age range. This occurrence seems to suggest that the results based on young OCs are still significantly sample dependent.
- Casamiquela et al. [Cas+19] investigated the Galactic gradient using new high-

resolution spectroscopy for 18 OCs which complemented with a compilation of data by Carrera et al. [Car+19], finding a present-day gradient for the youngest clusters (having $R_{GC} < 13$ kpc) in good agreement with our results for the whole and the inner DCEPs samples.

- Studying OCs from SDSS/APOGEE DR16, Donor et al. [Don+20] fitted the data using a two-fit line, obtaining a break at R_{GC} 13.9 kpc, after which the slope is comparable with a null one, thus confirming the results by Cunha et al. [Cun+16] and Netopil et al. [Net+16], but at variance with ours. However, again this result is based on only a few OCs, which in addition are much older than the typical DCEPs and thus could have migrated from other disc regions, thus not being representative of the present-day iron gradient. As for previous studies involving OCs, the sample was divided in 4 bins of age. The results found for ages lower than 0.4 Gyr and between 0.4 and 0.8 Gyrs are sensitively different from each other, but both in agreement with our inner slope within 2σ .
- On the far side of the MW, beyond the bulge, Minniti et al. [Min+20] characterized 30 DCEPs using near-infrared VVV photometry, and estimated two different slopes using either the whole sample or DCEPs with $R_{GC} \leq 17$ kpc. Both values are in agreement with our inner slope.
- Spina et al. [Spi+21], used OCs data from the APOGEE and GALAH surveys to estimate the iron gradient up to $R_{GC} \sim 13.9$ kpc, obtaining a slope steeper than ours, but still in agreement within 1σ with our "inner" slope and 2σ with the whole sample slope.
- It is worth mentioning two last papers: Gaia Collaboration et al. [Gai+22] based on the *Gaia*DR3 results and Randich et al. [Ran+22], which review the outcomes of the *Gaia*ESO survey (GES). In the former, the radial metallicity gradient was estimated for 503 open clusters. Splitting the sample in 4 groups depending on ages, they found a flattening of the gradient slope going toward larger ages (see their sect. 8 for more details). In Table 2.3 and Fig. 2.9 we report the radial gradient result obtained by Gaia Collaboration et al. [Gai+22] with the whole OC sample, which is in good agreement with our outcome. Randich et al. [Ran+22] presented an overview of the GES survey results for the Galactic OCs, comprising a study of the radial gradient. They confirm the flattening of the slope at higher distances, but again the gradient greatly depends on the age of the adopted clusters (see their fig. 26).

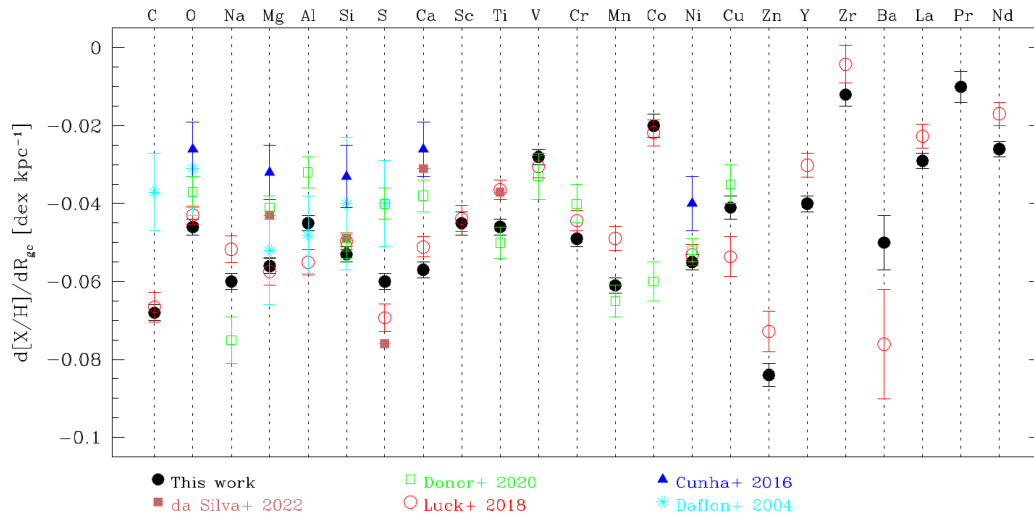


Figure 2.10: Radial gradients for each chemical species inferred in this study compared with literature.

2.6.2 Disc gradient for elements other than iron

In this section we summarize and discuss gradients inferred from the other elements shown in Fig. 2.8 and compare our results with other studies. In Fig. 2.10 we compare gradients derived in this study with results obtained by different authors using different tracers, for instance OCs (Cunha et al. [Cun+16] and Donor et al. [Don+20]), B-type stars (Daflon and Cunha [DC04]), and DCEPs (Luck [Luc18] and Silva et al. [Sil+22]). To be comparable with our results, since DCEPs are young objects, we selected from Donor et al. [Don+20] only clusters younger than 0.4 Gyr.

For light elements such as carbon our results are consistent with Luck [Luc18] while Daflon and Cunha [DC04] analysing a sample of B-type stars found a lower value. This perhaps could be due to the evolution in DCEPs, that alters the abundance of carbon in non homogeneous ways after the first dredge-up. For oxygen, our gradient is consistent with all the determinations found in literature, even when B-type stars are used as tracers as in Daflon and Cunha [DC04]. This is not surprising since oxygen abundance in DCEPs does not alter during the first dredge-up. As for carbon, sodium abundance is altered by evolution in DCEPs via the Na-Ne cycle (Sasselov [Sas86]), so our gradient is consistent with Luck [Luc18]’s value while Donor et al. [Don+20] found a steeper gradient.

Gradients for α -elements derived in this paper are consistent at least within 2σ with other studies, an exception is sulfur for which results from open cluster

and B-type stars are not consistent with those from DCEPs. For the other light elements, namely aluminum and scandium, results from various sources are in good agreement.

With the exception of cobalt, our gradients for iron-peak elements are consistent with the literature. For cobalt, Donor et al. [Don+20] found a steeper slope.

Also for heavy elements ($Z > 30$) our slopes are in agreement with the literature, at least at 2σ level.

2.7 Summary

In the context of the C-MetaLL project, we presented high-resolution UVES@VLT spectra for a sample of 65 DCEPs mostly located in the outskirts of the MW disc, at Galactocentric distances larger than 15 kpc. We analysed the observed spectra in detail to derive the main parameters for each target, such as effective temperature, surface gravity, microturbulence and radial velocity. It is worth noticing that we have carried out the effective temperature estimate using two different procedures: by adopting the LDR method and by minimizing the correlation between the abundance and the excitation potential. The two different approaches provided consistent results.

On this basis, we have derived the chemical abundances of 24 species for which we have detected and measured spectral lines. Studying their distribution we showed how they are sensibly under abundant with respect to the sun, except for Sc, Co and Zr, having nonetheless (as for the other elements) a mean abundance lower than the literature one.

Our sample includes objects in the range $-1.1 < [\text{Fe}/\text{H}] < +0.3$ dex, but the majority of the stars have iron abundances lower than about -0.3 dex, constituting the most metal-poor DCEPs ever studied with high-resolution spectroscopy and extending the metallicity range of the MW DCEPs even below the metallicity of the Small Magellanic Cloud (SMC) DCEPs (see Romaniello et al. [Rom+08]). We analyzed all the chemical abundances as a function of iron. All of them either decrease or remain constant as iron increases, with the only exception of Zn that shows a positive trend.

We complemented our sample with recent literature results to obtain a data-set including 637 confirmed DCEPs with individual metallicities from high-resolution spectroscopy. For all these objects, we adopted *Gaia* EDR3 photometry and the iron abundance to calculate accurate distances based on the PWZ relation in the *Gaia* bands by using the same method as in Ripepi et al. [Rip+22]. The resulting spatial distribution of our outer sample clearly depicts the shape of a spiral arm

extending for about 60 deg in azimuth at approximately constant Galactocentric distance between 16-18 kpc. Based on the comparison with Minniti et al. [Min+21] disc model, we identify this spiral arm as the Outer.

The distribution of DCEPs in height below/above the Galactic disc plane reveals a larger scatter for $\phi > 0$ and $R_{GC} > 10$ kpc while the disc warp starts to be visible at $R_{GC} > 10$ kpc. Our data allows us to conclude that the disc continues to bend with the same slope also between 15-18 kpc and possibly up to 25 kpc, even if we have only one star at this distance and no one between 20 and 25 kpc. On the other hand, for $\phi < 0$ the warp is barely visible, but we do not have enough data beyond $R_{GC} > 13$ kpc, so that no firm conclusion can be driven. Also the metallicity distribution appears different moving from negative to positive ϕ values as in the latter the iron abundance seems to be more metal poor at fixed R_{GC} values for R_{GC} larger than ~ 12 kpc.

We studied the iron abundance Galactic radial gradient, which can now be studied up to 20 kpc from the Galactic centre. The analysis of the data plausibly revealed the presence of an already suggested break in the distribution around 9.25 kpc which led us to divide the DCEP data-set into inner and outer samples. A linear fit to the two samples allows us to estimate two different slopes: -0.063 ± 0.007 and -0.079 ± 0.003 dex kpc^{-1} for the inner and outer samples, respectively. The two slopes are different at more than 1σ . A fit to the entire sample provides instead a slope of -0.060 ± 0.002 dex kpc^{-1} , which is in very good agreement with previous literature determinations of the gradient using DCEPs, all conducted without any separation in the sample. Since the rms are comparable, we conclude that the hypothesis of the presence of the break cannot be ruled out. Future works with a more homogeneous and extended sample will allow us to further test the plausibility of the presence of such a break.

We also carried out a detailed comparison between our results and the radial metallicity gradients estimated using the OCs. As a result we found good agreement between the inner slope and most of the previous works. On the other hand, our outer slope reflects a steeper trend, opposite to what is found for OCs for which, in general, the relation becomes almost flat. However, if we restrict the comparison to OCs young enough to have not undergone a significant migration, we find a good agreement with the work by Netopil et al. [Net+16] for OCs with $\text{Age} < 0.5$ Gyr and Donor et al. [Don+20] for OCs with $0.4 < \text{Age} < 0.8$ Gyr. A good agreement for the outer slope is also found with the work by Spina et al. [Spi+21] which does not show any slope difference with the age of the investigated OCs.

Finally, we studied Galactic radial gradients for the elements other than iron. Our gradients are consistent with the literature.

Acknowledgements

We thank the Referee for her/his helpful and insight comments, which helped to improve the manuscript. This work has made use of data from the European Space Agency (ESA) mission Gaia (<https://www.cosmos.esa.int/gaia>), processed by the Gaia Data Processing and Analysis Consortium ⁷. Funding for the DPAC has been provided by national institutions, in particular the institutions participating in the Gaia Multilateral Agreement. In particular, the Italian participation in DPAC has been supported by Istituto Nazionale di Astrofisica (INAF) and the Agenzia Spaziale Italiana (ASI) through grants I/037/08/0, I/058/10/0, 2014-025-R.0, and 2014-025-R.1.2015 to INAF (PI: M.G. Lattanzi). This research has made use of the SIMBAD database, operated at CDS, Strasbourg, France.

Data Availability

The only proprietary data used in this paper are represented by the UVES spectra. They are freely retrievable from the ESO archive also in the fully reduced and calibrated form. Any additional data request can be directed to the corresponding author (E. Trentin).

2.A Abundances for target stars

In this appendix we present the complete list of the chemical abundances for the 24 species detected in our stars.

⁷ DPAC, <https://www.cosmos.esa.int/web/gaia/dpac/consortium>

Table 2.5: Abundances expressed in solar terms for the chemical elements detected in our targets. In the first part of the table elements from C to Ca are shown.

Star	[C/H]	[O/H]	[Na/H]	[Mg/H]	[Al/H]	[Si/H]	[S/H]	[Ca/H]
ASAS J060450+1021.9	-0.83 ± 0.05	-0.61 ± 0.16	-0.07 ± 0.04	-0.40 ± 0.16	-0.17 ± 0.15	-0.44 ± 0.15	-0.41 ± 0.03	-0.46 ± 0.07
ASAS J062939-1840.5	-1.10 ± 0.10	—	-0.48 ± 0.19	-0.76 ± 0.11	-0.76 ± 0.15	-0.73 ± 0.20	—	-0.77 ± 0.14
ASAS J064001-0754.8	-0.99 ± 0.05	-0.49 ± 0.16	-0.22 ± 0.04	-0.52 ± 0.16	-0.48 ± 0.15	-0.40 ± 0.20	-0.36 ± 0.03	-0.51 ± 0.04
ASAS J065758-1521.4	-0.70 ± 0.05	-0.42 ± 0.16	-0.06 ± 0.04	-0.33 ± 0.16	-0.20 ± 0.15	-0.32 ± 0.09	-0.25 ± 0.03	-0.46 ± 0.11
ASAS J074401-3008.4	-0.79 ± 0.05	-0.45 ± 0.16	-0.20 ± 0.04	-0.65 ± 0.16	-0.23 ± 0.15	-0.32 ± 0.11	-0.38 ± 0.03	-0.53 ± 0.04
ASAS J074925-3814.4	—	-0.61 ± 0.16	-0.11 ± 0.07	-0.15 ± 0.16	-0.17 ± 0.15	-0.22 ± 0.05	-0.28 ± 0.03	-0.50 ± 0.05
ASAS J084127-4353.6	-0.59 ± 0.05	-0.49 ± 0.16	-0.00 ± 0.04	-0.05 ± 0.16	0.02 ± 0.15	0.08 ± 0.06	-0.18 ± 0.03	-0.15 ± 0.04
ASAS J164120-4739.6	—	0.14 ± 0.16	0.92 ± 0.05	0.10 ± 0.16	0.27 ± 0.15	—	—	0.16 ± 0.05
ASAS SN-J061713.86+022837.1	-0.97 ± 0.10	-0.24 ± 0.53	-0.29 ± 0.10	-0.27 ± 0.35	0.02 ± 0.03	-0.54 ± 0.05	-0.29 ± 0.03	-0.59 ± 0.19
ASAS SN-J063841.36-034927.7	-0.63 ± 0.05	-0.36 ± 0.16	0.00 ± 0.04	-0.24 ± 0.16	—	-0.26 ± 0.15	-0.25 ± 0.03	-0.20 ± 0.04
ASAS SN-J072739.70-252241.1	-0.72 ± 0.05	-0.36 ± 0.16	-0.10 ± 0.04	-0.46 ± 0.16	-0.10 ± 0.15	-0.25 ± 0.12	-0.29 ± 0.15	-0.34 ± 0.04
ASAS SN-J074354.86-323013.7	-0.42 ± 0.12	—	0.01 ± 0.04	-0.27 ± 0.16	—	-0.17 ± 0.12	-0.17 ± 0.03	-0.59 ± 0.15
ASAS SN-J091822.17-542444.5	—	-0.64 ± 0.16	0.08 ± 0.04	-0.02 ± 0.16	-0.28 ± 0.15	-0.25 ± 0.09	-0.43 ± 0.03	-0.23 ± 0.04
ATLAS J102.7978-10.2541	-0.78 ± 0.05	-0.61 ± 0.16	-0.03 ± 0.04	-0.11 ± 0.16	-0.23 ± 0.15	-0.29 ± 0.15	-0.31 ± 0.03	-0.29 ± 0.05
ATLAS J106.7120-14.0234	-0.77 ± 0.20	-0.08 ± 0.15	-0.11 ± 0.07	0.05 ± 0.10	—	-0.36 ± 0.18	-0.32 ± 0.22	-0.47 ± 0.11
ATLAS J113.8534-31.0749	-0.82 ± 0.05	-0.36 ± 0.16	-0.22 ± 0.04	-0.52 ± 0.16	-0.10 ± 0.15	-0.38 ± 0.17	-0.47 ± 0.03	-0.45 ± 0.04
BQ Vel	-0.79 ± 0.10	-0.24 ± 0.16	-0.12 ± 0.04	-0.11 ± 0.16	-0.23 ± 0.15	-0.07 ± 0.09	-0.35 ± 0.15	-0.42 ± 0.07
GDS J133950.2-634049	-0.33 ± 0.05	-0.17 ± 0.16	0.42 ± 0.05	0.10 ± 0.16	0.18 ± 0.15	0.26 ± 0.13	0.14 ± 0.03	0.13 ± 0.04
OGLE GD-CEP-0029	-0.30 ± 0.21	-0.05 ± 0.16	-0.14 ± 0.04	-0.21 ± 0.16	-0.10 ± 0.15	-0.02 ± 0.05	-0.27 ± 0.03	-0.54 ± 0.07
OGLE GD-CEP-0089	-0.81 ± 0.05	-0.36 ± 0.16	-0.18 ± 0.04	-0.52 ± 0.16	-0.23 ± 0.15	-0.38 ± 0.17	-0.31 ± 0.03	-0.39 ± 0.04
OGLE GD-CEP-0120	-0.83 ± 0.16	-0.55 ± 0.16	-0.40 ± 0.04	-0.40 ± 0.16	-0.23 ± 0.15	-0.44 ± 0.10	-0.47 ± 0.03	-0.64 ± 0.12
OGLE GD-CEP-0123	-0.91 ± 0.09	-0.36 ± 0.16	-0.20 ± 0.04	-0.52 ± 0.16	-0.10 ± 0.15	-0.34 ± 0.09	-0.28 ± 0.03	-0.49 ± 0.04
OGLE GD-CEP-0127	-0.76 ± 0.06	-0.74 ± 0.16	0.15 ± 0.04	-0.08 ± 0.16	-0.12 ± 0.15	0.13 ± 0.20	-0.29 ± 0.03	-0.21 ± 0.04
OGLE GD-CEP-0134	-0.66 ± 0.06	-0.11 ± 0.16	-0.25 ± 0.04	-0.52 ± 0.16	-0.11 ± 0.15	-0.32 ± 0.15	-0.25 ± 0.03	-0.59 ± 0.04
OGLE GD-CEP-0156	-0.89 ± 0.05	-0.55 ± 0.16	-0.22 ± 0.04	-0.48 ± 0.16	-0.23 ± 0.15	-0.38 ± 0.09	-0.44 ± 0.03	-0.57 ± 0.04
OGLE GD-CEP-0159	-0.86 ± 0.07	0.01 ± 0.16	-0.14 ± 0.04	-0.24 ± 0.16	-0.04 ± 0.15	-0.37 ± 0.04	-0.33 ± 0.03	-0.34 ± 0.15
OGLE GD-CEP-0162	-0.85 ± 0.05	-0.61 ± 0.16	-0.19 ± 0.04	-0.52 ± 0.16	-0.10 ± 0.15	-0.47 ± 0.18	-0.42 ± 0.03	-0.43 ± 0.04
OGLE GD-CEP-0168	-0.68 ± 0.06	-0.11 ± 0.16	-0.08 ± 0.04	-0.21 ± 0.16	-0.10 ± 0.15	-0.07 ± 0.16	-0.22 ± 0.03	-0.48 ± 0.17
OGLE GD-CEP-0176	-0.85 ± 0.05	-0.61 ± 0.16	-0.25 ± 0.04	-0.71 ± 0.16	-0.35 ± 0.15	-0.47 ± 0.10	-0.42 ± 0.15	-0.55 ± 0.04
OGLE GD-CEP-0179	-0.66 ± 0.06	-0.36 ± 0.16	0.04 ± 0.04	-0.33 ± 0.16	0.02 ± 0.15	-0.27 ± 0.14	-0.19 ± 0.03	-0.21 ± 0.04
OGLE GD-CEP-0181	-1.00 ± 0.05	-0.49 ± 0.16	-0.27 ± 0.04	-0.74 ± 0.16	-0.29 ± 0.15	-0.27 ± 0.14	-0.41 ± 0.03	-0.68 ± 0.14
OGLE GD-CEP-0185	-0.88 ± 0.05	—	-0.13 ± 0.04	-0.33 ± 0.16	-0.10 ± 0.15	-0.32 ± 0.11	-0.33 ± 0.03	-0.40 ± 0.04
OGLE GD-CEP-0186	-0.74 ± 0.07	-0.24 ± 0.16	0.21 ± 0.05	0.01 ± 0.16	-0.04 ± 0.15	-0.07 ± 0.19	-0.13 ± 0.03	-0.08 ± 0.04
OGLE GD-CEP-0196	-0.85 ± 0.07	-0.30 ± 0.16	-0.25 ± 0.04	-0.55 ± 0.16	-0.23 ± 0.15	-0.27 ± 0.15	-0.25 ± 0.04	-0.54 ± 0.04
OGLE GD-CEP-0206	-0.55 ± 0.05	-0.11 ± 0.16	-0.08 ± 0.04	-0.27 ± 0.16	-0.10 ± 0.15	0.13 ± 0.13	-0.14 ± 0.03	-0.30 ± 0.04
OGLE GD-CEP-0213	-0.89 ± 0.21	0.01 ± 0.15	-0.24 ± 0.06	-0.67 ± 0.04	-0.10 ± 0.10	-0.47 ± 0.17	-0.42 ± 0.03	-0.61 ± 0.07
OGLE GD-CEP-0214	-1.00 ± 0.05	-0.58 ± 0.16	-0.30 ± 0.04	-0.71 ± 0.16	-0.17 ± 0.15	-0.57 ± 0.13	-0.34 ± 0.03	-0.57 ± 0.04
OGLE GD-CEP-0224	-0.72 ± 0.12	—	-0.19 ± 0.06	0.12 ± 0.16	—	-0.07 ± 0.15	-0.23 ± 0.07	-0.38 ± 0.14
OGLE GD-CEP-0228	-0.81 ± 0.05	-0.49 ± 0.16	-0.10 ± 0.04	-0.36 ± 0.16	-0.04 ± 0.15	-0.38 ± 0.11	-0.28 ± 0.03	-0.47 ± 0.08
OGLE GD-CEP-0247	-1.09 ± 0.05	-0.24 ± 0.16	0.12 ± 0.04	-0.33 ± 0.16	0.02 ± 0.15	0.03 ± 0.18	-0.10 ± 0.03	-0.25 ± 0.05
OGLE GD-CEP-0252	-0.71 ± 0.05	-0.49 ± 0.16	-0.05 ± 0.04	-0.27 ± 0.16	0.02 ± 0.15	-0.29 ± 0.06	-0.28 ± 0.03	-0.39 ± 0.08
OGLE GD-CEP-0271	-0.91 ± 0.16	-0.36 ± 0.16	-0.50 ± 0.11	-0.52 ± 0.16	0.02 ± 0.15	-0.27 ± 0.20	-0.20 ± 0.06	-0.51 ± 0.04
OGLE GD-CEP-0316	-0.80 ± 0.07	-0.61 ± 0.16	0.04 ± 0.04	-0.15 ± 0.16	—	-0.28 ± 0.12	-0.21 ± 0.03	-0.29 ± 0.04
OGLE GD-CEP-0342	-1.15 ± 0.05	-0.36 ± 0.16	0.18 ± 0.04	-0.27 ± 0.16	-0.04 ± 0.15	-0.17 ± 0.11	-0.27 ± 0.03	-0.35 ± 0.04
OGLE GD-CEP-0348	-0.92 ± 0.05	-0.36 ± 0.16	-0.24 ± 0.04	-0.71 ± 0.16	0.02 ± 0.15	-0.32 ± 0.20	-0.13 ± 0.06	-0.44 ± 0.05
OGLE GD-CEP-0353	-1.09 ± 0.14	-0.36 ± 0.16	0.10 ± 0.04	-0.05 ± 0.16	-0.10 ± 0.15	-0.07 ± 0.04	-0.25 ± 0.03	-0.29 ± 0.05
OGLE GD-CEP-0516	-0.45 ± 0.05	-0.14 ± 0.16	-0.04 ± 0.04	-0.40 ± 0.16	0.02 ± 0.15	0.08 ± 0.11	-0.17 ± 0.03	-0.30 ± 0.11
OGLE GD-CEP-0568	-0.40 ± 0.46	-0.05 ± 0.16	0.29 ± 0.04	0.04 ± 0.16	-0.17 ± 0.15	0.23 ± 0.15	-0.11 ± 0.03	0.01 ± 0.05
OGLE GD-CEP-0575	-0.41 ± 0.16	-0.49 ± 0.16	0.07 ± 0.04	-0.18 ± 0.16	-0.04 ± 0.15	0.18 ± 0.13	0.04 ± 0.03	-0.31 ± 0.04
OGLE GD-CEP-0889	0.05 ± 0.20	-0.39 ± 0.06	0.41 ± 0.14	-0.11 ± 0.11	-0.07 ± 0.10	0.03 ± 0.06	-0.36 ± 0.03	-0.30 ± 0.17
OGLE GD-CEP-0974	0.34 ± 0.16	-0.11 ± 0.16	0.74 ± 0.05	0.10 ± 0.16	0.24 ± 0.15	0.23 ± 0.30	0.37 ± 0.03	0.32 ± 0.12
OGLE GD-CEP-0996	—	0.14 ± 0.16	1.05 ± 0.08	0.73 ± 0.16	0.36 ± 0.15	—	0.45 ± 0.03	0.36 ± 0.04
OGLE GD-CEP-1012	-0.16 ± 0.16	-0.05 ± 0.16	0.45 ± 0.04	0.10 ± 0.16	0.11 ± 0.15	0.33 ± 0.20	0.47 ± 0.04	0.23 ± 0.05
OGLE GD-CEP-1111	-0.03 ± 0.19	-0.36 ± 0.16	0.24 ± 0.08	0.51 ± 1.02	0.21 ± 0.10	0.24 ± 0.09	0.18 ± 0.13	-0.23 ± 0.08
OGLE GD-CEP-1210	—	0.14 ± 0.16	0.73 ± 0.04	0.34 ± 0.16	0.24 ± 0.15	0.43 ± 0.30	—	-0.10 ± 0.04
OGLE GD-CEP-1285	-0.39 ± 0.14	-0.00 ± 0.21	-0.36 ± 0.05	-0.32 ± 0.10	-0.10 ± 0.10	-0.35 ± 0.09	-0.59 ± 0.18	-0.74 ± 0.12
OGLE GD-CEP-1311	-0.75 ± 0.16	-0.61 ± 0.16	-0.14 ± 0.04	-0.11 ± 0.16	-0.10 ± 0.15	-0.27 ± 0.05	-0.24 ± 0.03	-0.41 ± 0.07
OGLE GD-CEP-1337	-1.01 ± 0.05	-0.66 ± 0.29	-0.30 ± 0.06	-0.40 ± 0.44	-0.10 ± 0.18	-0.57 ± 0.10	-0.37 ± 0.03	-0.68 ± 0.15
V1253 Cen	-0.50 ± 0.05	-0.55 ± 0.16	0.18 ± 0.04	-0.08 ± 0.16	-0.10 ± 0.15	-0.02 ± 0.17	0.25 ± 0.03	-0.03 ± 0.04
V1819 Ori	-0.60 ± 0.27	-0.17 ± 0.10	-0.25 ± 0.11	-0.51 ± 0.14	-0.02 ± 0.19	-0.62 ± 0.14	-0.48 ± 0.09	-0.60 ± 0.13
V418 CMa	-0.78 ± 0.16	-0.30 ± 0.16	-0.10 ± 0.04	-0.58 ± 0.16	-0.02 ± 0.15	-0.27 ± 0.11	-0.37 ± 0.03	-0.66 ± 0.12
V459 Sct	-0.32 ± 0.05	-0.24 ± 0.16	0.68 ± 0.05	0.17 ± 0.16	0.33 ± 0.15	0.22 ± 0.08	0.21 ± 0.03	0.19 ± 0.04
V480 Aql	0.47 ± 0.06	0.08 ± 0.16	0.91 ± 0.04	0.10 ± 0.16	0.33 ± 0.15	0.21 ± 0.05	0.68 ± 0.04	0.14 ± 0.04
V881 Cen	-0.12 ± 0.07	-0.05 ± 0.16	0.76 ± 0.04	0.04 ± 0.16	0.24 ± 0.15	0.23 ± 0.20	0.59 ± 0.03	0.24 ± 0.11
VX CMa	—	-0.49 ± 0.05	-0.40 ± 0.16	-0.07 ± 0.77	-0.10 ± 0.10	-0.70 ± 0.20	-0.63 ± 0.22	-0.61 ± 0.10

Table 2.5: Second part of the table, with chemical elements from Sc to Ni.

Star	[Sc/H]	[Ti/H]	[V/H]	[Cr/H]	[Mn/H]	[Fe/H]	[Co/H]	[Ni/H]
ASAS J060450+1021.9	0.05 ± 0.04	-0.41 ± 0.07	-0.03 ± 0.08	-0.05 ± 0.05	-0.80 ± 0.04	-0.50 ± 0.18	-0.11 ± 0.14	-0.47 ± 0.16
ASAS J062939-1840.5	0.02 ± 0.11	-0.53 ± 0.16	-0.66 ± 0.18	—	-1.13 ± 0.07	-1.10 ± 0.19	—	-0.82 ± 0.14
ASAS J064001-0754.8	-0.15 ± 0.04	-0.58 ± 0.17	-0.10 ± 0.08	-0.34 ± 0.05	-0.95 ± 0.16	-0.76 ± 0.12	-0.35 ± 0.16	-0.57 ± 0.16
ASAS J065758-1521.4	0.11 ± 0.04	-0.37 ± 0.11	-0.02 ± 0.08	-0.16 ± 0.04	-0.58 ± 0.55	-0.48 ± 0.11	0.01 ± 0.16	-0.47 ± 0.16
ASAS J074401-3008.4	-0.20 ± 0.04	-0.64 ± 0.15	-0.17 ± 0.08	-0.22 ± 0.05	-0.76 ± 0.16	-0.70 ± 0.15	-0.28 ± 0.17	-0.66 ± 0.16
ASAS J074925-814.4	0.19 ± 0.04	-0.38 ± 0.12	-0.27 ± 0.08	-0.34 ± 0.18	-0.68 ± 0.58	-0.58 ± 0.10	0.07 ± 0.10	-0.47 ± 0.16
ASAS J084127-4353.6	0.23 ± 0.04	-0.28 ± 0.21	-0.34 ± 0.09	-0.15 ± 0.18	-0.83 ± 0.08	-0.28 ± 0.16	0.33 ± 0.17	-0.28 ± 0.16
ASAS J164120-4739.6	0.81 ± 0.05	-0.05 ± 0.14	0.07 ± 0.09	0.32 ± 0.18	0.21 ± 0.16	0.18 ± 0.19	0.06 ± 0.16	0.03 ± 0.16
ASAS SN-J061713.86+022837.1	-0.33 ± 0.14	-0.69 ± 0.08	-0.30 ± 0.18	-0.60 ± 0.07	-0.32 ± 0.16	-0.72 ± 0.16	—	-0.38 ± 0.14
ASAS SN-J063841.36-034927.7	0.33 ± 0.04	-0.20 ± 0.19	-0.09 ± 0.08	-0.09 ± 0.06	-0.78 ± 0.05	-0.35 ± 0.14	0.26 ± 0.11	-0.44 ± 0.16
ASAS SN-J072739.70-252241.1	0.05 ± 0.04	-0.34 ± 0.13	0.02 ± 0.09	-0.16 ± 0.09	-0.89 ± 0.05	-0.48 ± 0.16	—	-0.53 ± 0.16
ASAS SN-J074354.86-323013.7	0.08 ± 0.04	-0.15 ± 0.17	0.13 ± 0.09	-0.20 ± 0.19	-0.74 ± 0.04	-0.43 ± 0.18	0.49 ± 0.14	-0.60 ± 0.16
ASAS SN-J091822.17-542444.5	0.10 ± 0.04	-0.65 ± 0.09	-0.38 ± 0.08	-0.19 ± 0.05	-0.57 ± 0.42	-0.40 ± 0.14	-0.46 ± 0.15	-0.47 ± 0.16
ATLAS J102.7978-10.2541	0.14 ± 0.04	-0.34 ± 0.13	-0.09 ± 0.09	-0.19 ± 0.05	-0.92 ± 0.05	-0.41 ± 0.16	0.22 ± 0.20	-0.38 ± 0.16
ATLAS J106.7120-14.0234	-0.18 ± 0.11	0.39 ± 0.09	0.04 ± 0.12	-0.52 ± 0.18	—	-0.58 ± 0.12	—	-0.35 ± 0.16
ATLAS J113.8534-31.0749	-0.13 ± 0.04	-0.57 ± 0.12	-0.11 ± 0.09	-0.41 ± 0.05	-0.70 ± 0.16	-0.66 ± 0.14	-0.38 ± 0.09	-0.41 ± 0.16
BQ Vel	0.14 ± 0.04	-0.40 ± 0.13	-0.35 ± 0.09	-0.34 ± 0.05	-0.61 ± 0.52	-0.50 ± 0.16	-0.05 ± 0.16	-0.47 ± 0.16
GDS J133950.2-634049	0.47 ± 0.04	0.03 ± 0.19	-0.16 ± 0.08	0.11 ± 0.10	-0.23 ± 0.04	0.05 ± 0.14	0.51 ± 0.49	0.03 ± 0.16
OGLE GD-CEP-0029	0.12 ± 0.09	-0.01 ± 0.15	-0.21 ± 0.08	-0.18 ± 0.14	-0.62 ± 0.04	-0.44 ± 0.16	0.02 ± 0.18	-0.22 ± 0.16
OGLE GD-CEP-0089	0.03 ± 0.04	-0.35 ± 0.16	-0.28 ± 0.08	-0.26 ± 0.13	-0.56 ± 0.47	-0.54 ± 0.16	-0.04 ± 0.13	-0.47 ± 0.16
OGLE GD-CEP-0120	-0.08 ± 0.04	-0.51 ± 0.16	-0.27 ± 0.12	-0.47 ± 0.09	-0.73 ± 0.42	-0.69 ± 0.13	-0.20 ± 0.17	-0.66 ± 0.16
OGLE GD-CEP-0123	-0.06 ± 0.04	-0.40 ± 0.13	0.07 ± 0.08	-0.31 ± 0.09	-0.98 ± 0.05	-0.63 ± 0.13	-0.10 ± 0.19	-0.60 ± 0.16
OGLE GD-CEP-0127	0.19 ± 0.04	-0.43 ± 0.17	-0.37 ± 0.08	-0.18 ± 0.04	-0.40 ± 0.39	-0.34 ± 0.12	-0.44 ± 0.11	-0.47 ± 0.16
OGLE GD-CEP-0134	-0.39 ± 0.04	-0.01 ± 0.18	0.01 ± 0.10	-0.23 ± 0.05	-0.95 ± 0.10	-0.62 ± 0.16	—	-0.41 ± 0.16
OGLE GD-CEP-0156	-0.34 ± 0.04	-0.55 ± 0.21	-0.29 ± 0.09	-0.28 ± 0.07	-0.96 ± 0.04	-0.65 ± 0.11	0.12 ± 0.17	-0.60 ± 0.16
OGLE GD-CEP-0159	0.12 ± 0.04	-0.32 ± 0.14	0.03 ± 0.10	-0.28 ± 0.04	-0.72 ± 0.10	-0.51 ± 0.13	0.16 ± 0.17	-0.47 ± 0.16
OGLE GD-CEP-0162	-0.18 ± 0.04	-0.48 ± 0.19	-0.21 ± 0.08	-0.38 ± 0.14	-0.90 ± 0.06	-0.62 ± 0.10	0.20 ± 0.12	-0.50 ± 0.16
OGLE GD-CEP-0168	0.04 ± 0.04	-0.09 ± 0.17	0.00 ± 0.08	-0.21 ± 0.09	-0.79 ± 0.04	-0.42 ± 0.11	0.15 ± 0.18	-0.34 ± 0.16
OGLE GD-CEP-0176	-0.32 ± 0.04	-0.87 ± 0.11	-0.26 ± 0.08	-0.34 ± 0.09	-0.54 ± 0.55	-0.74 ± 0.16	-0.15 ± 0.14	-0.72 ± 0.16
OGLE GD-CEP-0179	0.06 ± 0.04	-0.17 ± 0.16	-0.04 ± 0.08	-0.15 ± 0.09	-0.64 ± 0.04	-0.32 ± 0.20	—	-0.28 ± 0.16
OGLE GD-CEP-0181	-0.23 ± 0.04	-0.61 ± 0.18	-0.33 ± 0.08	-0.28 ± 0.05	-0.73 ± 0.69	-0.74 ± 0.14	0.01 ± 0.15	-0.60 ± 0.16
OGLE GD-CEP-0185	-0.04 ± 0.04	-0.44 ± 0.17	-0.16 ± 0.08	-0.25 ± 0.05	-0.53 ± 0.41	-0.54 ± 0.17	-0.11 ± 0.17	-0.50 ± 0.16
OGLE GD-CEP-0186	0.42 ± 0.04	-0.05 ± 0.13	0.06 ± 0.08	-0.03 ± 0.35	-0.59 ± 0.04	-0.16 ± 0.14	0.04 ± 0.17	-0.22 ± 0.16
OGLE GD-CEP-0196	-0.19 ± 0.04	-0.62 ± 0.18	-0.36 ± 0.09	-0.45 ± 0.05	-0.82 ± 0.04	-0.73 ± 0.15	0.15 ± 0.13	-0.60 ± 0.16
OGLE GD-CEP-0206	0.15 ± 0.04	-0.02 ± 0.17	-0.16 ± 0.09	-0.18 ± 0.19	-0.61 ± 0.04	-0.37 ± 0.18	—	-0.34 ± 0.16
OGLE GD-CEP-0213	0.55 ± 0.07	0.26 ± 0.17	-0.27 ± 0.21	-0.33 ± 0.14	-0.00 ± 0.19	-0.78 ± 0.16	0.07 ± 0.13	-0.45 ± 0.15
OGLE GD-CEP-0214	-0.35 ± 0.04	-0.66 ± 0.20	-0.25 ± 0.15	-0.34 ± 0.07	-0.29 ± 0.34	-0.69 ± 0.16	-0.07 ± 0.17	-0.60 ± 0.16
OGLE GD-CEP-0224	-0.05 ± 0.07	0.14 ± 0.16	-0.13 ± 0.15	-0.22 ± 0.18	-0.02 ± 0.10	-0.51 ± 0.13	—	-0.27 ± 0.08
OGLE GD-CEP-0228	0.12 ± 0.04	-0.33 ± 0.15	-0.08 ± 0.08	-0.17 ± 0.05	-0.39 ± 0.35	-0.47 ± 0.16	-0.04 ± 0.17	-0.47 ± 0.16
OGLE GD-CEP-0247	0.03 ± 0.04	-0.13 ± 0.18	-0.07 ± 0.08	-0.18 ± 0.11	-0.57 ± 0.04	-0.36 ± 0.15	0.24 ± 0.17	-0.41 ± 0.16
OGLE GD-CEP-0252	0.13 ± 0.04	-0.18 ± 0.17	-0.12 ± 0.08	-0.11 ± 0.08	-0.82 ± 0.08	-0.39 ± 0.13	—	-0.38 ± 0.16
OGLE GD-CEP-0271	-0.27 ± 0.04	-0.39 ± 0.16	0.11 ± 0.08	-0.52 ± 0.04	-1.00 ± 0.05	-0.66 ± 0.15	-0.29 ± 0.20	-0.47 ± 0.16
OGLE GD-CEP-0316	0.29 ± 0.04	-0.17 ± 0.14	0.14 ± 0.08	-0.18 ± 0.04	-0.40 ± 0.42	-0.33 ± 0.12	0.30 ± 0.15	-0.41 ± 0.16
OGLE GD-CEP-0342	-0.11 ± 0.06	-0.45 ± 0.12	-0.34 ± 0.08	-0.29 ± 0.05	-0.93 ± 0.08	-0.59 ± 0.11	0.18 ± 0.18	-0.53 ± 0.16
OGLE GD-CEP-0348	-0.22 ± 0.04	-0.54 ± 0.19	-0.34 ± 0.08	-0.42 ± 0.18	-1.02 ± 0.04	-0.63 ± 0.12	0.12 ± 0.17	-0.53 ± 0.16
OGLE GD-CEP-0353	0.25 ± 0.04	-0.22 ± 0.20	-0.20 ± 0.08	-0.14 ± 0.05	-0.41 ± 0.33	-0.41 ± 0.13	0.07 ± 0.17	-0.41 ± 0.16
OGLE GD-CEP-0516	0.00 ± 0.04	-0.39 ± 0.21	-0.02 ± 0.11	-0.08 ± 0.05	-0.48 ± 0.10	-0.54 ± 0.16	0.35 ± 0.15	-0.32 ± 0.16
OGLE GD-CEP-0568	0.53 ± 0.04	-0.27 ± 0.19	-0.14 ± 0.08	-0.12 ± 0.27	-0.41 ± 0.06	-0.20 ± 0.16	0.02 ± 0.13	-0.25 ± 0.16
OGLE GD-CEP-0575	0.17 ± 0.04	-0.38 ± 0.19	-0.26 ± 0.09	-0.18 ± 1.06	-0.35 ± 0.22	-0.37 ± 0.15	-0.12 ± 0.16	-0.22 ± 0.16
OGLE GD-CEP-0889	-0.00 ± 0.16	-0.05 ± 0.14	0.18 ± 0.11	-0.30 ± 0.27	-0.05 ± 0.05	-0.64 ± 0.18	0.43 ± 0.10	-0.45 ± 0.19
OGLE GD-CEP-0974	0.74 ± 0.04	0.02 ± 0.17	-0.05 ± 0.09	0.23 ± 0.35	0.11 ± 0.04	0.15 ± 0.14	0.11 ± 0.17	-0.03 ± 0.16
OGLE GD-CEP-0996	0.59 ± 0.04	0.38 ± 0.15	-0.01 ± 0.08	0.39 ± 0.10	0.18 ± 0.06	0.28 ± 0.18	0.51 ± 0.17	0.17 ± 0.16
OGLE GD-CEP-1012	0.83 ± 0.05	-0.05 ± 0.19	-0.13 ± 0.11	0.10 ± 0.05	0.26 ± 0.16	0.12 ± 0.16	0.01 ± 0.13	0.03 ± 0.16
OGLE GD-CEP-1111	0.43 ± 0.09	0.33 ± 0.15	0.02 ± 0.19	0.15 ± 0.16	0.27 ± 0.15	-0.09 ± 0.12	0.43 ± 0.18	0.15 ± 0.11
OGLE GD-CEP-1210	0.92 ± 0.04	0.03 ± 0.14	0.23 ± 0.08	0.36 ± 0.18	-0.26 ± 0.10	-0.00 ± 0.20	0.24 ± 0.17	0.03 ± 0.16
OGLE GD-CEP-1285	0.37 ± 0.11	0.25 ± 0.17	-0.23 ± 0.11	—	-0.03 ± 0.19	-1.07 ± 0.17	—	-0.59 ± 0.19
OGLE GD-CEP-1311	0.11 ± 0.04	-0.44 ± 0.12	-0.09 ± 0.08	-0.32 ± 0.05	-0.56 ± 0.45	-0.47 ± 0.10	-0.03 ± 0.17	-0.41 ± 0.16
OGLE GD-CEP-1337	0.00 ± 0.06	0.07 ± 0.14	-0.43 ± 0.14	-0.65 ± 0.07	-0.98 ± 0.20	-0.93 ± 0.17	-0.23 ± 0.16	-0.62 ± 0.14
V1253 Cen	0.31 ± 0.04	-0.13 ± 0.20	-0.08 ± 0.09	-0.06 ± 0.05	-0.50 ± 0.04	-0.26 ± 0.14	0.15 ± 0.20	-0.22 ± 0.16
V1819 Ori	0.50 ± 0.05	-0.07 ± 0.19	-0.17 ± 0.21	-0.81 ± 0.27	-0.13 ± 0.19	-0.85 ± 0.15	-0.30 ± 0.17	-0.49 ± 0.11
V418 CMa	-0.07 ± 0.04	-0.42 ± 0.15	-0.23 ± 0.10	-0.41 ± 0.19	-0.74 ± 0.69	-0.64 ± 0.13	-0.16 ± 0.17	-0.56 ± 0.16
V459 Sct	0.51 ± 0.04	0.18 ± 0.17	0.02 ± 0.08	0.30 ± 0.04	0.11 ± 0.11	0.22 ± 0.16	0.38 ± 0.18	0.22 ± 0.16
V480 Aql	0.70 ± 0.04	0.03 ± 0.19	0.15 ± 0.09	0.27 ± 0.35	0.11 ± 0.08	0.17 ± 0.16	0.15 ± 0.17	-0.03 ± 0.16
V881 Cen	0.64 ± 0.04	-0.11 ± 0.18	-0.09 ± 0.09	0.19 ± 0.18	0.04 ± 0.10	0.07 ± 0.11	-0.02 ± 0.17	0.09 ± 0.16
VX CMa	-0.46 ± 0.06	0.18 ± 0.13	-0.34 ± 0.14	-0.50 ± 0.13	-0.04 ± 0.04	-0.92 ± 0.17	-0.14 ± 0.21	-0.44 ± 0.14

Table 2.5: Third part of the table. Abundances for chemical elements from Cu to Nd.

Star	[Cu/H]	[Zn/H]	[Y/H]	[Zr/H]	[Ba/H]	[La/H]	[Pr/H]	[Nd/H]
ASAS J060450+1021.9	0.01 ± 0.05	-0.80 ± 0.16	-0.04 ± 0.04	0.43 ± 0.16	-0.18 ± 0.14	-0.09 ± 0.04	0.04 ± 0.16	-0.08 ± 0.05
ASAS J062939-1840.5	-0.69 ± 0.06	-1.45 ± 0.11	-0.60 ± 0.04	-0.12 ± 0.10	-0.22 ± 0.14	-0.47 ± 0.04	-0.51 ± 0.17	-0.51 ± 0.05
ASAS J064001-0754.8	-0.42 ± 0.07	-0.99 ± 0.16	-0.27 ± 0.04	0.33 ± 0.16	-0.21 ± 0.18	-0.32 ± 0.05	-0.33 ± 0.16	-0.44 ± 0.05
ASAS J065758-1521.4	-0.12 ± 0.08	-0.93 ± 0.16	-0.04 ± 0.04	0.42 ± 0.16	0.24 ± 0.14	-0.01 ± 0.04	-0.39 ± 0.16	-0.15 ± 0.05
ASAS J074401-3008.4	-0.23 ± 0.04	-0.91 ± 0.16	-0.23 ± 0.04	0.14 ± 0.16	-0.44 ± 0.13	-0.35 ± 0.04	-0.51 ± 0.16	-0.38 ± 0.04
ASAS J074925-3814.4	-0.47 ± 0.34	-0.46 ± 0.16	-0.16 ± 0.06	0.15 ± 0.16	0.08 ± 0.09	-0.09 ± 0.04	-0.22 ± 0.16	-0.43 ± 0.54
ASAS J084127-4353.6	0.10 ± 0.04	-0.21 ± 0.16	0.09 ± 0.04	0.11 ± 0.16	0.45 ± 0.10	-0.05 ± 0.04	-0.14 ± 0.16	-0.11 ± 0.06
ASAS J164120-4739.6	0.53 ± 0.20	0.42 ± 0.16	0.22 ± 0.06	0.50 ± 0.16	0.39 ± 0.10	0.19 ± 0.13	-0.43 ± 0.16	0.15 ± 0.05
ASAS SN-J061713.86+022837.1	0.15 ± 0.16	-0.90 ± 0.11	-0.20 ± 0.04	0.21 ± 0.04	-0.88 ± 0.10	0.05 ± 0.04	—	-0.38 ± 0.11
ASAS SN-J063841.36-034927.7	0.04 ± 0.06	-0.63 ± 0.16	0.08 ± 0.04	0.41 ± 0.16	0.28 ± 0.14	0.20 ± 0.04	-0.13 ± 0.16	-0.02 ± 0.12
ASAS SN-J072739.70-252241.1	-0.01 ± 0.09	-0.83 ± 0.16	0.00 ± 0.05	0.41 ± 0.16	0.05 ± 0.09	-0.04 ± 0.04	-0.20 ± 0.16	0.00 ± 0.05
ASAS SN-J074354.86-323013.7	0.08 ± 0.25	-0.71 ± 0.16	—	0.70 ± 0.16	1.01 ± 0.09	—	—	—
ASAS SN-J091822.17-542444.5	-0.21 ± 0.11	-0.87 ± 0.16	-0.27 ± 0.06	-0.11 ± 0.16	-0.36 ± 0.15	-0.19 ± 0.06	-0.64 ± 0.16	-0.27 ± 0.04
ATLAS J102.7978-10.2541	-0.04 ± 0.06	-0.73 ± 0.16	-0.15 ± 0.04	0.20 ± 0.16	0.14 ± 0.15	-0.05 ± 0.04	-0.28 ± 0.16	-0.12 ± 0.04
ATLAS J106.7120-14.0234	-0.10 ± 0.10	-0.52 ± 0.11	0.34 ± 0.11	0.74 ± 0.12	0.33 ± 0.11	-0.18 ± 0.05	-0.53 ± 0.40	0.03 ± 0.12
ATLAS J113.8534-31.0749	-0.35 ± 0.16	-0.99 ± 0.16	-0.25 ± 0.05	0.33 ± 0.16	-0.27 ± 0.14	-0.18 ± 0.04	—	-0.50 ± 0.07
BQ Vel	-0.38 ± 0.09	-0.85 ± 0.16	-0.22 ± 0.04	0.13 ± 0.16	0.04 ± 0.11	-0.14 ± 0.04	-0.24 ± 0.16	-0.52 ± 0.48
GDS J133950.2-634049	0.38 ± 0.05	0.10 ± 0.16	0.10 ± 0.04	0.34 ± 0.16	0.33 ± 0.19	-0.07 ± 0.04	-0.51 ± 0.16	-0.16 ± 0.07
OGLE GD-CEP-0029	0.11 ± 0.04	-0.74 ± 0.16	-0.12 ± 0.10	0.14 ± 0.16	0.23 ± 0.13	-0.07 ± 0.06	-0.28 ± 0.16	-0.18 ± 0.08
OGLE GD-CEP-0089	-0.04 ± 0.05	-0.85 ± 0.16	-0.07 ± 0.04	0.17 ± 0.16	-0.29 ± 0.11	-0.08 ± 0.04	-0.26 ± 0.16	-0.08 ± 0.04
OGLE GD-CEP-0120	-0.33 ± 0.06	-0.96 ± 0.16	-0.36 ± 0.04	0.06 ± 0.16	-0.56 ± 0.10	-0.27 ± 0.04	-0.32 ± 0.16	-0.47 ± 0.05
OGLE GD-CEP-0123	-0.17 ± 0.04	-0.85 ± 0.16	-0.21 ± 0.04	0.30 ± 0.16	-0.45 ± 0.10	-0.11 ± 0.05	-0.35 ± 0.16	-0.23 ± 0.04
OGLE GD-CEP-0127	-0.10 ± 0.32	-0.33 ± 0.16	-0.20 ± 0.08	0.00 ± 0.16	-0.05 ± 0.14	0.05 ± 0.06	-0.49 ± 0.16	-0.00 ± 0.04
OGLE GD-CEP-0134	0.30 ± 0.04	-0.90 ± 0.16	-0.20 ± 0.09	0.27 ± 0.16	-0.92 ± 0.13	-0.21 ± 0.10	—	-0.13 ± 0.06
OGLE GD-CEP-0156	-0.17 ± 0.06	-1.05 ± 0.16	-0.19 ± 0.06	0.15 ± 0.16	-0.61 ± 0.14	-0.32 ± 0.07	-0.39 ± 0.16	-0.42 ± 0.05
OGLE GD-CEP-0159	-0.13 ± 0.08	-0.83 ± 0.16	-0.08 ± 0.04	0.22 ± 0.16	-0.02 ± 0.10	-0.01 ± 0.04	-0.39 ± 0.16	-0.28 ± 0.32
OGLE GD-CEP-0162	-0.09 ± 0.04	-0.85 ± 0.16	-0.26 ± 0.04	0.15 ± 0.16	-0.46 ± 0.14	-0.61 ± 0.07	-0.51 ± 0.16	-0.18 ± 0.05
OGLE GD-CEP-0168	0.05 ± 0.05	-0.83 ± 0.16	-0.10 ± 0.04	0.35 ± 0.16	-0.19 ± 0.17	-0.07 ± 0.05	-0.51 ± 0.16	-0.49 ± 0.49
OGLE GD-CEP-0176	-0.34 ± 0.04	-1.01 ± 0.16	-0.27 ± 0.04	0.05 ± 0.16	-0.83 ± 0.15	-0.49 ± 0.04	-0.45 ± 0.16	-0.44 ± 0.05
OGLE GD-CEP-0179	0.21 ± 0.05	-0.77 ± 0.16	-0.04 ± 0.04	0.40 ± 0.16	-0.11 ± 0.09	0.10 ± 0.05	-0.38 ± 0.16	-0.14 ± 0.09
OGLE GD-CEP-0181	-0.50 ± 0.06	-1.05 ± 0.16	-0.32 ± 0.04	0.05 ± 0.16	-0.63 ± 0.14	-0.30 ± 0.04	-0.15 ± 0.16	-0.48 ± 0.04
OGLE GD-CEP-0185	-0.29 ± 0.07	-0.82 ± 0.16	-0.23 ± 0.04	0.13 ± 0.16	-0.32 ± 0.10	-0.20 ± 0.04	-0.36 ± 0.16	-0.30 ± 0.11
OGLE GD-CEP-0186	0.00 ± 0.10	-0.46 ± 0.16	0.05 ± 0.04	0.43 ± 0.16	0.50 ± 0.11	0.20 ± 0.04	-0.26 ± 0.16	0.03 ± 0.06
OGLE GD-CEP-0196	-0.26 ± 0.04	-0.90 ± 0.16	-0.36 ± 0.04	0.00 ± 0.16	-0.75 ± 0.10	-0.34 ± 0.04	-0.22 ± 0.16	-0.33 ± 0.04
OGLE GD-CEP-0206	0.36 ± 0.04	-0.71 ± 0.16	0.05 ± 0.04	0.38 ± 0.16	-0.11 ± 0.11	0.05 ± 0.04	-0.13 ± 0.16	0.04 ± 0.05
OGLE GD-CEP-0213	-0.22 ± 0.06	-1.01 ± 0.11	-0.32 ± 0.05	0.11 ± 1.06	-0.53 ± 0.16	-0.21 ± 0.15	-0.42 ± 0.16	-0.03 ± 0.14
OGLE GD-CEP-0214	0.03 ± 0.04	-0.87 ± 0.16	-0.35 ± 0.04	0.09 ± 0.16	-0.95 ± 0.10	-0.40 ± 0.12	-0.30 ± 0.16	-0.57 ± 0.06
OGLE GD-CEP-0224	0.08 ± 0.12	-0.76 ± 0.11	-0.15 ± 0.04	0.21 ± 0.14	-0.44 ± 0.16	0.10 ± 0.11	-0.20 ± 0.16	0.19 ± 0.11
OGLE GD-CEP-0228	-0.12 ± 0.06	-0.71 ± 0.16	-0.04 ± 0.04	0.32 ± 0.16	-0.10 ± 0.11	0.04 ± 0.04	-0.13 ± 0.16	-0.01 ± 0.04
OGLE GD-CEP-0247	0.10 ± 0.05	-0.71 ± 0.16	-0.10 ± 0.04	0.18 ± 0.16	-0.27 ± 0.11	-0.11 ± 0.04	-0.26 ± 0.16	-0.24 ± 0.04
OGLE GD-CEP-0252	0.21 ± 0.05	-0.58 ± 0.16	0.04 ± 0.04	0.38 ± 0.16	0.20 ± 0.09	0.09 ± 0.04	0.02 ± 0.16	-0.30 ± 0.66
OGLE GD-CEP-0271	-0.36 ± 0.06	-0.96 ± 0.16	-0.30 ± 0.05	0.27 ± 0.16	-0.58 ± 0.13	-0.23 ± 0.07	-0.51 ± 0.16	-0.34 ± 0.06
OGLE GD-CEP-0316	-0.06 ± 0.15	-0.58 ± 0.16	0.01 ± 0.04	0.29 ± 0.16	0.23 ± 0.12	0.09 ± 0.04	-0.26 ± 0.16	0.02 ± 0.05
OGLE GD-CEP-0342	-0.23 ± 0.06	-0.93 ± 0.16	-0.30 ± 0.05	0.04 ± 0.16	-0.15 ± 0.16	-0.40 ± 0.04	-0.49 ± 0.16	-0.31 ± 0.04
OGLE GD-CEP-0348	-0.20 ± 0.07	-0.93 ± 0.16	-0.42 ± 0.04	-0.01 ± 0.16	-0.69 ± 0.35	-0.34 ± 0.05	-0.24 ± 0.16	-0.34 ± 0.04
OGLE GD-CEP-0353	-0.20 ± 0.08	-0.65 ± 0.16	-0.15 ± 0.04	0.25 ± 0.16	-0.08 ± 0.09	-0.03 ± 0.04	-0.38 ± 0.16	-0.17 ± 0.08
OGLE GD-CEP-0516	-0.18 ± 0.05	-0.33 ± 0.16	-0.07 ± 0.04	0.24 ± 0.16	-0.36 ± 0.12	0.17 ± 0.05	—	-0.41 ± 0.04
OGLE GD-CEP-0568	-0.09 ± 0.28	-0.09 ± 0.16	0.06 ± 0.04	0.01 ± 0.16	0.30 ± 0.14	0.20 ± 0.07	-0.33 ± 0.16	0.09 ± 0.04
OGLE GD-CEP-0575	-0.30 ± 0.05	-0.16 ± 0.16	-0.19 ± 0.04	0.07 ± 0.16	-0.31 ± 0.09	-0.15 ± 0.04	-0.62 ± 0.16	-0.25 ± 0.04
OGLE GD-CEP-0889	-0.29 ± 0.35	-0.24 ± 0.11	-0.11 ± 0.12	0.29 ± 0.09	0.18 ± 0.20	-0.09 ± 0.14	—	-0.24 ± 0.16
OGLE GD-CEP-0974	0.40 ± 0.07	0.17 ± 0.16	0.08 ± 0.05	0.51 ± 0.16	-0.02 ± 0.12	0.08 ± 0.08	-0.40 ± 0.16	-0.02 ± 0.05
OGLE GD-CEP-0996	—	—	0.66 ± 0.16	0.33 ± 0.16	0.37 ± 0.45	—	—	0.05 ± 0.16
OGLE GD-CEP-1012	0.43 ± 0.19	0.13 ± 0.16	0.00 ± 0.09	0.46 ± 0.16	0.08 ± 0.19	0.15 ± 0.11	-0.38 ± 0.16	0.06 ± 0.07
OGLE GD-CEP-1111	0.61 ± 0.08	—	0.09 ± 0.09	0.59 ± 0.27	-0.24 ± 0.41	-0.25 ± 0.07	0.03 ± 0.16	0.17 ± 0.17
OGLE GD-CEP-1210	0.46 ± 0.12	0.29 ± 0.16	0.41 ± 0.19	0.85 ± 0.16	0.15 ± 0.17	0.19 ± 0.09	-0.30 ± 0.16	0.33 ± 0.05
OGLE GD-CEP-1285	-0.48 ± 0.12	-1.01 ± 0.11	-0.44 ± 0.11	0.17 ± 0.11	-1.11 ± 0.16	0.20 ± 0.04	—	-0.25 ± 0.17
OGLE GD-CEP-1311	-0.44 ± 0.36	-0.77 ± 0.16	-0.25 ± 0.04	0.15 ± 0.16	0.08 ± 0.11	-0.13 ± 0.04	-0.51 ± 0.16	-0.29 ± 0.04
OGLE GD-CEP-1337	-0.36 ± 0.12	-1.08 ± 0.11	-0.34 ± 0.11	—	-1.28 ± 0.11	-0.13 ± 0.15	-0.63 ± 0.16	-0.61 ± 0.16
V1253 Cen	-0.01 ± 0.07	-0.51 ± 0.16	0.00 ± 0.06	0.33 ± 0.16	0.17 ± 0.11	-0.04 ± 0.04	-0.40 ± 0.16	-0.11 ± 0.04
V1819 Ori	-0.48 ± 0.05	-1.02 ± 0.11	-0.22 ± 0.31	—	-0.61 ± 0.19	-0.29 ± 0.33	-0.63 ± 0.16	-0.22 ± 0.15
V418 CMa	-0.21 ± 0.06	-0.85 ± 0.16	-0.33 ± 0.04	0.10 ± 0.16	-0.33 ± 0.11	-0.23 ± 0.04	-0.24 ± 0.16	-0.27 ± 0.04
V459 Sct	0.49 ± 0.08	0.23 ± 0.16	0.17 ± 0.04	0.54 ± 0.16	0.15 ± 0.13	0.06 ± 0.04	-0.26 ± 0.16	-0.17 ± 0.10
V480 Aql	0.30 ± 0.25	0.20 ± 0.16	0.32 ± 0.10	0.53 ± 0.16	0.36 ± 0.09	0.34 ± 0.05	-0.48 ± 0.16	0.15 ± 0.04
V881 Cen	0.30 ± 0.09	0.17 ± 0.16	0.10 ± 0.05	0.39 ± 0.16	0.14 ± 0.12	0.14 ± 0.08	-0.41 ± 0.16	-0.08 ± 0.04
VX CMa	-0.45 ± 0.18	-1.12 ± 0.11	-0.47 ± 0.11	0.08 ± 0.40	-0.96 ± 0.17	-0.50 ± 0.06	-0.48 ± 0.16	-0.33 ± 0.13

3

Cepheid Metallicity in the Leavitt Law (C-MetaLL) survey: IV. The metallicity dependence of Cepheid period-luminosity relations

E. Trentin, V. Ripepi, R. Molinaro, G. Catanzaro, J. Storm, G. De Somma, M. Marconi, A. Bhardwaj, M. Gatto, V. Testa, I. Musella, G. Clementini, S. Leccia

This paper was published in A&A, Volume 681, id.A65, 20 pp.

3.1 Introduction

Classical Cepheids (DCEPs) are the most important standard candles of the extragalactic distance scale thanks to the Leavitt Law (Leavitt and Pickering [LP12]), which is a relationship between period and luminosity (PL) of DCEPs. Once calibrated using independent distances based on geometric methods such as trigonometric parallaxes, eclipsing binaries, and water masers, these relations constitute the first step in forming the cosmic distance scale, as they calibrate secondary distance indicators. These latter include Type Ia supernovae (SNIa), which in turn allow us to measure the distances of distant galaxies located in the steady Hubble flow. The calibration of this three-step procedure (also called the cosmic distance ladder) allows us to reach the Hubble flow, where the constant (the Hubble constant H_0) that connects the distance to the recession velocity of galaxies can be estimated (e.g. Freedman et al. [Fre+12], Riess et al. [Rie+16], and Sandage and Tammann [ST06] and references therein). The value of H_0 is an important quantity in cosmology because it sets the dimension and the age of the Universe. Therefore, measuring the value of the constant with an accuracy of 1% is one of the most important quests of modern astrophysics. However, there is currently a well-known discrepancy between the values of H_0 obtained by the SH0ES⁸ project through the cosmic distance ladder ($H_0 = 73.01 \pm 0.99 \text{ km s}^{-1} \text{ Mpc}^{-1}$, Riess et al. [Rie+22b]) and those measured by the Planck Cosmic Microwave Background (CMB) project using the flat Λ Cold Dark Matter (Λ CDM) model ($H_0 = 67.4 \pm 0.5 \text{ km s}^{-1} \text{ Mpc}^{-1}$, Planck Collaboration et al. [Pla+20]). No solution has yet been proposed for this 5σ discrepancy, and if confirmed, it would highlight the need for a revision of the Λ CDM model.

⁸ Supernovae, HO, for the Equation of State of Dark energy

In this context, one of the residual sources of uncertainty in the cosmic distance ladder is represented by the debated metallicity dependence of the DCEP PL relations used to calibrate the secondary distance indicators. Indeed, a metallicity variation is predicted to affect the shape and width of the DCEP instability strip (e.g. Caputo et al. [Cap+00]), which in turn affects the coefficient of the PL relations (De Somma et al. [De +22] and Marconi et al. [Mar+10; MFM05] and references therein). The dependence of the PL relations and of the reddening-free Wesenheit magnitudes⁹ on metallicity, however small, when involving near-infrared (NIR, see e.g. Fiorentino et al. [FMM13] and Gieren et al. [Gie+18]) colours must be taken into account to avoid systematic effects in the calibration of the extragalactic distance scale (e.g. Bono et al. [Bon+10], Riess et al. [Rie+16], and Romaniello et al. [Rom+08]).

Direct empirical evaluations of the metallicity dependence of PL relations using Galactic DCEPs with sound $[Fe/H]$ measurements based on high-resolution (HiRes hereafter) spectroscopy have been hampered so far by the lack of accurate independent distances for a significant number of Milky Way (MW) DCEPs. The advent of the *Gaia* mission (Gaia Collaboration et al. [Gai+16]) has completely changed this scenario. *Gaia* began providing accurate parallaxes with data release 2 (DR2, Gaia Collaboration et al. [Gai+18]), which were further improved with the early data release 3 (Gaia Collaboration et al. [Gai+21]). In addition, the *Gaia* mission secured the discovery of hundreds of new Galactic DCEPs (Clementini et al. [Cle+19] and Ripepi et al. [Rip+19; Rip+22]) which, together with those discovered by other surveys, such as the OGLE Galactic Disk survey (Udalski et al. [Uda+18]) and the Zwicky Transient Facility (ZTF, Chen et al. [Che+20]), constitute a formidable sample of DCEPs useful not only in the context of the extragalactic distance scale but also for Galactic studies (e.g. Lemasle et al. [Lem+22] and Trentin et al. [Tre+23] and references therein). However, until a few years ago, the number of DCEPs with metallicity measurements from HiRes spectroscopy was mainly restricted to the solar neighbourhood, where the DCEPs span a limited range in $[Fe/H]$, centred on solar or slightly supersolar values, with a small dispersion of 0.2-0.3 dex (e.g. Genovali et al. [Gen+14], Groenewegen [Gro18], Luck [Luc18], and Ripepi et al. [Rip+19]). This makes it very difficult to measure the metallicity dependence of PL relations using Galactic Cepheids with sound statistical significance.

In this context, a few years ago we started a project named C-MetaLL (Cepheid - Metallicity in the Leavitt Law, see Ripepi et al. [Rip+21a] for a full description), with

⁹ The Wesenheit magnitudes introduced by Madore [Mad82] provide a reddening-free magnitude by supposing that the adopted extinction law does not change significantly from star to star as can happen if the targets are placed in regions of the Galaxy with different chemical enrichment histories.

Table 3.1: Photometric, astrometric, and spectroscopic data for the DCEP sample used in this work. Only the first ten lines of the table are shown here to guide the reader to its content. The machine-readable version of the table will be published at the CDS (Centre de Données astronomiques de Strasbourg, <https://cds.u-strasbg.fr/>). The meaning of the different columns is as follows: (1) *Gaia* EDR3 identification; (2) other names of the DCEPs; (3) and (4) equatorial coordinates (J2000); (5) mode of pulsation – F, 1O, F1O, and 1O2O indicate the fundamental, first overtone, and the mixed-mode pulsation modes, respectively; (6) and (7) original parallax value and error from *Gaia* EDR3 catalogue; (8) parallax correction according to Lindegren et al. [Lin+21]; (9) RUWE value from *Gaia* EDR3; (10) Fidelity_v2 index from Rybizki et al. [Ryb+22]; (11) period of pulsation. For mixed-mode DCEPs, the longest period is listed; (12) and (13) E(B-V) and error; (14) to (29) magnitudes and errors for the G_{GRP} V , I , J , H , K_s bands, respectively; (30) and (31) iron abundance and error; (32) literature source of the iron abundance – G14=Genovali et al. [Gen+14], GALAH = Buder et al. [Bud+21]; GDR3 = *Gaia* DR3 (see Recio-Blanco et al. [Rec+23]); GC17=Gaia Collaboration et al. [Gal+17]; G18=Groenewegen [Gro18]; K22=Kovtyukh et al. [Kov+22]; PASTEL= Soubiran et al. [Sou+16]; R21=Ripepi et al. [Rip+21a]; T23=Trentin et al. [Tre+23]; (33) source for the values of $E(B-V)$ (in addition to those quoted for the metallicity) – VL07 = van Leeuwen et al. [van+07]; R21 means that the value of reddening was calculated using the period-colour relations published in Ripepi et al. [Rip+21a]; (34) and (35) source for the V and I magnitudes – Lit = compilation from the literature (mainly from G18); Gaia+P22 = magnitudes calculated on the basis of the *Gaia* bands using the transformations to the Johnson-Cousins system by Pancino et al. [Pan+22]; (36) flag related to the provenience of the [Fe/H] value: 0 = HiRes spectroscopy; 1 and 2 = *Gaia* RVS spectroscopy published in DR3 with good- and intermediate-quality according to the selections by Recio-Blanco et al. [Rec+23].

GaiaDR3	Name	RA (deg)	Dec (deg)	Mode	plx (mas)	e_plx (mas)	plx_corr (mas)	RUWE	f_v2	Period (days)	$E(B-V)$ (mag)	$e_{E(B-V)}$ (mag)	G (mag)	e_G (mag)	G_{GRP} (mag)	$e_{G_{\text{GRP}}}$ (mag)
(1)	(2)	(3)	(4)	(5)	(6)	(7)	(8)	(9)	(10)	(11)	(12)	(13)	(14)	(15)	(16)	(17)
3430067092837622272	AA Gem	91.64561	26.32922	DCEP_F	0.2749	0.0201	-0.0365	1.249	1.0	11.30157	0.345	0.036	9.363	0.005	9.956	0.007
3102535635624415872	AA Mon	104.34904	-3.84334	DCEP_F	0.3139	0.0171	-0.0024	1.163	1.0	3.93815	0.765	0.017	12.103	0.004	12.993	0.009
4260210878780635904	AA Ser	280.34068	-1.11122	DCEP_F	0.2408	0.0335	-0.0379	0.952	0.4	17.14211	1.295	0.139	10.910	0.002	12.485	0.004
473239154746762112	AB Cam	56.53439	58.78422	DCEP_F	0.2128	0.0234	-0.0278	1.276	1.0	5.78758	0.622	0.035	11.383	0.003	12.118	0.009
462252662762965120	AC Cam	50.94951	59.35567	DCEP_F	0.3206	0.0202	-0.0225	1.206	1.0	4.15677	0.904	0.090	11.830	0.003	12.805	0.049
3050050207554658048	AC Mon	105.24925	-8.70899	DCEP_F	0.3549	0.0211	-0.0280	1.379	1.0	8.01493	0.507	0.033	9.599	0.006	10.314	0.005
462407693902385792	AD Cam	52.35821	60.44646	DCEP_F	0.2965	0.0198	-0.0185	1.185	1.0	11.26305	0.873	0.012	11.711	0.014	12.773	0.016
6057514092119497472	AD Cru	183.24861	-62.09683	DCEP_F	0.2929	0.0154	-0.0224	1.017	1.0	6.39723	0.640	0.012	10.480	0.002	11.327	0.003
3378049163365268608	AD Gem	100.7813	20.93911	DCEP_F	0.3356	0.0223	-0.0342	0.969	1.0	3.78800	0.206	0.048	9.648	0.009	10.021	0.018
5614312705966204288	AD Pup	117.01605	-25.57778	DCEP_F	0.2331	0.0189	-0.0206	1.362	1.0	13.59681	0.363	0.020	9.541	0.003	10.125	0.015

GRP	e_{GRP}	V (mag)	e_V (mag)	I (mag)	e_I (mag)	J (mag)	e_J (mag)	H (mag)	e_H (mag)	K_s (mag)	e_{K_s} (mag)	[Fe/H] (dex)	$e_{\text{[Fe/H]}}$ (dex)	metSource	ebvSource	vSource	iSource	sflag
(18)	(19)	(20)	(21)	(22)	(23)	(24)	(25)	(26)	(27)	(28)	(29)	(30)	(31)	(32)	(33)	(34)	(35)	(36)
8.620	0.005	9.722	0.020	8.581	0.020	7.636	0.008	7.201	0.008	7.048	0.008	-0.08	0.12	G18	G18	Lit	Lit	0
11.174	0.004	12.744	0.020	11.085	0.020	9.729	0.008	9.199	0.008	8.953	0.008	-0.12	0.12	G18	G18	Lit	Lit	0
9.716	0.005	12.243	0.020	9.571	0.020	7.563	0.008	6.773	0.008	6.457	0.008	0.38	0.12	G18	G18	Lit	Lit	0
10.533	0.007	11.860	0.020	10.454	0.030	9.418	0.025	8.936	0.025	8.746	0.025	-0.11	0.12	G18	G18	Lit	GDR3+P22	0
10.822	0.009	12.605	0.020	10.697	0.020	9.325	0.025	8.752	0.025	8.499	0.025	-0.16	0.12	G18	G18	Lit	Lit	0
8.771	0.004	10.099	0.020	8.707	0.020	7.577	0.008	7.066	0.008	6.849	0.008	-0.06	0.12	G18	G18	Lit	Lit	0
10.690	0.010	12.560	0.020	10.587	0.030	8.988	0.025	8.363	0.025	8.109	0.025	-0.28	0.12	G18	G18	Lit	GDR3+P22	0
9.569	0.002	11.061	0.020	9.452	0.020	8.198	0.025	7.661	0.025	7.387	0.025	0.08	0.12	G18	G18	Lit	Lit	0
9.108	0.010	9.855	0.020	9.050	0.020	8.448	0.008	8.151	0.008	8.027	0.008	-0.14	0.12	G18	G18	Lit	Lit	0
8.786	0.008	9.919	0.020	8.736	0.020	7.723	0.025	7.341	0.025	7.144	0.025	-0.06	0.12	G18	G18	Lit	Lit	0

the goal being to measure the chemical abundance of a sample of 250-300 Galactic DCEPs through HiRes spectroscopy, expressly aiming to enlarge the iron abundance range towards the metal-poor regime —that is, $[\text{Fe}/\text{H}] < -0.4$ dex— where only a few stars have abundance measurements in the literature. In the first two papers of the series (Ripepi et al. [Rip+21a] and Trentin et al. [Tre+23]), we published accurate abundances for more than 25 chemical species for a total of 114 DCEPs. In particular, in Trentin et al. [Tre+23], we obtained measures for 43 objects with $[\text{Fe}/\text{H}] < -0.4$ dex, reaching abundances of as low as -1.1 dex.

The scope of this paper is to study the metallicity dependence of the PL relations using a $[\text{Fe}/\text{H}]$ range of more than 1 dex. In this way, we aim to be able to discern between the two scenarios that came out in the recent literature concerning the metallicity dependence of PL relations. In fact, in our previous works using Galactic DCEPs and *Gaia* parallaxes, we found a rather large dependence in the NIR bands of on the order of ~ -0.4 mag/dex (Ripepi et al. [Rip+20; Rip+21a]); or even larger when using the *Gaia* bands (~ -0.5 mag/dex Ripepi et al. [Rip+22]). These values are discrepant with those measured by the SH0ES group (~ -0.2 mag/dex Riess et al. [Rie+21a]) —which, on the other hand, used a calibrating sample of 75 DCEPs in the solar vicinity spanning a small $[\text{Fe}/\text{H}]$ range—, and are also different from those measured by Breuval et al. [Bre+21; Bre+22], who obtained similar results to the SH0ES group using three Cepheid samples in the Milky Way and the Large and Small Magellanic Clouds (LMC and SMC, respectively) as three representative objects with different mean metallicities.

The paper is organized as follows: in Sect. 3.2 we describe the sample of DCEPs and their properties. In Sect. 3.3, we describe the method we used to derive the period–luminosity–metallicity (PLZ) and period–Wesenheit–metallicity (PWZ) relations; in Sect. 3.4 and Sect. 3.5, we describe and discuss our results; and in Sect. 3.6 we outline our conclusions.

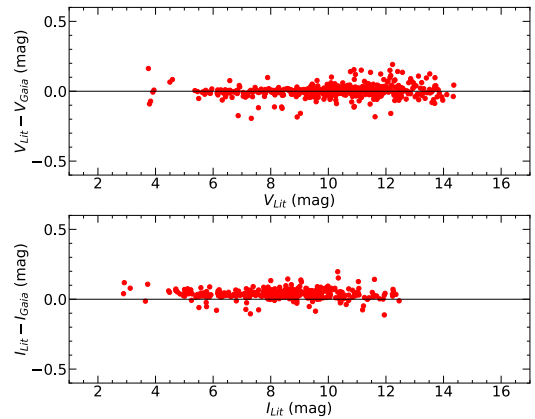


Figure 3.1: Comparison between the literature V , I photometry and that from *Gaia* through the transformation by Pancino et al. [Pan+22]. The top and bottom panels show the comparison in V and I bands, respectively.

3.2 Description of the data used in this work

In this section, we describe the sample of DCEPs used in this paper and their photometric, spectroscopic, and astrometric properties. All the data employed in our analysis are listed in Table 3.1.

3.2.1 Photometry

Optical V , I^{10} photometry is available in the literature for about 488 and 364 DCEPs of our sample, respectively (Groenewegen [Gro18] and Ripepi et al. [Rip+21a]). For the remaining stars, we decided to use the homogeneous and precise *Gaia* G , G_{BP} , G_{RP} photometry transformed into the Johnson-Cousins V , I bands by means of the relations published by Pancino et al. [Pan+22]. We calculated these aforementioned magnitudes for all the stars with full G , G_{BP} , G_{RP} values (all DCEPs except one) using the intensity-averaged magnitudes from the *Gaia* Vizier catalogue *I/358/vcep* (Ripepi et al. [Rip+22]) or the simple average magnitudes from the *Gaia* source catalogue (Vizier *I/355/gaiadr3*) for the few stars not present in the quoted catalogue.

Figure 3.1 shows the comparison between the literature V , I magnitudes and those calculated from the *Gaia* photometry for the stars for which both values are available. While the transformed V photometry appears perfectly compatible with that from the literature ($V_{Lit} - V_{Gaia} \sim 0.0$ with dispersion $\sigma \sim 0.04$ mag), the transformed I photometry appears to be slightly too faint: $I_{Lit} - I_{Gaia} \sim 0.035$ (mag) with a dispersion of $\sigma \sim 0.035$ mag. Therefore, we used the transformed V bands with no modification, while we corrected the transformed I bands by increasing their value by 0.035 mag. As for the uncertainties, we assumed 0.02 mag in both V and I for the literature sample when the number is not available in the original publication, while for the remaining stars, we propagated the errors, also taking into account (summing in quadrature) the uncertainties in the transformations provided by Pancino et al. [Pan+22].

For a handful of stars, the DCEPs (G_{BP} - G_{RP}) colours were beyond the validity limit of the Pancino et al. [Pan+22] relations. For these stars, we adopted the synthetic V , I magnitudes calculated by Gaia Collaboration et al. [Gai+23] based on *Gaia* DR3 photometry. Near-infrared J , H , and K_S band photometry is from van Leeuwen et al. [van+07], Gaia Collaboration et al. [Gai+17], Groenewegen [Gro18] and Ripepi et al. [Rip+21a] for the literature sample, and is derived from single-epoch 2MASS photometry (Skrutskie et al. [Skr+06]) for the remaining stars. To this aim, we adopted the procedure outlined in Ripepi et al. [Rip+21a], using the ephemerides

¹⁰ The I photometry is in the Cousins system

(periods and epochs of maximum light) from the *Gaia* VizieR catalogue *I/358/vcep*. As in our previous work, the uncertainties on the mean magnitudes were calculated using Monte Carlo simulations, varying the 2MASS magnitude and the phase of the single-epoch photometry within their errors, where the last quantity was calculated using the errors on the periods given in the *Gaia* catalogue.

In this work, we also considered the Wesenheit indices, which are reddening-free quantities by construction (Brodie and Madore [BM80]). These are obtained by combining the standard magnitude in a given photometric band with a colour term according to the following equation:

$$W_{X_1, X_2 - X_3} = X_1 - \xi_1^{2,3} \cdot (X_2 - X_3), \quad (3.1)$$

where X_i indicates the generic band and the coefficient $\xi_1^{2,3}$ coincides with the total-to-selective absorption and is obtained by assuming an extinction law. The photometric band combinations adopted in this work are listed in Table 3.2, together with the coefficient of the colour term. In order to transform the Johnson-Cousins-2MASS ground-based H , V , and I photometry into the HST correspondent F160W, F555W, and F814W filters, we considered the photometric transformations by Riess et al. [Rie+21a]. We note that, for brevity, in the following the calibrated Wesenheit in the HST bands is referred to as $W_{H,V-I}^{cHST}$ ¹¹.

In analogy with photometry, the reddening for the literature sample was taken from van Leeuwen et al. [van+07], *Gaia* Collaboration et al. [Gai+17], Groenewegen [Gro18] and Ripepi et al. [Rip+21a], while for the remaining stars, we used the same period-colour relations used in Ripepi et al. [Rip+21a] involving $(V - I)$ colour (their eq. 4), obtaining $E(V - I)$ excesses that were converted into the corresponding $E(B - V)$ ones using the relation $E(V - I) = 1.28 E(B - V)$ (Tammann et al. [TSR03a]). The uncertainties on these

reddening values were calculated by summing in quadrature the rms of eq. 4 in Ripepi et al. [Rip+21a], with the errors on V and I magnitudes. However, to be

Table 3.2: Photometric bands and colour coefficients adopted to calculate the Wesenheit magnitudes considered in this work. The Wesenheit magnitude names are contained in column 1, while the ξ values from the Cardelli law (Cardelli et al. [CCM89]) are in column 2.

Bands	ξ
$W_{G,GBP-GRP}$	1.9
$W_{H,V-I}$	0.461
$W_{H,V-I}^{cHST}$	0.386
$W_{K_S,V-K_S}$	0.130
$W_{K_S,J-K_S}$	0.690

¹¹ We caution the reader that the conversion equations in Riess et al. [Rie+21a] contain a typo regarding the F814W filter. In this work we used the correct relation $F814W = V - 0.48(V - H) - 0.025$ instead of $F814W = V - 0.48(J - H) - 0.025$

conservative, we assumed an uncertainty of 10% on the reddening for values of $E(B - V) > 1.0$ mag.

3.2.2 Metallicity

Metallicities were taken from various literature sources. A large part of the sample is the same as in Trentin et al. [Tre+23] (see their sect. 4.1). More specifically, we considered the large compilation of homogenised literature iron abundances for 436 DCEPs presented by Groenewegen [Gro18] (G18 hereinafter), complemented with literature results for a few additional stars by Gaia Collaboration et al. [Gai+17] (GC17 hereinafter). To these data, we added the following samples: (i) 49 DCEPs presented in Catanzaro et al. [Cat+20] and Ripepi et al. [Rip+21a; Rip+21b] (collectively called R21 hereinafter); (ii) the sample of 65 DCEPs published in Trentin et al. [Tre+23] (called T23 hereafter); (iii) the 104 stars by Kovtyukh et al. [Kov+22] (K22 hereinafter) after removing the large overlap with the R21 and T23 sample (see Trentin et al. [Tre+23] for full details and the homogenisation procedure we adopted in merging the samples); and (iv) a few stars with HiRes metallicities from the GALAH Survey (GALactic Archaeology with HERMES; Buder et al. [Bud+21] stars OGLE-GD-CEP-0059, OGLE-GD-CEP-0058, V1253 Cen) and from the PASTEL catalogue (Soubiran et al. [Sou+16] star OGLE-GD-CEP-0117). With these additions, the total number of DCEPs with metallicities from HiRes spectroscopy is 635. Concerning homogeneity, apart from the few stars from GALAH, PASTEL, or GC17, the main samples adopted in this work are the G18, K22, and combined C-MetaLL data. As mentioned above, the G18 sample is already homogeneous, while the K22 abundances were homogenised with those of the C-MetaLL sample in Trentin et al. [Tre+23]. As discussed in Ripepi et al. [Rip+21b],

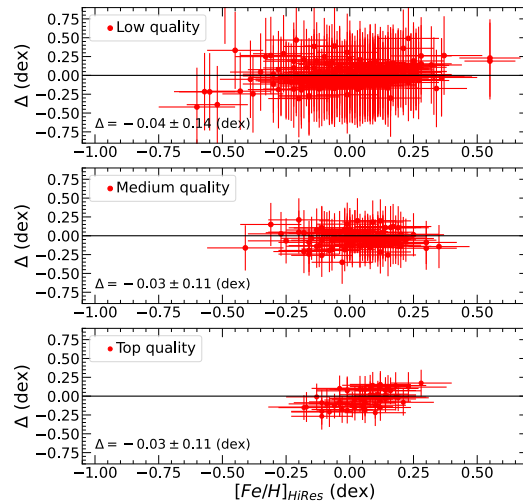


Figure 3.2: Comparison between the $[\text{Fe}/\text{H}]$ from HiRes data and *Gaia* $[\text{M}/\text{H}]$. From top to bottom, the different panels show the comparison for the low-, medium-, and high-quality *Gaia* data, respectively (see text for details). In each panel, the average difference Δ and its dispersion is displayed.

the C-MetaLL data have only two stars in common with G18, namely X Sct and V5567 Sgr. For these two stars, the abundances agree well within 0.5σ .

In addition to this already large sample, we decided to exploit the recent results released by the *Gaia* DR3. To this aim, we cross-matched the DCEP catalogue published by *Gaia* DR3 (Vizier catalogue *I/358/vcep*) as amended by Ripepi et al. [Rip+22] with that of the astrophysical parameters (Vizier catalogue *I/355/paramp*), retaining only matching stars that have a global metallicity value ($[M/H]$) derived from the medium-resolution spectra obtained with the Radial Velocity Spectrometer (RVS, see Recio-Blanco et al. [Rec+23] for details). The total number of matching stars is 983, among which 475 have HiRes metallicity estimations from the literature. *Gaia* metallicities were corrected following the recipe by Recio-Blanco et al. [Rec+23] (their eq. 4 and table 5), and then we assigned a data-quality flag to every object. Assigned flags are 1, 2, and 3, which refer to high-, medium-, and low-quality, respectively, according to Recio-Blanco et al. [Rec+23] (see sect. 9). The *Gaia* abundances were derived using the stacked RVS spectra over all the epochs of observations. The resulting spectra are therefore an average of many spectra over the pulsation cycle. As the DCEPs vary in terms of effective temperature, surface gravity, and microturbulent velocity along the pulsation cycle, we can in principle expect an impact on the derived abundances. In addition, the abundances published in the *Gaia* Astrophysical parameters are the mean metallicities $[M/H]$, which may differ from the $[Fe/H]$ scale used for the HiRes sample. To investigate these potential concerns, we compared the corrected *Gaia* metallicities with those from the HiRes sample for the 475 stars in common. The result is shown in Fig. 3.2. There is good overall agreement for all the *Gaia* subsamples (low, medium, and high quality). In all cases, the average difference between HiRes and *Gaia* results is very low, namely $\Delta \sim -0.03$ dex, with a comfortable moderate dispersion of the order of 0.11-0.13 dex (worse for the low-quality *Gaia* data), indicating that the *Gaia* spectroscopic results are of comparable quality to the HiRes ones overall and that the data can be used together. This is especially true for $[Fe/H]_{HiRes} > -0.3$ dex. Below this value, the *Gaia* sample is dominated by low-quality data and the dispersion becomes significantly larger (top panel).

We corrected for the small offset of the *Gaia* data and decided to use only the medium- and high-quality data in the following in order to avoid including some unreliable abundance values from the low-quality data. The resulting sample is then composed of 910 DCEPs divided into 282 DCEP_1Os, 22 DCEP_1O2Os, 581 DCEP_Fs, and 25 DCEP_F1Os, where DCEP_1O2Os and DCEP_F1Os represent multi-mode pulsators. For these two last cases, we adopted the longest period, that is, the 1O period for the 1O2O pulsators and the F one for the F1O DCEPs. Therefore, our sample includes the equivalent of 304 1O and 606 F mode DCEPs.

3.2.3 Astrometry

To carry out our analysis, we adopted the parallaxes from *Gaia* DR3, which were individually corrected for the zero point offset, adopting the recipe by Lindegren et al. [Lin+21]¹² (L21). We highlight the characteristic shape of the correction, with a sharp hump around $G \sim 12$ mag, the explanation for which can be found in Lindegren et al. [Lin+21]. The individual corrections are shown in Fig. 3.3 as a function of the magnitude and of the ecliptic latitude. As criteria of the goodness of the astrometry, we adopted two indicators: (i) the *fidelity_v2* index as tabulated by Rybizki et al. [Ryb+22], retaining only objects with values larger than 0.5, and (ii) the *RUWE* parameter published in *Gaia* DR3. Although the *Gaia* documentation recommends using a threshold below 1.4 for good astrometric solutions, we choose to be less conservative and use a slightly larger threshold equal to 1.5. This choice allows us to retain possibly good objects falling just outside the 1.4 threshold. In any case, our robust outlier-removal procedure (see Sect. 3.3) removes possible deviating stars introduced by the slightly enlarged adopted threshold.

The simultaneous use of the *fidelity_v2* and *RUWE* parameters led us to reject 78 objects from our sample. A large fraction of the rejected DCEPs, namely 35, have $G \leq 7$ mag. This is not surprising, as *Gaia* parallaxes are known to be uncertain for such bright stars (e.g. Lindegren et al. [Lin+21]).

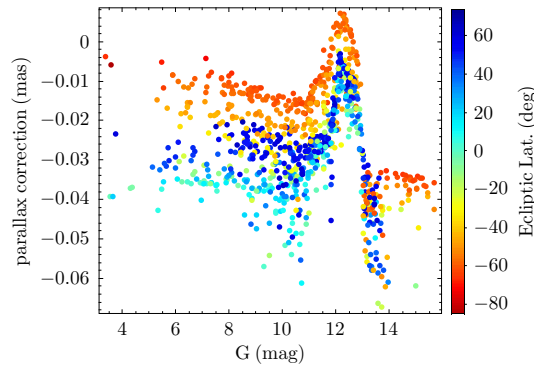


Figure 3.3: Individual parallax corrections from L21 as a function of the G magnitude. The points are colour coded according to the ecliptic latitude.

3.3 Derivation of the PLZ/PWZ relations

In this section, we describe the procedure adopted to calibrate the *PLZ/PWZ* relations. The approach is the same as in Ripepi et al. [Rip+20] and Ripepi et al. [Rip+21a]. To avoid any bias, the whole DCEPs sample was considered, including negative parallaxes, and without any selection on the parallax relative errors. Moreover, we adopted the astrometry-based-luminosity (ABL) formalism (Arenou

¹² <https://www.cosmos.esa.int/web/gaia/edr3-code>

and Luri [AL99] and Feast and Catchpole [FC97]), which allows us to treat the parallax ϖ as a linear parameter:

$$ABL = \varpi 10^{0.2m-2} = 10^{0.2(\alpha+(\beta+\delta[Fe/H])(\log P-\log P_0)+\gamma[Fe/H])}, \quad (3.2)$$

where the parallax ϖ , the apparent generic magnitude m , the period P , and the metallicity $[Fe/H]$ are the observables, while the unknowns are the four parameters α , β , γ , and δ (intercept, slope, metallicity dependence of the intercept, and the metallicity dependence of the slope, respectively).

The P_0 quantity is a pivoting period ($10d$) adopted to reduce the correlation between the α and β parameters, which dominate the PL and PW relations. To take into account the presence of possible outlier measurements, we applied multiple sigma-clipping removals but limited the number of rejected data to $\sim 10\%$ of the full sample. Based on the results described in the previous papers of this series, we decided to exclude the case with no metallicity dependence at all (i.e. $\gamma \neq 0$) in Eq. 3.2. Finally, the 1O pulsators are included in the fitting sample by fundamentalising their periods according to the relation by Alcock et al. [Alc+95] and Feast and Catchpole [FC97]. In the following sections, we consider two data samples: (i) the *Lit+DR3* sample, which includes all the selected sources introduced in Sect. 3.2; and (ii) the *Lit* sample, which was obtained by excluding the sources with only a Gaia DR3 metallicity estimate, therefore retaining only DCEPs with metallicity measures from ground-based HiRes

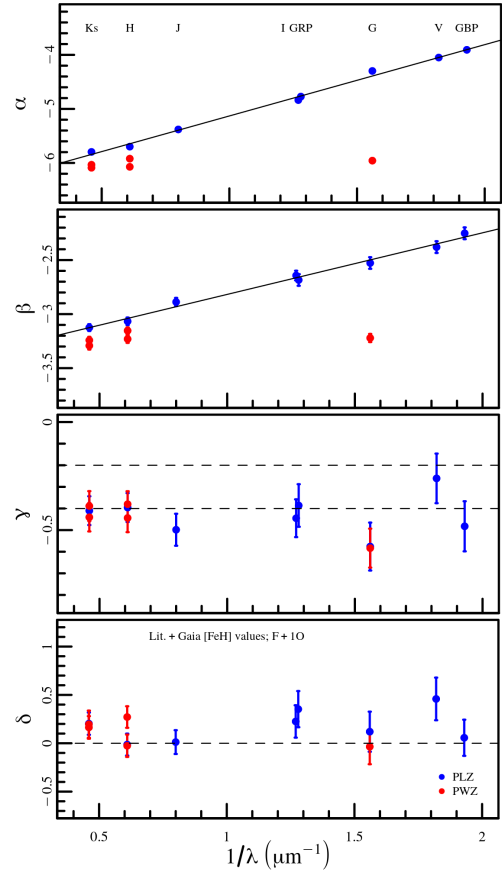


Figure 3.4: Coefficients of PLZ/PWZ relations obtained from the fit to the *Lit. + Gaia* sample plotted against the λ^{-1} parameter. From top to bottom, the panels correspond to the α , β , γ , and δ coefficients. In each panel, PLZ and PWZ coefficients are plotted with blue and red symbols respectively, while the solid line shows the linear fit only for the PLZ relations. Grey dashed lines in the γ panel delimit the range of results in the literature (-0.2 to -0.4 mag/dex, see Breuval et al. [Bre+22] and Sect. 3.5.4), while in the δ panel, it corresponds to the value 0.

spectrographs. The uncertainties on the parameters calculated in the following analysis are obtained through the bootstrap technique. A set of 1000 resampling experiments is performed and the coefficients of the Eq. 3.2 are calculated for each obtained random data set. Finally, the quoted errors are estimated by considering the robust standard deviation of the obtained coefficient distributions.

3.4 Results

3.4.1 Literature and *Gaia* DR3 sample

The results of the fitting procedure obtained for this case are listed in Table 3.3. We studied the dependence of the fitted *PLZ*/*PWZ* coefficients on the central wavelength of the considered filters. To associate a characteristic wavelength to the Wesenheit magnitudes, we decided to consider the central wavelength of the main band (e.g. *G* band for the $W_{G,BP-RP}$ case). The results of this analysis are shown in Fig. 3.4 for the F+1O sample (i.e. the sample including both F and fundamentalised 1O pulsators) and assuming a metallicity dependence also in the slope of the *PLZ*/*PWZ* relation (i.e. $\delta \neq 0$).

Looking at the *PLZ* coefficients (blue filled circles), a strong linear dependence as a function of the λ^{-1} is evident only for the α and β coefficients (correlation coefficient $R^2 \simeq 1$), while for γ and δ the slope of the fit is consistent with zero. The relations between α , β , and λ^{-1} are the following:

$$\alpha = (0.618 \pm 0.003) \cdot \lambda^{-1} + (-3.428 \pm 0.006),$$

with $rms = 0.019$, $R^2 = 0.99$, and

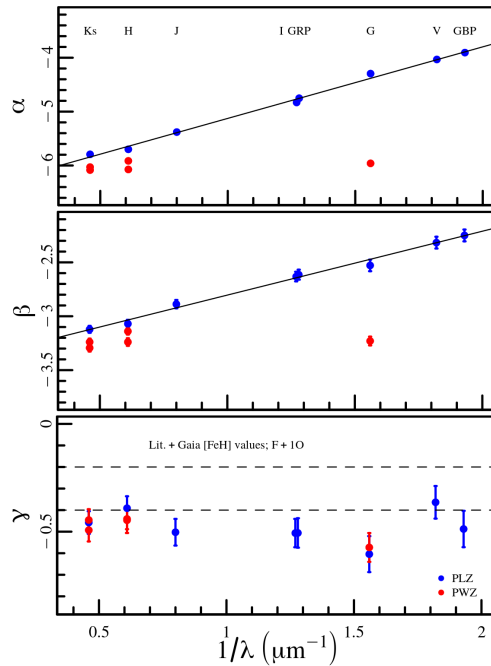


Figure 3.5: Same as Fig. 3.4 but for the case neglecting the metallicity dependence in the *PLZ*/*PLW* slope (i.e. $\delta = 0$).

Table 3.3: Results of the fitting using the Lit.+ Gaia data set. The ID identifies each different fit to the data; α , β , γ and δ are the coefficients of the PLZ/PWZ relations; μ_0^{LMC} represents the true distance modulus of the LMC; rms is the root mean square; Band specifies the photometric band considered in the fit; Mode identifies the sample adopted; N_{dat} is the number of DCEPs adopted.

ID	α	β	γ	δ	μ_0^{LMC}	rms	Band	Mode	N_{dat}
1	-4.248 ± 0.025	-2.566 ± 0.063	-0.611 ± 0.121	–	18.398 ± 0.058	0.022	PLG	F	481
2	-4.255 ± 0.028	-2.620 ± 0.066	-0.571 ± 0.133	0.615 ± 0.363	18.294 ± 0.071	0.024	PLG	F	485
3	-4.295 ± 0.022	-2.529 ± 0.053	-0.604 ± 0.083	–	18.435 ± 0.034	0.027	PLG	F+1O	754
4	-4.298 ± 0.023	-2.527 ± 0.052	-0.576 ± 0.114	0.120 ± 0.213	18.426 ± 0.035	0.027	PLG	F+1O	753
5	-3.867 ± 0.028	-2.344 ± 0.064	-0.487 ± 0.117	–	18.422 ± 0.056	0.025	PLG _{BP}	F	467
6	-3.882 ± 0.031	-2.375 ± 0.068	-0.385 ± 0.146	0.213 ± 0.344	18.427 ± 0.067	0.026	PLG _{BP}	F	470
7	-3.905 ± 0.024	-2.250 ± 0.055	-0.488 ± 0.086	–	18.459 ± 0.038	0.030	PLG _{BP}	F+1O	743
8	-3.907 ± 0.026	-2.252 ± 0.056	-0.482 ± 0.113	0.057 ± 0.190	18.450 ± 0.032	0.030	PLG _{BP}	F+1O	746
9	-4.696 ± 0.017	-2.665 ± 0.051	-0.563 ± 0.085	–	18.346 ± 0.040	0.014	PLG _{RP}	F	458
10	-4.700 ± 0.018	-2.690 ± 0.057	-0.556 ± 0.100	0.315 ± 0.327	18.300 ± 0.058	0.014	PLG _{RP}	F	457
11	-4.752 ± 0.020	-2.614 ± 0.046	-0.506 ± 0.069	–	18.423 ± 0.031	0.018	PLG _{RP}	F+1O	739
12	-4.772 ± 0.022	-2.684 ± 0.052	-0.386 ± 0.100	0.353 ± 0.193	18.391 ± 0.030	0.018	PLG _{RP}	F+1O	744
13	-5.663 ± 0.016	-3.087 ± 0.048	-0.511 ± 0.078	–	18.382 ± 0.034	0.010	PLH	F	488
14	-5.668 ± 0.016	-3.106 ± 0.050	-0.478 ± 0.087	0.208 ± 0.275	18.354 ± 0.046	0.010	PLH	F	487
15	-5.699 ± 0.013	-3.070 ± 0.036	-0.391 ± 0.056	–	18.465 ± 0.022	0.011	PLH	F+1O	742
16	-5.699 ± 0.013	-3.067 ± 0.035	-0.396 ± 0.065	-0.014 ± 0.110	18.466 ± 0.023	0.011	PLH	F+1O	742
17	-4.774 ± 0.017	-2.676 ± 0.052	-0.602 ± 0.084	–	18.361 ± 0.039	0.013	PLI	F	460
18	-4.779 ± 0.018	-2.722 ± 0.058	-0.561 ± 0.096	0.482 ± 0.308	18.278 ± 0.055	0.014	PLI	F	464
19	-4.830 ± 0.019	-2.632 ± 0.045	-0.507 ± 0.065	–	18.452 ± 0.029	0.018	PLI	F+1O	735
20	-4.837 ± 0.020	-2.643 ± 0.044	-0.445 ± 0.091	0.226 ± 0.168	18.433 ± 0.026	0.017	PLI	F+1O	736
21	-5.343 ± 0.017	-2.945 ± 0.052	-0.575 ± 0.086	–	18.361 ± 0.040	0.011	PLJ	F	485
22	-5.344 ± 0.018	-2.948 ± 0.055	-0.564 ± 0.096	0.036 ± 0.296	18.357 ± 0.054	0.011	PLJ	F	482
23	-5.380 ± 0.014	-2.888 ± 0.038	-0.503 ± 0.061	–	18.438 ± 0.025	0.014	PLJ	F+1O	755
24	-5.380 ± 0.014	-2.888 ± 0.038	-0.498 ± 0.074	0.012 ± 0.121	18.436 ± 0.025	0.014	PLJ	F+1O	756
25	-5.766 ± 0.016	-3.145 ± 0.046	-0.527 ± 0.080	–	18.374 ± 0.037	0.009	PLK	F	477
26	-5.773 ± 0.018	-3.179 ± 0.052	-0.481 ± 0.088	0.350 ± 0.266	18.324 ± 0.050	0.009	PLK	F	482
27	-5.793 ± 0.014	-3.121 ± 0.032	-0.458 ± 0.052	–	18.420 ± 0.024	0.010	PLK	F+1O	743
28	-5.796 ± 0.014	-3.125 ± 0.031	-0.410 ± 0.066	0.203 ± 0.117	18.400 ± 0.023	0.010	PLK	F+1O	741
29	-3.975 ± 0.018	-2.354 ± 0.057	-0.423 ± 0.090	–	18.415 ± 0.045	0.021	PLV	F	460
30	-3.976 ± 0.019	-2.362 ± 0.058	-0.404 ± 0.108	0.106 ± 0.330	18.406 ± 0.053	0.021	PLV	F	459
31	-4.033 ± 0.022	-2.317 ± 0.055	-0.364 ± 0.076	–	18.490 ± 0.036	0.026	PLV	F+1O	738
32	-4.050 ± 0.024	-2.380 ± 0.054	-0.261 ± 0.115	0.458 ± 0.226	18.420 ± 0.034	0.028	PLV	F+1O	746
33	-5.917 ± 0.017	-3.245 ± 0.055	-0.745 ± 0.085	–	18.310 ± 0.036	0.009	PW _{G,GBP-GRP}	F	478
34	-5.927 ± 0.018	-3.292 ± 0.044	-0.659 ± 0.100	0.559 ± 0.273	18.254 ± 0.048	0.009	PW _{G,GBP-GRP}	F	484
35	-5.960 ± 0.018	-3.230 ± 0.041	-0.573 ± 0.066	–	18.436 ± 0.028	0.010	PW _{G,GBP-GRP}	F+1O	726
36	-5.958 ± 0.017	-3.221 ± 0.038	-0.583 ± 0.089	-0.036 ± 0.174	18.439 ± 0.028	0.010	PW _{G,GBP-GRP}	F+1O	725
37	-6.042 ± 0.016	-3.239 ± 0.051	-0.551 ± 0.082	–	18.385 ± 0.034	0.008	PW _{H,V-I}	F	487
38	-6.050 ± 0.015	-3.279 ± 0.039	-0.502 ± 0.079	0.390 ± 0.250	18.333 ± 0.047	0.008	PW _{H,V-I}	F	491
39	-6.073 ± 0.013	-3.239 ± 0.035	-0.447 ± 0.058	–	18.457 ± 0.023	0.010	PW _{H,V-I}	F+1O	747
40	-6.072 ± 0.014	-3.231 ± 0.035	-0.444 ± 0.067	-0.026 ± 0.115	18.464 ± 0.023	0.010	PW _{H,V-I}	F+1O	746
41	-5.908 ± 0.014	-3.167 ± 0.040	-0.338 ± 0.067	–	18.421 ± 0.032	0.006	PW _{H,V-I} ^{CHST}	F	369
42	-5.903 ± 0.015	-3.207 ± 0.049	-0.366 ± 0.078	0.366 ± 0.259	18.325 ± 0.047	0.007	PW _{H,V-I} ^{CHST}	F	393
43	-5.915 ± 0.013	-3.133 ± 0.036	-0.369 ± 0.063	–	18.414 ± 0.028	0.008	PW _{H,V-I} ^{CHST}	F+1O	491
44	-5.922 ± 0.013	-3.156 ± 0.035	-0.322 ± 0.071	0.267 ± 0.110	18.369 ± 0.026	0.008	PW _{H,V-I} ^{CHST}	F+1O	499
45	-6.064 ± 0.016	-3.286 ± 0.045	-0.494 ± 0.074	–	18.378 ± 0.035	0.008	PW _{K_S,J-K_S}	F	480
46	-6.070 ± 0.015	-3.336 ± 0.041	-0.470 ± 0.080	0.482 ± 0.231	18.283 ± 0.045	0.008	PW _{K_S,J-K_S}	F	481
47	-6.085 ± 0.015	-3.294 ± 0.035	-0.446 ± 0.049	–	18.407 ± 0.022	0.009	PW _{K_S,J-K_S}	F+1O	737
48	-6.089 ± 0.015	-3.292 ± 0.035	-0.389 ± 0.070	0.197 ± 0.138	18.395 ± 0.023	0.009	PW _{K_S,J-K_S}	F+1O	731
49	-6.016 ± 0.016	-3.261 ± 0.047	-0.507 ± 0.077	–	18.386 ± 0.035	0.008	PW _{K_S,V-K_S}	F	477
50	-6.020 ± 0.017	-3.285 ± 0.052	-0.471 ± 0.086	0.269 ± 0.265	18.350 ± 0.048	0.008	PW _{K_S,V-K_S}	F	481
51	-6.030 ± 0.013	-3.239 ± 0.032	-0.493 ± 0.052	–	18.405 ± 0.022	0.009	PW _{K_S,V-K_S}	F+1O	735
52	-6.034 ± 0.013	-3.242 ± 0.031	-0.440 ± 0.065	0.164 ± 0.114	18.396 ± 0.023	0.009	PW _{K_S,V-K_S}	F+1O	732

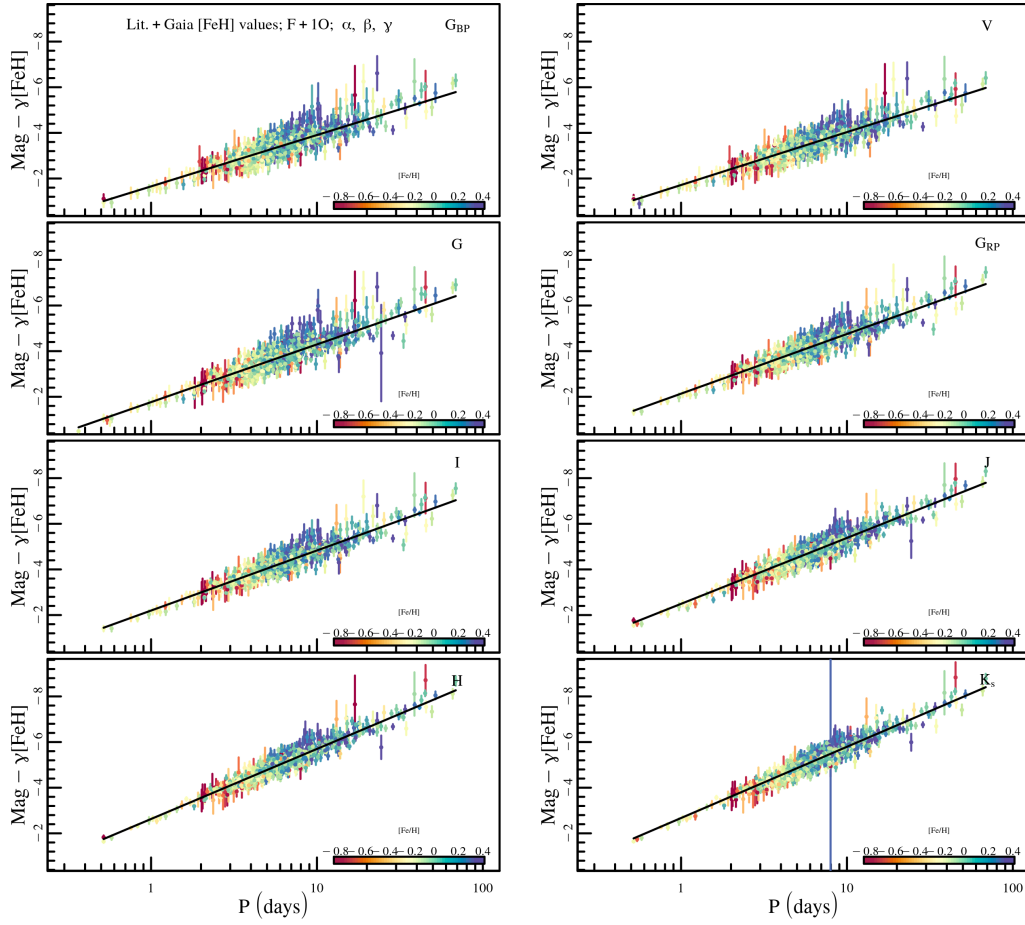


Figure 3.6: PL relations for the bands studied in the paper where the magnitudes have been subtracted by the metallicity contribution. The colour bar represents the metallicity.

$$\beta = (1.345 \pm 0.026) \cdot \lambda^{-1} + (-6.49 \pm 0.04),$$

with $rms = 0.059$, $R^2 = 0.99$. The strong dependence of the slope on the wavelength is a well-known feature, as thoroughly discussed by Madore and Freedman [MF11]. A similar discussion is valid for the case where the δ coefficient is neglected in Eq. 3.2. The estimated parameters are shown in Fig. 3.5, while the linear equations for α and β coefficients are the following:

$$\alpha = (0.64 \pm 0.04) \cdot \lambda^{-1} + (-3.45 \pm 0.03),$$

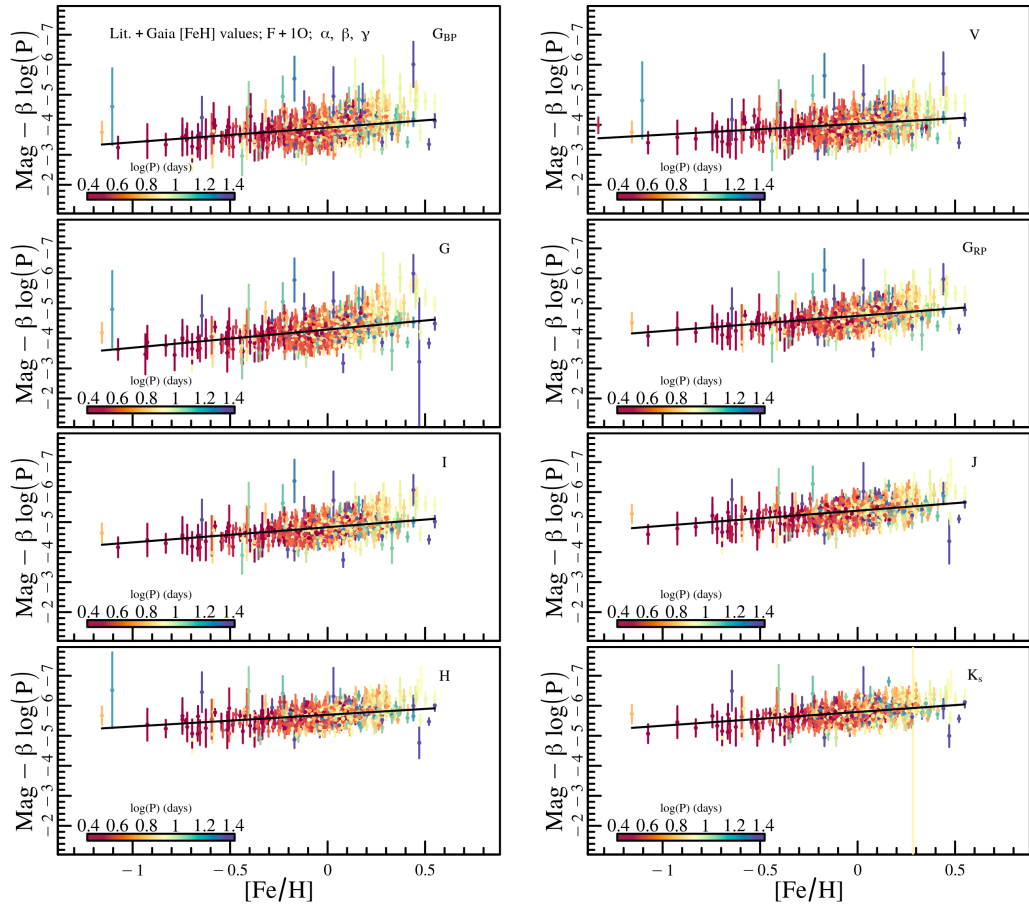


Figure 3.7: Visualization of the PL dependence on the metallicity. The y-axis is the magnitudes subtracted by the period contribution and the x-axis is the metallicity. The colour bar represents the logarithm of the period.

with $rms = 0.02$, $R^2 = 0.99$, and

$$\beta = (1.37 \pm 0.04) \cdot \lambda^{-1} + (-6.50 \pm 0.05),$$

with $rms = 0.06$, $R^2 = 0.99$. Comparing these results with those in the previous case, we found good agreement between all the parameters. To easily compare our γ values with those in the recent literature, we traced two reference lines in the third panel of Figs. 3.4 and 3.5 corresponding to $\gamma = -0.2$ and -0.4 dex. Indeed, this range of values includes almost all the recent estimates for the value of γ (see Table 1 of Breuval et al. [Bre+22] and Sect. 3.5.4 for a comprehensive list of recent results). Concerning the δ parameter, the bottom panel of Fig. 3.4 shows a

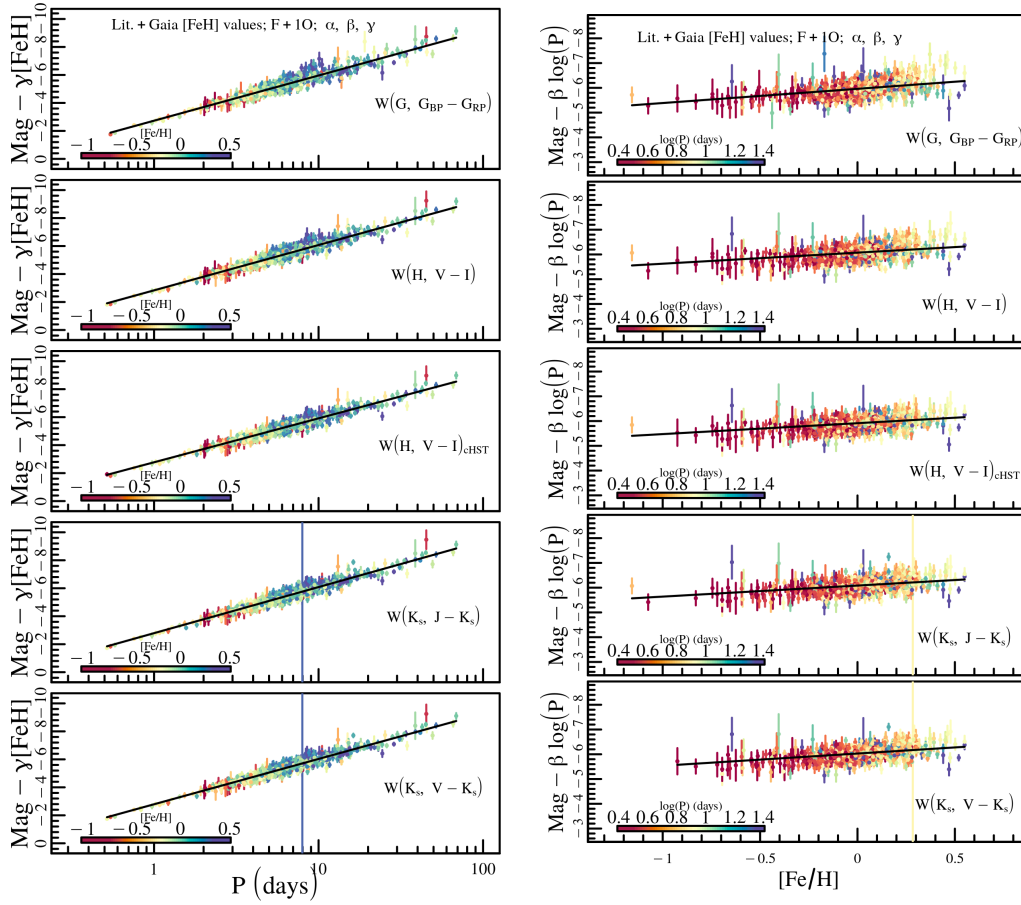


Figure 3.8: Same as Fig. 3.6 but for the PWZ relations. **Figure 3.9:** Same as Fig. 3.7 but for the PWZ relations.

significant metallicity dependence of the slopes only in the cases of the V -band PL . We note that in this case, the corresponding γ coefficients is highly consistent with the average literature values.

For the sake of completeness, in Appendix 3.A we also plot the results obtained by fitting the Eq. 3.2 to the sample including only the F pulsators (see Fig. 3.20 (a) and Fig. 3.20 (b)). The exclusion of the fundamentalised 1O pulsators increases the errors on all the coefficients, especially for δ . More specifically, we notice that the α and the β coefficients, within the errors, are found to be slightly increased and decreased, respectively, while the γ values are bigger (in an absolute sense), except for cases of the G and G_{bp} magnitudes. The δ parameter assumes also higher values in general and is more scattered compared with the F+1O case, but the large

uncertainties prevent us from drawing firm conclusions. To help in visualisation of the fitted relations listed in Table 3.3, we considered $\delta = 0$, because in this case, the dependence on $\log(P)$ in Eq. 3.2 can be separated from that on metallicity. Figures 3.6 and 3.7 show the projections of the *PLZ* relations in two dimensions using P and $[\text{Fe}/\text{H}]$ on the x-axis, respectively.

Similarly, Figs. 3.8 and 3.9 display the same projections for the *PWZ* relations. Figures 3.6 and 3.8 show no colour trend with metallicity, indicating that the correction for this parameter was effective. On the other hand, Figs. 3.7 and 3.9 display the metallicity dependence of the intercepts of the *PL* and *PW* relations, respectively, in a direct way. In these figures, the slopes of the solid lines, representing the fits for the different magnitudes, are a direct visualisation of the values of γ . It is possible to appreciate the relevance and importance of the extension towards the metal-poor regime for the determination of this parameter. Indeed, even a small number of objects with $[\text{Fe}/\text{H}] < -0.4$ dex can significantly affect and constrain the slope in these plots.

3.4.2 Literature sample only

The results of the fitting procedure obtained including the literature sample only are listed in Table 3.4. Similarly to the case above, we fitted α and β coefficients as a function of λ^{-1} of the specific band (only for *PLZ*). These fits are shown in the top two panels of Fig. 3.10 and their equations are:

$$\alpha = (0.563 \pm 0.017) \cdot \lambda^{-1} + (-3.37 \pm 0.03),$$

with $rms = 0.04$, $R^2 = 0.99$, and

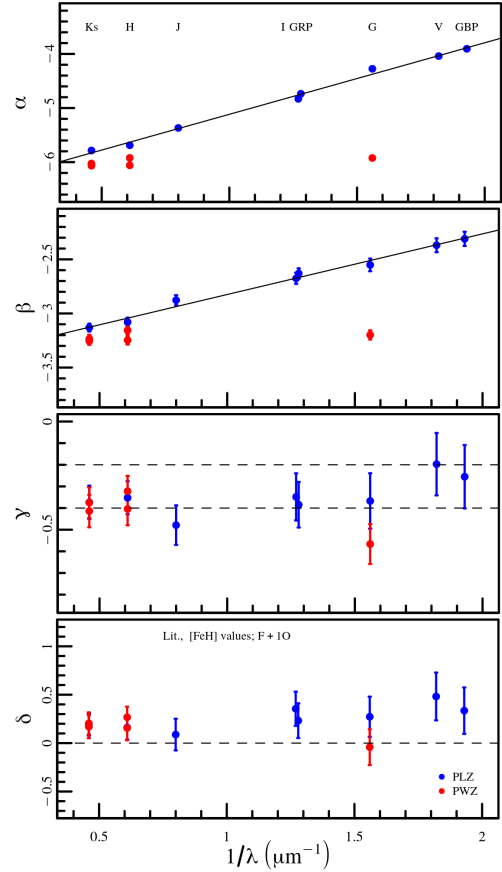


Figure 3.10: Same as Fig. 3.4 but for the Lit. sample.

Table 3.4: Fitting results from the Lit. data set. The meaning of the columns is the same as in Table 3.3.

ID	α	β	γ	δ	μ_0^{LMC}	rms	Band	Mode	N_{dat}
1	-4.253 ± 0.026	-2.591 ± 0.061	-0.403 ± 0.133	–	18.484 ± 0.064	0.020	PLG	F	386
2	-4.258 ± 0.029	-2.610 ± 0.065	-0.370 ± 0.143	0.211 ± 0.320	18.453 ± 0.067	0.020	PLG	F	388
3	-4.268 ± 0.025	-2.529 ± 0.057	-0.431 ± 0.108	–	18.485 ± 0.049	0.021	PLG	F+1O	503
4	-4.275 ± 0.026	-2.551 ± 0.057	-0.367 ± 0.129	0.272 ± 0.207	18.447 ± 0.042	0.022	PLG	F+1O	510
5	-3.843 ± 0.020	-2.361 ± 0.060	-0.417 ± 0.112	–	18.423 ± 0.052	0.022	PLG _{BP}	F	377
6	-3.845 ± 0.022	-2.367 ± 0.064	-0.407 ± 0.124	0.070 ± 0.316	18.414 ± 0.060	0.022	PLG _{BP}	F	377
7	-3.897 ± 0.028	-2.286 ± 0.062	-0.330 ± 0.123	–	18.498 ± 0.058	0.025	PLG _{BP}	F+1O	498
8	-3.905 ± 0.030	-2.311 ± 0.065	-0.255 ± 0.148	0.335 ± 0.244	18.451 ± 0.050	0.024	PLG _{BP}	F+1O	500
9	-4.702 ± 0.018	-2.667 ± 0.054	-0.481 ± 0.094	–	18.384 ± 0.044	0.012	PLG _{RP}	F	376
10	-4.706 ± 0.019	-2.681 ± 0.057	-0.461 ± 0.106	0.162 ± 0.310	18.356 ± 0.056	0.012	PLG _{RP}	F	373
11	-4.725 ± 0.018	-2.606 ± 0.051	-0.460 ± 0.083	–	18.420 ± 0.037	0.014	PLG _{RP}	F+1O	489
12	-4.736 ± 0.019	-2.631 ± 0.049	-0.385 ± 0.104	0.232 ± 0.180	18.407 ± 0.035	0.014	PLG _{RP}	F+1O	494
13	-5.669 ± 0.016	-3.103 ± 0.046	-0.374 ± 0.081	–	18.441 ± 0.035	0.008	PLH	F	384
14	-5.668 ± 0.017	-3.107 ± 0.050	-0.385 ± 0.088	0.045 ± 0.270	18.440 ± 0.049	0.008	PLH	F	383
15	-5.684 ± 0.014	-3.068 ± 0.042	-0.386 ± 0.070	–	18.454 ± 0.028	0.009	PLH	F+1O	505
16	-5.688 ± 0.015	-3.080 ± 0.040	-0.352 ± 0.076	0.161 ± 0.124	18.438 ± 0.028	0.009	PLH	F+1O	508
17	-4.781 ± 0.017	-2.723 ± 0.050	-0.444 ± 0.089	–	18.411 ± 0.042	0.011	PLI	F	362
18	-4.784 ± 0.018	-2.744 ± 0.056	-0.420 ± 0.100	0.285 ± 0.322	18.365 ± 0.062	0.011	PLI	F	359
19	-4.805 ± 0.017	-2.632 ± 0.049	-0.472 ± 0.081	–	18.439 ± 0.036	0.014	PLI	F+1O	495
20	-4.830 ± 0.023	-2.675 ± 0.051	-0.348 ± 0.110	0.355 ± 0.176	18.421 ± 0.034	0.014	PLI	F+1O	504
21	-5.346 ± 0.017	-2.948 ± 0.054	-0.506 ± 0.093	–	18.397 ± 0.042	0.010	PLJ	F	391
22	-5.345 ± 0.018	-2.947 ± 0.055	-0.509 ± 0.102	-0.014 ± 0.304	18.400 ± 0.057	0.010	PLJ	F	390
23	-5.366 ± 0.016	-2.873 ± 0.047	-0.504 ± 0.082	–	18.430 ± 0.034	0.012	PLJ	F+1O	520
24	-5.369 ± 0.019	-2.878 ± 0.047	-0.479 ± 0.090	0.088 ± 0.159	18.427 ± 0.037	0.012	PLJ	F+1O	516
25	-5.775 ± 0.017	-3.158 ± 0.045	-0.378 ± 0.076	–	18.458 ± 0.036	0.007	PLK	F	368
26	-5.774 ± 0.018	-3.176 ± 0.051	-0.386 ± 0.089	0.171 ± 0.265	18.426 ± 0.048	0.008	PLK	F	376
27	-5.780 ± 0.015	-3.121 ± 0.037	-0.433 ± 0.065	–	18.444 ± 0.029	0.008	PLK	F+1O	483
28	-5.786 ± 0.015	-3.130 ± 0.036	-0.374 ± 0.075	0.191 ± 0.114	18.419 ± 0.026	0.008	PLK	F+1O	487
29	-3.974 ± 0.019	-2.372 ± 0.058	-0.370 ± 0.103	–	18.432 ± 0.051	0.019	PLV	F	366
30	-3.977 ± 0.020	-2.386 ± 0.060	-0.348 ± 0.119	0.108 ± 0.337	18.415 ± 0.061	0.019	PLV	F	365
31	-4.002 ± 0.020	-2.299 ± 0.060	-0.396 ± 0.103	–	18.453 ± 0.049	0.022	PLV	F+1O	491
32	-4.040 ± 0.029	-2.370 ± 0.066	-0.197 ± 0.147	0.482 ± 0.247	18.434 ± 0.050	0.023	PLV	F+1O	501
33	-5.910 ± 0.017	-3.234 ± 0.054	-0.637 ± 0.085	–	18.380 ± 0.037	0.007	PW _{G,G_{BP}-G_{RP}}	F	378
34	-5.917 ± 0.019	-3.264 ± 0.057	-0.608 ± 0.102	0.436 ± 0.318	18.312 ± 0.053	0.007	PW _{G,G_{BP}-G_{RP}}	F	385
35	-5.925 ± 0.016	-3.199 ± 0.043	-0.553 ± 0.072	–	18.424 ± 0.030	0.008	PW _{G,G_{BP}-G_{RP}}	F+1O	499
36	-5.924 ± 0.016	-3.198 ± 0.043	-0.566 ± 0.092	-0.042 ± 0.183	18.422 ± 0.032	0.008	PW _{G,G_{BP}-G_{RP}}	F+1O	499
37	-6.045 ± 0.016	-3.253 ± 0.050	-0.426 ± 0.085	–	18.442 ± 0.035	0.007	PW _{H,V-I}	F	392
38	-6.048 ± 0.017	-3.273 ± 0.051	-0.409 ± 0.088	0.207 ± 0.293	18.410 ± 0.056	0.007	PW _{H,V-I}	F	394
39	-6.055 ± 0.015	-3.242 ± 0.040	-0.454 ± 0.069	–	18.434 ± 0.027	0.008	PW _{H,V-I}	F+1O	516
40	-6.059 ± 0.015	-3.248 ± 0.039	-0.404 ± 0.077	0.157 ± 0.128	18.426 ± 0.028	0.008	PW _{H,V-I}	F+1O	512
41	-5.908 ± 0.014	-3.167 ± 0.040	-0.338 ± 0.067	–	18.421 ± 0.032	0.006	PW _{H,V-I} ^{CHST}	F	369
42	-5.903 ± 0.015	-3.207 ± 0.049	-0.366 ± 0.078	0.366 ± 0.259	18.325 ± 0.047	0.007	PW _{H,V-I} ^{CHST}	F	393
43	-5.915 ± 0.013	-3.133 ± 0.036	-0.369 ± 0.063	–	18.414 ± 0.028	0.008	PW _{H,V-I} ^{CHST}	F+1O	491
44	-5.922 ± 0.013	-3.156 ± 0.035	-0.322 ± 0.071	0.267 ± 0.110	18.369 ± 0.026	0.008	PW _{H,V-I} ^{CHST}	F+1O	499
45	-6.066 ± 0.015	-3.297 ± 0.041	-0.414 ± 0.072	–	18.433 ± 0.034	0.007	PW _{K_S,J-K_S}	F	381
46	-6.066 ± 0.017	-3.345 ± 0.054	-0.389 ± 0.084	0.598 ± 0.285	18.297 ± 0.056	0.007	PW _{K_S,J-K_S}	F	393
47	-6.069 ± 0.015	-3.260 ± 0.040	-0.440 ± 0.061	–	18.409 ± 0.027	0.007	PW _{K_S,J-K_S}	F+1O	500
48	-6.067 ± 0.014	-3.255 ± 0.035	-0.375 ± 0.070	0.203 ± 0.112	18.396 ± 0.025	0.007	PW _{K_S,J-K_S}	F+1O	498
49	-6.023 ± 0.016	-3.267 ± 0.047	-0.383 ± 0.077	–	18.447 ± 0.035	0.007	PW _{K_S,V-K_S}	F	381
50	-6.027 ± 0.018	-3.276 ± 0.052	-0.382 ± 0.088	0.155 ± 0.270	18.433 ± 0.049	0.007	PW _{K_S,V-K_S}	F	380
51	-6.022 ± 0.015	-3.228 ± 0.037	-0.464 ± 0.064	–	18.417 ± 0.028	0.007	PW _{K_S,V-K_S}	F+1O	503
52	-6.026 ± 0.015	-3.234 ± 0.037	-0.414 ± 0.075	0.169 ± 0.118	18.402 ± 0.027	0.008	PW _{K_S,V-K_S}	F+1O	506

$$\beta = (1.32 \pm 0.04) \cdot \lambda^{-1} + (-6.43 \pm 0.06),$$

with $rms = 0.06$, $R^2 = 0.99$. The fits shown in Fig. 3.5 ($\delta = 0$ case for the Lit. sample) for α and β are respectively

$$\alpha = (0.596 \pm 0.016) \cdot \lambda^{-1} + (-3.382 \pm 0.032),$$

with $rms = 0.035$, $R^2 = 0.99$, and

$$\beta = (1.335 \pm 0.037) \cdot \lambda^{-1} + (-6.443 \pm 0.051),$$

with $rms = 0.057$, $R^2 = 0.99$.

The inclusion of the δ parameter in the fit of the Lit. sample only determines a general decrease (in an absolute sense) in the γ values, which are closer to the $-0.2, -0.4$ mag/dex range typical of previous works. However, at the same time, the δ parameters show a considerable dependence of the *PLZ/PWZ* slopes on metallicity. If instead the δ parameter is neglected, as shown in Fig. 3.11, we again find an increase in the absolute value of γ , as already found for the Lit.+Gaia case. Figures 3.21 (a) and 3.21 (b) in Appendix 3.A report the above analysis considering only the F pulsators. A comparison of the results obtained for the F+10 and the F samples reveals no significant differences.

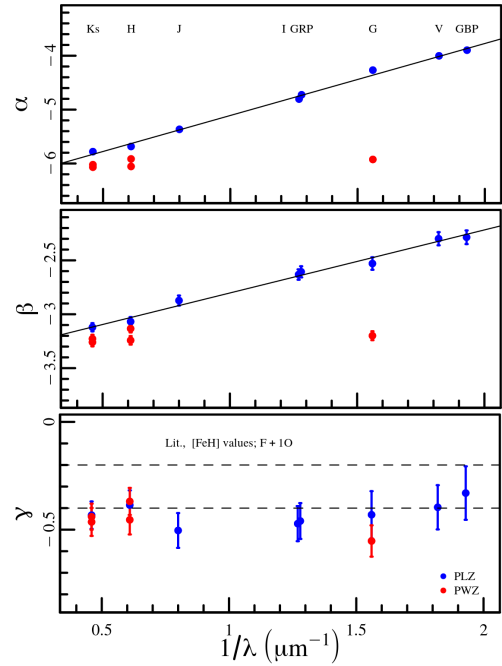


Figure 3.11: Same as Fig. 3.5 but for the Lit. sample.

3.4.3 Comparison between Lit.+Gaia and Lit. samples

It is interesting to study the impact of the inclusion of the *Gaia* DCEP sample together with the HiRes one. To this aim, we compared the estimated parameters for both cases in Figs. 3.12 and 3.13 for the *PLZ* and *PWZ* relations, respectively. While the α and β parameters seem to be quite robust, for γ and δ the Lit. sample presents slightly smaller and higher values (in an absolute sense) compared with the Lit.+Gaia data set, respectively. However, in almost all the cases, the differences are insignificant within 1σ . For this reason, we expect to find similar trends whether we use the Lit.+Gaia or the Lit. sample. Therefore, unless specified, we refer in the following discussions to the Lit.+Gaia sample only. In Appendix 3.B, the reader can find analogous figures to those shown here.

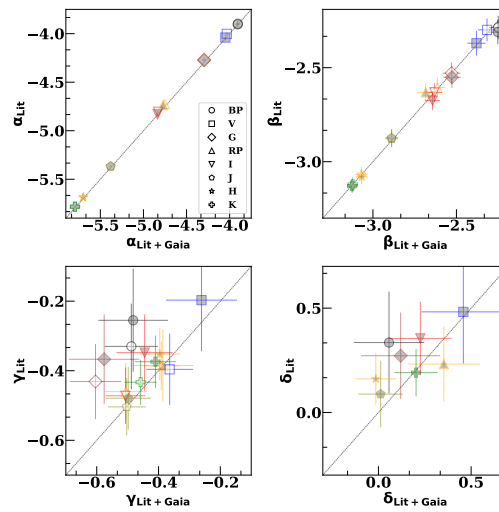


Figure 3.12: Comparison between the *PLZ* coefficients obtained with the Lit.+Gaia data set and the Lit. data set. From top-left to bottom-right, the panels show the results for the α , β , γ , and δ coefficients, respectively. For each coefficient, different photometric bands are plotted using different symbols, as labelled in the top-left panel. Grey-filled and empty symbols indicate the fit results including or excluding the δ parameter, respectively.

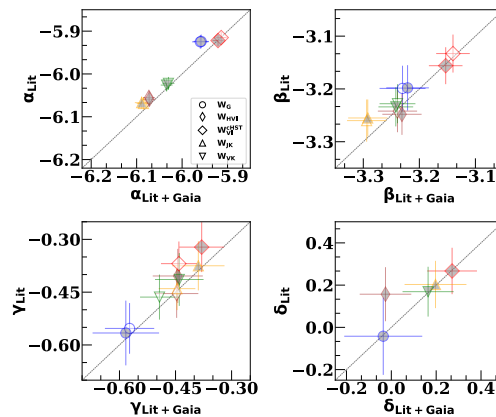


Figure 3.13: Same as Fig. 3.12 but for the *PWZ* relations.

3.5 Discussion

3.5.1 Parallax correction

A well-known feature of *Gaia* parallaxes in DR3 is the need for a global offset in the parallaxes after the L21 correction (e.g. Molinaro et al. [Mol+23] and Riess et al. [Rie+21a; Rie+22b] and references therein). The exact value of this offset is debated and appears to depend on the properties (e.g. location on the sky, magnitude, and colour) and kind of stellar tracer adopted for its estimation (see discussion in Molinaro et al. [Mol+23]). To take into account this feature, we also conducted the *PLZ/PWZ* fit after adding the global offset to the EDR3 parallax values of $-14 \mu\text{as}$ (Riess et al. [Rie+21a]) or $-22 \mu\text{as}$ (Molinaro et al. [Mol+23]). A graphical comparison between these different cases for the Lit.+Gaia sample is shown in Figs. 3.14 and 3.15 for the *PLZ* and *PWZ*, respectively. The introduction of the parallax correction increases the absolute values of α and β by 1%-4%, while γ decreases monotonically (in an absolute sense) for larger values of the parallax offset. This is particularly visible for the *PWZ* relations, which show much less scatter than the *PLZ* ones. In any case, the maximum variation is barely larger than 1σ . The δ coefficient varies less than γ with a slightly decreasing trend; although this latter is insignificant at the 1σ level.

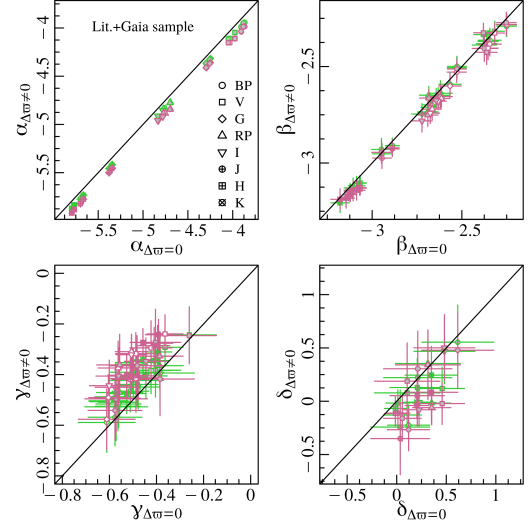


Figure 3.14: Comparison between the *PLZ* coefficients obtained for different global offset values. The coefficient values obtained without offset assumption are chosen as reference and are on the x-axis, while those obtained whilst assuming the global parallax offset by Riess et al. [Rie+21a] and Molinaro et al. [Mol+23] are on the y-axis and are plotted with green and pink symbols, respectively. From top-left to bottom-right, the panels show the results for the α , β , γ , and δ coefficients, respectively. For each coefficient, different photometric bands are plotted using different symbols, as labelled in the top-left panel, while grey-filled and white-filled symbols indicate the fit results including or excluding the δ parameter, respectively.

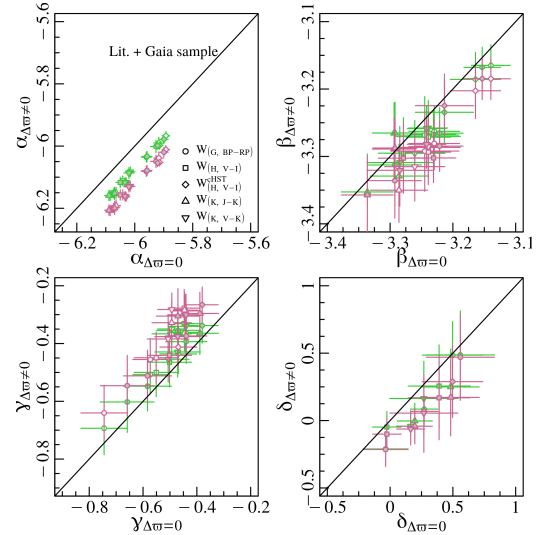


Figure 3.15: Same as Fig. 3.14 but for the *PWZ* coefficients.

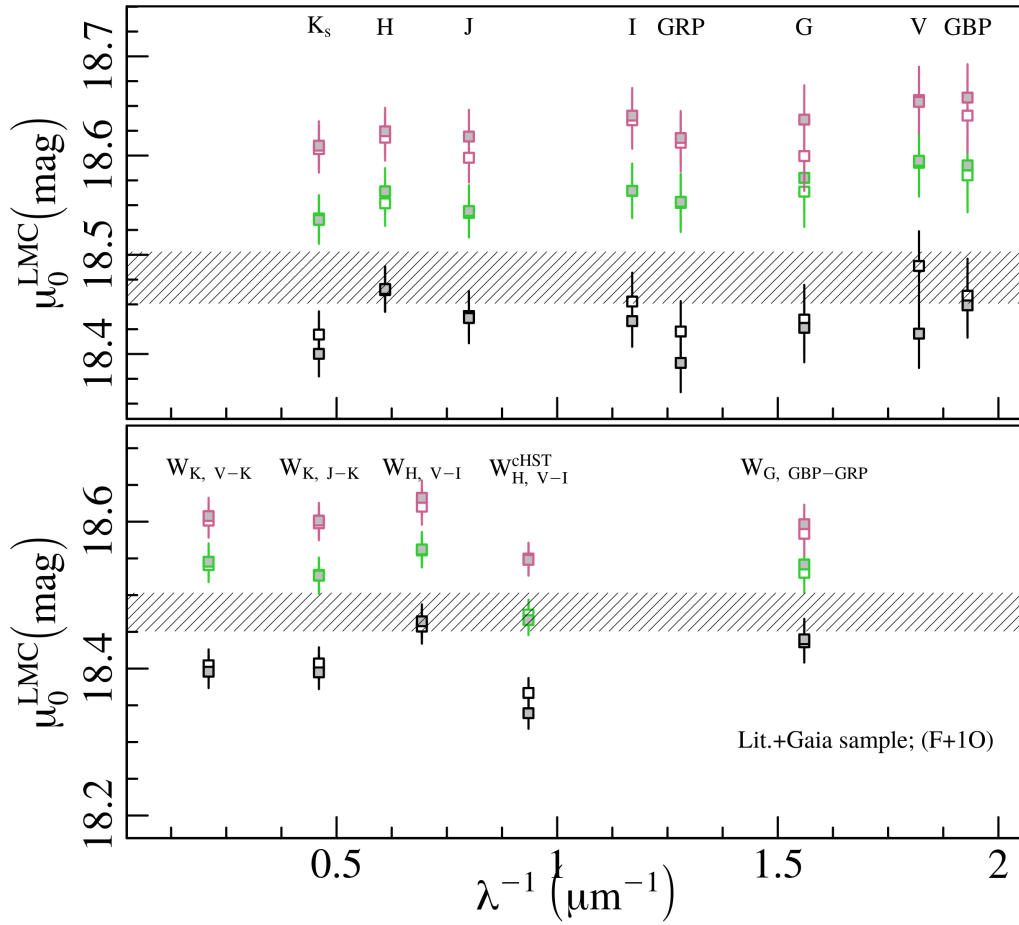


Figure 3.16: LMC distance modulus obtained using the relations of Table 3.3 for the F+10 cases plotted against the central wavelength of the considered photometric bands. To avoid labels and symbols overlapping, the I band result has been shifted by $-0.1\mu m^{-1}$. The top panel shows the results for the *PLZ* relations, while the bottom panel shows those for the *PWZ* relations. Different colours indicate the results obtained for different parallax shift values: L21 correction (black squares), L21 + Riess et al. [Rie+21a] offset (green squares), L21 + Molinaro et al. [Mol+23] (violet squares). Empty and grey-filled squares indicate the results obtained excluding and including the δ coefficient, respectively.

Overall, these effects have already been found and are coherent with those discussed in Rippepi et al. [Rip+21a]. In practice, the introduction of a significant global parallax zero point offset tends to reconcile our metallicity dependence with typical literature values, as γ tends to diminish with increasing offset (both in an absolute sense). However, as discussed in the following section, the adoption of large offset values affects the absolute distance scale.

3.5.2 Distance to the LMC

To test the goodness of our *PLZ/PWZ* relations and to understand which parameter affects the calibration, we used our relations to estimate the distance to the LMC and compared the results with the currently accepted geometric value $\mu_0 = 18.477 \pm 0.026$ mag (Pietrzyński et al. [Pie+19]). To this aim, we used the method described in detail in Ripepi et al. [Rip+21a]. The distance moduli μ_0^{LMC} obtained in this way are listed in Tables 3.3 and 3.4 for the Lit.+Gaia and Lit. samples, respectively. The samples including only F pulsators generally give poorer results than the F+10 sample, and therefore in the following discussion we use only the latter data set. Figure 3.16 shows the resulting μ_0^{LMC} for the *PLZ/PWZ* relations for Lit.+Gaia samples. The introduction of the global parallax correction worsens the distance estimation. More precisely, the results with no correction and with Riess et al. [Rie+21a] correction are very close to the lower and upper allowed limit, respectively. This suggests for the correction an intermediate value between the two cases, with the exception of $W_{H,V-I}^{cHST}$ where Riess et al. [Rie+21a] correction perfectly adjusts the value of μ_0^{LMC} . Therefore, if we use the Pietrzyński et al. [Pie+19] distance of the LMC as a reference, we have to conclude that the rather

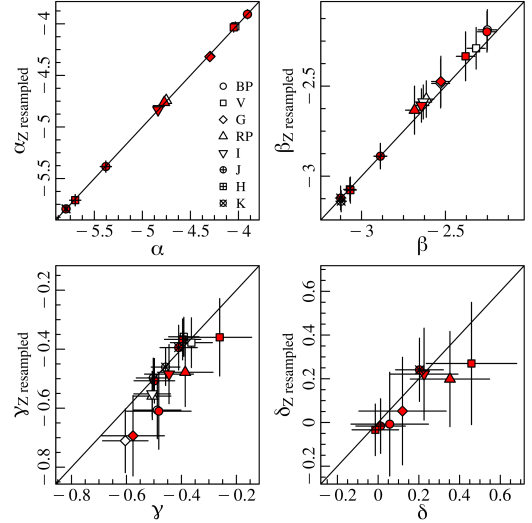


Figure 3.17: Comparison between the *PLZ* coefficients obtained with the resampling in metallicity with those obtained using the entire data set. From top-left to bottom-right, the panels show the results for the α , β , γ , and δ coefficients, respectively. For each coefficient, different photometric bands are plotted using different symbols, as labelled in the top-left panel. In contrast, red-filled and white-filled symbols indicate the fit results including or excluding the δ parameter, respectively.

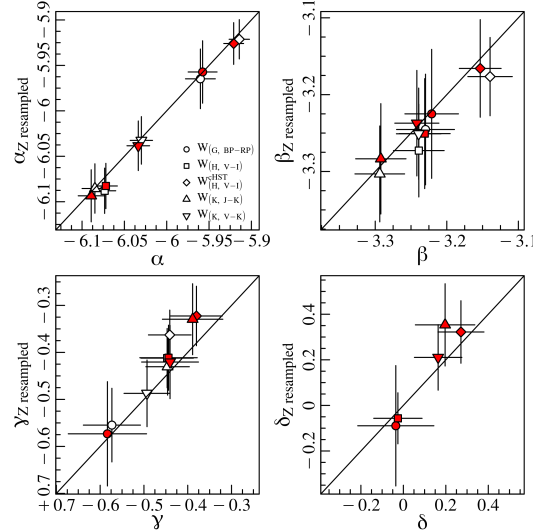


Figure 3.18: Same as Fig. 3.17, but for the *PWZ* coefficients.

large values of γ found in this work are favoured over the smaller ones from the recent literature.

3.5.3 Metallicity sampling

Although the results of our C-MetaLL project considerably enlarged the number of DCEPs with $[Fe/H] < -0.5$ dex, these objects represent less than 10% of the pulsators used in this work, while the majority of the sources are distributed around the solar value. To test whether this unbalanced metallicity distribution could affect our determination of the PLZ/PWZ relations, we conducted an experiment in order to recalculate these relationships by resampling the input data such that its metallicity distribution is uniform over the whole range. To this aim, we divided the sample into five bins in metallicity, imposing the same number of stars in each bin.

As there are few stars in the low-metallicity regime, the sources with $[Fe/H] < -0.5$ dex were all kept in the same bin and their number, $N_{[Fe/H < -0.5]} = 44$ (considering the astrometric selection described in Sect. 3.2.3), set the number of pulsators included in each of the four remaining bins, whose size is approximately 0.25 dex in metallicity. The DCEPs populating each bin, apart from the lowest metallicity one, were randomly picked. Having resampled the data, we carried out the fit as in Sect. 3.3 considering the Gaia+Lit. data set only, given that the other cases provide similar results. We also restricted the test to the F+1O sample, because the number of F pulsators in the most metal-poor bin is less than half of the F+1O combined sample, meaning that the total number of DCEPs used for the fit would be too small to achieve meaningful results. We repeated 10,000 times the fitting procedure, obtaining a distribution of values for the α , β , γ , and δ coefficients. Their median values and relative uncertainties (scaled median absolute deviation (MAD)) are compared with the results obtained using the entire sample in Fig. 3.17 and 3.18 for PLZ and PWZ , respectively. Both figures show excellent agreement for all of the coefficients. Therefore, we can conclude that the results obtained in this work are not affected by the unbalanced metallicity distribution of the sample.

3.5.4 Comparison with the literature

Figure 3.19 shows several empirical estimations of γ throughout the last 20 years. Results from the present work are also plotted, considering the case of the Lit.+Gaia data sample. In more detail, different techniques have been used in order to analyse the metallicity effect on the PL and PW relations. Early studies adopting distances from the Baade-Wesselink (BW) analysis (e.g. Groenewegen [Gro13] and Storm



Figure 3.19: Literature estimation of the γ coefficient for *PLZ* (left panel) and *PWZ* (right panel) relations over the last 20 years. Bands are divided by colour and sorted by year of publication from bottom to top. Symbols correspond to the method used to derive the metallicity coefficient. The vertical shaded region corresponds to the range of intervals between -0.4 and -0.2 mag/dex (see text for detail). For the complete list of sources, see Fig.1 from Romaniello et al. [Rom+08] and Table 1 from Breuval et al. [Bre+22].

et al. [Sto+04; Sto+11]) reported very small values for the γ parameter in the V , I , and K bands and in the W_{JK} , W_{VK} , and W_{VI} Wesenheit magnitudes. More recently, a stronger effect ($\gamma \sim -0.2$ mag/dex) —albeit weaker than the effect found in the present work— was found in the same bands by Gieren et al. [Gie+18] from a BW analysis of DCEPs in the Galaxy, LMC, and SMC, which were used to extend the range of metallicity of the pulsators adopted in the analysis. The advent of *Gaia* DR2 parallaxes permitted us to obtain the first reliable evaluation of the γ term using only Galactic DCEPs with metallicities from HiRes spectroscopy. In particular, Groenewegen [Gro18] and later Ripepi et al. [Rip+19; Rip+20] found $\gamma \sim -0.1 - 0.4$ mag/dex in a variety of bands and Wesenheit magnitudes (see Fig. 3.19), which is closer to the values found in this paper, but with a significance of generally lower than 1σ , owing to the still insufficient precision of DR2 parallaxes. The improved *Gaia* EDR3 parallaxes instead allowed us to obtain larger (in an absolute sense) γ values in the first paper of the C-MetaLL project (Ripepi et al. [Rip+21a]) and for the W_G magnitude (Ripepi et al. [Rip+22]). Other studies (Breuval et al. [Bre+21; Bre+22], Fouqué et al. [Fou+07], Groenewegen et al. [Gro+04], and Wielgórski et al. [Wie+17]), together with the already quoted Gieren et al. [Gie+18], compared the properties (i.e. the zero points of the PL or PW relations) of the DCEPs in the MW and in the more metal-poor galaxies LMC and SMC to estimate the extent of the γ value. In particular, Breuval et al. [Bre+21; Bre+22], used geometric distances for the DCEPs in the MW (from *Gaia* EDR3 parallaxes) and in the Magellanic Clouds (from eclipsing binaries) to estimate γ in the same bands and Wesenheit magnitudes as those treated in the present work, after fixing the slope of the PL and PW relations to that of the LMC, with results ranging between -0.178 and -0.462 mag/dex. In the context of the SH0ES project (Riess et al. [Rie+16; Rie+19; Rie+21a; Rie+22b]), the metallicity effect is one of the outputs of the process for the estimation of H_0 . In these cases, the γ coefficient in the $W_{H,V-I}^{HST}$ magnitude used by the SH0ES team is of the order of -0.2 mag/dex, while we obtain a slightly larger (in an absolute sense) value in our best case, that is, with the Lit.+*Gaia* sample without the δ term (see e.g. Fig. 3.5).

Recent theoretical studies (Anderson et al. [And+16] and De Somma et al. [De+22]) also predict mild effects of the metallicity, with γ ranging from -0.27 to -0.13 mag/dex, although we note that the models by De Somma et al. [De+22] only deal with PW relations.

We notice that in almost all cases, we find larger γ values (in an absolute sense) than the literature, although most of them are distributed along the lower limit in the literature of -0.4 mag/dex (see also Fig. 3.4). On the other side, for the V -band a smaller coefficient is found, in agreement with the upper limit of -0.2 mag/dex.

3.6 Conclusion

In this fourth paper of the C-MetaLL series, we studied the metallicity dependence of the PL relations in the following bands: G_{BP} , G_{RP} , G , I , V , J , H , and K_S , and of the PW relations in the following Wesenheit magnitudes: $W_{G, BP-RP}$, $W_{H, V-I}$, $W_{H, V-I}^{cHST}$, $W_{J, J-K}$, and $W_{V, V-K}$. To this end, we exploited the literature to compile a sample of 910 DCEPs with $[Fe/H]$ measured from HiRes spectroscopy and complemented it with a number of stars with metallicity measurements based on the *Gaia* RVS instrument as released in DR3. For all these stars, we provide a table with photometry in the G_{BP} , G_{RP} , G , I , V , J , H , and K_S bands, metallicity, and astrometry from *Gaia* DR3.

We carried out our analysis adopting two different samples: one composed only of literature data and one including both the latter and *Gaia* DR3 results. In order to estimate the parameters of the PLZ/PWZ relations, we used the ABL formalism, which allowed us to treat the parallax ϖ linearly and to preserve the statistical properties of its uncertainties. We considered two functional forms for the PLZ and PWZ relations including (i) the metallicity dependence on the intercept only (three-parameter case); and (ii) the metallicity dependence on both intercept and slope (four-parameter case). The main findings of our analysis can be summarised as follows:

1. Regarding PLZ relations, both α and β show a linear dependence on wavelength. We provide the linear relationships between these quantities and λ^{-1} . These relations do not change considerably when we use the Lit.+Gaia or Lit. samples, nor when we carry out a three- or four-parameter fit. Because of the low wavelength coverage, no clear dependence can be discussed for the PWZ relations.
2. A clear negative dependence of the intercept on metallicity (γ -coefficient) is found for all the PL and PW relations. For the three-parameter solutions, the values of γ are around $-0.4 : -0.5$ dex with no clear dependence on wavelength. Thus, this work confirms our previous results reported by Molinaro et al. [Mol+23] and Ripepi et al. [Rip+21a]. For the four-parameter solutions, the values of γ generally slightly decrease (in an absolute sense), especially for the Lit. only sample. In general, the γ coefficients found in this work are larger (in an absolute sense) than those in the literature, which range between -0.2 and -0.4 dex.
3. The dependence of the slope on metallicity (δ coefficient) remains undetermined. Indeed, in about half of the cases, δ assumes values comparable with

zero within 1σ for the Gaia+Lit. sample, while, especially in the Lit. case, δ generally assumes a positive value comprised between 0 and +0.5.

4. The main difference between using the F and F+1O samples is that larger error bars are found in the former case, especially for the γ and δ coefficients.
5. The inclusion of global zero point offset to the individually corrected parallaxes according to L21 has a larger impact on the γ coefficients than on the δ ones. More specifically, the adoption of offsets by $-14 \mu\text{as}$ (Riess et al. [Rie+21a]) and $-22 \mu\text{as}$ (Molinaro et al. [Mol+23]) implicates smaller and smaller values of γ (in an absolute sense), which is in better agreement with recent literature. However, if we use the geometric distance of the LMC by Pietrzyński et al. [Pie+19] as a reference and calculate the distance of this galaxy using our relations with and without the global offset, we find that good agreement for the distance of the LMC is found for values of the offset in between null and the $14 \mu\text{as}$ values. It is worth noting that for the $W_{cH,V-I}^{cHST}$ magnitude Riess et al. [Rie+21a] offset represents the best correction. These results support larger values (in an absolute sense) of the γ value.
6. We investigated the possible effect of an uneven distribution in the metallicity of the sample used in this work by resampling our data set in order to have a balanced number of DCEPs at every metallicity value. We carried out the fitting procedure on 10,000 samples extracted from the total sample, obtaining a value for the four coefficients of the fit for every data set. The medians of the obtained distributions for all the coefficients appear to be in excellent agreement with those obtained using the entire sample. Therefore, we can conclude that the results obtained in this work are not affected by the sample's unbalanced distribution in metallicity.

The results presented in this paper show the importance of the extension of the metallicity range when carrying out the analysis. Further observations in order to gather HiRes spectroscopy of MW metal-poor DCEPs will offer the opportunity to better constrain the dependence on the metallicity of both the intercept and the slope. In particular, regions in the Galactic anti-centre direction are the most promising targets for future observations, where DCEPs are expected to have $[\text{Fe}/\text{H}] < -0.3 : -0.4$ dex, and can therefore be used to further populate the metal-poor tail of the DCEP distribution.

Acknowledgements

We thank our anonymous Referee for their helpful comments which helped us to improve the paper. We warmly thank A. Riess for useful discussion on this paper and L. Breuval for indicating us the presence of a typo in one of equation from the literature that we used in this work. Part of this work was supported by the German *Deutsche Forschungsgemeinschaft*, DFG project number Ts 17/2–1.

This work has made use of data from the European Space Agency (ESA) mission Gaia (<https://www.cosmos.esa.int/gaia>), processed by the Gaia Data Processing and Analysis Consortium (DPAC, <https://www.cosmos.esa.int/web/gaia/dpac/consortium>). Funding for the DPAC has been provided by national institutions, in particular, the institutions participating in the Gaia Multilateral Agreement.

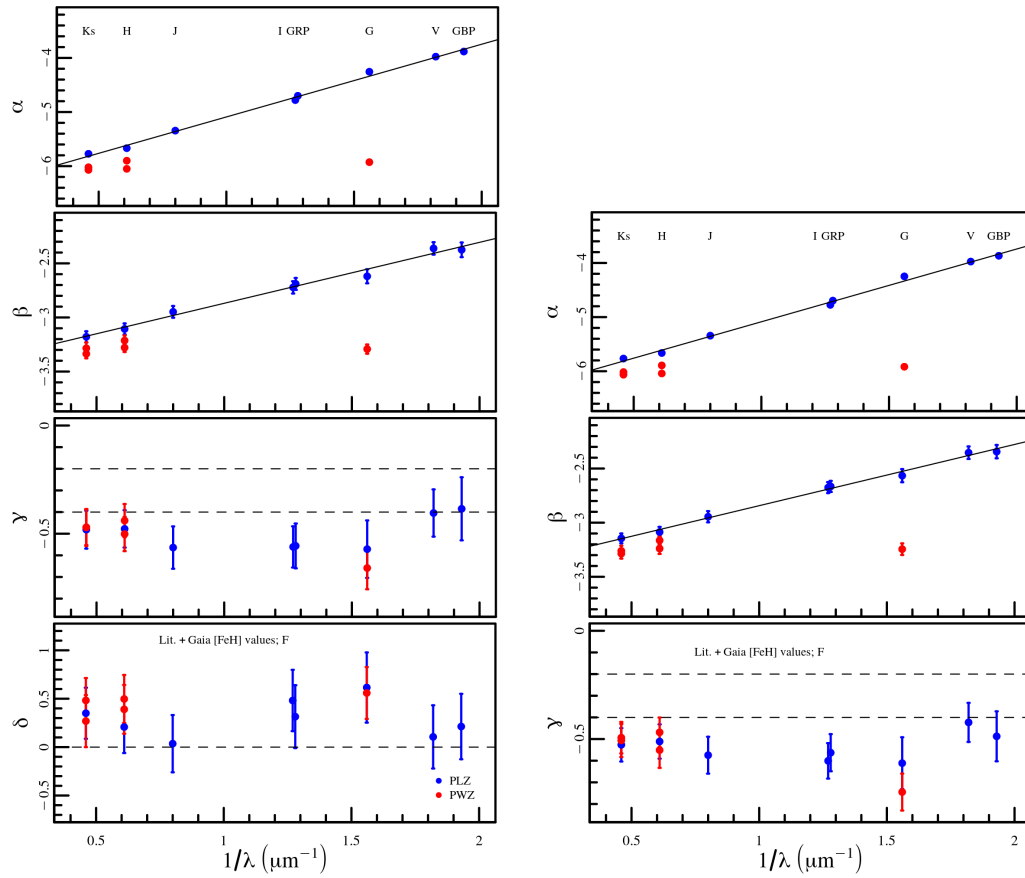
This research has made use of the VizieR catalogue access tool, CDS, Strasbourg, France. This research has made use of the SIMBAD database, operated at CDS, Strasbourg, France. I.M. acknowledges partial financial support by INAF, Minigrant "Are the Ultra Long Period Cepheids cosmological standard candles?" We acknowledge funding from INAF GO-GTO grant 2023 "C-MetaLL - Cepheid metallicity in the Leavitt law" (P.I. V. Ripepi)

3.A PLZ/PWZ coefficients for the F pulsators only sample

For completeness, we provide figures that are analogous to Fig. 3.4, Fig. 3.5, Fig. 3.10, and Fig. 3.11, showing the fit results of the sample Lit.+Gaia and Lit. including only the F pulsators.

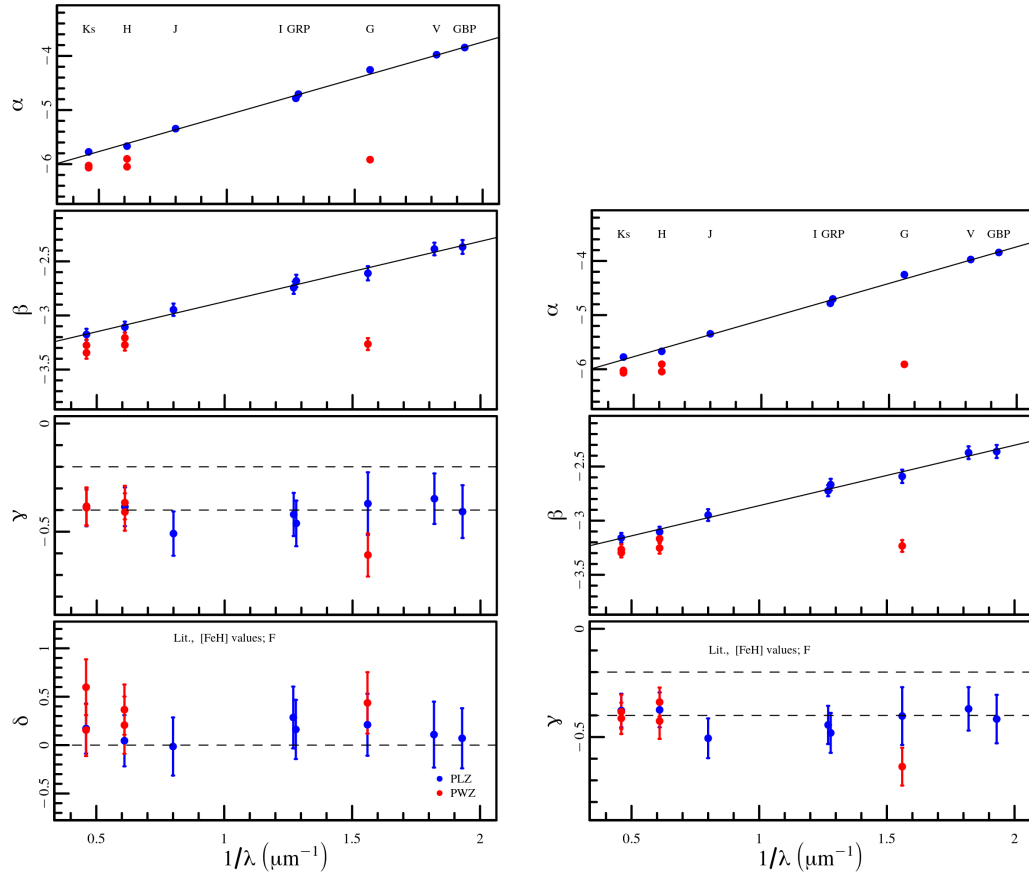
3.B Parallax correction for the Lit. sample

Here, we provide figures analogues to Fig. 3.14, Fig. 3.15, and Fig. 3.16 for the Lit. sample.



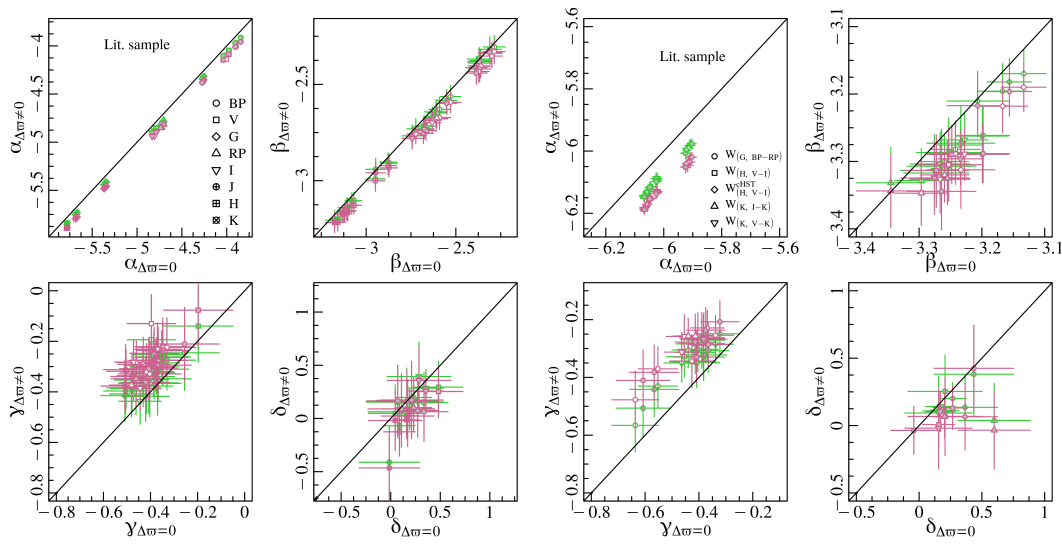
(a) Same as Fig. 3.4 but for the Lit.+Gaia data set (b) Same as Fig. 3.5 but for the Lit.+Gaia data set including only F pulsators.

Figure 3.20



(a) Same as Fig. 3.10 but for the Lit. data set (b) Same as Fig. 3.11 but for the Lit. data set including only F pulsators.

Figure 3.21



(a) Same as Fig. 3.14 but for the Lit. sample.

(b) Same as Fig. 3.15 but for the Lit. sample.

Figure 3.22

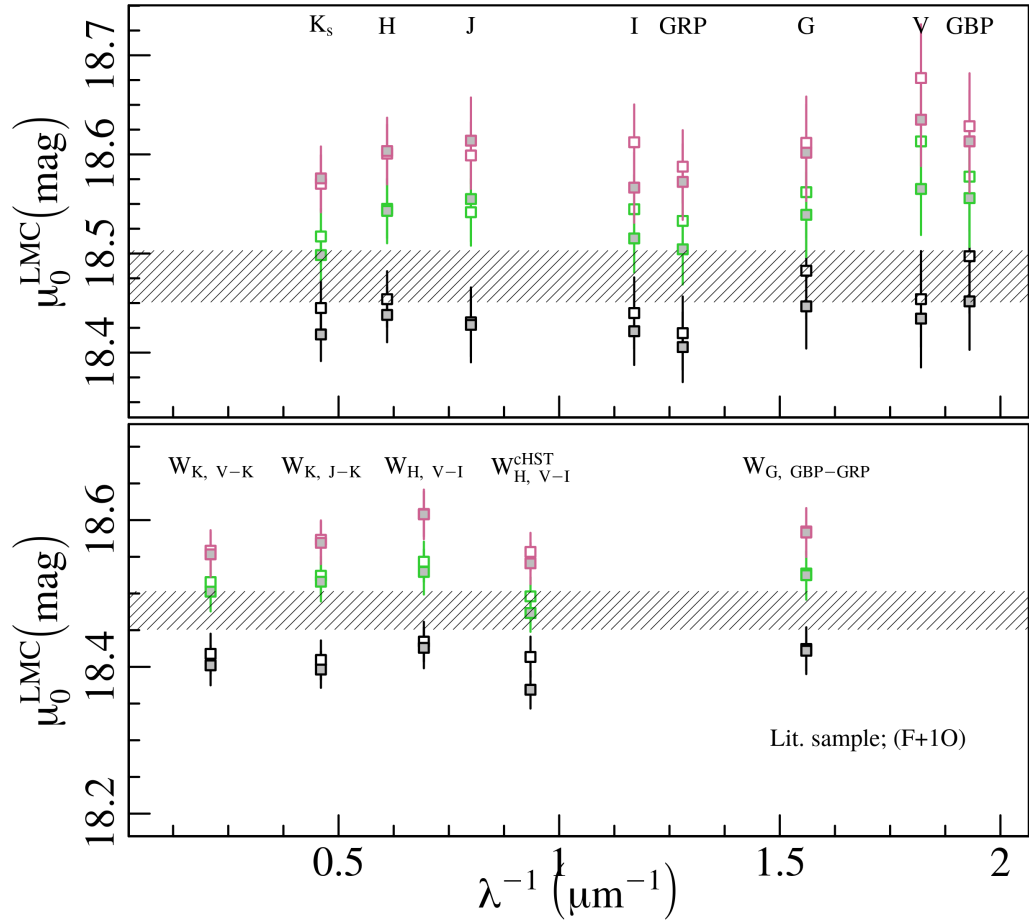


Figure 3.23: Same as Fig. 3.16 but for the Lit. sample.

4

Cepheid Metallicity in the Leavitt Law (C- MetaLL) survey: VI: Radial abundance gradients of 29 chemical species in the Milky Way disc

E. Trentin, G. Catanzaro, V. Ripepi, J. Alonso-Santiago, R. Molinaro, J. Storm, G. De Somma, M. Marconi, A. Bhardwaj, M. Gatto, I. Musella, V. Testa,

This paper was published in A&A, Volume 690, id.A246, 16 pp.¹³

4.1 Introduction

Classical Cepheids (DCEPs) play a fundamental role as standard candles in determining extragalactic distances due to the Leavitt law (Leavitt and Pickering [LP12]), a relationship between period and luminosity (PL). Calibrated using independent distances based on geometric methods such as trigonometric parallaxes, eclipsing binaries, and water masers, these relations serve as the first step in constructing the cosmic distance scale. This way, they calibrate secondary distance indicators, including type Ia supernovae (SNe Ia), allowing us to measure the distances of distant galaxies in the steady Hubble flow. The calibration of this three-step procedure, often referred to as the cosmic distance ladder, enables us to reach the Hubble flow and measure the Hubble constant, H_0 , which connects the distance and the recession velocity of galaxies (e.g. Freedman et al. [Fre+12], Riess et al. [Rie+16], and Sandage and Tammann [ST06] and references therein).

In recent years, a still unresolved debate has taken place regarding the well-known discrepancy between the values of H_0 obtained by the SH0ES¹⁴ project through the cosmic distance ladder ($H_0 = 73.01 \pm 0.99 \text{ km s}^{-1} \text{ Mpc}^{-1}$, Riess et al. [Rie+22b]) and the value computed by the Planck cosmic microwave background (CMB) project based on the flat Λ cold dark matter (Λ CDM) model ($H_0 = 67.4 \pm 0.5 \text{ km s}^{-1} \text{ Mpc}^{-1}$, Planck Collaboration et al. [Pla+20]). If no solution is found for this intricate H_0 tension, this could hint at the need for a revision of the

¹³ Based on the European Southern Observatory programs 108.227Z; 109.231T; 110.23WM and on the Telescopio Nazionale Galileo programmes A43TAC_16; A44TAC_27; A45TAC_12; A46TAC_15. Based on observations obtained at the Canada-France-Hawaii Telescope (CFHT) which is operated by the National Research Council of Canada, the Institut National des Sciences de l'Univers of the Centre National de la Recherche Scientifique of France, and the University of Hawaii.

¹⁴ Supernovae, HO, for the Equation of State of Dark energy

Table 4.1: Main properties of the 180 programme DCEPs. Meaning of the columns: Star = literature name of the DCEP, Gaia_source_id= Gaia DR3 identifier, RA, Dec = equatorial co-ordinates at J2000, Period and Mode = period and mode of pulsation; DCEP_F, DCEP_IO, and DCEP_MULTI refer to fundamental, first overtone, and multimode DCEPs, respectively. G , G_{BP} , and G_{RP} are the magnitudes in the Gaia bands. ω and σ are the Gaia parallax and its error. D and σ are the distances and its error. Source shows the instrument used to observe the star. Notes report the origin of the periods (and modes) as well as of the photometry: 'SOS' means that the periods and the photometry come from Gaia DR3 using the specific pipeline for the DCEP variables (see Kipepi et al. [Rip+23]); 'DR3' means that the photometry is from the general DR3 source (see GaiaVallenari, while 'P21' means that the periods are from Piet2021. Note that the distances for the four stars most likely classified as type II Cepheids are probably wrong (see Appendix 4.A). A portion of the Table is shown here for guidance regarding its form and content. The machine-readable version of the full table will be published at the Centre de Données astronomiques de Strasbourg (CDS, <https://cds.u-strasbg.fr/>).

Star	Gaia_source_id	RA deg	Dec deg	Period days	Mode	G mag	G_{BP} mag	G_{RP} mag	ω mas	σ mas	D kpc	σ kpc	Source	Notes
AA Gem	3430067092837622272	06:06:34.95	+26:19:45.2	11.31285	DCEP_F	9.363	9.956	8.62	0.2749	0.0177	3.81	0.11	ESPaDOnS	SOS,SOS
AD Pup	5614312705966204288	07:48:03.85	-25:34:40.0	13.59738	DCEP_F	9.541	10.125	8.786	0.2331	0.0165	0.82	0.04	ESPaDOnS	P21,DR3
AP Sgr	4066429066901946368	18:13:02.50	-23:07:02.3	5.05808	DCEP_F	6.922	7.46	6.219	1.1815	0.024	2.85	0.12	ESPaDOnS	SOS,SOS
AQ Pup	5597379741549105280	07:58:22.09	-29:07:48.3	30.15959	DCEP_F	8.127	8.974	7.25	0.2751	0.0226	3.98	0.14	ESPaDOnS	SOS,SOS
ASAS-SN J065046.50-085808.7	3050543819559526912	06:50:46.50	-08:58:08.8	6.94564	DCEP_F	13.49	14.402	12.547	0.1198	0.0179	2.66	0.10	UVES,P110	SOS,SOS

Λ CDM model. It is therefore critical to evaluate the discrepancy through the analysis of the residual systematics (see e.g. Dainotti et al. [Dai+21], Freedman [Fre21], and Riess et al. [Rie+21b] and reference therein).

Metallicity may play an important role as one of the possible residual sources of uncertainty in the cosmic distance ladder, influencing the calibration of the DCEP PL relations. Since the shape and width of the DCEP instability strip are predicted to be affected by metallicity variations (e.g. Caputo et al. [Cap+00]), a direct consequence should be seen when estimating the PL relations coefficients De Somma et al. [De +22] and Marconi et al. [Mar+10; MMF05] and references therein). To avoid systematic effects in the calibration of the extragalactic distance scale (e.g. Bono et al. [Bon+10], Riess et al. [Rie+16], and Romaniello et al. [Rom+08]), one has to also consider the metallicity dependence of the PL relations and the reddening-free Wesenheit magnitudes (Madore [Mad82]) in those cases in which the metallicity effect might be small, such as when dealing with the near-infrared regime (NIR, see e.g. Fiorentino et al. [FMM13] and Gieren et al. [Gie+18]).

In the past, the lack of accurate independent distances hampered direct empirical evaluations of the metallicity dependence of PL relations using Galactic DCEPs with precise $[Fe/H]$ measurements based on high-resolution (HiRes hereafter) spectroscopy, but this scenario completely changed with the advent of the *Gaia* mission (Gaia Collaboration et al. [Gai+16]). Accurate parallaxes were provided with data release 2 (DR2, Gaia Collaboration et al. [Gai+18] and further improved with the early data release 3 (EDR3, Gaia Collaboration et al. [Gai+21]), in addition to the discovery of hundreds of new Galactic DCEPs (Clementini et al. [Cle+19] and Ripepi et al. [Rip+19; Rip+22]). A substantial sample can thus be considered when other surveys are taken into consideration, such as the Optical Gravitational Lensing Experiment (OGLE) Galactic Disk survey (Udalski et al. [Uda+18]) and the Zwicky Transient Facility (ZTF, Chen et al. [Che+20]), making it possible to improve not only studies related to the cosmic distance scale but also Galactic studies (e.g. Lemasle et al. [Lem+22] and Trentin et al. [Tre+23] and references therein). Another constraint was the limited availability of HiRes measurements confined to the solar neighbourhood. This restriction resulted in a narrow range of $[Fe/H]$ values centred on solar or slightly supersolar values, with a small dispersion of 0.2-0.3 dex (e.g. Genovali et al. [Gen+14], Groenewegen [Gro18], Luck [Luc18], and Ripepi et al. [Rip+19]). Consequently, this limitation hindered the ability to generate results with statistical significance.

To overcome these problems, we started a project named C-MetaLL¹⁵ (Cepheid - Metallicity in the Leavitt Law, see Ripepi et al. [Rip+21a] for a full description),

¹⁵ <https://sites.google.com/inaf.it/c-metall/home>

Table 4.2: Estimated chemical abundances for the 180 analysed DCEPs. The table is divided into three parts. The first and last columns report the name of the star and the source, respectively (see Table 4.3 and 4.1). The other columns report the estimated abundances (and relative errors) in solar terms for the chemical species analysed in this work. The machine-readable version of the full table will be published at the Centre de Données astronomiques de Strasbourg (CDS, <https://cds.u-strasbg.fr/>).

Star	[C/H]	[O/H]	[Na/H]	[Mg/H]	[Al/H]	[Si/H]	[S/H]	[Ca/H]	[Sc/H]	[Ti/H]	...
AA Gem	-0.54 ± 0.03	-0.04 ± 0.09	0.16 ± 0.1	0.14 ± 0.05	0.11 ± 0.09	-0.24 ± 0.1	-0.12 ± 0.02	-0.09 ± 0.02	0.23 ± 0.06	0.04 ± 0.08	...
AD Pup	-0.41 ± 0.11	0.16 ± 0.11	0.16 ± 0.19	0.39 ± 0.03	0.14 ± 0.11	-0.22 ± 0.11	-0.06 ± 0.01	-0.19 ± 0.09	0.17 ± 0.09	0.05 ± 0.11	...
AP Sgr	-0.22 ± 0.11	0.2 ± 0.11	-0.03 ± 0.16	0.1 ± 0.1	0.23 ± 0.11	0.01 ± 0.1	0.17 ± 0.02	0.05 ± 0.05	0.3 ± 0.06	0.09 ± 0.1	...
...	[V/H]	[Cr/H]	[Mn/H]	[Fe/H]	[Co/H]	[Ni/H]	[Cu/H]	[Zn/H]	[Sr/H]	[Y/H]	...
...	0.05 ± 0.07	-0.09 ± 0.04	-0.28 ± 0.04	-0.15 ± 0.07	-0.17 ± 0.05	-0.02 ± 0.09	0.03 ± 0.1	0.04 ± 0.2	0.21 ± 0.09	-0.29 ± 0.08	...
...	0.06 ± 0.07	-0.13 ± 0.08	-0.32 ± 0.1	-0.13 ± 0.08	0.06 ± 0.06	-0.13 ± 0.11	-0.2 ± 0.11	-0.35 ± 0.11	0.28 ± 0.11	-0.22 ± 0.09	...
...	0.0 ± 0.1	-0.02 ± 0.09	-0.26 ± 0.05	-0.02 ± 0.09	0.62 ± 0.04	0.25 ± 0.11	-0.15 ± 0.13	-0.18 ± 0.13	0.25 ± 0.11	-0.19 ± 0.01	...
...	[Zr/H]	[Ba/H]	[La/H]	[Ce/H]	[Pr/H]	[Nd/H]	[Sm/H]	[Eu/H]	[Gd/H]	Source	...
...	0.24 ± 0.34	0.04 ± 0.05	0.22 ± 0.07	0.16 ± 0.09	-0.3 ± 0.09	0.15 ± 0.07	0.12 ± 0.05	—	0.22 ± 0.09	ESPaDOnS	...
...	0.17 ± 0.41	0.32 ± 0.11	0.02 ± 0.11	-0.01 ± 0.11	-0.4 ± 0.11	0.15 ± 0.09	0.14 ± 0.1	—	0.31 ± 0.11	ESPaDOnS	...
...	0.32 ± 0.37	0.21 ± 0.11	-0.02 ± 0.02	-0.13 ± 0.11	-0.21 ± 0.11	0.09 ± 0.1	0.09 ± 0.09	—	-0.03 ± 0.11	ESPaDOnS	...

with the primary goal of measuring the chemical abundance of a sample of at least 300 Galactic DCEPs through HiRes spectroscopy, as well as providing homogeneous multi-band time-series photometry. The main aim was to enlarge the iron abundance range towards the metal-poor regime – that is, $[\text{Fe}/\text{H}] < -0.4$ dex – in which only a few Galactic stars had abundance measurements in the literature. In the first two papers of the series (Ripepi et al. [Rip+21a] and Trentin et al. [Tre+23]) (R21 and T23 from now on, respectively), we published accurate abundances for more than 25 chemical species for a total of 114 DCEPs, while the first results for the photometric part were presented in Bhardwaj2024. In particular, in T23, we obtained measurements for 43 objects with $[\text{Fe}/\text{H}] < -0.4$ dex, reaching abundances as low as -1.1 dex. This paper represents the sixth manuscript in the series and a direct follow-up of T23, presenting the spectroscopic analysis of 180 new stars based on a total of 331 HiRes spectra and the study of the galactic gradient for 29 chemical elements.

While the main scope of this work is to study the metallicity dependence of the DCEP PL relations in the context of the extragalactic distance scale, the sample of DCEPs presented in this work, in conjunction with our previous results, nevertheless amounts to a total of 294 DCEPs with a homogeneous derivation of stellar parameters and abundances. In addition, as we shall see later in this article, our sample is evenly distributed in metallicity, spanning a range from $+0.5$ dex to -1 dex in $[\text{Fe}/\text{H}]$ and 5 to 20 kpc in Galactocentric radius. The aforementioned characteristics make our sample an appropriate testing ground for the study of the Galactic disc abundance gradient, in comparison with literature works that in general use heterogeneous spectroscopic samples or datasets heavily unbalanced towards the solar vicinity (daSilva2023; Matsunaga2023; Lemasle et al. [Lem+18], Luck [Luc18], Minniti et al. [Min+20], and Ripepi et al. [Rip+22]).

The paper is organised as follows: in Sect. 4.2, we describe the sample of DCEPs and their properties; in Sect. 4.3, we describe the analysis technique; in Sect. 4.4 and Sect. 4.5, we describe and discuss our results; and in Sect. 4.6, we outline our conclusions.

4.2 Observations

4.2.1 Sample

The sample of DCEPs presented in this work was selected from the DCEP catalogue published in *Gaia* data release 3 (DR3 Ripepi et al. [Rip+23]). We chose the pulsators with the intention of maximising the number of objects with low metallicity and

long periods. This is because the main scope of the C-MetaLL survey is to derive accurate PL and PW relations for Galactic DCEPs. To this aim, we have had to enlarge the range covered by the independent variables in the quoted relations as much as possible; namely, periods and metallicities. Therefore, we have had to observe both short- and long-period DCEPs as well as metal-rich and metal-poor pulsators. While the periods are known, the metallicity can only be guessed based on the position of the stars in the disc, which, as was mentioned in the previous section, is well known to exhibit a metallicity gradient from the centre to the anti-centre of the Galaxy. Thus, our observations aimed to maximise the most distant objects in the anticentre direction, possibly those with longer periods, which are rarer (since their evolutionary times are faster than those of shorter-period DCEPs). The list of the 180 targets is shown in Table 4.1, in which we list the main characteristics of the stars, including their periods, modes of pulsation, and distances.

These last quantities were calculated based on the PWZ relation published by Ripepi et al. [Rip+22] with the procedure outlined in detail in Sect. 2.2 of **GaiaDrimmel2023**. In brief, we used *Gaia* photometry (see Table 4.1) to calculate the apparent Wesenheit magnitude $W = G - 1.90 \times (G_{BP} - G_{RP})$ (Ripepi et al. [Rip+19]). Then, we inserted the periods and $[Fe/H]$ values (measured in this paper) in the quoted PWZ to obtain the absolute W magnitude. The distance calculation was then straightforward, using the definition of distance modulus. The conversion in Galactocentric radii R_{GC} was obtained in the usual way, adopting a distance of the Sun from the Galactic centre, $R_{\odot} = 8277 \pm 9(\text{stat}) \pm 30(\text{sys})$

pc (Gravity Collaboration et al. [Gra+22]) (for full details, we refer the reader to **GaiaDrimmel2023**). The distribution of the targets along the Milky Way (MW) disc is displayed in Fig. 4.1. The distribution of the programme stars ranges from about 5 to 18 kpc in Galactocentric radii (R_{GC}) and covers all four Galactic quadrants, with a significant concentration in the third. In the figure, the stars are colour-coded according to their periods. The period distribution shows short-period DCEPs at larger Galactic radii, especially in the third quadrant. This is not

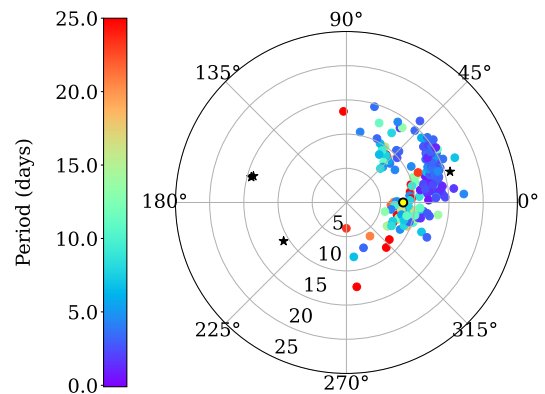


Figure 4.1: Map along the Galactic disc of the programme stars. The points are colour-coded according to the pulsator’s period. The position of the sun is shown with a yellow-black circle. The four stars probably belonging to the type II Cepheid class are shown with black stars (see text).

Table 4.3: Log of the observations for the 331 spectra analysed in this work. The different columns report: the name of the star, the heliocentric Julian day on which the spectrum has been collected, the phase, exposure time, S/N per pixel, effective temperature, logarithm of gravity, microturbulent velocity, broadening velocity, heliocentric radial velocity, and the instrument used to collect the HiRes spectroscopy. The phases were calculated adopting periods and epochs of maximum light from the *Gaia* DR3 catalogue (Ripepi et al. [Rip+23]), except for seven stars for which we report details on the phase determination in Appendix 4.B. A portion is shown here for guidance regarding its form and content. The machine-readable version of the full table will be published at the Centre de Données astronomiques de Strasbourg (CDS, <https://cds.u-strasbg.fr/>).

Star	HJD days	Phase	Texp s	S/N	T_{eff} K	$\log g$ dex	ξ km s ⁻¹	V_{broad} km s ⁻¹	RV km s ⁻¹	Source
AA Gem	59269.76384	0.920	750	102	5656 ± 68	0.92 ± 0.05	3.0 ± 0.2	11.0 ± 1.0	0.9 ± 0.3	ESPaDOnS
AA Gem	59630.79632	0.833	410	92	5877 ± 66	1.22 ± 0.05	3.3 ± 0.2	12.0 ± 1.0	0.8 ± 0.2	ESPaDOnS
AA Gem	59838.14990	0.162	500	80	4887 ± 68	0.1 ± 0.05	2.8 ± 0.2	9.0 ± 1.0	24.6 ± 0.2	ESPaDOnS
AD Pup	59269.81690	0.369	750	78	5128 ± 100	0.38 ± 0.05	2.7 ± 0.2	6.0 ± 1.0	74.0 ± 0.3	ESPaDOnS
AD Pup	59630.82225	0.918	410	77	5983 ± 83	0.58 ± 0.05	3.4 ± 0.3	10.0 ± 1.0	68.3 ± 0.2	ESPaDOnS

a coincidence, but because there exists a period-age relation for DCEPs (see e.g. **Bono2005**) so that shorter periods indicate larger ages. It has been found that at larger Galactocentric radii the DCEPs are on average older (e.g. **desomma2020b**; **Desomma2021**; Skowron et al. [Sko+19]). This explains the lack of long-period DCEPs at large radii in our sample. An additional feature displayed in Fig. 4.1 is the presence of three stars with polar angles between 135° and 225°, namely, Gaia DR2 4087335043492541696, V532 Sco, and ASAS-SN J165340.10-332041.7. Given the peculiar position along the Galactic disc, these pulsators may be type II Cepheids. An in-depth analysis of these objects is provided in Appendix 4.A. In addition, a fourth star, OGLE CEP-GD-0069, which was originally classified as DCEP in Udalski et al. [Uda+18], turned out to be a BL Her variable according to Ripepi et al. [Rip+23]. This star is also discussed in the appendix. Given their uncertain nature, these four stars have been excluded from the following analysis.

4.2.2 Instruments used for the observations and data reduction

For the observations, three instruments were used:

- The Ultraviolet and Visual Echelle Spectrograph (UVES, **UVES_Dekker2000**)¹⁶, attached at Unit Telescope 2 (UT2) of Very Large Telescope (VLT), placed at

¹⁶ <https://www.eso.org/sci/facilities/paranal/instruments/uves.html>

Paranal (Chile). The red arm was used, equipped with the grism CD#3, covering the wavelength interval 4760–6840 Å, and with the central wavelength at 5800 Å. The 1 arcsec slit, which provides a dispersion of $R \sim 47,000$ (sampling 2 px), was selected for all the targets.

- The High Accuracy Radial velocity Planet Searcher for the Northern hemisphere (HARPS-N, [HARPS_Mayor2003](#); [HARPS_Cosentino2012](#)¹⁷), attached at the 3.5m Telescopio Nazionale Galileo (TNG). HARPS-N features an echelle spectrograph covering the wavelength range between 3830 to 6930 Å, with a spectral resolution of $R=115,000$ (sampling 3.3 px).
- The Echelle SpectroPolarimetric Device for the Observation of Stars (ESPaDONs¹⁸) attached at the 3.6m Canada-France-Hawaii Telescope (CFHT). ESPaDONs provides a spectral resolution of $R=81,000$ (sampling 0.69 px) in the wavelength range between 3700 and 10500 Å.

Typically, we obtained 1-2 epoch spectra with UVES, 2-3 with CFHT, and three or more with HARP-N. The signal-to-noise ratio (S/N) was larger than 40 for about 80% of the spectra. In total, in this work, we analysed 331 spectra for 180 DCEPs. A complete list of the time of acquisition and the individual S/N values is reported in [Table 4.3](#).

Reduction of all the spectra, which included bias subtraction, spectrum extraction, flat-fielding, and wavelength calibration, was done by automatic pipelines provided by the three instrument teams so that we downloaded the science-ready one-dimensional spectra (for more details on the data reduction of HARPS-N, UVES and ESPaDONs spectra, see [Bhardwaj2024](#); [Ripepi et al. \[Rip+21a\]](#) and [Trentin et al. \[Tre+23\]](#), respectively).

Finally, from [Table 4.1](#) it can be noted that the stars OGLE-GD-CEP-0026, OGLE-GD-CEP-1278, and OGLE-GD-CEP-1290 have been observed with both the UVES and HARP-N instruments. These stars are therefore useful for cross-checking the results obtained with the different instruments (see [Sect. 4.4](#)).

4.3 Spectroscopy

4.3.1 Stellar parameters

The adopted method for our spectroscopic analysis is the same as was used in [T23](#); here, we only report the main procedure. The initial step in measuring chemical

¹⁷ <https://www.tng.iac.es/instruments/harps/>

¹⁸ <https://www.cfht.hawaii.edu/Instruments/Spectroscopy/Espadons/>

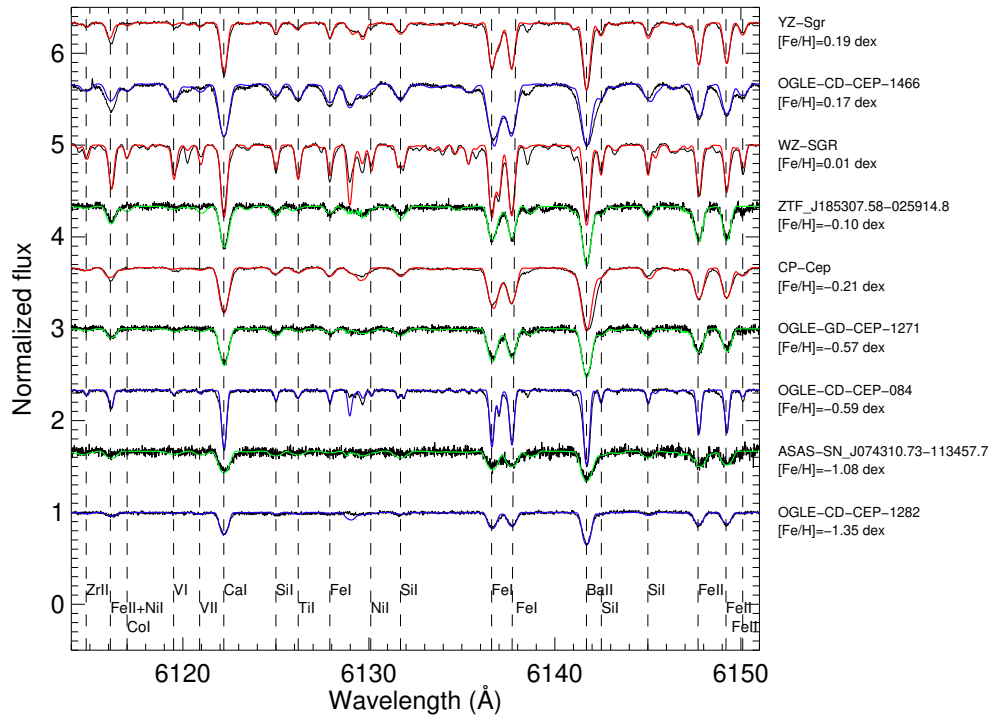


Figure 4.2: Example of spectral synthesis for our targets in the region from $\lambda = 6110 \text{ \AA}$ to $\lambda = 6151 \text{ \AA}$. The colours differ according to the particular instrumental equipment, specifically in red the ESPaDOnS spectra, in green the HARPS spectra, and in blue the UVES spectra. The spectra are ordered, from top to bottom, by decreasing metallicity. The main spectral lines have been identified at the bottom.

abundances involves determining the primary atmospheric parameters, including the effective temperature (T_{eff}), surface gravity ($\log g$), microturbulent velocity (ξ), and the line-broadening parameter (V_{broad}), defined as the full width at half maximum (FWHM) of a Gaussian line-broadening function representing the combination of macroturbulence and rotational velocity (with macroturbulence often playing a dominant role in the case of DCEPs).

A tool widely adopted in the literature for estimating effective temperature is the line depth ratio (LDR) method (**gray1991precise**; Kovtyukh and Gorlova [KG00]). This method offers the advantage of being sensitive to temperature variations, while remaining unaffected by abundance changes and interstellar reddening. Typically, for each spectrum in our targets, we measured approximately 32 LDRs listed in

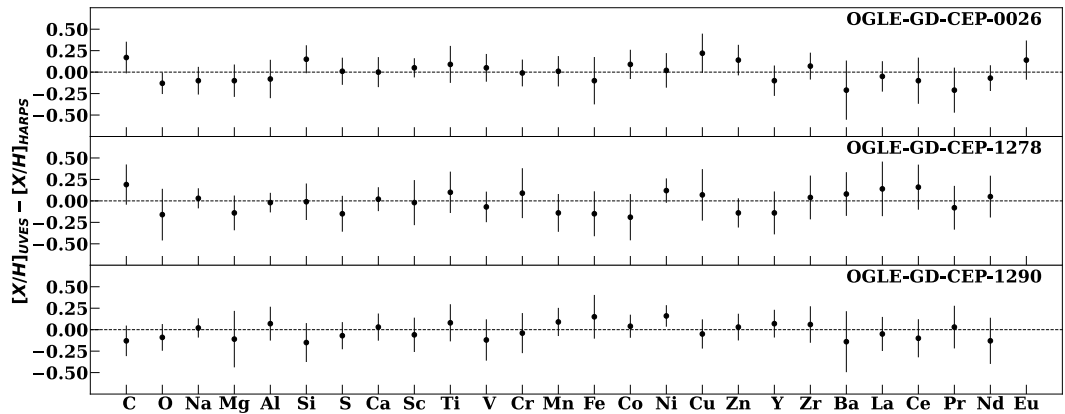


Figure 4.3: Differences between the UVES and HARPS chemical abundances for each star observed with both instruments.

Kovtyukh and Gorlova [KG00]. The mean values and weighted standard deviation were used as the final temperatures and errors.

For the remaining parameters (ξ and $\log g$), we employed an iterative approach. The estimation of microturbulence involved ensuring that iron abundances showed no dependence on equivalent widths (EWs); that is, that the slope of $[\text{Fe}/\text{H}]$ against EWs is null. To achieve this occurrence, we initially measured the EWs of 145 Fe I lines using a custom *Python* semi-automatic routine. The line sample was extracted from the list published by Romaniello et al. [Rom+08], and the routine minimised errors in continuum estimation on the spectral line wings. EWs were converted to abundances using the WIDTH9 code (Kurucz and Avrett [KA81]), applied to the corresponding atmospheric model calculated using ATLAS9 (Kurucz [Kur93]). In this calculation, the influence of $\log g$ was not considered, as neutral iron lines are insensitive to it. Subsequently, surface gravities were estimated through a similar iterative procedure, imposing ionisation equilibrium between Fe I and Fe II. The adopted list of 24 Fe II lines was extracted from Romaniello et al. [Rom+08]. Errors were estimated through the propagation of errors derived from the linear fits.

4.3.2 Abundances

To circumvent issues arising from spectral line blending due to line-broadening, a spectral synthesis technique was applied to our spectra. Synthetic spectra were generated in three steps: i) plane-parallel local thermodynamic equilibrium (LTE) atmosphere models were computed using the ATLAS9 code (Kurucz [Kur93]), employing the stellar parameters; ii) stellar spectra were synthesised using SYNTH

(Kurucz and Avrett [KA81]); and iii) the synthetic spectra were convoluted to account for instrumental and line-broadening. This convolution was evaluated by matching the synthetic line profiles to a selected set of observed metal lines.

For a total of 29 different chemical elements including Fe, it was possible to detect the spectral lines used for the estimation of the abundances. For all elements, we performed the following analysis: we divided the observed spectra into intervals, 25 Å or 50 Å wide, and derived the abundances in each interval by performing a χ^2 minimisation of the differences between the observed and synthetic spectra. The minimisation algorithm was written in Python, using the *amoeba* routine.

We considered several sources of uncertainties in our abundances. First, we evaluated the expected errors caused by variations in the fundamental stellar parameters of $\delta T_{\text{eff}} = \pm 150$ K, $\delta \log g = \pm 0.2$ dex, and $\delta \xi = \pm 0.3$ km s⁻¹. According to our simulations, those errors contribute $\approx \pm 0.1$ dex to the total error budget. Total errors were evaluated by summing in quadrature the value obtained by the error propagation and the standard deviations obtained from the average abundances. For those elements for which only one spectral line could be detected, we evaluated the error only by considering error propagation on the fundamental stellar parameters.

The adopted lists of spectral lines and atomic parameters were taken from Castelli and Hubrig [CH04], who updated the original parameters of Kurucz [Kur95]. When necessary, we also checked the NIST database (Ralchenko and Reader [RR19]). In Fig. 4.2, we plot an example of some of the spectra analysed in this work. More details about the spectral lines that can be typically detected and used to estimate chemical abundances can be found in R21 and T23. The final list of LTE abundances for all the stars is reported in Table 4.2. All the abundances are referred to the solar value (**grevesse2011chemical**).

4.4 Results

4.4.1 Abundances results

As a first step in the analysis of our results, we verified that for the three targets observed with both UVES and HARPS-N and mentioned in Sect. 4.2.2 we find consistent results among the estimated abundances. In this perspective, the homogeneity in the analysis method should not be influenced significantly by the use of the different instruments to observe our targets. As is shown in Fig. 4.3, for all three stars we find comparable chemical values between the UVES and HARPS spectra and no systematics are detected.

In Fig. 4.4, we show histogram distributions of each derived element abundance,

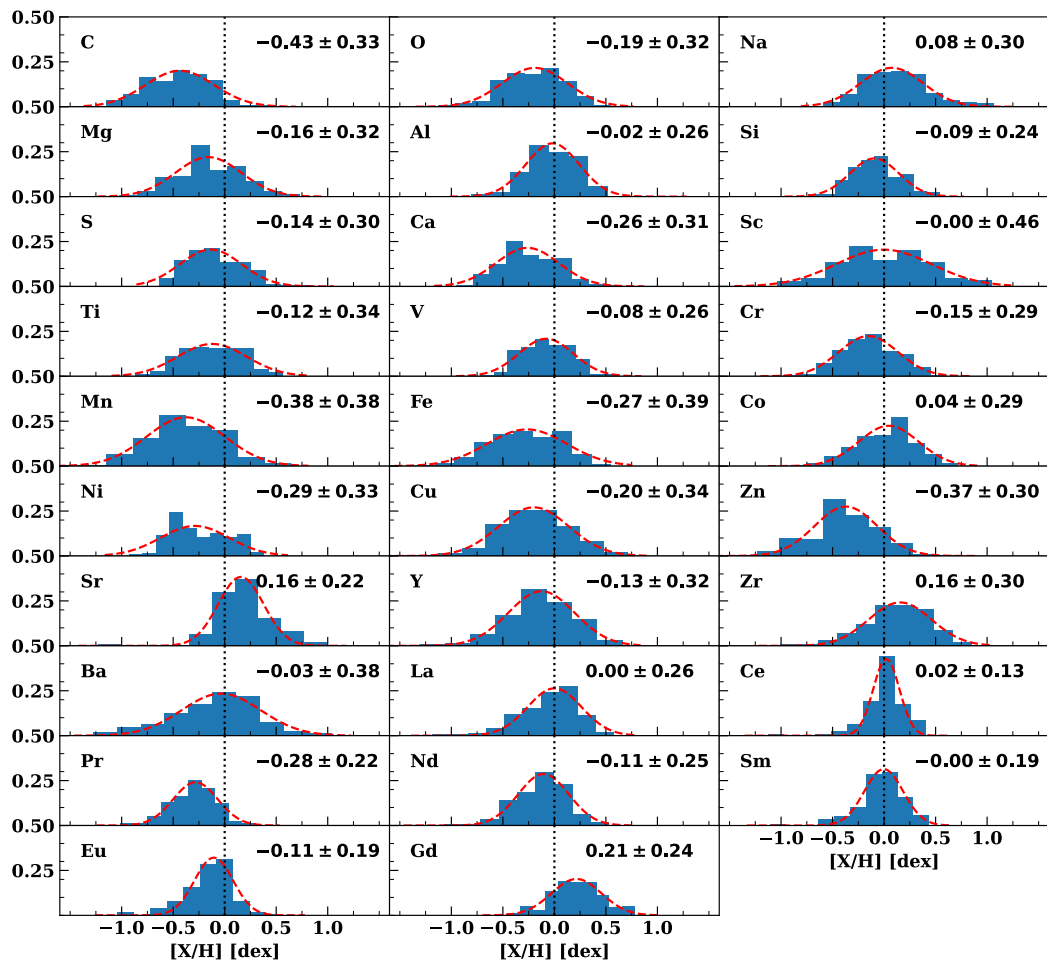


Figure 4.4: Histograms of the distribution of the chemical abundances derived in this study. Gaussian fits have been superimposed (dashed red lines) with the respective mean value and FWHM reported in each panel.

for a total of 29 different chemical species. Bins have been fixed to 0.15 dex, reflecting typical error values. Each distribution has been fitted with a Gaussian curve. It is worth noting that most of these Gaussian curves have FWHM > 0.25 dex, which means that for these elements we have an almost homogeneous distribution over a broad range of values. Moreover, when confronting current Fig. 4.4 with Fig. 3 of T23, it is possible to appreciate how this new sample better covers the whole range of abundances without sharp ‘jumps’ among bins that appeared in T23 for elements (see for example the O, Ca, and Fe panels). We complemented our sample

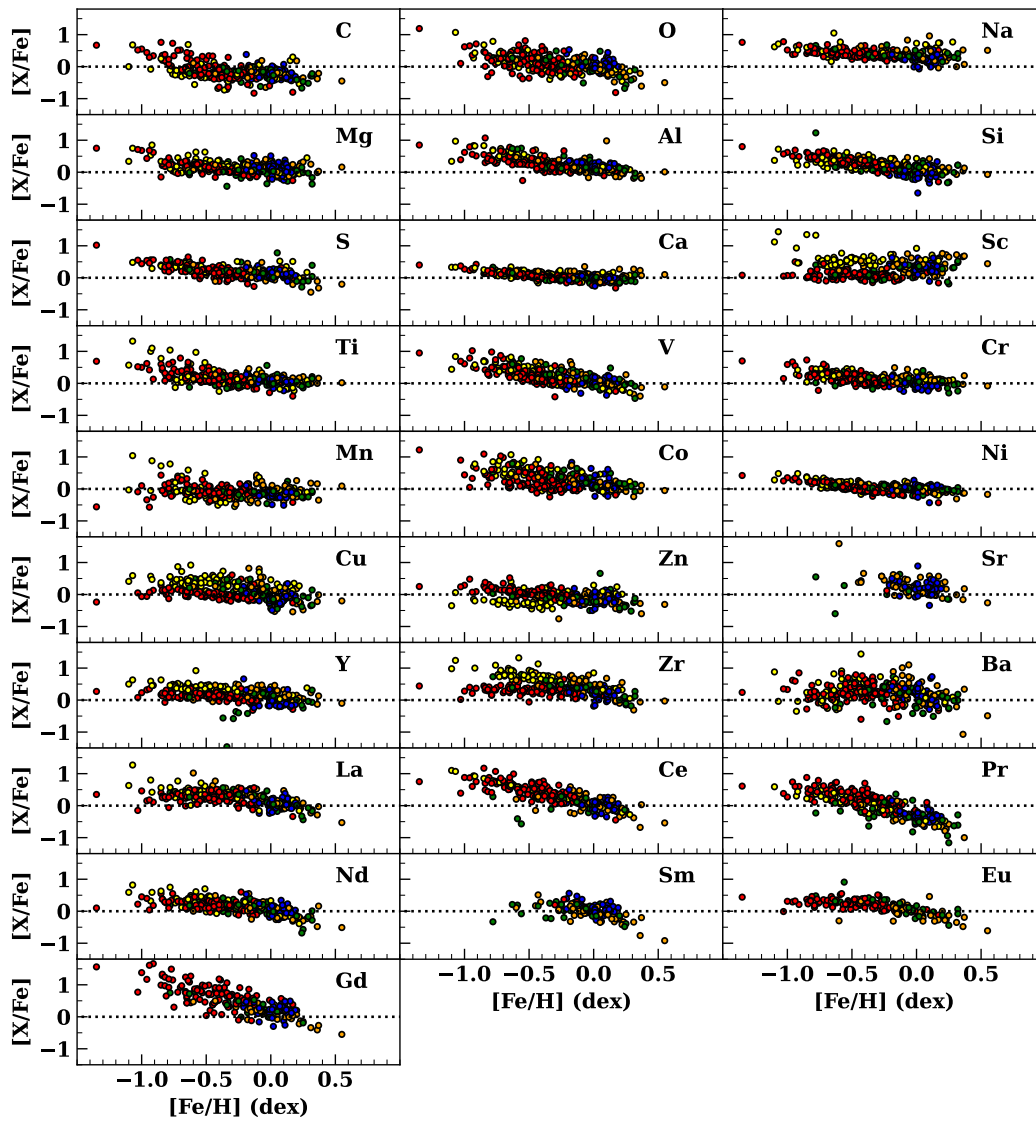


Figure 4.5: Chemical elements in the form of $[X/Fe]$ plotted against the iron content. The colours differ according to the particular instrumental equipment, specifically in red the UVES spectra, in green the HARPS spectra, and in blue the ESPaDOnS spectra. The targets from R21 and T23 are depicted in orange and yellow, respectively (see also Fig. 4.6 and 4.9 for the colour legend).

with those presented in the previous C-MetaLL papers, R21 and T23, reaching a total of 292 pulsators analysed homogeneously.

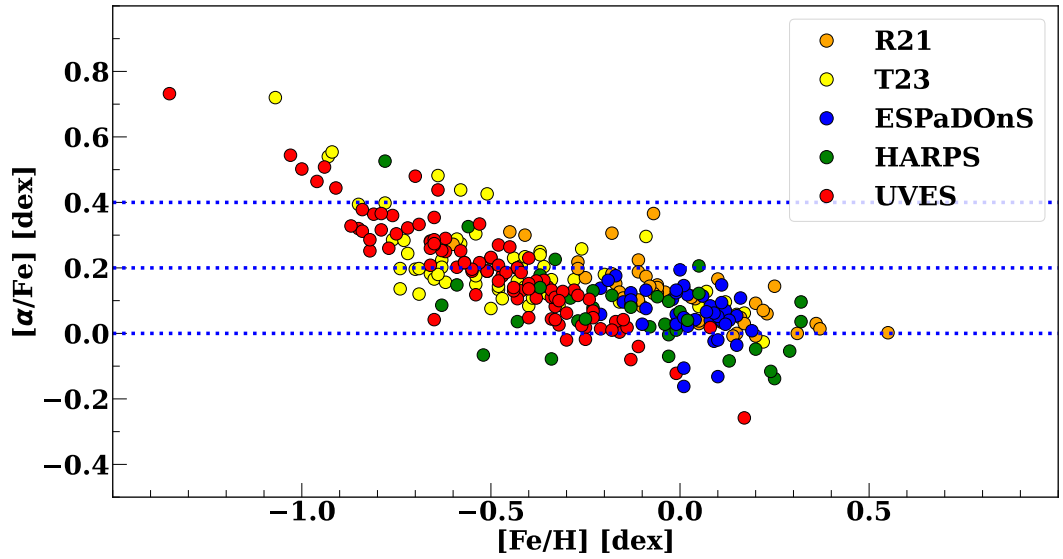


Figure 4.6: α -elements abundance in the form of $[\alpha/\text{Fe}]$ plotted against the iron content. The colour pattern, the same as in Fig. 4.5, is described in the upper right legend. The horizontal dotted blue lines highlight $[\alpha/\text{Fe}]$ abundances at 0.4, 0.2, and 0 dex. Typical errors for the abundances are around 0.15 dex.

In Fig. 4.5, we plot each element (in its $[X/\text{Fe}]$ form) in relation to iron. Generally, we confirm all the trends already found in R21 and T23, in which we divided the chemical species into groups according to their main channel of formation within the stellar evolution models. In more detail, for light and α elements (from C to Ti), we observe a descending behaviour at lower metallicities until $[\text{Fe}/\text{H}] \approx -0.5$ dex, with a flattening effect at higher values. Moreover, we note that while in T23 the region with over solar abundances at lower $[\text{Fe}/\text{H}]$ was poorly populated with stars that appeared as outliers (yellow points), in this work we can confirm a negative trend that flattens at higher iron abundances. In Fig. 4.6, we have plotted the α elements versus $[\text{Fe}/\text{H}]$ (to estimate α , we used the average between $[\text{Mg}/\text{Fe}]$, $[\text{Si}/\text{Fe}]$, $[\text{S}/\text{Fe}]$, $[\text{Ca}/\text{Fe}]$, and $[\text{Ti}/\text{Fe}]$), confirming the α enhancement at lower metallicities that had already been observed in the literature from both an observational (Hayden2015; duffau2017; Trentin et al. [Tre+23]) and a theoretical (tinsley1979; matteucci1990; palicio2023) context. It is important to highlight that $[\text{Fe}/\text{H}]$ and $[\alpha/\text{Fe}]$ depend on both age and birth radius (see for example wielen1996birth; ness2019galactic). Since all the objects are Cepheids, the relation illustrates the $[\text{Fe}/\text{H}]$ dependence of $[\alpha/\text{Fe}]$ at a fixed age. In other

words, $[\text{Fe}/\text{H}]$ represents in this case the (birth) Galactocentric radius rather than age.

We note that for the Sc element, most of the low-metallicity stars studied in this paper appear systematically less abundant (around solar values) and with a flatter distribution than those presented in T23, which are clearly over-abundant and with a slight descending trend towards higher $[\text{Fe}/\text{H}]$ values. In order to investigate this discrepancy between the two samples, we selected stars with similar atmospheric parameters (and possibly similar $[\text{Fe}/\text{H}]$ abundances) and compared the spectra around the available scandium lines. An example with the two targets, BQ Vel from T23 and ATLAS-J104.8954-08.3771, is shown in Fig. 4.7.

It was indeed found that stars from T23 show more intense Sc lines (that is, higher abundances) than those presented in this work. This suggests that this effect could be real and not caused by systematics in the analysis. Possible effects due to different instruments are also excluded since most of the stars involved were observed with UVES.

Iron peak elements (from V to Zn) present a descending trend over the range of metallicities, with the exceptions of Mn and Zn, which appear flatter. It is worth noting how for the latter element the objects presented in this work, observed with UVES (red points), populate the over-solar and solar abundance zone at lower metallicities, while most of the previous targets from T23 (also observed with UVES) were found to be under-solar. This is a similar but opposite behaviour to the Sc case. In the wavelength range covered with the UVES instrument, however, there is only one available neutral zinc line at $\lambda\lambda$ 6362.338 Å. Although this line is weak and could be difficult to detect when the S/N is not optimal, a difference in the line depth has indeed been observed as in the case of Sc (see Fig. 4.8). A similar study has been performed for the Copper, for which there are two neutral lines, at $\lambda\lambda$ 5105.5 and 5218.201 Å. In this case, the UVES targets are slightly under-abundant with respect to the other samples, but again a visual inspection confirmed this difference.

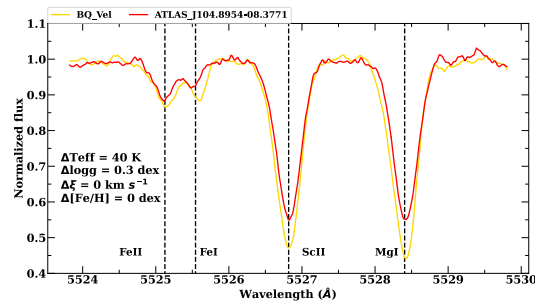


Figure 4.7: Example of two spectra around the Sc II line at $\lambda\lambda$ 5526.818Å for the stars BQ Vel (in yellow from the T23) and ATLAS-J104.8954-08.3771 (in red from the UVES sample analysed in this paper). Other spectral lines are highlighted with dashed black lines. Atmospheric parameters and metallicity differences between the two targets are reported.

For heavier elements (from Sr to Gd), we either find a descending behaviour (Y, Ce, Pr, Gd) or a sort of arch-form trend with a bump at $[\text{Fe}/\text{H}] \approx -0.2$ dex (Ba, La, Nd, and Eu), after which we find that abundances decrease with increasing metallicities. This curved trend was already found in the literature related to open cluster (OC) studies (e.g. [molero2023](#)) and is typical of those elements produced via the s-process. While the descending branch at higher metallicities is caused by the iron production from SNe Ia, at lower metallicities pollution from low- and intermediate-mass stars during the AGB phase cause the rising trend.

Given the low number of stars, we cannot draw a firm conclusion for both Sr and Sm. As happened for Sc, Cu, and Zn, and also for the zirconium (Zr II line at $\lambda\lambda$ 6114.853Å), there seems to be a sort of bifurcation at the low-metallicity tail. We point out that we found the arch-form trend for some of the r-process elements as well (i.e. La and Eu).

4.4.2 Radial gradients and spatial distribution

Following the same procedure described in R21 and T23 and outlined in Sect. 4.2.1, we estimated the Galactocentric distances, R_{GC} , and estimated the radial gradients for all the available chemical species. All of the fits were carried out with the *python LtsFit* package (Cappellari et al. [[Cap+13](#)]), which allows one to use weights on both axes and implements a robust outlier removal and error estimation of the fitted parameters. In Fig. 4.9, we plot the iron radial Galactic gradient. As was expected, we found a clear negative trend. Moreover, an almost homogeneous distribution in metallicity is reflected in a homogeneous distribution in terms of distance, with the stars spanning a Galactocentric distance between 5 and 20 kpc.

Since in T23 we lacked a fair amount of stars with distances between 12 and 16 kpc and we had to complement the sample with literature stars, we might find different results between the current work and the previous one. One first difference is indeed the lack of a visible break at around 9.25 kpc. This is confirmed when

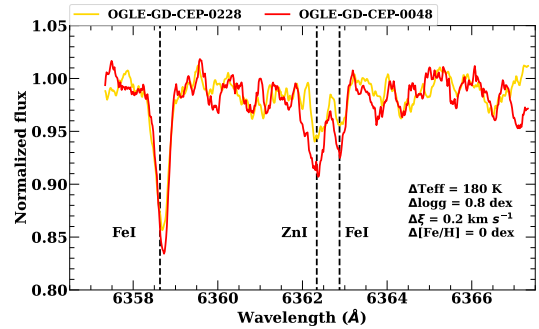


Figure 4.8: Example of two spectra around the Zn I line at $\lambda\lambda$ 6362.338Å for the stars OGLE-GD-CEP-0228 (in yellow from the T23) and OGLE-GD-CEP-0048 (in red from the UVES sample analysed in this paper). Other spectral lines are highlighted with dashed black lines. Atmospheric parameters and metallicity differences between the two targets are reported.

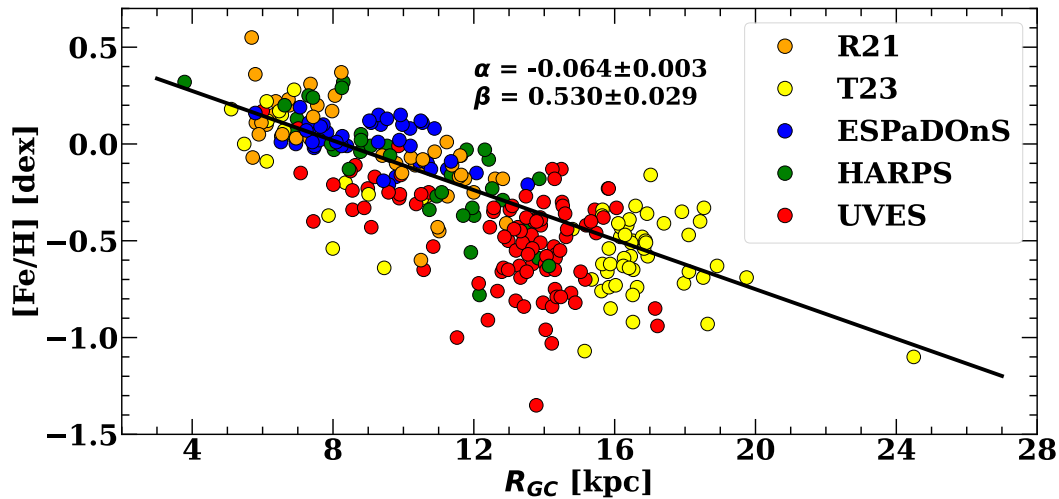


Figure 4.9: Galactic iron radial gradient. The colours are the same as in Fig. 4.5. The black line represents the linear fit computed. Results of the fit are reported both in the figure and in Table 4.4. Typical errors for $[\text{Fe}/\text{H}]$ are around 0.15 dex.

trying to compute a two-line fit that overlaps almost perfectly with the current result. From a quantitative point of view, we did not note a big discrepancy in the value of the slope. In more detail, we found a slightly higher value (in an absolute sense) but still comparable with both the single-line case and the inner slope of the two-line fit. Similarly, when considering the results in T23 obtained after a binning division of the sample, to compensate for the non-uniform distribution, the overall slope is in agreement with our most recent study (there is a good agreement with the two-line fit as well). This puts a further emphasis on the importance of having access to as uniform and homogeneous a sample of stars as possible in terms of distance (and metallicity), one of the key points of the C-MetaLL project. Similarly to what happened in T23, we found some outliers quite far below the linear fit. These objects were observed mostly with UVES (red and yellow points) but stars observed with HARPS (orange and green points) are found as well. Since all the spectra were analysed with the same method and the measurement errors do not justify their behavior, we can consider these outliers to be real.

In Fig. 4.10, we show the radiant galactic gradient for the other 28 elements. The estimated coefficients, together with the root mean square (rms), are listed in Table 4.4. These results generally agree with those listed in T23. As was already seen in T23, Ba has the largest dispersion. Other elements (i.e. Sc, Ti, and Zn) present instead a difference of $>0.01 \text{ dex kpc}^{-1}$. In these cases, we tried to repeat the linear regression including the literature sample used in T23 as well, obtaining results

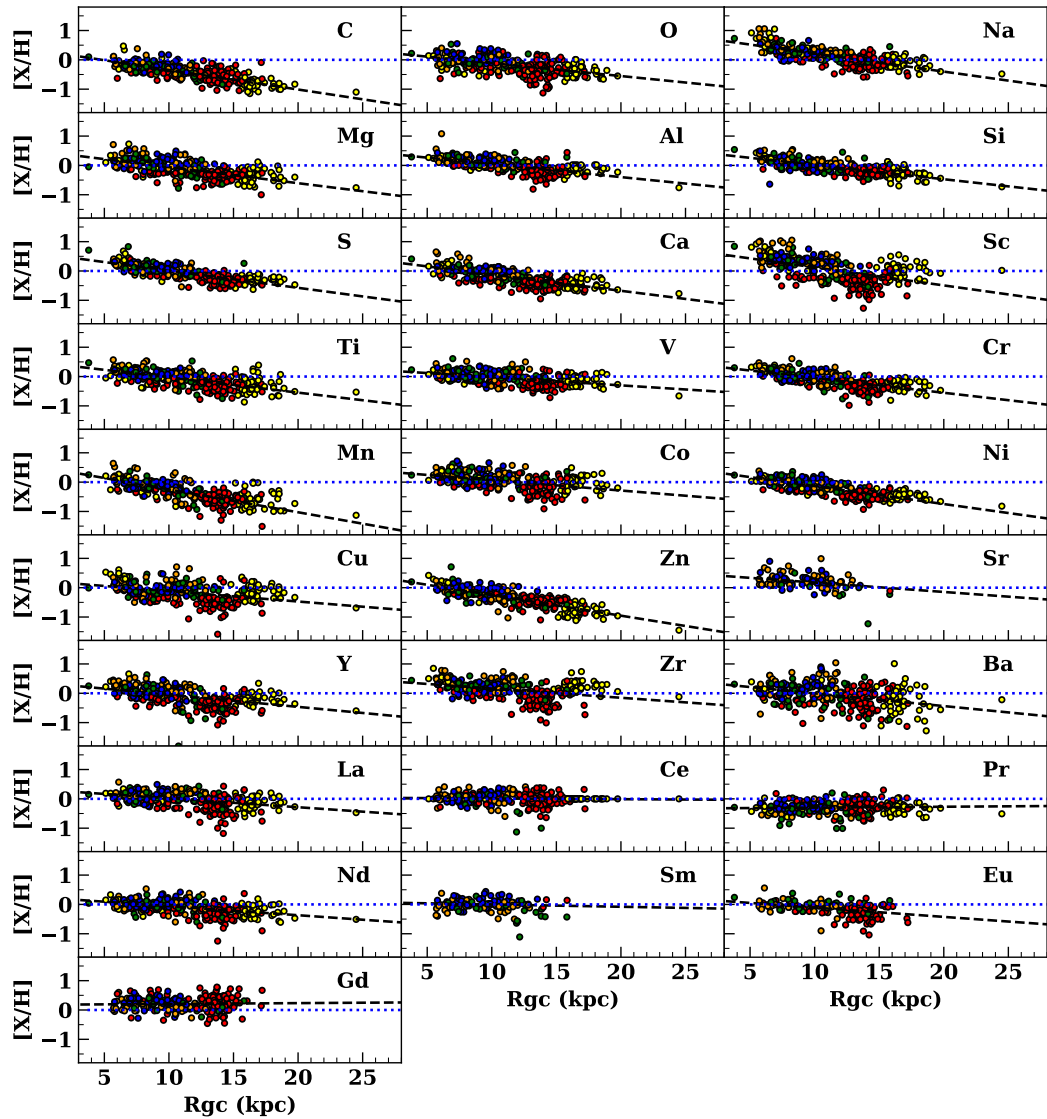


Figure 4.10: Galactic radial gradient for all the estimated chemical elements. The lines and colours are the same as in Fig. 4.9. The linear coefficients are listed in Table 4.4

in perfect agreement with those of this work, once again highlighting the role of the farthest (and most metal-poor) objects and their weight in the linear fit. This is further highlighted when considering the significant difference in the number of objects used in the two works, counterbalanced by the homogeneity of the analysis and the sampling of the stars along the Galactocentric radii.

To achieve more information about the distribution in the Galaxy of our sample, we have plotted our targets in polar coordinates in Fig. 4.11. We computed the azimuthal gradient at different R_{GC} but we did not find significant results (see Fig. 4.12). Given the peculiar distribution already discussed in T23, we superimposed the spiral arms described in Reid et al. [Rei+19] (a similar study has been done by drimmel2024). As was already done in Minniti et al. [Min+21] for stars beyond the Galactic bulge, we extended the outermost spiral structures and obtained a qualitative fit for the furthest stars. The slight adjustments to the spiral structure parameters are within the 1σ errors reported in Table 2 by Reid et al. [Rei+19]. In more detail, we notice that at distances larger than 12.5 kpc, most of the targets studied in this work seem to finely trace the Outer arm, while those presented in T23 seem to better fit the extension to the second and third Galactic quadrants of the Sct-Cen-OSC arm (and not the Outer one stated in T23). The fit presented in this paper could be a pivotal piece of information in extending the OSC arm, which is poorly constrained in this region of the MW (see e.g. Dame2011; sun2015; Minniti et al. [Min+21] and Reid et al. [Rei+19]).

Taking into consideration this information, we can find a possible justification for the anomalous behaviour of the DCEPs studied here concerning the Sc, Cu, Zn, and Zr abundances that have been discussed in the previous section. As is shown in Fig. 4.13, the evident and abrupt abundance change for the outermost stars could be because these two ‘blocks’ of stars are tracing two different spiral arms (Outer

Table 4.4: Results of the fitting. Coefficients of the linear fit of the form $[X/H]=\alpha \times R_{GC} + \beta$ with relative dispersion coefficient.

El	α (dex kpc ⁻¹)	β (dex)	rms (dex)
C	-0.067 ± 0.003	0.320 ± 0.035	0.13
O	-0.044 ± 0.004	0.329 ± 0.050	0.19
Na	-0.061 ± 0.003	0.828 ± 0.039	0.16
Mg	-0.055 ± 0.004	0.488 ± 0.047	0.19
Al	-0.044 ± 0.003	0.486 ± 0.035	0.12
Si	-0.049 ± 0.002	0.501 ± 0.029	0.08
S	-0.059 ± 0.003	0.596 ± 0.032	0.13
Ca	-0.055 ± 0.003	0.434 ± 0.035	0.15
Sc	-0.061 ± 0.006	0.736 ± 0.071	0.33
Ti	-0.052 ± 0.004	0.488 ± 0.043	0.16
V	-0.028 ± 0.003	0.259 ± 0.040	0.16
Cr	-0.051 ± 0.003	0.458 ± 0.038	0.14
Mn	-0.078 ± 0.004	0.529 ± 0.044	0.17
Fe	-0.064 ± 0.003	0.530 ± 0.029	0.11
Co	-0.035 ± 0.004	0.422 ± 0.053	0.20
Ni	-0.061 ± 0.003	0.478 ± 0.034	0.11
Cu	-0.035 ± 0.005	0.236 ± 0.059	0.26
Zn	-0.070 ± 0.003	0.451 ± 0.035	0.11
Sr	-0.032 ± 0.009	0.496 ± 0.088	0.15
Y	-0.041 ± 0.004	0.366 ± 0.049	0.22
Zr	-0.031 ± 0.005	0.474 ± 0.057	0.23
Ba	-0.043 ± 0.006	0.429 ± 0.073	0.33
La	-0.030 ± 0.004	0.319 ± 0.044	0.19
Ce	-0.002 ± 0.002	0.037 ± 0.026	0.10
Pr	0.003 ± 0.004	-0.329 ± 0.044	0.13
Nd	-0.031 ± 0.003	0.245 ± 0.039	0.16
Sm	-0.008 ± 0.008	0.077 ± 0.077	0.15
Eu	-0.032 ± 0.005	0.209 ± 0.054	0.13
Gd	0.003 ± 0.006	0.178 ± 0.071	0.21

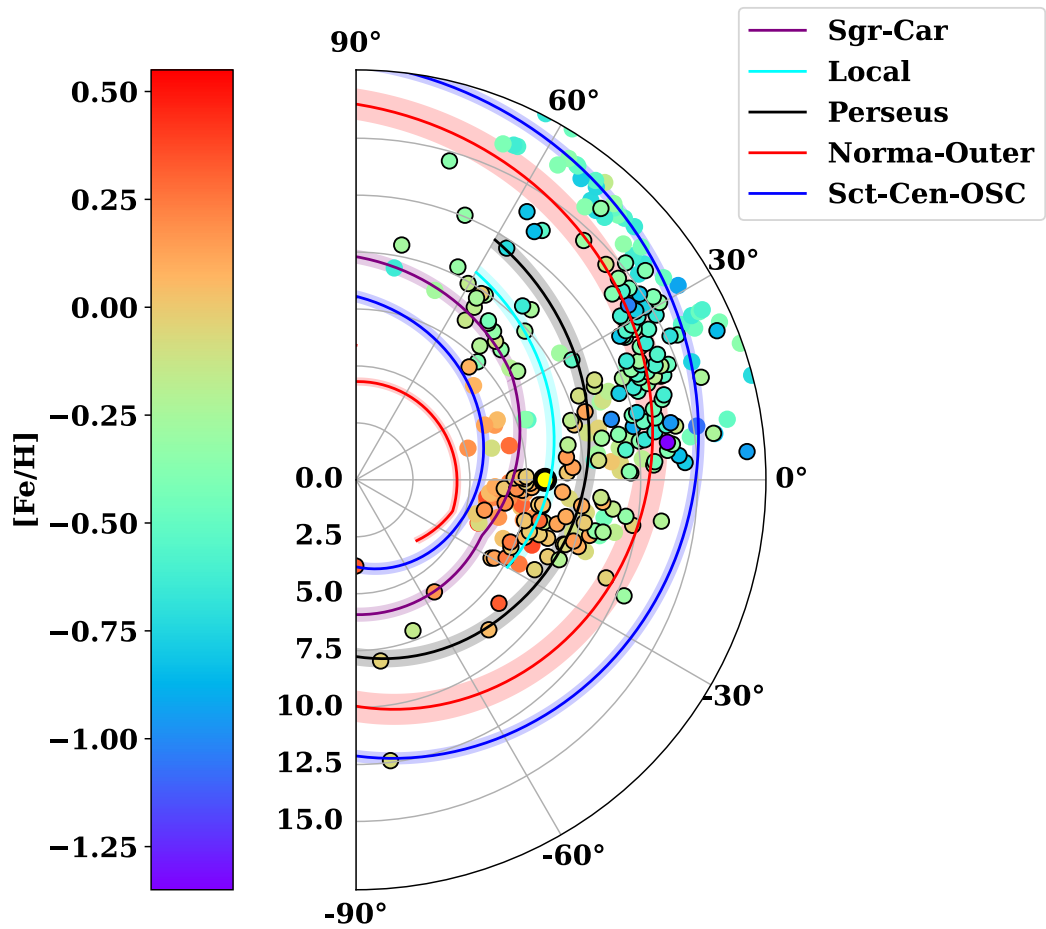


Figure 4.11: Galactic polar distribution of the stars. The new targets presented in this work are highlighted with black borders. The points are colour-coded according to $[\text{Fe}/\text{H}]$ values and specified on the colour bar. The position of the sun is shown with a yellow-black symbol. Spiral arms from Reid et al. [Rei+19] are superimposed. The colours are explained in the upper right legend.

and OSC) and not only the Outer arm stated in T23.¹⁹ No firm conclusion could be drawn about the opposite behaviour of Zn compared with the other three elements. Lastly, it is worth noting that minor differences may also be seen in the interval 6-11 kpc (for example in Sc, Cu, and Zr) between the different samples of our project. Since we can exclude a bias between the different samples (see e.g. Fig. 4.7 and 4.8

¹⁹ Note that the stars investigated in T23 were on average slightly more distant than the ones studied in this work

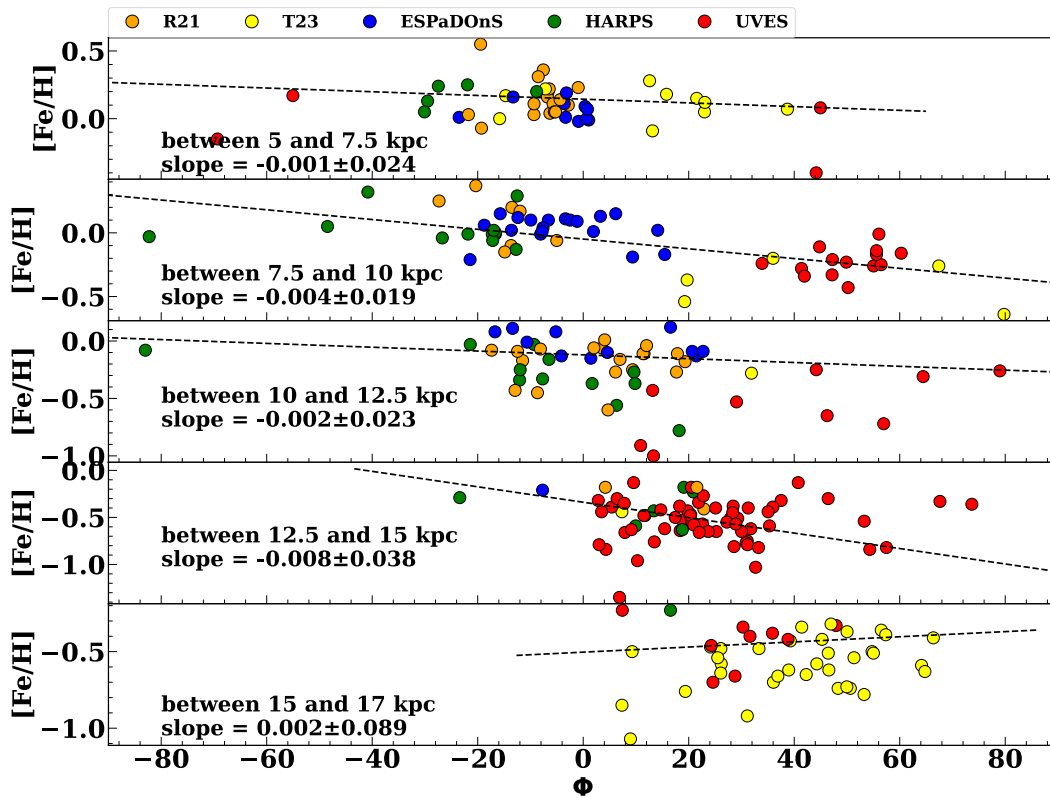


Figure 4.12: Galactic iron azimuthal gradient for different R_{GC} ranges. The colours are the same as in Fig. 4.5. The dashed black line represents the linear fit computed. In each panel, results of the slope are reported as well as the R_{GC} range.

and the relative discussion), these differences may be real and explained by the association of our stars with different spiral arms.

4.5 Comparison with recent literature results

In this section, we compare our results with those found in the literature in recent years. Similar to what was done in T23, we focus our attention on studies involving either Cepheids or OCs, since they span a wide range of ages and represent optimal tracers. Since our slope is in agreement with our previous work, we refer to this paper for a comparison with less recent literature works to avoid redundancies in the discussion. Recently, [daSilva2023](#) collected 356 DCEPs and compared the linear and logarithmic regression along the Galactocentric distance axis for $[Fe/H]$,

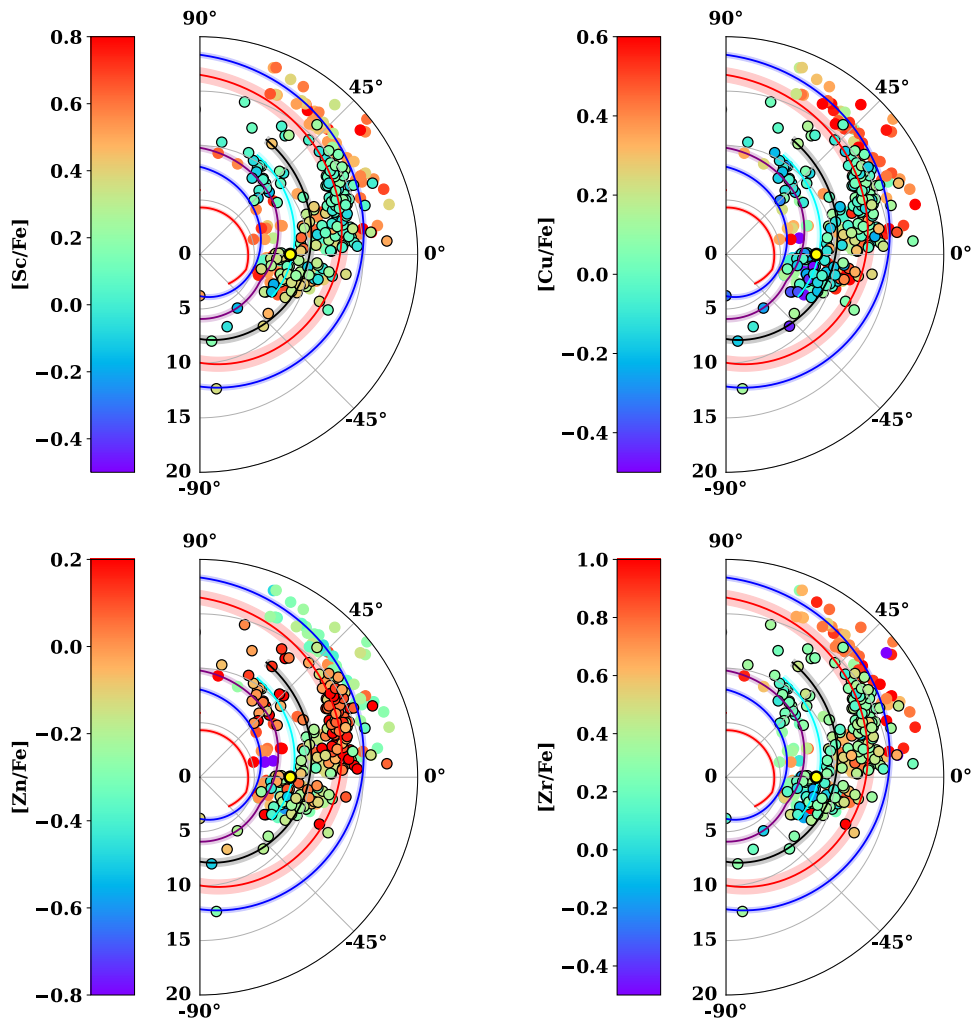


Figure 4.13: Galactic polar distribution of the stars. The new targets presented in this work are highlighted with black borders. The points are colour-coded according to the chemical element specified on the colour bar. The position of the sun is shown with a yellow-black symbol. We alert the reader to the different colour bar scales for each element.

[O/H], and [S/H], finding a change of slope that flattens after around 12.5 kpc, a feature not found in this work. Regarding the linear fit, their values strongly disagree with ours:

$$\text{O} : (-0.029 \pm 0.006)R_{GC} + (0.21 \pm 0.05)$$

$$\text{S} : (-0.081 \pm 0.004)R_{GC} + (0.59 \pm 0.03)$$

$$\text{Fe} : (-0.041 \pm 0.003)R_{GC} + (0.32 \pm 0.02)$$

As was already stated in their work, a possible explanation could be related to the different models used to derive abundances (see their section 4.1) and distances (see their section 2.3). Another cause of this discrepancy could be related to the different amount of targets available at $R_{GC} > 15$ kpc. Nonetheless, similarly to what was stated in their work, we find a strong difference between the O and S gradients, the latter being considerably steeper than the former.

In the near-infrared YJ bands, **Matsunaga2023** reveal for the first time a gradient through the analysis of 16 cepheids, with a possible steepening of the gradient for $R_{GC} > 5.6$ kpc. Although their fit for $R_{GC} < 15$ kpc DCEPs ($[\text{Fe}/\text{H}] = (-0.050 \pm 0.003)R_{GC} + (0.423 \pm 0.029)$) including literature stars from Luck [**Luc18**] results in slightly steeper slope than **daSilva2023**, it is still in disagreement with our slope by more than 2σ . We point out how in this case the work of **Matsunaga2023** is mostly focussed on the inner Galactic disc.

In a recent study related to OCs, **Magrini2023** use a sample of objects available in the final release of the *Gaia*–ESO survey, for a total of 67 open clusters. Their slope from a single line fit, $[\text{Fe}/\text{H}] = (-0.054 \pm 0.004)R_{GC} + (0.474 \pm 0.045)$, is flatter by more than 1σ . On the other side, when considering a two-line fit with a break at $R_{GC} = 11.2$ kpc, an agreement with their inner slope is found ($[\text{Fe}/\text{H}] = (-0.081 \pm 0.008)R_{GC} + (0.692 \pm 0.068)$) only at 2σ . Although their outer slope is considerably flatter ($[\text{Fe}/\text{H}] = (-0.044 \pm 0.014)R_{GC} + (0.376 \pm 0.178)$), there is still statistical agreement.

A similar discussion applies to the study by **yogesh2024**, who collected a remarkable sample of 1879 OCs to study the evolution of metallicity in the Galactic disc. About 90% of their objects are younger than 1 Gyr and the resulting slope (for $R_{GC} < 12.8$ kpc) is in agreement with our work (-0.070 ± 0.002 dex kpc^{-1}) at 1.5σ .

In their investigation into the origin of neutron-capture elements, **molero2023** derived chemical evolution models, starting with the two-infall model by **chiappini1997**, and confronted them with observational data from the 6th Data Release of the *Gaia*–ESO survey. Their observation (with OCs) and prediction (Model R-150) for the present-time radial gradient for $[\text{Fe}/\text{H}]$ and $[\text{Eu}/\text{H}]$ are in good agreement with our results (see their table 2).

Except for a slightly shallower slope documented in **netopil2022** (-0.058 dex kpc^{-1}), derived from a merged dataset of individual studies and the Apache Point Observatory Galactic Evolution Experiment (APOGEE) survey comprising 136 OCs, our findings align well with several other OC studies previously explored in depth by **Magrini2023**, specifically those by **spina2022** and **zhang2021a**, which report slopes of -0.064 ± 0.007 and -0.066 ± 0.005 , respectively.

On the contrary, **myers2022** identify a somewhat steeper slope (-0.073 ± 0.002 dex kpc^{-1}), although one that is statistically consistent when focussing solely on

young OCs (age < 1Gyr) (refer to table 2 of **Magrini2023**). Of note are the findings of **Magrini2023**, particularly in their tables A.8 and A.10, for which linear weighted fits were conducted for various chemical species. Overall, strong concordance is observed both in the overall fit and when restricting the analysis to young OCs (age < 1Gyr).

4.6 Summary

In the context of the C-MetaLL project, we have presented the results obtained from 331 HiRes spectra collected with the UVES/VLT, HARPS-N/TNG, and ESPaDOnS/CFHT instruments for a sample of 180 individual DCEPs located over a wide range of Galactocentric radii ($5 < R_{GC} < 20$ kpc). For each target, we derived accurate atmospheric parameters, radial velocities, and abundances for up to 29 different species. The iron abundances range between +0.5 and -1 dex with a rather even distribution of DCEPs with metallicity. The sample presented in this paper was complemented with the data already published in the context of the C-MetaLL survey, resulting in a total of 292 pulsators whose spectra have been analysed in a homogeneous way. In this work, we have exploited our homogeneous sample to study the abundance gradients of the Galactic disc in a range of Galactocentric radii spanning the range of 5-20 kpc. Here, we report the main results of this work:

- Studying the relation between each chemical species (in its $[X/Fe]$ form) and iron, we observe an α enhancement for $[Fe/H] < -0.5$ dex. This is a well-known occurrence, already observed both empirically (**Hayden2015**; **duffau2017**; Trentin et al. [**Tre+23**]) and theoretically (**tinsley1979**; **matteucci1990**; **palicio2023**). At higher metallicities, this negative trend flattens.
- Iron peak and heavy elements generally present a negative gradient compared with the iron content, while those produced via the s-process (namely, Zr, Ba, and La) show an arch-form behaviour (**molero2023**), with a change of trend at $[Fe/H] \approx -0.2$ dex.
- For some elements (Sc, Cu, Zn, and Zr), we have found an apparent bias in the abundances between T23 and this study at lower metallicities, with Zn having an opposite behaviour to what appears for Sc, Cu, and Zr. Based on a direct visual comparison of the spectra for stars with similar atmospheric parameters and iron content, we have confirmed the difference in the line depths for the available spectral lines for these elements.

- As was expected, we have found a clear negative radial gradient for most of the elements (except Ce, Pr, Sm, and Gd). Our targets are evenly distributed over a broad range of distances. When complementing our sample with other literature stars from other works (as was done in T23, for example), the slopes do not significantly change. Good agreement is found with other DCEP and OC works in the most recent literature.
- Focussing on the case of iron, we did not find any evidence for a break at any galactic radii and the estimated slope ($-0.064 \pm 0.003 \text{ dex kpc}^{-1}$) is in good agreement compared with both the single-line case of Trentin et al. [Tre+23] and the inner slope (when considering their two-line case).
- Superimposing the polar distribution of our dataset with the Galactic spiral arms (Minniti et al. [Min+21] and Reid et al. [Rei+19]), we found a qualitative fit for our farthest star, which traces both the Outer and the extension of OSC arms. Should this result be confirmed in further works, it would be possible to put better constraints on both the spiral structures in a region that is still poorly explored (in particular on the OSC arm).
- The possible association of our targets with the two spiral arms mentioned above could qualitatively justify the apparent change of abundance trend for Sc, Cu, Zn, and Zr. Interestingly enough, the polar representation of the distribution of these four elements shows a peculiar behaviour of zinc. This species appears more abundant in the stars associated with the Outer arm, while the opposite is visible for Sc, Cu, and Zr. No clear explanation has been found for this behaviour.

Finally, the homogeneous sample of DCEPs with metallicities from HiRes spectroscopy will be exploited in a forthcoming paper for the study of the metallicity dependence of the DCEP PL relations.

Acknowledgements

This research has made use of the SIMBAD database operated at CDS, Strasbourg, France. We acknowledge funding from INAF GO-GTO grant 2023 “C-MetaLL - Cepheid metallicity in the Leavitt law” (P.I. V. Ripepi).

This work has made use of data from the European Space Agency (ESA) mission Gaia (<https://www.cosmos.esa.int/gaia>), processed by the Gaia Data Processing and Analysis Consortium (DPAC, <https://www.cosmos.esa.int/web/gaia/dpac/consortium>). Funding for the DPAC has been provided by national institutions, in particular,

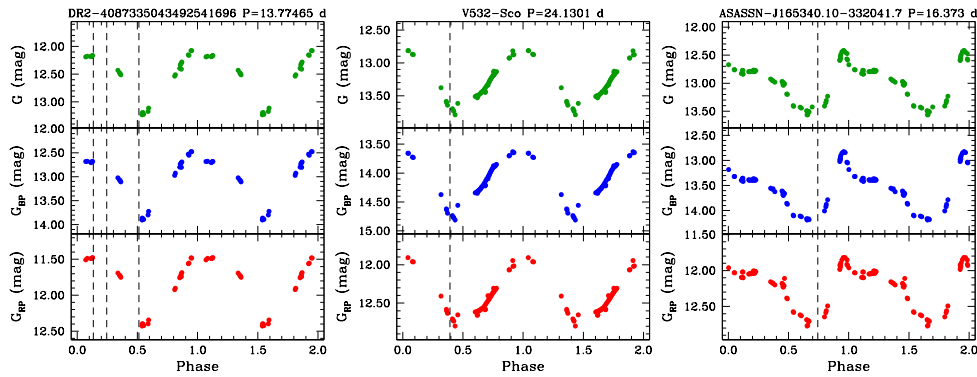


Figure 4.14: Light curves in the *Gaia* bands for the three stars with uncertain classification. The dashed lines show the phases at which the spectra were observed.

the institutions participating in the Gaia Multilateral Agreement. This research was supported by the Munich Institute for Astro-, Particle and BioPhysics (MI-APbP), which is funded by the Deutsche Forschungsgemeinschaft (DFG, German Research Foundation) under Germany’s Excellence Strategy – EXC-2094 – 390783311. This research was supported by the International Space Science Institute (ISSI) in Bern/Beijing through ISSI/ISSI-BJ International Team project ID #24-603 - “EXPANDING Universe” (EXPloiting Precision AstroNOMical Distance INDicators in the Gaia Universe).

4.A Stars with uncertain classification

As mentioned in Sect. 4.2.1, the three stars Gaia DR2 4087335043492541696, ASASSN J165340.10-332041.7 and V532 Sco deserve an in-depth analysis to ascertain whether or not they could be type II Cepheids. To this aim, we plot in Fig. 4.14 the light curves in the *Gaia* bands for the three stars, where the phases at which the spectra were observed are reported. These light curves were used by Ripepi et al. [Rip+23] to classify these objects as fundamental DCEPs. However, the three stars have been classified as belonging to the W Vir class (type II Cepheids) by several authors in the literature. In more detail:

- Gaia DR2 4087335043492541696, also known as V410 Sgr or OGLE BLG-T2CEP-1340 has been classified as W Vir by several authors in the literature, e.g. **Jurkovic2023** based on Kepler K2 data and **Sos2020** based on *V, I* photometry in the context of the OGLE (Optical Gravitational Lensing Experiment) survey, just to mention the most recent works.

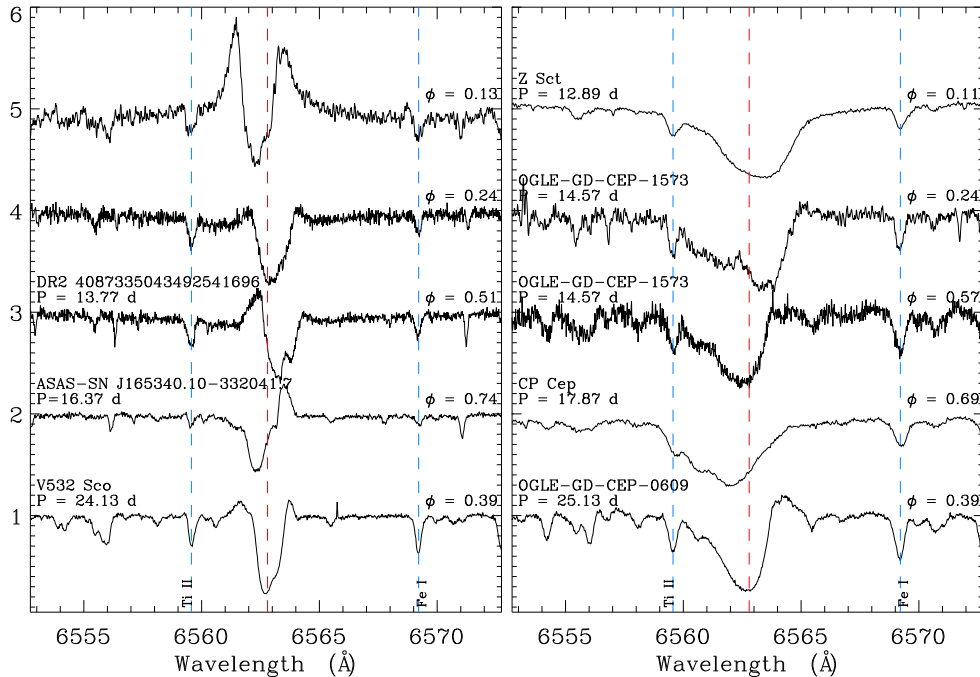


Figure 4.15: Left panel- $H\alpha$ profiles for the three stars with uncertain classification. Profiles are plotted in the rest frame of the stellar atmosphere as measured from the metal lines. Phases at which the spectra were observed are reported in the plot. Right panel- $H\alpha$ profiles for classical cepheids extracted from our sample, with similar periods and phases.

- ASAS-SN J165340.10-332041.7, also known as OGLE BLG-T2CEP-1089 has been considered as DCEP by **Jayasinghe2018** and Skowron et al. [**Sko+19**], but lately re-classified as W Vir by **Sos2020**.
- V532 Sco, also known as SV HV 10484 or OGLE BLG-T2CEP-1229 has been classified as W Vir by **Harris1985**, a classification subsequently confirmed by **Sos2020**.

We analyse now the spectra of the three stars searching for features which could possibly allow us to classify them in terms of DCEPs or W Vir stars. As showed in Fig. 4.15, we focus our attention to the $H\alpha$ region where, according to **Schmidt2004** two features, due to the presence of violent shocks in the moving atmospheres of the type II Cepheids can help us to distinguish between Type I and type II Cepheids: i) the difference in velocity between the $H\alpha$ and the metallic

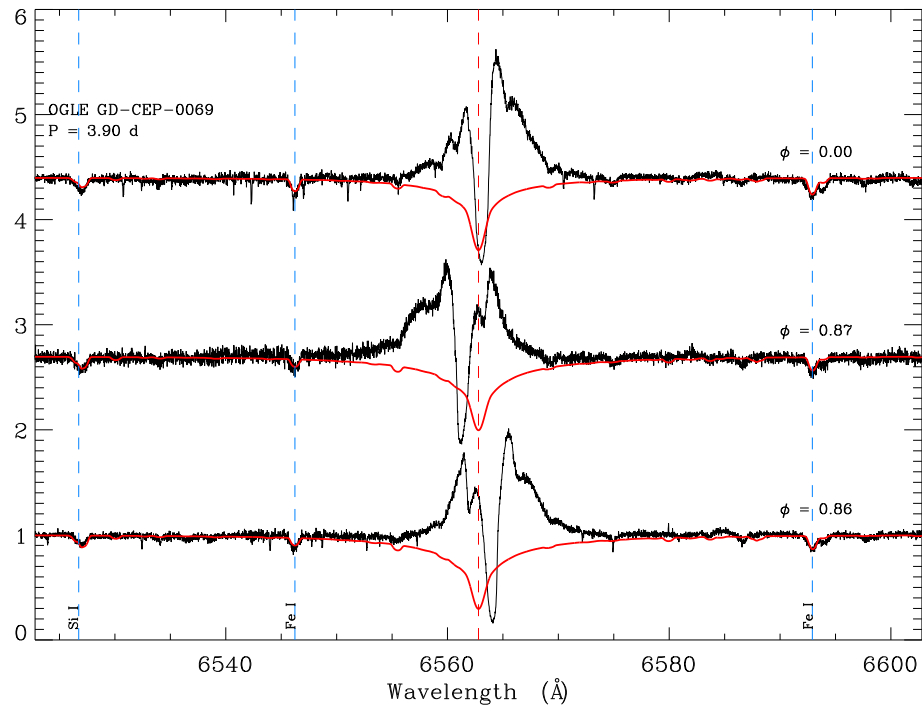


Figure 4.16: $H\alpha$ profiles for OGLE CEP-CD-0069. As in Fig. 4.15 profiles are plotted in the rest frame of the stellar atmosphere as measured from the metal lines. The overplotted synthetic spectra have been calculated with the respective parameters reported in Table 4.3 and Table 4.2. Phases at which the spectra were observed are reported in the plot.

lines and ii) the presence of strong emission in $H\alpha$ from approximately half the cycle till phase 0.1 after the maximum. The left panel of Fig. 4.15 shows the three epoch spectra of Gaia DR2 4087335043492541696 and the single-epoch spectra for ASAS-SN J165340.10-332041.7 and V532 Sco. For comparison, the right panel shows the spectra of different DCEPs with periods and phases similar to those of the three investigated stars. The difference in velocity between $H\alpha$ and the metallic lines can be clearly seen for Gaia DR2 4087335043492541696, especially at $\phi = 0.13$ and 0.51, and for ASAS-SN J165340.10-332041.7. However, similar differential velocities can also be seen in DCEPs, therefore, as noted by Schmidt2004, this feature is not a good discriminant, at least for periods larger than 8 days. However, the presence of $H\alpha$ emission or P-Cygni profiles (both direct and inverse) is evident in almost all the left-panel spectra, while it is almost absent among DCEPs. An exception appears to be V532 Sco, whose spectrum is the most similar to the relative DCEPs’.

On these bases we conclude that Gaia DR2 4087335043492541696 and ASAS-SN J165340.10-332041.7 are almost certainly W Vir pulsators, while the classification of V532 Sco remains uncertain. As for OGLE CEP-GD-0069, Fig. 4.16 show the spectra at three different phases in comparison with synthetic spectra calculated with the proper atmospheric parameters. The same arguments adopted for the previous three stars attains in this case, and we can confirm that OGLE CEP-GD-0069 is a type II Cepheids of BL Her subtype.

4.B Phases for seven DCEPs devoid of Gaia periods and epochs of maximum light.

To use epochs close to the spectroscopy observations we proceeded as follows:

- AP Sgr: the period and epoch of maximum light was calculated directly from *Gaia* DR3 G-band time series using the *Period04* package (Lenz2005). As a result, we obtained $P=5.05790$ days and $\text{Epoch}=58992.77858$ days, where the errors are on the last digits.
- T Mon, U Sgr: for these stars, we have recent periods (at epoch 59591.5 days) provided by Csornyei2022. To determine epochs close to our observations we used again *Period04* but imposed the period instead of recalculating it. Therefore the adopted periods and epochs of maximum light are $P=27.033911203$ days; $\text{Epoch}=59576.79823$ days; $P=6.745265182$ days $\text{Epoch}=59587.19128$ days for T Mon and U Sgr, respectively.
- ASAS J060722+0834.0, DP Mon, NSVS 2150508; V981 Mon: for these stars we adopted periods and epochs of maximum light from the All-Sky Automated Survey for Supernovae (ASAS-SN Shappee2014; Christy2023).

In this thesis, we explored the importance of spectroscopic analysis using High-Resolution spectra for Classical Cepheids and the influence of the metallicity in calibrating the PLZ and PWZ relations. The core of the thesis was based on three published papers, part of the C-MetaLL project.

In Chapter 2 and 4 we presented the results obtained from a total of around 400 HiRes spectra collected with the UVES/VLT, HARPS-N/TNG, and ESPaDOnS/CFHT instruments for a sample of 65 and 180 individual DCEPs, respectively. These stars are located over a wide range of Galactocentric radii ($5 < R_{GC} < 20$ kpc). For each target, we derived accurate atmospheric parameters, radial velocities, and abundances for up to 29 different species. The iron abundances range between +0.5 and -1 dex, constituting the most metal-poor Classical Cepheids ever studied with high-resolution spectroscopy in the MW disc and extending the metallicity range of the MW DCEPs even below the metallicity of the Small Magellanic Cloud (SMC) DCEPs (see Romaniello et al. [Rom+08]).

In more detail, in Chapter 2, we provided an effective temperature estimate using two distinct procedures: the LDR method and minimizing the correlation between abundance and excitation potential. When both methods were applied to a star, they yielded consistent results. These techniques were introduced in Chapter 1, alongside the methodology for estimating microturbulence velocity, surface gravity, and broadening velocity.

To expand our sample, we incorporated recent samples from the literature, compiling a dataset of 637 confirmed DCEPs with individual metallicities obtained from high-resolution spectroscopy. For these objects, we utilized *Gaia* EDR3 photometry and iron abundance measurements to determine distances using the PWZ relation in *Gaia* bands (Ripepi et al. [Rip+22]). With this broader dataset, we revealed a spatial distribution forming a spiral arm spanning approximately 60 degrees in azimuth at a nearly constant Galactocentric distance of 16-18 kpc. Initially, we hypothesized that these more distant data points traced the Outer Arm. The distribution of DCEPs above and below the Galactic disk plane shows an increasing scatter for $\phi > 0$ and $R_{GC} > 10$ kpc, where a warp in the disk becomes evident beyond $R_{GC} > 10$ kpc. Our data suggest that the disk continues to bend with a similar slope between 15-18 kpc, potentially extending up to 25 kpc, although we only have one star at this extreme distance, with none between 20 and 25 kpc. Conversely, for $\phi < 0$, the

warp is barely discernible, though data are sparse beyond $R_{GC} > 13$ kpc, limiting firm conclusions. Finally, we investigated the metallicity gradient of the Galactic disk, finding a slope of $-0.060 \pm 0.002 \text{ dex kpc}^{-1}$, consistent with prior studies on DCEPs and open clusters. We also identified a potential break in the gradient at $R_{GC} = 9.25$ kpc, with slopes of -0.063 ± 0.007 and $-0.079 \pm 0.003 \text{ dex kpc}^{-1}$ for the inner and outer samples, respectively, differing by more than 1σ .

With the available extended metallicity range, in the fourth paper of the C-MetaLL series (Chapter 3), we analyzed the metallicity dependence of *PL* relations in the bands G_{BP} , G_{RP} , G , I , V , J , H , and K_S , and of *PW* relations in the Wesenheit magnitudes $W_{G, BP-RP}$, $W_{H, V-I}$, $W_{H, V-I}^{cHST}$, $W_{J, J-K}$, and $W_{V, V-K}$.

Our final sample included 910 DCEPs with $[\text{Fe}/\text{H}]$ values either from high-resolution spectroscopy or based on *Gaia* RVS data from DR3. We compiled a table for these stars, listing photometry in the bands G_{BP} , G_{RP} , G , I , V , J , H , and K_S , alongside metallicity and astrometry from *Gaia* DR3.

We conducted our analysis using several combinations of samples, based on either using metallicities solely from literature data or also incorporating *Gaia* DR3 results and whether to include first overtone pulsators (whose period was properly fundamentalised following Alcock et al. [Alc+95] and Feast and Catchpole [FC97]). The main difference between using the F and F+1O samples is that larger error bars are found in the former case, especially for the γ and δ coefficients. To estimate the parameters of the *PLZ*/*PWZ* relations, we used the ABL formalism, allowing us to treat parallax ϖ linearly and preserve the statistical properties of its uncertainties. Furthermore, the *PLZ* and *PWZ* relations were examined using two models: one in which metallicity affects only the intercept (three-parameter model) and another in which it influences both the intercept and slope (four-parameter model).

Regardless of the fit and the sample used, both the intercept and slope of the *PLZ* relations (α and β) showed a linear dependence on wavelength and we provided a linear fit between these coefficients and λ^{-1} . Due to limited wavelength coverage, no definite trend could be found for the *PWZ* relations. Similarly, the dependence of the slope on metallicity (δ coefficient) remains undetermined. Although for some cases this parameter results comparable with zero (within 1σ), in other cases we reported a positive value ranging between 0 and +0.5. On the other side, we found a negative dependence of the intercept on metallicity (γ -coefficient) for all the *PL* and *PW* relations, stronger than those listed in the recent literature (between -0.2 and -0.4 dex). For the three-parameter solutions, the values of γ were around $-0.4 : -0.5$ dex, and they slightly decreased in an absolute sense for the four-parameter solutions. No clear dependence on wavelength was found. Following what was done in the first paper of the C-MetaLL project (Ripepi et al. [Rip+21a]), we explored the effect of including a global zero point offset to the individually

corrected parallaxes according to Lindegren et al. [Lin+21]. Two cases were taken into consideration: an offset of $-14 \mu\text{as}$ (Riess et al. [Rie+21a]) and another $-22 \mu\text{as}$ (Molinaro et al. [Mol+23]).

Although the general consequence was to decrease (in the absolute sense) the value of γ , almost aligning our results with those from the literature, a dramatic effect was reported when estimating the geometric distance of the LMC. Using Pietrzyński et al. [Pie+19] as a reference, we found that good agreement for the distance of the LMC is found for values of the offset in between null and the $14 \mu\text{as}$ values. A special case is the $W_{cH,V-I}^{cHST}$ magnitude, for which the Riess et al. [Rie+21a] offset represents the best correction.

Although the sample's unbalanced distribution in metallicity did not affect significantly the previous results, it remains of fundamental importance to build a more homogeneous sample, possibly with an even distribution in the metallicity.

Such a sample was presented in Chapter 4, composed of objects published only in the context of the C-MetaLL survey, resulting in a total of 292 pulsators. In the sixth paper of the project, we partially rectified some of the results presented in Chapter 2. In particular, we did not find any evidence of a break at any galactic radii, and the newly estimated slope ($-0.064 \pm 0.003 \text{ dex kpc}^{-1}$) was in good agreement with both the single-case scenario and the inner slope for the two-line case of Chapter 2. Furthermore, we superimposed the Galactic spiral arms adapted from Minniti et al. [Min+21] and Reid et al. [Rei+19] to the polar distribution of our new homogeneous sample, finding that a better fit for the stars presented in Chapter 2 (Trentin et al. [Tre+23]) put them in the extension of OSC arms, while closer stars at $\sim 12.5 \text{ kpc}$ fit the Outer arm. These results offer the possibility of further studying the Galactic structure in regions still poorly constrained, as in the case of the OSC arm. Other peculiar behaviours emerged for other elements (Sc, Cu, Zn, and Zr) in the form of an abundance shift, with Zn acting oppositely respect with to the other elements. At first, we confirmed the existence of these "anomalies" through a direct visual inspection of the spectral lines generated by these elements. The different depths of the lines for stars with similar atmospheric parameters and iron content are translated in a difference of abundance. Then, looking at the previous associations of our object with the Galactic arms, we could qualitatively justify the abrupt change of abundances for Sc, Cu, Zn, and Zr. These element species appear more abundant (or less abundant for Zn) for the stars associated with the OSC arm.

In the future, the homogeneity of the sample will be of pivotal importance for the study of the metallicity dependence of both *PLZ* and *PWZ* relations, especially in the present state where the size of the sample is becoming large enough to be used alone without the need to include other sources of literature outside the C-MetaLL project. Further observations will offer the opportunity to better constrain the

dependence on the metallicity of both the intercept and the slope. In particular, regions in the Galactic anti-centre direction are the most promising targets for future observations, where DCEPs are expected to have $[\text{Fe}/\text{H}] < -0.3 : -0.4$ dex, and can therefore be used to further populate the metal-poor tail of the DCEP distribution. However, far Cepheids are more affected by the dust, so they might be too faint to be observed in the optical bands. This is why another possible road to drive can be the observation of Classical Cepheids in the NIR bands, where the extinction is greatly reduced.

Bibliography

- [Abd+22] Elcio Abdalla, Guillermo Franco Abellán, Amin Aboubrahim, Adriano Agnello, Özgür Akarsu, Yashar Akrami, George Alestas, Daniel Aloni, Luca Amendola, Luis A Anchordoqui, et al. **Cosmology intertwined: A review of the particle physics, astrophysics, and cosmology associated with the cosmological tensions and anomalies.** *Journal of High Energy Astrophysics* 34 (2022), 49–211 (see page 17).
- [AL99] Frédéric Arenou and Xavier Luri. **Distances and absolute magnitudes from trigonometric parallaxes.** In: *Harmonizing Cosmic Distance Scales in a Post-HIPPARCOS Era*. Ed. by Daniel Egret and Andre Heck. Vol. 167. Astronomical Society of the Pacific Conference Series. Jan. 1999, 13–32. arXiv: [astro-ph/9812094](https://arxiv.org/abs/astro-ph/9812094) [[astro-ph](https://arxiv.org/abs/astro-ph)] (see page 73).
- [Alc+95] C. Alcock, R. A. Allsman, T. S. Axelrod, D. P. Bennett, K. H. Cook, K. C. Freeman, K. Griest, S. L. Marshall, B. A. Peterson, M. R. Pratt, P. J. Quinn, J. Reimann, A. W. Rodgers, C. W. Stubbs, W. Sutherland, and D. L. Welch. **The MACHO Project LMC Variable Star Inventory. I. Beat Cepheids—Conclusive Evidence for the Excitation of the Second Overtone in Classical Cepheids.** *AJ* 109 (Apr. 1995), 1653. doi: [10.1086/117392](https://doi.org/10.1086/117392). arXiv: [astro-ph/9411061](https://arxiv.org/abs/astro-ph/9411061) [[astro-ph](https://arxiv.org/abs/astro-ph)] (see pages 74, 128).
- [And+13] S. M. Andrievsky, J. R. D. Lépine, S. A. Korotin, R. E. Luck, V. V. Kovtyukh, and W. J. Maciel. **Barium abundances in Cepheids.** *MNRAS* 428:4 (Feb. 2013), 3252–3261. doi: [10.1093/mnras/sts270](https://doi.org/10.1093/mnras/sts270). arXiv: [1210.6211](https://arxiv.org/abs/1210.6211) [[astro-ph](https://arxiv.org/abs/astro-ph).GA] (see page 46).
- [And+16] R. I. Anderson, S. Casertano, A. G. Riess, C. Melis, B. Holl, T. Semaan, P. I. Papics, S. Blanco-Cuaresma, L. Eyer, N. Mowlavi, L. Palaversa, and M. Roelens. **Vetting Galactic Leavitt Law Calibrators Using Radial Velocities: On the Variability, Binarity, and Possible Parallax Error of 19 Long-period Cepheids.** *ApJS* 226:2, 18 (Oct. 2016), 18. doi: [10.3847/0067-0049/226/2/18](https://doi.org/10.3847/0067-0049/226/2/18). arXiv: [1608.00556](https://arxiv.org/abs/1608.00556) [[astro-ph](https://arxiv.org/abs/astro-ph).SR] (see page 89).
- [Arg+04] D Argast, Ma Samland, F-K Thielemann, and Y-Z Qian. **Neutron star mergers versus core-collapse supernovae as dominant r-process sites in the early Galaxy.** *Astronomy & Astrophysics* 416:3 (2004), 997–1011 (see page 46).

- [Baa26] Walter Baade. **Über eine Möglichkeit, die Pulsationstheorie der delta Cephei-Veränderlichen zu prüfen.** *Astronomische Nachrichten*, volume 228, Issue 20, p. 359–228 (1926), 359 (see page 17).
- [Ben+07] G Fritz Benedict, Barbara E McArthur, Michael W Feast, Thomas G Barnes, Thomas E Harrison, Richard J Patterson, John W Menzies, Jacob L Bean, and Wendy L Freedman. **Hubble Space Telescope fine guidance sensor parallaxes of galactic cepheid variable stars: period-luminosity relations.** *The Astronomical Journal* 133:4 (2007), 1810 (see page 17).
- [BM80] J. P. Brodie and B. F. Madore. **The period-luminosity relation for Cepheids. I - Numerical simulations.** *MNRAS* 191 (June 1980), 841–854. DOI: [10.1093/mnras/191.4.841](https://doi.org/10.1093/mnras/191.4.841) (see page 70).
- [BMS99a] Giuseppe Bono, Marcella Marconi, and Robert F Stellingwerf. **Classical Cepheid pulsation models. I. Physical structure.** *The Astrophysical Journal Supplement Series* 122:1 (1999), 167 (see page 15).
- [BMS99b] Giuseppe Bono, Marcella Marconi, and Robert F. Stellingwerf. **Classical Cepheid Pulsation Models. I. Physical Structure.** *ApJS* 122:1 (May 1999), 167–205. DOI: [10.1086/313207](https://doi.org/10.1086/313207) (see page 48).
- [Bon+10] G. Bono, F. Caputo, M. Marconi, and I. Musella. **Insights into the Cepheid Distance Scale.** *ApJ* 715:1 (May 2010), 277–291. DOI: [10.1088/0004-637X/715/1/277](https://doi.org/10.1088/0004-637X/715/1/277). arXiv: [1004.0363](https://arxiv.org/abs/1004.0363) [astro-ph. SR] (see pages 66, 99).
- [Bre+21] Louise Breuval, Pierre Kervella, Piotr Wielgórski, Wolfgang Gieren, Dariusz Graczyk, Boris Trahin, Grzegorz Pietrzyński, Frédéric Arenou, Behnam Javanmardi, and Bartłomiej Zgirski. **The Influence of Metallicity on the Leavitt Law from Geometrical Distances of Milky Way and Magellanic Cloud Cepheids.** *ApJ* 913:1, 38 (May 2021), 38. DOI: [10.3847/1538-4357/abf0ae](https://doi.org/10.3847/1538-4357/abf0ae). arXiv: [2103.10894](https://arxiv.org/abs/2103.10894) [astro-ph. GA] (see pages 34, 68, 89).
- [Bre+22] Louise Breuval, Adam G. Riess, Pierre Kervella, Richard I. Anderson, and Martino Romaniello. **An Improved Calibration of the Wavelength Dependence of Metallicity on the Cepheid Leavitt Law.** *ApJ* 939:2, 89 (Nov. 2022), 89. DOI: [10.3847/1538-4357/ac97e2](https://doi.org/10.3847/1538-4357/ac97e2). arXiv: [2205.06280](https://arxiv.org/abs/2205.06280) [astro-ph. GA] (see pages 68, 74, 78, 88, 89).
- [Bud+21] Sven Buder, Sanjib Sharma, Janez Kos, Anish M. Amarsi, Thomas Nordlander, Karin Lind, Sarah L. Martell, Martin Asplund, Joss Bland-Hawthorn, Andrew R. Casey, Gayandhi M. de Silva, Valentina D’Orazi, Ken C. Freeman, Michael R. Hayden, Geraint F. Lewis, Jane Lin, Katharine J. Schlesinger, Jeffrey D. Simpson, Dennis Stello, Daniel B. Zucker, Tomaz Zwitter, Kevin L. Beeson, Tobias Buck, Luca Casagrande, Jake T. Clark, Klemen Čotar, Gary S. da Costa, Richard de Grijs, Diane Feuillet, Jonathan Horner, Prajwal R. Kafle, Shourya

- Khanna, Chiaki Kobayashi, Fan Liu, Benjamin T. Montet, Govind Nandakumar, David M. Nataf, Melissa K. Ness, Lorenzo Spina, Thor Tepper-García, Yuan-Sen Ting, Gregor Traven, Rok Vogrinčič, Robert A. Wittenmyer, Rosemary F. G. Wyse, Maruša Žerjal, and Galah Collaboration. **The GALAH+ survey: Third data release**. *MNRAS* 506:1 (Sept. 2021), 150–201. doi: [10.1093/mnras/stab1242](https://doi.org/10.1093/mnras/stab1242). arXiv: [2011.02505](https://arxiv.org/abs/2011.02505) [[astro-ph.GA](#)] (see pages 67, 71).
- [Cap+00] F. Caputo, M. Marconi, I. Musella, and P. Santolamazza. **Theoretical models for classical Cepheids. VII. Metallicity effects on the Cepheid distance scale**. *A&A* 359 (July 2000), 1059–1067. arXiv: [astro-ph/0006228](https://arxiv.org/abs/astro-ph/0006228) [[astro-ph](#)] (see pages 33, 66, 99).
- [Cap+13] Michele Cappellari, Nicholas Scott, Katherine Alatalo, Leo Blitz, Maxime Bois, Frédéric Bournaud, M. Bureau, Alison F. Crocker, Roger L. Davies, Timothy A. Davis, P. T. de Zeeuw, Pierre-Alain Duc, Eric Emsellem, Sadegh Khochfar, Davor Krajnović, Harald Kuntschner, Richard M. McDermid, Raffaella Morganti, Thorsten Naab, Tom Oosterloo, Marc Sarzi, Paolo Serra, Anne-Marie Weijmans, and Lisa M. Young. **The ATLAS^{3D} project - XV. Benchmark for early-type galaxies scaling relations from 260 dynamical models: mass-to-light ratio, dark matter, Fundamental Plane and Mass Plane**. *MNRAS* 432:3 (July 2013), 1709–1741. doi: [10.1093/mnras/stt562](https://doi.org/10.1093/mnras/stt562). arXiv: [1208.3522](https://arxiv.org/abs/1208.3522) [[astro-ph.CO](#)] (see pages 51, 112).
- [Car+19] R Carrera, A Bragaglia, T Cantat-Gaudin, A Vallenari, L Balaguer-Núñez, D Bossini, L Casamiquela, C Jordi, R Sordo, and C Soubiran. **Open clusters in APOGEE and GALAH-Combining Gaia and ground-based spectroscopic surveys**. *Astronomy & Astrophysics* 623 (2019), A80 (see page 56).
- [Cas+19] L Casamiquela, S Blanco-Cuaresma, R Carrera, L Balaguer-Núñez, C Jordi, F Anders, C Chiappini, J Carbajo-Hijarrubia, DS Aguado, A del Pino, et al. **OCCASO-III. Iron peak and α elements of 18 open clusters. Comparison with chemical evolution models and field stars**. *Monthly Notices of the Royal Astronomical Society* 490:2 (2019), 1821–1842 (see pages 34, 49, 55).
- [Cat+20] G. Catanzaro, V. Ripepi, G. Clementini, F. Cusano, G. De Somma, S. Leccia, M. Marconi, R. Molinaro, M. I. Moretti, I. Musella, and V. Testa. **V363 Casiopeiae: a new lithium-rich Galactic Cepheid**. *A&A* 639L4 (July 2020), L4. doi: [10.1051/0004-6361/202038486](https://doi.org/10.1051/0004-6361/202038486). arXiv: [2006.03299](https://arxiv.org/abs/2006.03299) [[astro-ph.SR](#)] (see pages 44, 71).
- [Cat07] Márcio Catelan. **Structure and evolution of low-mass stars: an overview and some open problems**. *arXiv preprint astro-ph/0703724* (2007) (see page 4).
- [CCM89] Jason A. Cardelli, Geoffrey C. Clayton, and John S. Mathis. **The Relationship between Infrared, Optical, and Ultraviolet Extinction**. *ApJ* 345 (Oct. 1989), 245. doi: [10.1086/167900](https://doi.org/10.1086/167900) (see page 70).

- [CH04] F Castelli and S Hubrig. **A spectroscopic atlas of the HgMn star HD 175640 (B9 V) 3040–10 000 Å**. *Astronomy & Astrophysics* 425:1 (2004), 263–270 (see pages 41, 107).
- [Che+20] Xiaodian Chen, Shu Wang, Licai Deng, Richard de Grijs, Ming Yang, and Hao Tian. **The Zwicky Transient Facility Catalog of Periodic Variable Stars**. *ApJS* 249:1, 18 (July 2020), 18. DOI: [10.3847/1538-4365/ab9cae](https://doi.org/10.3847/1538-4365/ab9cae). arXiv: 2005.08662 [astro-ph. SR] (see pages 66, 99).
- [Cla03] Donald Clayton. **Handbook of Isotopes in the Cosmos**. 2003 (see page 46).
- [Cle+16] G. Clementini, V. Ripepi, S. Leccia, N. Mowlavi, I. Lecoœur-Taibi, M. Marconi, L. Szabados, L. Eyer, L. P. Guy, L. Rimoldini, G. Jevardat de Fombelle, B. Holl, G. Busso, J. Charnas, J. Cuypers, F. De Angeli, J. De Ridder, J. Debosscher, D. W. Evans, P. Klagyivik, I. Musella, K. Nienartowicz, D. Ordóñez, S. Regibo, M. Riello, L. M. Sarro, and M. Süveges. **Gaia Data Release 1. The Cepheid and RR Lyrae star pipeline and its application to the south ecliptic pole region**. *A&A* 595A133 (Nov. 2016), A133. DOI: [10.1051/0004-6361/201629583](https://doi.org/10.1051/0004-6361/201629583). arXiv: 1609.04269 [astro-ph. SR] (see page 48).
- [Cle+19] G. Clementini, V. Ripepi, R. Molinaro, A. Garofalo, T. Muraveva, L. Rimoldini, L. P. Guy, G. Jevardat de Fombelle, K. Nienartowicz, O. Marchal, M. Audard, B. Holl, S. Leccia, M. Marconi, I. Musella, N. Mowlavi, I. Lecoœur-Taibi, L. Eyer, J. De Ridder, S. Regibo, L. M. Sarro, L. Szabados, D. W. Evans, and M. Riello. **Gaia Data Release 2. Specific characterisation and validation of all-sky Cepheids and RR Lyrae stars**. *A&A* 622A60 (Feb. 2019), A60. DOI: [10.1051/0004-6361/201833374](https://doi.org/10.1051/0004-6361/201833374). arXiv: 1805.02079 [astro-ph. SR] (see pages 66, 99).
- [Cow+21] John J Cowan, Christopher Sneden, James E Lawler, Ani Aprahamian, Michael Wiescher, Karlheinz Langanke, Gabriel Martínez-Pinedo, and Friedrich-Karl Thielemann. **Origin of the heaviest elements: The rapid neutron-capture process**. *Reviews of Modern Physics* 93:1 (2021), 015002 (see page 46).
- [Cow34] TG Cowling. **The stability of gaseous stars**. *Monthly Notices of the Royal Astronomical Society, Vol. 94, p. 768-782* 94 (1934), 768–782 (see page 13).
- [Cow35] TG Cowling. **The stability of gaseous stars (Second paper)**. *Monthly Notices of the Royal Astronomical Society, Vol. 96, p. 42 96* (1935), 42 (see page 13).
- [Cox55] John Paul Cox. **The pulsational stability of models for red giant stars**. Indiana University, 1955 (see page 13).
- [Cox67] John P Cox. **The linear theory: initiation of pulsational instability in stars**. In: *Aerodynamic Phenomena in Stellar Atmospheres*. Vol. 28. 1967, 3 (see page 13).

- [CS15] Márcio Catelan and Horace A Smith. **Pulsating stars**. John Wiley & Sons, 2015 (see pages 12, 14).
- [Cun+16] Katia Cunha, Peter M Frinchaboy, Diogo Souto, Benjamin Thompson, Gail Zasowski, C Allende Prieto, Ricardo Carrera, Cristina Chiappini, John Donor, Anibal García-Hernández, et al. **Chemical abundance gradients from open clusters in the Milky Way disk: Results from the APOGEE survey**. *Astronomische Nachrichten* 337:8-9 (2016), 922–925 (see pages 34, 49, 54–57).
- [CW58] John P Cox and Charles Whitney. **Stellar Pulsation. IV. a Semitheoretical Period-Luminosity Relation for Classical Cepheids**. *Astrophysical Journal*, vol. 127, p. 561 127 (1958), 561 (see page 2).
- [Dai+21] M. G. Dainotti, B. De Simone, T. Schiavone, G. Montani, E. Rinaldi, and G. Lambiase. **On the Hubble Constant Tension in the SNe Ia Pantheon Sample**. *ApJ* 912:2, 150 (May 2021), 150. DOI: 10.3847/1538-4357/abeb73. arXiv: 2103.02117 [astro-ph.CO] (see pages 33, 99).
- [DC04] Simone Daflon and Katia Cunha. **Galactic Metallicity Gradients Derived from a Sample of OB Stars**. *ApJ* 617:2 (Dec. 2004), 1115–1126. DOI: 10.1086/425607. arXiv: astro-ph/0409084 [astro-ph] (see page 57).
- [De +22] Giulia De Somma, Marcella Marconi, Roberto Molinaro, Vincenzo Ripepi, Silvio Leccia, and Ilaria Musella. **An Updated Metal-dependent Theoretical Scenario for Classical Cepheids**. *ApJS* 262:1, 25 (Sept. 2022), 25. DOI: 10.3847/1538-4365/ac7f3b. arXiv: 2206.11154 [astro-ph.SR] (see pages 66, 89, 99).
- [Di +21] Eleonora Di Valentino, Olga Mena, Supriya Pan, Luca Visinelli, Weiqiang Yang, Alessandro Melchiorri, David F Mota, Adam G Riess, and Joseph Silk. **In the realm of the Hubble tension—a review of solutions**. *Classical and Quantum Gravity* 38:15 (2021), 153001 (see page 17).
- [Don+20] John Donor, Peter M Frinchaboy, Katia Cunha, Julia E O’Connell, Carlos Allende Prieto, Andrés Almeida, Friedrich Anders, Rachael Beaton, Dmitry Bizyaev, Joel R Brownstein, et al. **The Open Cluster Chemical Abundances and Mapping Survey. IV. Abundances for 128 Open Clusters Using SDSS/APOGEE DR16**. *The Astronomical Journal* 159:5 (2020), 199 (see pages 34, 49, 56–59).
- [Edd88] Arthur Stanley Eddington. **The internal constitution of the stars**. Cambridge University Press, 1988 (see pages 10, 13).

- [Eks+12] S. Ekström, C. Georgy, P. Eggenberger, G. Meynet, N. Mowlavi, A. Wyttenbach, A. Granada, T. Decressin, R. Hirschi, U. Frischknecht, C. Charbonnel, and A. Maeder. **Grids of stellar models with rotation. I. Models from 0.8 to 120 M_{\odot} at solar metallicity ($Z = 0.014$).** *A&A* 537A146 (Jan. 2012), A146. DOI: [10.1051/0004-6361/201117751](https://doi.org/10.1051/0004-6361/201117751). arXiv: [1110.5049](https://arxiv.org/abs/1110.5049) [[astro-ph.SR](#)] (see pages 4, 5).
- [EM08] Laurent Eyer and Nami Mowlavi. **Variable stars across the observational HR diagram.** In: *Journal of Physics: Conference Series*. Vol. 118. 1. IOP Publishing. 2008, 012010 (see page 2).
- [FC97] M. W. Feast and R. M. Catchpole. **The Cepheid period-luminosity zero-point from HIPPARCOS trigonometrical parallaxes.** *MNRAS* 286:1 (Mar. 1997), L1–L5. DOI: [10.1093/mnras/286.1.L1](https://doi.org/10.1093/mnras/286.1.L1) (see pages 73, 74, 128).
- [FMM13] Giuliana Fiorentino, Ilaria Musella, and Marcella Marconi. **Cepheid theoretical models and observations in HST/WFC3 filters: the effect on the Hubble constant H_0 .** *MNRAS* 434:4 (Oct. 2013), 2866–2876. DOI: [10.1093/mnras/stt1193](https://doi.org/10.1093/mnras/stt1193). arXiv: [1306.6276](https://arxiv.org/abs/1306.6276) [[astro-ph.CO](#)] (see pages 66, 99).
- [Fou+07] P. Fouqué, P. Arriagada, J. Storm, T. G. Barnes, N. Nardetto, A. Mérand, P. Kervella, W. Gieren, D. Bersier, G. F. Benedict, and B. E. McArthur. **A new calibration of Galactic Cepheid period-luminosity relations from B to K bands, and a comparison to LMC relations.** *A&A* 476:1 (Dec. 2007), 73–81. DOI: [10.1051/0004-6361:20078187](https://doi.org/10.1051/0004-6361:20078187). arXiv: [0709.3255](https://arxiv.org/abs/0709.3255) [[astro-ph](#)] (see page 89).
- [Fre+01] Wendy L. Freedman, Barry F. Madore, Brad K. Gibson, Laura Ferrarese, Daniel D. Kelson, Shoko Sakai, Jeremy R. Mould, Robert C. Kennicutt Jr, Holland C. Ford, John A. Graham, et al. **Final results from the Hubble Space Telescope key project to measure the Hubble constant.** *The Astrophysical Journal* 553:1 (2001), 47 (see page 17).
- [Fre+12] Wendy L. Freedman, Barry F. Madore, Victoria Scowcroft, Chris Burns, Andy Monson, S. Eric Persson, Mark Seibert, and Jane Rigby. **Carnegie Hubble Program: A Mid-infrared Calibration of the Hubble Constant.** *ApJ* 758:1, 24 (Oct. 2012), 24. DOI: [10.1088/0004-637X/758/1/24](https://doi.org/10.1088/0004-637X/758/1/24). arXiv: [1208.3281](https://arxiv.org/abs/1208.3281) [[astro-ph.CO](#)] (see pages 33, 65, 97).
- [Fre21] Wendy L. Freedman. **Measurements of the Hubble Constant: Tensions in Perspective.** *ApJ* 919:1, 16 (Sept. 2021), 16. DOI: [10.3847/1538-4357/ac0e95](https://doi.org/10.3847/1538-4357/ac0e95). arXiv: [2106.15656](https://arxiv.org/abs/2106.15656) [[astro-ph.CO](#)] (see pages 33, 99).

- [Fri+13] Peter M Frinchaboy, Benjamin Thompson, Kelly M Jackson, Julia O’Connell, Brianne Meyer, Gail Zasowski, Steven R Majewski, S Drew Chojnowski, Jennifer A Johnson, Carlos Allende Prieto, et al. **The open cluster chemical analysis and mapping survey: local Galactic metallicity gradient with APOGEE using SDSS DR10**. *The Astrophysical Journal Letters* 777:1 (2013), L1 (see page 54).
- [Gai+16] Gaia Collaboration et al. **The Gaia mission**. *A&A* 595A1 (Nov. 2016), A1. doi: 10.1051/0004-6361/201629272. arXiv: 1609.04153 [astro-ph.IM] (see pages 17, 18, 34, 66, 99).
- [Gai+17] Gaia Collaboration et al. **Gaia Data Release 1. Testing parallaxes with local Cepheids and RR Lyrae stars**. *A&A* 605A79 (Sept. 2017), A79. doi: 10.1051/0004-6361/201629925. arXiv: 1705.00688 [astro-ph.SR] (see pages 44, 67, 69–71).
- [Gai+18] Gaia Collaboration et al. **Gaia Data Release 2. Summary of the contents and survey properties**. *A&A* 616A1 (Aug. 2018), A1. doi: 10.1051/0004-6361/201833051. arXiv: 1804.09365 [astro-ph.GA] (see pages 34, 66, 99).
- [Gai+21] Gaia Collaboration et al. **Gaia Early Data Release 3. Summary of the contents and survey properties**. *A&A* 649A1 (May 2021), A1. doi: 10.1051/0004-6361/202039657. arXiv: 2012.01533 [astro-ph.GA] (see pages 34, 48, 66, 99).
- [Gai+22] Gaia Collaboration et al. **Gaia Data Release 3: Chemical cartography of the Milky Way**. *arXiv e-prints* arXiv:2206.05534 (June 2022), arXiv:2206.05534. arXiv: 2206.05534 [astro-ph.GA] (see pages 49, 56).
- [Gai+23] Gaia Collaboration et al. **Gaia Data Release 3. The Galaxy in your preferred colours: Synthetic photometry from Gaia low-resolution spectra**. *A&A* 674A33 (June 2023), A33. doi: 10.1051/0004-6361/202243709. arXiv: 2206.06215 [astro-ph.SR] (see page 69).
- [Gen+14] K. Genovali, B. Lemasle, G. Bono, M. Romaniello, M. Fabrizio, I. Ferraro, G. Iannicola, C. D. Laney, M. Nonino, M. Bergemann, R. Buonanno, P. François, L. Inno, R. -P. Kudritzki, N. Matsunaga, S. Pedicelli, F. Primas, and F. Thévenin. **On the fine structure of the Cepheid metallicity gradient in the Galactic thin disk**. *A&A* 566A37 (June 2014), A37. doi: 10.1051/0004-6361/201323198. arXiv: 1403.6128 [astro-ph.GA] (see pages 34, 49, 51, 54, 66, 67, 99).
- [Gie+12] Wolfgang Gieren, Jesper Storm, Nicolas Nardetto, Alexandre Gallenne, Grzegorz Pietrzyński, Pascal Fouqué, Thomas G Barnes, and Daniel Majaess. **Cepheid distances from the Baade–Wesselink method**. *Proceedings of the International Astronomical Union* 8:S289 (2012), 138–144 (see page 18).

- [Gie+18] W. Gieren, J. Storm, P. Konorski, M. Górski, B. Pilecki, I. Thompson, G. Pietrzyński, D. Graczyk, T. G. Barnes, P. Fouqué, N. Nardetto, A. Gallenne, P. Karczmarek, K. Suchomska, P. Wielgórski, M. Taormina, and B. Zgirski. **The effect of metallicity on Cepheid period-luminosity relations from a Baade-Wesselink analysis of Cepheids in the Milky Way and Magellanic Clouds**★. *A&A* 620A99 (Dec. 2018), A99. DOI: [10.1051/0004-6361/201833263](https://doi.org/10.1051/0004-6361/201833263). arXiv: 1809.04073 [[astro-ph.SR](#)] (see pages 66, 89, 99).
- [Gor+03] Karl D. Gordon, Geoffrey C. Clayton, K. A. Misselt, Arlo U. Landolt, and Michael J. Wolff. **A Quantitative Comparison of the Small Magellanic Cloud, Large Magellanic Cloud, and Milky Way Ultraviolet to Near-Infrared Extinction Curves**. *ApJ* 594:1 (Sept. 2003), 279–293. DOI: [10.1086/376774](https://doi.org/10.1086/376774). arXiv: [astro-ph/0305257](https://arxiv.org/abs/astro-ph/0305257) [[astro-ph](#)] (see page 48).
- [Gra+22] Gravity Collaboration, R. Abuter, N. Aimar, A. Amorim, J. Ball, M. Bauböck, J. P. Berger, H. Bonnet, G. Bourdarot, W. Brandner, V. Cardoso, Y. Clénet, Y. Dallilar, R. Davies, P. T. de Zeeuw, J. Dexter, A. Drescher, F. Eisenhauer, N. M. Förster Schreiber, A. Foschi, P. Garcia, F. Gao, E. Gendron, R. Genzel, S. Gillessen, M. Habibi, X. Haubois, G. Heißel, T. Henning, S. Hippler, M. Horrobin, L. Jochum, L. Jocou, A. Kaufer, P. Kervella, S. Lacour, V. Lapeyrère, J. -B. Le Bouquin, P. Léna, D. Lutz, T. Ott, T. Paumard, K. Perraut, G. Perrin, O. Pfuhl, S. Rabien, J. Shangguan, T. Shimizu, S. Scheithauer, J. Stadler, A. W. Stephens, O. Straub, C. Straubmeier, E. Sturm, L. J. Tacconi, K. R. W. Tristram, F. Vincent, S. von Fellenberg, F. Widmann, E. Wieprecht, E. Wiezorrek, J. Woillez, S. Yazici, and A. Young. **Mass distribution in the Galactic Center based on interferometric astrometry of multiple stellar orbits**. *A&A* 657L12 (Jan. 2022), L12. DOI: [10.1051/0004-6361/202142465](https://doi.org/10.1051/0004-6361/202142465) (see pages 48, 102).
- [Gra21] David F Gray. **The observation and analysis of stellar photospheres**. Cambridge university press, 2021 (see pages 19, 20, 23, 29).
- [Gra75] David F Gray. **Atmospheric turbulence measured in stars above the main sequence**. *Astrophysical Journal*, vol. 202, Nov. 15, 1975, pt. 1, p. 148–164. *Research supported by the National Research Council of Canada*. 202 (1975), 148–164 (see page 30).
- [Gro+04] M. A. T. Groenewegen, M. Romaniello, F. Primas, and M. Mottini. **The metallicity dependence of the Cepheid PL-relation**. *A&A* 420 (June 2004), 655–663. DOI: [10.1051/0004-6361:20035926](https://doi.org/10.1051/0004-6361:20035926). arXiv: [astro-ph/0403177](https://arxiv.org/abs/astro-ph/0403177) [[astro-ph](#)] (see page 89).
- [Gro13] MAT Groenewegen. **Baade-Wesselink distances to Galactic and Magellanic Cloud Cepheids and the effect of metallicity**. *Astronomy & Astrophysics* 550 (2013), A70 (see page 87).

- [Gro18] M. A. T. Groenewegen. **The Cepheid period-luminosity-metallicity relation based on Gaia DR2 data**. *A&A* 619A8 (Nov. 2018), A8. DOI: [10.1051/0004-6361/201833478](https://doi.org/10.1051/0004-6361/201833478). arXiv: 1808.05796 [astro-ph. SR] (see pages 34, 43, 66, 67, 69–71, 89, 99).
- [Hay+17] M. R. Hayden, A. Recio-Blanco, P. de Laverny, S. Mikolaitis, and C. C. Worley. **The AMBRE project: The thick thin disk and thin thick disk of the Milky Way**. *A&A* 608L1 (Dec. 2017), L1. DOI: [10.1051/0004-6361/201731494](https://doi.org/10.1051/0004-6361/201731494). arXiv: 1712.02358 [astro-ph. GA] (see page 47).
- [Her05] Falk Herwig. **Evolution of asymptotic giant branch stars**. *Annu. Rev. Astron. Astrophys.* 43:1 (2005), 435–479 (see page 7).
- [HT25] Johan Holtzmark and B Trumphy. **Über die Verbreiterung von Spektrallinien. III**. *Zeitschrift für Physik* 31:1 (1925), 803–812 (see page 23).
- [Ibe65] Icko Iben Jr. **Stellar Evolution. I. The Approach to the Main Sequence**. *Astrophysical Journal*, vol. 141, p. 993 141 (1965), 993 (see page 4).
- [Ibe67] Icko Iben Jr. **Stellar evolution within and off the main sequence**. *Annual Review of Astronomy and Astrophysics* 5:1 (1967), 571–626 (see page 44).
- [Jan79] KA Janes. **Evidence for an abundance gradient in the galactic disk**. *The Astrophysical Journal Supplement Series* 39 (1979), 135–156 (see page 53).
- [Jor+10] C. Jordi, M. Gebran, J. M. Carrasco, J. de Bruijne, H. Voss, C. Fabricius, J. Knude, A. Vallenari, R. Kohley, and A. Mora. **Gaia broad band photometry**. *A&A* 523A48 (Nov. 2010), A48. DOI: [10.1051/0004-6361/201015441](https://doi.org/10.1051/0004-6361/201015441). arXiv: 1008.0815 [astro-ph. IM] (see page 47).
- [KA81] Robert L Kurucz and Eugene H Avrett. **Solar spectrum synthesis. I. A sample atlas from 224 to 300 nm**. *SAO Special Report* 391 (1981) (see pages 39, 106, 107).
- [KC68] David S King and John P Cox. **Pulsating stars**. *Publications of the Astronomical Society of the Pacific* 80:475 (1968), 365 (see page 15).
- [KG00] VV Kovtyukh and NI Gorlova. **Precise temperatures of classical Cepheids and yellow supergiants from line-depth ratios**. *Astronomy and Astrophysics* 358 (2000), 587–592 (see pages 28, 35, 38, 105, 106).
- [KL16] Amanda I Karakas and Maria Lugaro. **Stellar yields from metal-rich asymptotic giant branch models**. *The Astrophysical Journal* 825:1 (2016), 26 (see page 46).
- [Kor+12] O Korobkin, Stephan Rosswog, A Arcones, and C Winteler. **On the astrophysical robustness of the neutron star merger r-process**. *Monthly Notices of the Royal Astronomical Society* 426:3 (2012), 1940–1949 (see page 46).

- [Kov+22] V. Kovtyukh, B. Lemasle, G. Bono, I. A. Usenko, R. da Silva, A. Kniazev, E. K. Grebel, I. L. Andronov, L. Shakun, and L. Chinarova. **The MAGIC project - III. Radial and azimuthal Galactic abundance gradients using classical Cepheids**. *MNRAS* 510:2 (Feb. 2022), 1894–1901. DOI: [10.1093/mnras/stab3530](https://doi.org/10.1093/mnras/stab3530). arXiv: [2112.04258](https://arxiv.org/abs/2112.04258) [astro-ph. GA] (see pages 44, 67, 71).
- [Kra23] Hendrik A Kramers. **XCIII. On the theory of X-ray absorption and of the continuous X-ray spectrum**. *The London, Edinburgh, and Dublin Philosophical Magazine and Journal of Science* 46:275 (1923), 836–871 (see page 13).
- [Kur93] Robert L Kurucz. **A new opacity-sampling model atmosphere program for arbitrary abundances**. In: *International Astronomical Union Colloquium*. Vol. 138. Cambridge University Press. 1993, 87–97 (see pages 39, 106).
- [Kur95] RL Kurucz. **Kurucz CD-Rom No. 23**. *Atomic Line List* (1995) (see pages 41, 107).
- [Lan+09] John D Landstreet, Friedrich Kupka, HA Ford, T Officer, TAA Sigut, J Silaj, S Strasser, and A Townshend. **Atmospheric velocity fields in tepid main sequence stars**. *Astronomy & Astrophysics* 503:3 (2009), 973–984 (see page 31).
- [Lea08] Henrietta S Leavitt. **1777 variables in the Magellanic Clouds**. *Annals of Harvard College Observatory*, vol. 60, pp. 87-108.3 60 (1908), 87–108 (see page 3).
- [Lem+18] Bertrand Lemasle, Gergely Hajdu, Valery Kovtyukh, Laura Inno, EK Grebel, Márcio Catelan, Giuseppe Bono, Patrick François, Alexei Kniazev, Ronaldo da Silva, et al. **Milky Way metallicity gradient from Gaia DR2 F/10 double-mode Cepheids**. *Astronomy & Astrophysics* 618 (2018), A160 (see pages 34, 49, 54, 101).
- [Lem+22] B. Lemasle, H. N. Lala, V. Kovtyukh, M. Hanke, Z. Prudil, G. Bono, V. F. Braga, R. da Silva, M. Fabrizio, G. Fiorentino, P. François, E. K. Grebel, and A. Kniazev. **Tracing the Milky Way warp and spiral arms with classical Cepheids**. *A&A* 668A40 (Dec. 2022), A40. DOI: [10.1051/0004-6361/202243273](https://doi.org/10.1051/0004-6361/202243273). arXiv: [2209.02731](https://arxiv.org/abs/2209.02731) [astro-ph. GA] (see pages 66, 99).
- [Lin+21] L. Lindgren, U. Bastian, M. Biermann, A. Bombrun, A. de Torres, E. Gerlach, R. Geyer, J. Hernández, T. Hilger, D. Hobbs, S. A. Klioner, U. Lammers, P. J. McMillan, M. Ramos-Lerate, H. Steidelmüller, C. A. Stephenson, and F. van Leeuwen. **Gaia Early Data Release 3. Parallax bias versus magnitude, colour, and position**. *A&A* 649A4 (May 2021), A4. DOI: [10.1051/0004-6361/202039653](https://doi.org/10.1051/0004-6361/202039653). arXiv: [2012.01742](https://arxiv.org/abs/2012.01742) [astro-ph. IM] (see pages 67, 73, 129).
- [LL11] R. Earle Luck and David L. Lambert. **The Distribution of the Elements in the Galactic Disk. III. A Reconsideration of Cepheids from $l = 30^\circ$ to 250°** . *AJ* 142:4, 136 (Oct. 2011), 136. DOI: [10.1088/0004-6256/142/4/136](https://doi.org/10.1088/0004-6256/142/4/136). arXiv: [1108.1947](https://arxiv.org/abs/1108.1947) [astro-ph. GA] (see pages 34, 35, 49, 54).

- [LP12] Henrietta S. Leavitt and Edward C. Pickering. **Periods of 25 Variable Stars in the Small Magellanic Cloud.** *Harvard College Observatory Circular* 173 (Mar. 1912), 1–3 (see pages 3, 33, 65, 97).
- [LSB55] Paul Ledoux, R Simon, and J Bielaire. **Sur les oscillations radiales de modèles stellaires à grande concentration massique.** In: *Annales d'astrophysique*. Vol. 18. Caisse nationale de la recherche scientifique, Paris, France. 1955 (see page 13).
- [Luc18] R. Earle Luck. **Cepheid Abundances: Multiphase Results and Spatial Gradients.** *AJ* 156:4, 171 (Oct. 2018), 171. DOI: 10.3847/1538-3881/aadcac. arXiv: 1808.05863 [astro-ph.SR] (see pages 34, 44, 49, 54, 57, 66, 99, 101, 119).
- [Mad82] B. F. Madore. **The period-luminosity relation. IV. Intrinsic relations and reddening for the Large Magellanic Cloud Cepheids.** *ApJ* 253 (Feb. 1982), 575–579. DOI: 10.1086/159659 (see pages 16, 33, 47, 66, 99).
- [Mag+10] Laura Magrini, Sofia Randich, Manuela Zoccali, Lucie Jilkova, Giovanni Carraro, Daniele Galli, Enrico Maiorca, and Maurizio Busso. **Open clusters towards the Galactic centre: chemistry and dynamics-A VLT spectroscopic study of NGC 6192, NGC 6404, NGC 6583.** *Astronomy & Astrophysics* 523 (2010), A11 (see page 54).
- [Mar+10] M. Marconi, I. Musella, G. Fiorentino, G. Clementini, A. Aloisi, F. Annibali, R. Contreras Ramos, A. Saha, M. Tosi, and R. P. van der Marel. **Pulsation Models for Ultra-low ($Z = 0.0004$) Metallicity Classical Cepheids.** *ApJ* 713:1 (Apr. 2010), 615–625. DOI: 10.1088/0004-637X/713/1/615. arXiv: 1002.4752 [astro-ph.SR] (see pages 66, 99).
- [Mat21] Francesca Matteucci. **Modelling the chemical evolution of the Milky Way.** *A&A Rev.* 29:1, 5 (Dec. 2021), 5. DOI: 10.1007/s00159-021-00133-8. arXiv: 2106.13145 [astro-ph.GA] (see page 47).
- [MB20] A Mucciarelli and P Bonifacio. **Facing problems in the determination of stellar temperatures and gravities: Galactic globular clusters.** *Astronomy & Astrophysics* 640 (2020), A87 (see page 38).
- [MF11] Barry F Madore and Wendy L Freedman. **Multi-Wavelength Characteristics of Period–Luminosity Relations.** *The Astrophysical Journal* 744:2 (2011), 132 (see page 77).
- [Mil30] Edward Arthur Milne. **Handbuch der Astrophysik. Bd. 3: Hälfte 2: Grundlagen der Astrophysik; Teil 3, 1.** Springer, 1930 (see page 23).

- [Min+20] J. H. Minniti, L. Sbordone, A. Rojas-Arriagada, M. Zoccali, R. Contreras Ramos, D. Minniti, M. Marconi, V. F. Braga, M. Catelan, S. Duffau, W. Gieren, and A. A. R. Valcarce. **Using classical Cepheids to study the far side of the Milky Way disk. I. Spectroscopic classification and the metallicity gradient.** *A&A* 640A92 (Aug. 2020), A92. DOI: [10.1051/0004-6361/202037575](https://doi.org/10.1051/0004-6361/202037575). arXiv: 2007.03122 [astro-ph.GA] (see pages 34, 49, 56, 101).
- [Min+21] JH Minniti, M Zoccali, A Rojas-Arriagada, D Minniti, L Sbordone, R Contreras Ramos, Vittorio Francesco Braga, M Catelan, S Duffau, W Gieren, et al. **Using classical Cepheids to study the far side of the Milky Way disk. II. The spiral structure in the first and fourth Galactic quadrants.** *arXiv preprint arXiv:2107.03464* (2021) (see pages 53, 59, 115, 121, 129).
- [MMF05] M. Marconi, I. Musella, and G. Fiorentino. **Cepheid Pulsation Models at Varying Metallicity and $\Delta Y/\Delta Z$.** *ApJ* 632:1 (Oct. 2005), 590–610. DOI: [10.1086/432790](https://doi.org/10.1086/432790). arXiv: astro-ph/0506207 [astro-ph] (see pages 66, 99).
- [Mol+23] R Molinaro, V Ripepi, M Marconi, M Romaniello, G Catanzaro, F Cusano, G De Somma, I Musella, J Storm, and E Trentin. **Cepheid metallicity in the Leavitt law (C-MetaLL) survey – III. Simultaneous derivation of the Gaia parallax offset and period–luminosity–metallicity coefficients.** *MNRAS* 520:3 (Feb. 2023), 4154–4166. ISSN: 0035-8711. DOI: [10.1093/mnras/stad440](https://doi.org/10.1093/mnras/stad440). eprint: <https://academic.oup.com/mnras/article-pdf/520/3/4154/49279293/stad440.pdf>. URL: <https://doi.org/10.1093/mnras/stad440> (see pages 84, 85, 90, 91, 129).
- [Net+16] Martin Netopil, Ernst Paunzen, Ulrike Heiter, and Caroline Soubiran. **On the metallicity of open clusters-III. Homogenised sample.** *Astronomy & Astrophysics* 585 (2016), A150 (see pages 34, 49, 55, 56, 59).
- [Pal18] Frédéric Paletou. **On Milne–Barbier–Unsöld relationships.** *Open Astronomy* 27:1 (2018), 76–79 (see page 25).
- [Pan+22] E. Pancino, P. M. Marrese, S. Marinoni, N. Sanna, A. Turchi, M. Tsantaki, M. Rainer, G. Altavilla, M. Monelli, and L. Monaco. **The Gaia EDR3 view of Johnson-Kron-Cousins standard stars: the curated Landolt and Stetson collections.** *A&A* 664A109 (Aug. 2022), A109. DOI: [10.1051/0004-6361/202243939](https://doi.org/10.1051/0004-6361/202243939). arXiv: 2205.06186 [astro-ph.SR] (see pages 67–69).
- [Pie+19] G. Pietrzyński, D. Graczyk, A. Gallenne, W. Gieren, I. B. Thompson, B. Pilecki, P. Karczmarek, M. Górski, K. Suchomska, M. Taormina, B. Zgirski, P. Wielgórski, Z. Kołaczkowski, P. Konorski, S. Villanova, N. Nardetto, P. Kervella, F. Bresolin, R. P. Kudritzki, J. Storm, R. Smolec, and W. Narloch. **A distance to the Large Magellanic Cloud that is precise to one per cent.** *Nature* 567:7747 (Mar. 2019), 200–203. DOI: [10.1038/s41586-019-0999-4](https://doi.org/10.1038/s41586-019-0999-4). arXiv: 1903.08096 [astro-ph.GA] (see pages 86, 91, 129).

- [Pla+20] Planck Collaboration et al. **Planck 2018 results. VI. Cosmological parameters**. *A&A* 641A6 (Sept. 2020), A6. DOI: [10.1051/0004-6361/201833910](https://doi.org/10.1051/0004-6361/201833910). arXiv: [1807.06209](https://arxiv.org/abs/1807.06209) [[astro-ph.CO](#)] (see pages 17, 33, 65, 97).
- [Pog+21] E. Poggio, R. Drimmel, T. Cantat-Gaudin, P. Ramos, V. Ripepi, E. Zari, R. Andrae, R. Blomme, L. Chemin, G. Clementini, F. Figueras, M. Fouesneau, Y. Frémat, A. Lobel, D. J. Marshall, T. Muraveva, and M. Romero-Gómez. **Galactic spiral structure revealed by Gaia EDR3**. *A&A* 651A104 (July 2021), A104. DOI: [10.1051/0004-6361/202140687](https://doi.org/10.1051/0004-6361/202140687). arXiv: [2103.01970](https://arxiv.org/abs/2103.01970) [[astro-ph.GA](#)] (see page 48).
- [Rab57] Irving N Rabinowitz. **On the Pulsational Stability of Stars with Convective Envelopes**. *Astrophysical Journal*, vol. 126, p. 386 126 (1957), 386 (see page 13).
- [Ran+22] S Randich, G Gilmore, L Magrini, GG Sacco, RJ Jackson, RD Jeffries, CC Worley, A Hourihane, A Gonneau, C Viscasillas Vázquez, et al. **The Gaia-ESO Public Spectroscopic Survey: Implementation, data products, open cluster survey, science, and legacy**. *arXiv preprint arXiv:2206.02901* (2022) (see page 56).
- [Rec+23] A. Recio-Blanco, P. de Laverny, P. A. Palicio, G. Kordopatis, M. A. Álvarez, M. Schultheis, G. Contursi, H. Zhao, G. Torralba Elipe, C. Ordenovic, M. Manteiga, C. Dafonte, I. Oreshina-Slezak, A. Bijaoui, Y. Frémat, G. Seabroke, F. Pailler, E. Spitoni, E. Poggio, O. L. Creevey, A. Abreu Aramburu, S. Accart, R. Andrae, C. A. L. Bailer-Jones, I. Bellas-Velidis, N. Brouillet, E. Brugaletta, A. Burlacu, R. Carballo, L. Casamiquela, A. Chiavassa, W. J. Cooper, A. Dapergolas, L. Delchambre, T. E. Dharmawardena, R. Drimmel, B. Edvardsson, M. Fouesneau, D. Garabato, P. García-Lario, M. García-Torres, A. Gavel, A. Gomez, I. González-Santamaría, D. Hatzidimitriou, U. Heiter, A. Jean-Antoine Piccolo, M. Kontizas, A. J. Korn, A. C. Lanzafame, Y. Lebreton, Y. Le Fustec, E. L. Licata, H. E. P. Lindstrøm, E. Livanou, A. Lobel, A. Lorca, A. Magdaleno Romeo, F. Marocco, D. J. Marshall, N. Mary, C. Nicolas, L. Pallas-Quintela, C. Panem, B. Pichon, F. Riclet, C. Robin, J. Rybizki, R. Santoveña, A. Silvelo, R. L. Smart, L. M. Sarro, R. Sordo, C. Soubiran, M. Süveges, A. Ulla, A. Vallenari, J. Zorec, E. Utrilla, and J. Bakker. **Gaia Data Release 3. Analysis of RVS spectra using the General Stellar Parametriser from spectroscopy**. *A&A* 674A29 (June 2023), A29. DOI: [10.1051/0004-6361/202243750](https://doi.org/10.1051/0004-6361/202243750). arXiv: [2206.05541](https://arxiv.org/abs/2206.05541) [[astro-ph.GA](#)] (see pages 67, 72).
- [Rei+19] M. J. Reid, K. M. Menten, A. Brunthaler, X. W. Zheng, T. M. Dame, Y. Xu, J. Li, N. Sakai, Y. Wu, K. Immer, B. Zhang, A. Sanna, L. Moscadelli, K. L. J. Rygl, A. Bartkiewicz, B. Hu, L. H. Quiroga-Nuñez, and H. J. van Langevelde. **Trigonometric Parallaxes of High-mass Star-forming Regions: Our**

- View of the Milky Way.** *ApJ* 885:2, 131 (Nov. 2019), 131. DOI: [10.3847/1538-4357/ab4a11](https://doi.org/10.3847/1538-4357/ab4a11). arXiv: [1910.03357](https://arxiv.org/abs/1910.03357) [[astro-ph.GA](#)] (see pages 115, 116, 121, 129).
- [Rie+14] Adam G Riess, Stefano Casertano, Jay Anderson, John MacKenty, and Alexei V Filippenko. **Parallax beyond a kiloparsec from spatially scanning the wide field camera 3 on the Hubble Space Telescope.** *The Astrophysical Journal* 785:2 (2014), 161 (see page 17).
- [Rie+16] Adam G. Riess, Lucas M. Macri, Samantha L. Hoffmann, Dan Scolnic, Stefano Casertano, Alexei V. Filippenko, Brad E. Tucker, Mark J. Reid, David O. Jones, Jeffrey M. Silverman, Ryan Chornock, Peter Challis, Wenlong Yuan, Peter J. Brown, and Ryan J. Foley. **A 2.4% Determination of the Local Value of the Hubble Constant.** *ApJ* 826:1, 56 (July 2016), 56. DOI: [10.3847/0004-637X/826/1/56](https://doi.org/10.3847/0004-637X/826/1/56). arXiv: [1604.01424](https://arxiv.org/abs/1604.01424) [[astro-ph.CO](#)] (see pages 33, 65, 66, 89, 97, 99).
- [Rie+19] Adam G. Riess, Stefano Casertano, Wenlong Yuan, Lucas M. Macri, and Dan Scolnic. **Large Magellanic Cloud Cepheid Standards Provide a 1% Foundation for the Determination of the Hubble Constant and Stronger Evidence for Physics beyond Λ CDM.** *ApJ* 876:1, 85 (May 2019), 85. DOI: [10.3847/1538-4357/ab1422](https://doi.org/10.3847/1538-4357/ab1422). arXiv: [1903.07603](https://arxiv.org/abs/1903.07603) [[astro-ph.CO](#)] (see pages 33, 89).
- [Rie+21a] Adam G. Riess, Stefano Casertano, Wenlong Yuan, J. Bradley Bowers, Lucas Macri, Joel C. Zinn, and Dan Scolnic. **Cosmic Distances Calibrated to 1% Precision with Gaia EDR3 Parallaxes and Hubble Space Telescope Photometry of 75 Milky Way Cepheids Confirm Tension with Λ CDM.** *ApJ* 908:1, L6 (Feb. 2021), L6. DOI: [10.3847/2041-8213/abdbaf](https://doi.org/10.3847/2041-8213/abdbaf). arXiv: [2012.08534](https://arxiv.org/abs/2012.08534) [[astro-ph.CO](#)] (see pages 33, 34, 68, 70, 84–86, 89, 91, 129).
- [Rie+21b] Adam G. Riess, Wenlong Yuan, Lucas M. Macri, Dan Scolnic, Dillon Brout, Stefano Casertano, David O. Jones, Yukei Murakami, Louise Breuval, Thomas G. Brink, Alexei V. Filippenko, Samantha Hoffmann, Saurabh W. Jha, W. D'arcy Kenworthy, John Mackenty, Benjamin E. Stahl, and Weikang Zheng. **A Comprehensive Measurement of the Local Value of the Hubble Constant with 1 km/s/Mpc Uncertainty from the Hubble Space Telescope and the SH0ES Team.** *arXiv e-prints* arXiv:2112.04510 (Dec. 2021), arXiv:2112.04510. arXiv: [2112.04510](https://arxiv.org/abs/2112.04510) [[astro-ph.CO](#)] (see pages 33, 99).
- [Rie+22a] Adam G Riess, Wenlong Yuan, Lucas M Macri, Dan Scolnic, Dillon Brout, Stefano Casertano, David O Jones, Yukei Murakami, Gagandeep S Anand, Louise Breuval, et al. **A comprehensive measurement of the local value of the Hubble constant with 1 km s⁻¹ Mpc⁻¹ uncertainty from the**

- Hubble Space Telescope and the SH0ES team.** *The Astrophysical journal letters* 934:1 (2022), L7 (see page 17).
- [Rie+22b] Adam G. Riess, Wenlong Yuan, Lucas M. Macri, Dan Scolnic, Dillon Brout, Stefano Casertano, David O. Jones, Yukei Murakami, Gagandeep S. Anand, Louise Breuval, Thomas G. Brink, Alexei V. Filippenko, Samantha Hoffmann, Saurabh W. Jha, W. D'arcy Kenworthy, John Mackenty, Benjamin E. Stahl, and WeiKang Zheng. **A Comprehensive Measurement of the Local Value of the Hubble Constant with $1 \text{ km s}^{-1} \text{ Mpc}^{-1}$ Uncertainty from the Hubble Space Telescope and the SH0ES Team.** *ApJ* 934:1, L7 (July 2022), L7. DOI: [10.3847/2041-8213/ac5c5b](https://doi.org/10.3847/2041-8213/ac5c5b). arXiv: [2112.04510](https://arxiv.org/abs/2112.04510) [[astro-ph.CO](https://arxiv.org/archive/astro-ph)] (see pages 65, 84, 89, 97).
- [Rip+19] V. Ripepi, R. Molinaro, I. Musella, M. Marconi, S. Leccia, and L. Eyer. **Reclassification of Cepheids in the Gaia Data Release 2. Period-luminosity and period-Wesenheit relations in the Gaia passbands.** *A&A* 625A14 (May 2019), A14. DOI: [10.1051/0004-6361/201834506](https://doi.org/10.1051/0004-6361/201834506). arXiv: [1810.10486](https://arxiv.org/abs/1810.10486) [[astro-ph.SR](https://arxiv.org/archive/astro-ph)] (see pages 34, 47, 48, 66, 89, 99, 102).
- [Rip+20] V. Ripepi, G. Catanzaro, R. Molinaro, M. Marconi, G. Clementini, F. Cusano, G. De Somma, S. Leccia, I. Musella, and V. Testa. **Period-luminosity-metallicity relation of classical Cepheids.** *A&A* 642A230 (Oct. 2020), A230. DOI: [10.1051/0004-6361/202038714](https://doi.org/10.1051/0004-6361/202038714). arXiv: [2008.04608](https://arxiv.org/abs/2008.04608) [[astro-ph.SR](https://arxiv.org/archive/astro-ph)] (see pages 34, 68, 73, 89).
- [Rip+21a] V. Ripepi, G. Catanzaro, R. Molinaro, M. Gatto, G. De Somma, M. Marconi, M. Romaniello, S. Leccia, I. Musella, E. Trentin, G. Clementini, V. Testa, F. Cusano, and J. Storm. **Cepheid metallicity in the Leavitt law (C-metal) survey - I. HARPS-N@TNG spectroscopy of 47 classical Cepheids and 1 BL Her variables.** *MNRAS* 508:3 (Dec. 2021), 4047–4071. DOI: [10.1093/mnras/stab2460](https://doi.org/10.1093/mnras/stab2460). arXiv: [2108.11391](https://arxiv.org/abs/2108.11391) [[astro-ph.GA](https://arxiv.org/archive/astro-ph)] (see pages 34, 44, 66–71, 73, 85, 86, 89, 90, 99, 101, 104, 128).
- [Rip+21b] V. Ripepi, G. Catanzaro, L. Molnár, E. Plachy, M. Marconi, G. Clementini, R. Molinaro, G. De Somma, S. Leccia, S. Mancino, I. Musella, F. Cusano, and V. Testa. **HD 344787: a true Polaris analogue?** *A&A* 647A111 (Mar. 2021), A111. DOI: [10.1051/0004-6361/202040123](https://doi.org/10.1051/0004-6361/202040123). arXiv: [2101.08553](https://arxiv.org/abs/2101.08553) [[astro-ph.SR](https://arxiv.org/archive/astro-ph)] (see pages 44, 71).
- [Rip+22] V. Ripepi, G. Catanzaro, G. Clementini, G. De Somma, R. Drimmel, S. Leccia, M. Marconi, R. Molinaro, I. Musella, and E. Poggio. **Classical Cepheid period-Wesenheit-metallicity relation in the Gaia bands.** *A&A* 659A167 (Mar. 2022), A167. DOI: [10.1051/0004-6361/202142649](https://doi.org/10.1051/0004-6361/202142649). arXiv: [2201.01126](https://arxiv.org/abs/2201.01126) [[astro-ph.SR](https://arxiv.org/archive/astro-ph)] (see pages 34, 35, 48, 49, 54, 58, 66, 68, 69, 72, 89, 99, 101, 102, 127).

- [Rip+23] V. Ripepi, G. Clementini, R. Molinaro, S. Leccia, E. Plachy, L. Molnár, L. Rimoldini, I. Musella, M. Marconi, A. Garofalo, M. Audard, B. Holl, D. W. Evans, G. Jevardat de Fombelle, I. Lecoœur-Taibi, O. Marchal, N. Mowlavi, T. Muraveva, K. Nienartowicz, P. Sartoretti, L. Szabados, and L. Eyer. **Gaia Data Release 3. Specific processing and validation of all sky RR Lyrae and Cepheid stars: The Cepheid sample.** *A&A* 674A17 (June 2023), A17. DOI: [10.1051/0004-6361/202243990](https://doi.org/10.1051/0004-6361/202243990). arXiv: [2206.06212](https://arxiv.org/abs/2206.06212) [[astro-ph.SR](#)] (see pages 18, 98, 101, 103, 122).
- [Rit79] August Ritter. **Untersuchungen über die Höhe der Atmosphäre und die Constitution gasförmiger Weltkörper.** *Annalen der Physik* 243:6 (1879), 304–317 (see page 10).
- [Rom+08] M. Romaniello, F. Primas, M. Mottini, S. Pedicelli, B. Lemasle, G. Bono, P. François, M. A. T. Groenewegen, and C. D. Laney. **The influence of chemical composition on the properties of Cepheid stars. II. The iron content.** *A&A* 488:2 (Sept. 2008), 731–747. DOI: [10.1051/0004-6361:20065661](https://doi.org/10.1051/0004-6361:20065661). arXiv: [0807.1196](https://arxiv.org/abs/0807.1196) [[astro-ph](#)] (see pages 39, 58, 66, 88, 99, 106, 127).
- [Rom+10] D. Romano, A. I. Karakas, M. Tosi, and F. Matteucci. **Quantifying the uncertainties of chemical evolution studies. II. Stellar yields.** *A&A* 522A32 (Nov. 2010), A32. DOI: [10.1051/0004-6361/201014483](https://doi.org/10.1051/0004-6361/201014483). arXiv: [1006.5863](https://arxiv.org/abs/1006.5863) [[astro-ph.GA](#)] (see page 46).
- [Ros28] Svein Rosseland. **Viscosity in the stars.** *Monthly Notices of the Royal Astronomical Society, Vol. 89, p. 49-53* 89 (1928), 49–53 (see page 24).
- [RR19] A KramidaYu Ralchenko and J Reader. **NIST Atomic Spectra Database (version 5.7. 1).** *National Institute of Standards and Technology, Gaithersburg, MD.* DOI: <https://doi.org/10.18434/T4W30F> (2019) (see pages 41, 107).
- [Ryb+22] Jan Rybizki, Gregory M. Green, Hans-Walter Rix, Kareem El-Badry, Markus Demleitner, Eleonora Zari, Andrzej Udalski, Richard L. Smart, and Andrew Gould. **A classifier for spurious astrometric solutions in Gaia eDR3.** *MNRAS* 510:2 (Feb. 2022), 2597–2616. DOI: [10.1093/mnras/stab3588](https://doi.org/10.1093/mnras/stab3588). arXiv: [2101.11641](https://arxiv.org/abs/2101.11641) [[astro-ph.IM](#)] (see pages 67, 73).
- [Sah21] Meghnad N Saha. **On a physical theory of stellar spectra.** *Proceedings of the Royal Society of London. Series A, Containing Papers of a Mathematical and Physical Character* 99:697 (1921), 135–153 (see page 23).
- [San04] Eric L Sandquist. **A high relative precision colour–magnitude diagram of M67.** *Monthly Notices of the Royal Astronomical Society* 347:1 (2004), 101–118 (see page 5).

- [Sas86] DIMITAR D Sasselov. **Normal supergiants and their imitations. I. Sodium as a mass indicator?** *Publications of the Astronomical Society of the Pacific* 98:604 (1986), 561 (see pages 45, 57).
- [SC05] Maurizio Salaris and Santi Cassisi. **Evolution of stars and stellar populations.** John Wiley & Sons, 2005 (see page 4).
- [Sha14] Harlow Shapley. **On the nature and cause of Cepheid variation.** *Astrophysical Journal*, vol. 40, p. 448 40 (1914), 448 (see page 2).
- [Sil+18] V. Silva Aguirre, M. Bojsen-Hansen, D. Slumstrup, L. Casagrande, D. Kawata, I. Ciucă, R. Handberg, M. N. Lund, J. R. Mosumgaard, D. Huber, J. A. Johnson, M. H. Pinsonneault, A. M. Serenelli, D. Stello, J. Tayar, J. C. Bird, S. Cassisi, M. Hon, M. Martig, P. E. Nissen, H. W. Rix, R. Schönrich, C. Sahlholdt, W. H. Trick, and J. Yu. **Confirming chemical clocks: asteroseismic age dissection of the Milky Way disc(s).** *MNRAS* 475:4 (Apr. 2018), 5487–5500. DOI: [10.1093/mnras/sty150](https://doi.org/10.1093/mnras/sty150). arXiv: [1710.09847](https://arxiv.org/abs/1710.09847) [[astro-ph.GA](#)] (see page 47).
- [Sil+22] R da Silva, J Crestani, G Bono, VF Braga, V D’Orazi, B Lemasle, M Bergemann, M Dall’Ora, G Fiorentino, P François, et al. **A new and homogeneous metallicity scale for Galactic classical Cepheids II. The abundance of iron and alpha elements.** *arXiv preprint arXiv:2202.07945* (2022) (see pages 34, 49, 54, 57).
- [Sim+04] Jennifer Simmerer, Christopher Sneden, John J. Cowan, Jason Collier, Vincent M. Woolf, and James E. Lawler. **The Rise of the s-Process in the Galaxy.** *ApJ* 617:2 (Dec. 2004), 1091–1114. DOI: [10.1086/424504](https://doi.org/10.1086/424504). arXiv: [astro-ph/0410396](https://arxiv.org/abs/astro-ph/0410396) [[astro-ph](#)] (see page 46).
- [Sko+19] Dorota M. Skowron, Jan Skowron, Przemek Mróz, Andrzej Udalski, Paweł Pietrukowicz, Igor Soszyński, Michał K. Szymański, Radosław Poleski, Szymon Kozłowski, Krzysztof Ulaczyk, Krzysztof Rybicki, and Patryk Iwanek. **A three-dimensional map of the Milky Way using classical Cepheid variable stars.** *Science* 365:6452 (Aug. 2019), 478–482. DOI: [10.1126/science.aau3181](https://doi.org/10.1126/science.aau3181). arXiv: [1806.10653](https://arxiv.org/abs/1806.10653) [[astro-ph.GA](#)] (see pages 35, 53, 103, 123).
- [Skr+06] M. F. Skrutskie, R. M. Cutri, R. Stiening, M. D. Weinberg, S. Schneider, J. M. Carpenter, C. Beichman, R. Capps, T. Chester, J. Elias, J. Huchra, J. Liebert, C. Lonsdale, D. G. Monet, S. Price, P. Seitzer, T. Jarrett, J. D. Kirkpatrick, J. E. Gizis, E. Howard, T. Evans, J. Fowler, L. Fullmer, R. Hurt, R. Light, E. L. Kopan, K. A. Marsh, H. L. McCallon, R. Tam, S. Van Dyk, and S. Wheelock. **The Two Micron All Sky Survey (2MASS).** *AJ* 131:2 (Feb. 2006), 1163–1183. DOI: [10.1086/498708](https://doi.org/10.1086/498708) (see page 69).

- [Sou+16] Caroline Soubiran, Jean-François Le Campion, Nathalie Brouillet, and Laurent Chemin. **The PASTEL catalogue: 2016 version**. *A&A* 591A118 (June 2016), A118. DOI: [10.1051/0004-6361/201628497](https://doi.org/10.1051/0004-6361/201628497). arXiv: [1605.07384](https://arxiv.org/abs/1605.07384) [[astro-ph.SR](#)] (see pages 67, 71).
- [Spi+19] E. Spitoni, V. Silva Aguirre, F. Matteucci, F. Calura, and V. Grisoni. **Galactic Archaeology with asteroseismic ages: Evidence for delayed gas infall in the formation of the Milky Way disc**. *A&A* 623A60 (Mar. 2019), A60. DOI: [10.1051/0004-6361/201834188](https://doi.org/10.1051/0004-6361/201834188). arXiv: [1809.00914](https://arxiv.org/abs/1809.00914) [[astro-ph.GA](#)] (see page 47).
- [Spi+21] Lorenzo Spina, Yuan-Sen Ting, Gayandhi M De Silva, Neige Frankel, Sanjib Sharma, Tristan Cantat-Gaudin, Meridith Joyce, Dennis Stello, Amanda I Karakas, Martin B Asplund, et al. **The GALAH survey: tracing the Galactic disc with open clusters**. *Monthly Notices of the Royal Astronomical Society* 503:3 (2021), 3279–3296 (see pages 34, 49, 56, 59).
- [ST06] Allan Sandage and Gustav A. Tammann. **Absolute Magnitude Calibrations of Population I and II Cepheids and Other Pulsating Variables in the Instability Strip of the Hertzsprung-Russell Diagram**. *ARA&A* 44:1 (Sept. 2006), 93–140. DOI: [10.1146/annurev.astro.43.072103.150612](https://doi.org/10.1146/annurev.astro.43.072103.150612) (see pages 33, 65, 97).
- [Ste08] Joel Stebbins. **The light-curve of delta Cephei**. *Astrophysical Journal*, 27, 188-193 (1908) 27 (1908) (see page 2).
- [Ste10] Joel Stebbins. **The measurement of the light of stars with a selenium photometer, with an application to the variations of Algol**. *Astrophysical Journal*, 32, 185-214 (1910) 32 (1910) (see page 2).
- [Sto+04] J. Storm, B. W. Carney, W. P. Gieren, P. Fouqué, W. L. Freedman, B. F. Madore, and M. J. Habgood. **BVRIJK light curves and radial velocity curves for selected Magellanic Cloud Cepheids**. *A&A* 415 (Feb. 2004), 521–529. DOI: [10.1051/0004-6361:20034633](https://doi.org/10.1051/0004-6361:20034633). arXiv: [astro-ph/0401151](https://arxiv.org/abs/astro-ph/0401151) [[astro-ph](#)] (see page 87).
- [Sto+11] J. Storm, W. Gieren, P. Fouqué, T. G. Barnes, G. Pietrzyński, N. Nardetto, M. Weber, T. Granzer, and K. G. Strassmeier. **Calibrating the Cepheid period-luminosity relation from the infrared surface brightness technique. I. The p-factor, the Milky Way relations, and a universal K-band relation**. *A&A* 534A94 (Oct. 2011), A94. DOI: [10.1051/0004-6361/201117155](https://doi.org/10.1051/0004-6361/201117155). arXiv: [1109.2017](https://arxiv.org/abs/1109.2017) [[astro-ph.CO](#)] (see pages 17, 87, 89).
- [Str29] Otto Struve. **The stark effect in stellar spectra**. *Astrophysical Journal*, vol. 69, p. 173 69 (1929), 173 (see page 23).

- [Sur+08] Rebecca Surman, Gail C Mclaughlin, Maximilian Ruffert, H-Th Janka, and William Raphael Hix. **r-Process nucleosynthesis in hot accretion disk flows from black hole-neutron star mergers**. *The Astrophysical Journal* 679:2 (2008), L117 (see page 46).
- [Swe71] Allen V Sweigart. **A Method for Suppression of the Thermal Instability in Helium-Shell Stars**. *The Astrophysical Journal* 168 (1971), 79 (see page 14).
- [Swe87] Allen V Sweigart. **Evolutionary sequences for horizontal branch stars**. *Astrophysical Journal Supplement Series (ISSN 0067-0049)*, vol. 65, Sept. 1987, p. 95-135. 65 (1987), 95–135 (see page 14).
- [Swe97] Allen V Sweigart. **Effects of helium mixing on the evolution of globular cluster stars**. *The Astrophysical Journal* 474:1 (1997), L23 (see page 14).
- [Tre+23] E. Trentin, V. Ripepi, G. Catanzaro, J. Storm, M. Marconi, G. De Somma, V. Testa, and I. Musella. **Cepheid Metallicity in the Leavitt Law (C-Met-aLL) survey - II. High-resolution spectroscopy of the most metal poor Galactic Cepheids**. *MNRAS* 519:2 (Feb. 2023), 2331–2348. DOI: [10.1093/mnras/stac2459](https://doi.org/10.1093/mnras/stac2459). arXiv: [2209.03792](https://arxiv.org/abs/2209.03792) [[astro-ph.GA](#)] (see pages 66–68, 71, 99, 101, 104, 110, 120, 121, 129).
- [TSR03a] G. A. Tammann, A. Sandage, and B. Reindl. **New Period-Luminosity and Period-Color relations of classical Cepheids: I. Cepheids in the Galaxy**. *A&A* 404 (June 2003), 423–448. DOI: [10.1051/0004-6361:20030354](https://doi.org/10.1051/0004-6361:20030354). arXiv: [astro-ph/0303378](https://arxiv.org/abs/astro-ph/0303378) [[astro-ph](#)] (see page 70).
- [TSR03b] GA Tammann, A Sandage, and Bernd Reindl. **New period-luminosity and period-color relations of classical Cepheids: I. Cepheids in the Galaxy**. *Astronomy & Astrophysics* 404:2 (2003), 423–448 (see page 5).
- [Tur96] David G Turner. **The progenitors of classical Cepheid variables**. *Journal of the Royal Astronomical Society of Canada*, vol. 90, p. 82 90 (1996), 82 (see page 3).
- [Uda+18] A. Udalski, I. Soszyński, P. Pietrukowicz, M. K. Szymański, D. M. Skowron, J. Skowron, P. Mróz, R. Poleski, S. Kozłowski, K. Ulaczyk, K. Rybicki, P. Iwanek, and M. Wrona. **OGLE Collection of Galactic Cepheids**. *Acta Astron.* 68:4 (Dec. 2018), 315–339. DOI: [10.32023/0001-5237/68.4.1](https://doi.org/10.32023/0001-5237/68.4.1). arXiv: [1810.09489](https://arxiv.org/abs/1810.09489) [[astro-ph.SR](#)] (see pages 66, 99, 103).
- [van+07] Floor van Leeuwen, Michael W. Feast, Patricia A. Whitelock, and Clifton D. Laney. **Cepheid parallaxes and the Hubble constant**. *MNRAS* 379:2 (Aug. 2007), 723–737. DOI: [10.1111/j.1365-2966.2007.11972.x](https://doi.org/10.1111/j.1365-2966.2007.11972.x). arXiv: [0705.1592](https://arxiv.org/abs/0705.1592) [[astro-ph](#)] (see pages 67, 69, 70).

- [Vog90] Hermann Carl Vogel. **Spectrographische beobachtungen an algol**. *Astronomische Nachrichten*, volume 123, Issue 19, p. 289–123 (1890), 289 (see page 1).
- [VTR19] Licia Verde, Tommaso Treu, and Adam G. Riess. **Tensions between the early and late Universe**. *Nature Astronomy* 3 (Sept. 2019), 891–895. DOI: 10.1038/s41550-019-0902-0. arXiv: 1907.10625 [astro-ph.CO] (see page 33).
- [Wes46] A. J. Wesselink. **The observations of brightness, colour and radial velocity of δ Cephei and the pulsation hypothesis (Errata: 10 258, 310)**. *Bull. Astron. Inst. Netherlands* 10 (Jan. 1946), 91 (see page 17).
- [Wie+17] Piotr Wielgórski, Grzegorz Pietrzyński, Wolfgang Gieren, Marek Górski, Rolf-Peter Kudritzki, Bartłomiej Zgirski, Fabio Bresolin, Jesper Storm, Noriyuki Matsunaga, Dariusz Graczyk, and Igor Soszyński. **A Precision Determination of the Effect of Metallicity on Cepheid Absolute Magnitudes in VI-JHK Bands from Magellanic Cloud Cepheids**. *ApJ* 842:2, 116 (June 2017), 116. DOI: 10.3847/1538-4357/aa7565. arXiv: 1705.10855 [astro-ph.SR] (see page 89).
- [YCF12] David Yong, Bruce W Carney, and Eileen D Friel. **Elemental abundance ratios in stars of the outer galactic disk. IV. A new sample of open clusters**. *The Astronomical Journal* 144:4 (2012), 95 (see page 54).
- [Zhe53] SA Zhevakin. **K Teorii Cefeid. I**. *Astronomicheskii zhurnal* 30 (1953), 161–179 (see page 2).

List of Publications

- **Cepheid Metallicity in the Leavitt Law (C-MetaLL) survey: VI. Radial abundance gradients of 29 chemical species in the Milky Way disc**
 - Trentin, E.; Catanzaro, G. ; Ripepi, V. ; Alonso-Santiago, J. ; Molinaro, R. ; Storm, J. ; De Somma, G. ; Marconi, M. ; Bhardwaj, A. ; Gatto, M. ; Musella, I. ; Testa, V.
 - Pub Date: Oct 2024,A&A, Volume 690, id.A246, 16 pp., DOI: 10.1051/0004-6361/202450376
- **Discovery of a dormant 33 solar-mass black hole in pre-release Gaia astrometry**
 - Gaia Collaboration;...*Trentin, E...*
 - Pub Date: Jun 2024,A&A, Volume 686, id.L2, 23 pp., DOI: 10.1051/0004-6361/202449763
- **The Hertzsprung progression of classical Cepheids in the Gaia era**
 - Marconi, Marcella; De Somma, Giulia ; Molinaro, Roberto ; Bhardwaj, Anupam; Ripepi, Vincenzo ; Musella, Ilaria; Sicignano, Teresa ; *Trentin, Erasmo*; Leccia, Silvio
 - Pub Date: Apr 2024,MNRAS, Volume 529, Issue 4, pp.4210-4233, DOI: 10.1093/mnras/stae734
- **Classical Cepheid pulsation properties in the Rubin-LSST filters**
 - De Somma, Giulia; Marconi, Marcella; Cassisi, Santi; Molinaro, Roberto ; Bhardwaj, Anupam ; Ripepi, Vincenzo ; Musella, Ilaria; Pietrinferni, Adriano ; Sicignano, Teresa ; *Trentin, Erasmo*; Leccia, Silvio
 - Pub Date: Mar 2024,MNRAS, Volume 528, Issue 4, pp.6637-6659 , DOI: 10.1093/mnras/stae450

- **Cepheid Metallicity in the Leavitt Law (C-MetaLL) survey. V. New multiband (grizJHKs) Cepheid light curves and period-luminosity relations**
 - Bhardwaj, A.; Ripepi, V.; Testa, V. ; Molinaro, R.; Marconi, M. ; De Somma, G.; *Trentin, E.* ; Musella, I.; Storm, J.; Sicignano, T. ; Catanzaro, G.
 - Pub Date: Mar 2024,A&A, Volume 683, id.A234, 17 pp. , DOI:10.1051/0004-6361/202348140
- **Asiago Spectroscopic classification of SN 2024cao and AT 2024ccb within the 2023 NEON Observing School**
 - Reguitti, A.... *Trentin, E.*...
 - Pub Date: Feb 2024,Transient Name Server AstroNote 2024-50
- **OGLE-GD-CEP-0516: The most metal-poor lithium-rich Galactic Cepheid**
 - Catanzaro, G.; Ripepi, V.; Salaris, M. ; *Trentin, E.*
 - Pub Date: Feb 2024,A&A, Volume 682, id.L21, 7 pp., DOI:10.1051/0004-6361/202449160
- **First spectroscopic investigation of anomalous Cepheid variables**
 - Ripepi, V.; Catanzaro, G. ; *Trentin, E.*; Straniero, O.; Mucciarelli, A.; Marconi, M. ; Bhardwaj, A. ; Fiorentino, G. ; Monelli, M.; Storm, J.; De Somma, G.; Leccia, S. ; Molinaro, R. ; Musella, I.; Sicignano, T.
 - Pub Date: Feb 2024,A&A, Volume 682, id.A1, 19 pp. ,DOI:10.1051/0004-6361/202347991
- **Cepheid Metallicity in the Leavitt Law (C- MetaLL) survey. IV. The metallicity dependence of Cepheid period-luminosity relations**
 - *Trentin, E.*; Ripepi, V. ; Molinaro, R. ; Catanzaro, G. ; Storm, J. ; De Somma, G.; Marconi, M. ; Bhardwaj, A. ; Gatto, M. ; Testa, V. ; Musella, I. ; Clementini, G. ; Leccia, S.
 - Pub Date: Jan 2024,A&A, Volume 681, id.A65, 20 pp.,DOI:10.1051/0004-6361/202347195
- **High-resolution Spectroscopic Metallicities of Milky Way Cepheid Standards and Their Impact on the Leavitt Law and the Hubble Constant**

- Bhardwaj, Anupam; Riess, Adam G.; Catanzaro, Giovanni; **Trentin, Erasmo**; Ripepi, Vincenzo; Rejkuba, Marina; Marconi, Marcella; Ngeow, Chow-Choong; Macri, Lucas M.; Romaniello, Martino ; Molinaro, Roberto; Singh, Harinder P.; Kanbur, Shashi M.
- Pub Date: Sep 2023,ApJ, Volume 955, Issue 1, id.L13, 8 pp.,DOI:10.3847/2041-8213/acf710
- **Cepheid metallicity in the Leavitt law (C-MetaLL) survey - III. Simultaneous derivation of the Gaia parallax offset and period-luminosity-metallicity coefficients**
 - Molinaro, R. ; Ripepi, V. ; Marconi, M.; Romaniello, M. ; Catanzaro, G.; Cusano, F. ; De Somma, G.; Musella, I.; Storm, J.; **Trentin, E.**
 - Pub Date: Apr 2023,MNRAS, Volume 520, Issue 3, pp.4154-4166, DOI:10.1093/mnras/stad440
- **Cepheid Metallicity in the Leavitt Law (C- MetaLL) survey - II. High-resolution spectroscopy of the most metal poor Galactic Cepheids**
 - **Trentin, E.**; Ripepi V.; Catanzaro G.; Storm J.; Marconi M.; De Somma G.; Testa, V. Musella I.
 - Pub Date: Feb 2023,MNRAS, Volume 519, Issue 2 pp. 2331-2348, DOI: 10.1093/mnras/stac2459
- **Cepheid metallicity in the Leavitt law (C-metall) survey - I. HARPS-N@TNG spectroscopy of 47 classical Cepheids and 1 BL Her variables**
 - Ripepi, V.; Catanzaro, G.; Molinaro, R. ; Gatto, M.; De Somma, G.; Marconi, M.; Romaniello, M. ; Leccia, S. ; Musella, I.; **Trentin, E.**; Clementini, G. ; Testa, V.; Cusano, F. ; Storm, J.
 - Pub Date: Dec 2021,MNRAS, Volume 508, Issue 3 pp. 4047-4071, DOI: 10.1093/mnras/stab2460

Conferences and Workshops

- **Resolved stellar populations from photographic plates to large surveys. A celebration of Peter B. Stetson's career in astronomy**
 - Oct 2024, Florence, Italy
 - Contributed talk
- **NEON Observing School**

- Feb 2024, Asiago, Italy
 - 2 weeks Observing school
- **STARS (Across the Universe)**
 - Oct 2023, Naples, Italy
 - Contributed talk
- **GaiaUnlimited Community Workshop 2: The Gaia selection function and how to use the GaiaUnlimited tools**
 - Oct 2023, Turin, Italy
 - Workshop
- **Stellar Variability, Stellar Multiplicity: Periodicity in Time & Motion MW-GAIA WG2 Hybrid Workshop**
 - Jun 2023, Sofia, Bulgaria
 - Poster at the WG2 Workshop
- **IAU Symposium 376: At the cross-roads of astrophysics and cosmology: Period–luminosity relations in the 2020s**
 - Apr 2023, Budapest, Hungary
 - Contributed talk
- **IAU Symposium 376 International Spring School**
 - Apr 2023, Budapest, Hungary
 - Spring school: Modern methods of cosmic distance determination
- **RRLCep2022 Large-scale surveys as bridges between spectroscopy and photometry**
 - Sep 2022, La Palma, Spain
 - Contributed talk
- **Second ESCAPE VO School**
 - Feb 2022, online
 - Virtual Observatory School
- **MW-Gaia: Stellar Spectroscopy and Astrophysical Parameterisation from Gaia to Large Spectroscopic Surveys**

- Sep 2021, online
- Phd Working group
- **Practical applications of Machine Learning in modern Astronomy**
 - Nov 2020, online
 - DESY Machine Learning Workshop